The Structure of the RC-LH1 Complex from *Rps. acidophila*: Optical Single-Molecule Spectroscopy and Numerical Simulations

Der Universität Bayreuth
zur Erlangung des Grades eines
Doktors der Naturwissenschaften (Dr. rer. nat.)
eingereichte Abhandlung

von

Paul Sebastian Böhm

aus Heltau (Rumänien)

1. Gutachter: Prof. Dr. J. Köhler
2. Gutachter: Prof. Dr. M. Lippitz

Tag der Einreichung: 15. Oktober 2014
Tag des Kolloquiums: 4. März 2015

Scientific publications of results presented in this work

- P.S. Böhm, J. Southall, R.J. Cogdell and J. Köhler Single-Molecule Spectroscopy on RC-LH1 Complexes of *Rhodopseudomonas acidophila* Strain 10050. *J. Phys. Chem. B* **117** 3120–3126 (2013).
- P.S. Böhm, R. Kunz, J. Southall, R.J. Cogdell and J. Köhler Does the Reconstitution of RC-LH1 Complexes from *Rhodopseudomonas acidophila* Strain 10050 into a Phospholipid Bilayer Yield the Optimum Environment for Optical Spectroscopy? *J. Phys. Chem. B* **117** 15004–15013 (2013).

Contents

List of abbreviations

AFM	atomic force microscopy
BChl	bacteriochlorophyll
D	debye, unit of the electric dipole moment, $1D \approx 0.21\ e\mathring{A}$ (e: elementary unit of charge)
Da	dalton, unified atomic mass unit, $1\ Da \mathrel{\hat{=}} 1\ u$
DDM	dodecyl-β-D-maltoside
DOPC	1,2-dioleoyl-*sn*-glycero-3-phosphocholine
$fwhm$	full width at half-maximum
LDAO	lauryldimethylamine N-oxide
LH	light-harvesting
PDB	protein database
PSU	photosynthetic unit
PSB	phonon side-band
PVA	polyvinyl alcohol
Q_B	ubiquinone
Q_BH_2	ubiquinol
Rb.	*Rhodobacter*
RC	reaction center
Rps.	*Rhodopseudomonas*
Rsp.	*Rhodospirillum*
sdev	standard deviation
T.	*Thermochromatium*
Tris	tris-hydroxymethyl-aminomethane
ZPL	zero-phonon line

1 Introduction

Photosynthesis, the biological process whereby solar energy is stored as a fuel, is the vital link between the energy of the sun and life on earth [1]. Due to their comparatively simple structural organization, purple photosynthetic bacteria have proved to be excellent model organisms with which to study the early reactions of photosynthesis. Purple bacteria are anaerobic photosynthetic organisms that live in the anaerobic layers of ponds, lakes and streams [2]. This ecological niche entails that the spectrum of the solar radiation that reaches the purple bacteria has previously been filtered by the chlorophyll containing plants and algae located in the oxygenic phototrophs, in the water layers above the purple bacteria. The filtering removes the blue and red light from the spectrum and accordingly, purple bacteria have to 'make their living' by utilizing green light and the light from the near infra-red (NIR) spectral region. For this purpose purple bacteria incorporate bacteriochlorophyll (BChl) and carotenoid molecules as their light-absorbing pigments, whose major absorption bands lie in the required spectral regions.
As in the habitat of purple bacteria, at the bottom of ponds, light conditions are quite dark in comparison to *e.g.* bright daylight at the surface, they make use of a light-harvesting (LH) antenna system. These are pigment-protein complexes responsible for the absorption of light and the rapid and efficient transfer of this absorbed energy to a reaction center (RC), where it is used to initiate a transmembrane charge separation. The effect of the LH apparatus is to increase the cross-section for light-absorption of each RC, or, putting it differently, to concentrate diffuse solar energy at the RC [2]. Furthermore, depending on the light-conditions under which they are grown, purple bacteria are able to adapt the size of the LH apparatus per RC, where this size is increased under low-light illumination and decreased under high-light illumination [3]. Finally, the absorption cross-section of a bacterial cell is physically increased, as the LH system and all further constituents of the photosynthetic apparatus are located in and on intracytoplasmic membranes, which are infoldings of the cell membrane towards the cytoplasmic space of the cell in form of vesicles, tubes or lamellae.
Most purple bacterial species contain two types of antenna complexes, the peripheral light-harvesting 2 (LH2) complex and the light-harvesting 1 (LH1) complex

which forms a closely associated unit with a RC, known as the RC-LH1 core complex. The LH2 complexes are not in direct contact with the RC, but are arranged around the RC-LH1 complexes in a two-dimensional array. The shape of both types of LH complexes is predominantly circular and the pigment molecules are non-covalently bound within a protein scaffold. In the LH2 complexes one can actually distinguish between two characteristic rings of BChl molecules, the B800 ring and the B850 ring, whereas in LH1 only one ring of BChl molecules can be found, the B880 ring. The different BChl assemblies are named according to their absorption maxima in the NIR. The hierarchical arrangement of these BChl arrays - high-energy pigments are physically distant from the RC, while low-energy pigments are physically closer to the RC - results in a rapid and very efficient funneling of the excitation energy to a RC [4].
A process that greatly helps in maintaining a high transfer efficiency to a RC, is the quantum coherent sharing of excitation between multiple pigments in strongly coupled pigment aggregates [5]. This process, also referred to as excitonic coupling, combines the transition-dipole moments of the pigments involved, and modifies the excited-state energy levels, thereby enabling rapid transfer of excitation over large distances. As a result of the excitonic coupling of the pigments in the LH complexes and in the RC, Förster resonant energy transfer (FRET) rates between the LH complexes and between the LH1 complex and the RC become high enough, to ensure that the energy of most photons absorbed by the LH2 complexes reaches a RC within about 100 ps, thus achieving a transfer efficiency of about 90% in the photosynthetic apparatus of purple bacteria.
Lately the effect of quantum coherence, manifesting itself in characteristic quantum beating signals between the electronic energy eigenstates, on the energy transfer efficiency received increasing interest in literature ([1, 6, 7] and references therein). For instance, in [7], where quantum coherent energy transfer was first identified in individual LH2 complexes, it was argued that long-lived quantum coherence might render the energy transfer process robust against intrinsic disorder in the pigment-protein complexes, being a prerequisite for efficient light harvesting. Even more specific, in [1] electronic coherences were revealed between excitonic states as well as between excitonic and charge-transfer states in a photosynthetic RC, and evidence was presented for a strong correlation between the degree of electronic coherence and efficient and ultrafast charge separation in the RC.
When the excitation has reached the RC, charge separation takes place as an excited electron is transferred in several steps to an ubiquinone molecule which is loosely bound in the RC. After a second turnover the fully reduced ubiquinone leaves the RC-LH1 complex and passes into the membrane space, in order to transfer electrons to the cytochrome b/c_1 complex as part of a cyclic electron transport pathway that drives bacterial photosynthesis. It seems that different species of purple bacteria have evolved different types of RC-LH1 complexes to enable the transfer of ubiquinone through the LH1 complex [8]. With the recent presenta-

tion of the crystal structure of the RC-LH1 complex from *Thermochromatium (T.) tepidum* [9], one can basically distinguish between three different types of RC-LH1 complexes: The first type is dimeric, where a S-shaped LH1 complex surrounds two RCs, and the two latter types are monomeric, with one RC encircled by an elliptical LH1 complex, respectively. Both the dimeric complex and one of the monomeric complexes contain gaps in their LH1 aggregates (two for the dimeric LH1 and one for the monomeric LH1) and it was argued that these gaps may act as a gate for the shuttling of ubiquinone. For the remaining monomeric RC-LH1 type, defined by the RC-LH1 complex from *T. tepidum*, the LH1 complex forms a completely closed ring around the RC. Here, channels have been found in the LH1 complex at a level corresponding to the middle of the transmembrane region and it was suggested that these channels provide the same function as the gaps in the two other types of RC-LH1 complexes. To date, structural information on the RC-LH1 complex from *Rhodopseudomonas (Rps.) acidophila* which is investigated in this thesis, is very limited. It is only known that the RC-LH1 complexes from this bacterial species are in all likelihood monomeric [2, 10].

In this thesis single-molecule spectroscopy has been performed on individual RC-LH1 complexes. The intriguing feature of this type of spectroscopy is, that spectral details become visible that are otherwise buried under the ensemble average [11, 12]. In fluorescence-excitation spectra of individual LH complexes, the number of absorption lines, their spectral positions and the mutual orientation of their corresponding transition-dipole moments, provides information about the electronic structure of the strongly coupled pigment aggregates. By combining this information with the results from numerical simulations, it is possible to make predictions on the specific geometric arrangement of the pigments in these aggregates [13–15]. Since the native photosynthetic membrane comprises a variety of different pigment-protein and protein complexes, a systematic investigation of a specific, individual complex is not possible in this environment. For investigation, the different components of the photosynthetic apparatus are therefore detergent-solubilized from their host biological membrane and separated from each other. This can pose a problem, since it is generally assumed that the LH complexes are more stable and fully native when they are housed in a lipid bilayer as compared to a detergent environment [16–19], and in particular LH1 complexes are considered to be more fragile than LH2 complexes [2, 20].

This thesis is structured as follows: In chapter 2 the biological and photo-physical properties of the photosynthetic apparatus of purple bacteria are introduced. In chapter 3 the sample preparation and the low-temperature single-molecule setup are described. Chapter 4 is divided in two parts: In the first part RC-LH1 complexes from *Rps. acidophila* are revisited for single-molecule spectroscopy, this time applying a relatively mild detergent, and the results are compared to a precursor study, where the complexes were stabilized in a more deactivating detergent. In the second part, the influence of the environment on the spectra of the RC-LH1

complexes from *Rps. acidophila* is investigated, thereby seeking to test whether the immobilization of the complexes in a polyvinyl alcohol matrix might lead to a deformation of the LH1 structure. In chapter 5 the statistical distributions of the spectral features of the RC-LH1 complexes are compared to the data from numerical simulations of different LH1 model structures. In doing so, a LH1 model is found that can satisfyingly reproduce the experimental data. Finally, in chapter 6 an alternative interpretation of the spectral characteristics of the RC-LH1 complexes is proposed, taking the specific overlap between the exciton wavefunctions for the exciton relaxation dynamics into account.

2 Light-harvesting complexes

2.1 The photosynthetic apparatus of purple bacteria

The photosynthetic apparatus of purple bacteria resides in the intracytoplasmic membrane of the bacterial cell. It consists of several transmembrane protein and pigment-protein complexes. Generally, one distinguishes between the primary "light-reactions" of the photosynthetic process, followed by the "dark-reactions". In this section, firstly the "light-reactions" will be described and the components of the photosynthetic apparatus which are involved in them, and subsequently the "dark" processes will be referred to.
The "light-reactions" take place within the so called photosynthetic unit (PSU) which, for most purple bacterial species, consists of two well defined pigment-protein complexes - the peripheral light-harvesting 2 (LH2) complex and the reaction-center light-harvesting 1 (RC-LH1) core complex [2, 4]. Thereby, each LH1 complex directly surrounds a RC, whereas the LH2 complexes are not in direct contact with a RC, but are arranged around the RC-LH1 complexes in a two-dimensional array (Figure 2.1a,b). Generally, the "light-reactions" occurring in the PSU can be divided into four basic steps: (I.) Absorption of sunlight by the light-harvesting complexes LH2 and LH1, (II.) ultrafast transfer of the excitation energy to a photo-active pigment pair (special pair, P) in the RC, (III.) oxidation of P upon its relaxation from the excited state and (IV.) stabilization of the charge-separated state by secondary electron transfer reactions (for I. and II. see Figure 2.1b, for III. and IV. *vide infra*). Regarding the steps I and II, the light-harvesting antennas LH2 and LH1 drastically increase the effective cross-section for light absorption of each RC. Thus, while under bright sunlight a single chlorophyll molecule would only absorb about 10 photons per second, the maximum turnover rate of a purple bacterial RC is about 1000 Hz [4, 22]. Furthermore, depending on the light intensity under which they are grown, purple bacteria are able to adapt the ratio of peripheral LH2 complexes per RC-LH1 core complex, where this ratio is increased under low-light conditions and decreased under high-light conditions [3]. In this way, the bacteria

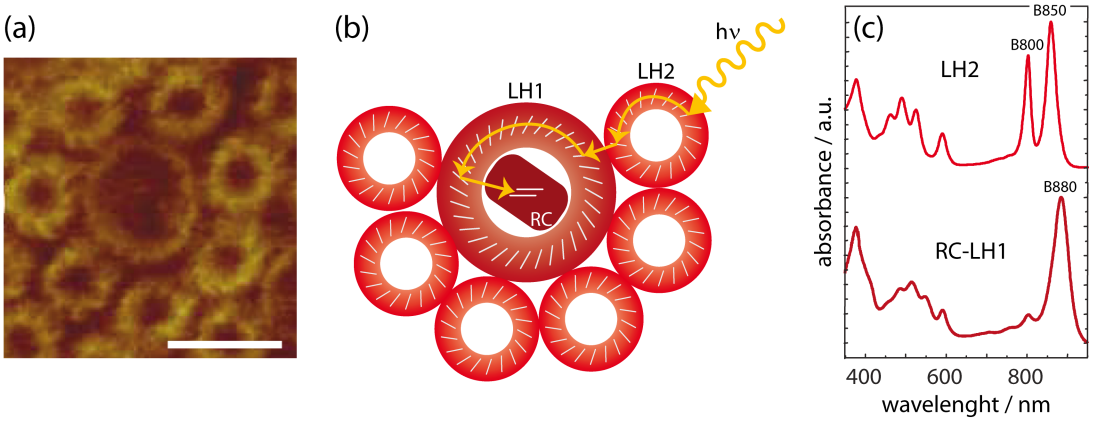

Figure 2.1: *(a) High-resolution atomic force microscopy (AFM)-topograph of a native photosynthetic membrane (scale bar, 10 nm, from [3]). The constituents of the photosynthetic unit (PSU) are well discernable - seven peripheral LH2 complexes (small rings) surround one RC-LH1 core complex (large ring). (b) Sketch of the PSU indicating the primary steps in bacterial photosynthesis - absorption of light by the light-harvesting complexes LH2 and LH1, and efficient transfer of the energy to a photo-active pigment pair (special pair, P) in the RC. The white bars indicate the bacteriochlorophyll (BChl) a molecules of the B850 and the B880 pigment arrays in LH2 and LH1, respectively, and the two BChl a molecules of the RC special pair, P. The pigment molecules are held in place by a protein scaffold indicated in red (adapted from [21]). (c) Room-temperature absorption spectra of the LH2 and RC-LH1 complexes from Rps. acidophila solubilized from their native membrane environment (from [2]). The characteristic absorption bands of the LH complexes in the near infra-red (NIR) are indicated, B800 and B850 for LH2 and B880 for LH1. The P absorption of the RC (≈ 870 nm, [4]) is hidden under the LH1 B880 band.*

ensure efficient photon capture at low-intensity illumination and prevent photodamage at high-intensity illumination. During the last decade atomic force microscopy (AFM) has proven a powerful tool to reveal the supramolecular assembly of the pigment-protein complexes in the PSU of native membranes (Figure 2.1a, see [23] for a review).

Through interactions with the protein scaffold and with each other the absorption wavelengths of the pigment molecules in the light-harvesting complexes LH2 and LH1 can be specifically tuned (this will be discussed in greater detail in the progress of this work). As a result, LH2 complexes have two strong absorption bands in the near infra-red (NIR) at about 800 and 850 nm, while LH1 complexes only have a single strong absorption band at about 880 nm (Figure 2.1c). In this way, purple bacteria do not only broaden the wavelength range over which light can be absorbed, but also make use of the concept of the energy funnel [2, 4]. This concept bases on the principle that light-harvesting complexes which are more distant from the RC absorb at shorter wavelengths (LH2), while light-harvesting complexes proximal to

the RC absorb at longer wavelengths (LH1). Energy transfer then occurs from the high-energy pigments (LH2) to the lower-energy pigments (LH1) which are physically closer to the RC. The small amount of energy loss during each transfer step provides a degree of irreversibility to the process.

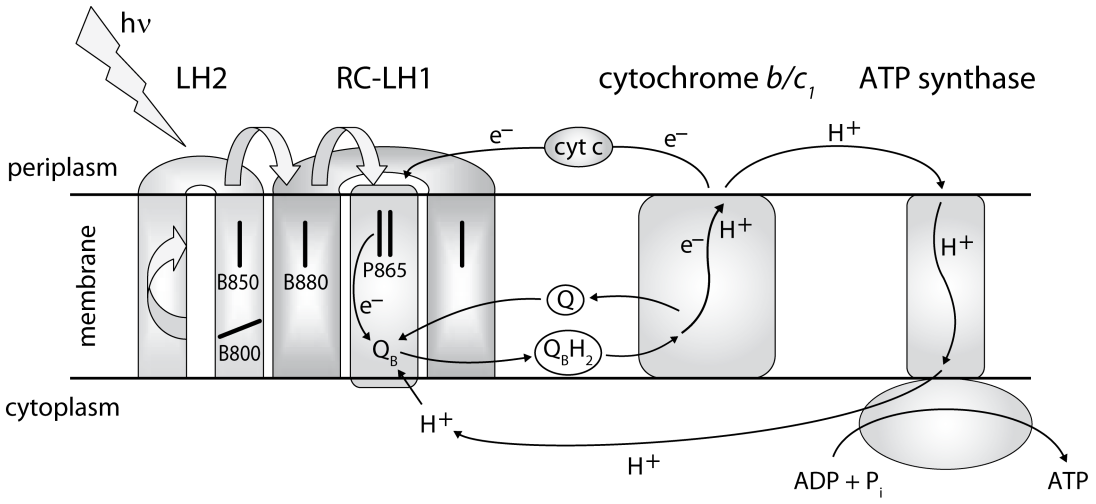

Figure 2.2: *Cartoon of a section through the intracytoplasmic membrane of a purple bacterium, showing the different components of the photosynthetic apparatus and the various steps of the cyclic electron transfer in bacterial photosynthesis (adapted from [2]). The black bars in the light-harvesting complexes indicate the positions and orientations of the B800 and B850 BChls in LH2, the B880 BChls in LH1 and the special pair (P) BChls in the RC. The numbers indicate the respective absorption maxima of the pigments, in nm. The gray arrows indicate energy transfer upon absorption of light and the black arrows follow the cyclic electron transfer pathway which is coupled to the translocation of protons from the cytoplasm to the periplasm. For details see text.*

In the cartoon of the photosynthetic membrane in Figure 2.2 the complete photosynthetic process of purple bacteria, comprising both the "light-reactions" and the "dark-reactions", is sketched. Beginning with the absorption of light, this process finally ends with the formation of adenosine triphosphate (ATP) from adenosine diphosphate (ADP) and inorganic phosphate (P_i). In the following the crucial steps of this photo-induced cyclic electron transfer chain will be briefly described [2, 4, 24–26]. "Light-reactions" (*vide supra*): Upon absorption of a photon by a pigment molecule in one of the peripheral antenna complexes the excitation energy is transferred via neighboring pigments and complexes to the special pair (P) in the RC within about 60 *ps* [27]. Thereby, the energy transfer from LH1 to P, occurring roughly within 35 *ps*, is the rate-limiting step of the overall trapping process which still has a high quantum yield of about 95%. In the RC the energy is used for the release of an electron upon relaxation of the excited P. "Dark-reactions": In a stepwise electron transfer the electron finally reaches Q_B, where in the last step the

electron is transferred from the permanently bound, primary ubiquinone Q_A to the exchangeable, secondary ubiquinone Q_B. As wasteful back reactions, in which the electron returns to the oxidized P from one of the acceptors in the electron transfer chain, are by at least a factor of 50 slower than the forward reactions, this leads to a stable charge separation across the membrane. After a second turnover, the now doubly reduced Q_B picks up two protons from the cytoplasmic space to form ubiquinol, Q_BH_2. Q_BH_2 which is only weakly bound in the RC, leaves the RC through the LH1 complex into the membrane lipid phase towards the cytochrome b/c_1 complex. There Q_BH_2 is oxidized by cytochrome c (cyt c), a reaction catalyzed by the cytochorme b/c_1 complex which releases two protons into the periplasmic space. The cyclic electron transfer is completed by the reduction of the photo-oxidized primary electron donor P by cyt c. In the RC, Q_BH_2 is replaced by an oxidized ubiquinone (shown as Q in Figure 2.2) from the membrane lipid phase. Regarding the overall process, it can be seen that the cyclic electron transfer is coupled to the translocation of protons from the cytoplasm to the periplasm, resulting in a proton gradient across the membrane. This so called proton motive force is then used to fuel the ATP synthase for the phosphorylation of ADP to ATP. With this last step, the conversion of solar energy into chemically bound energy is completed and ATP can now be used as energy source for the metabolism of the bacterium.

2.2 Pigment molecules

As already seen, chlorophyll molecules accomplish different functions in the photosynthetic process, such as light harvesting and excitation transfer in the antenna system, and charge separation in the RC. Most species of purple bacteria express BChl *a* as their chlorophyll pigment and only few species express BChl *b*, but not both types are expressed in the same species [4].
The structure of BChl *a* is depicted in Figure 2.3a. It consists of a planar, squarish (side length ≈ 10 *Å*) bacteriochlorin ring with a central Mg^{2+}-ion and a covalently bound phytol chain which serves as anchor for the pigment in the protein scaffold. The conjugated double bonds in the bacteriochlorin ring are responsible for the characteristic BChl *a* absorption spectrum (Figure 2.3b). The main electronically excited singlet states of BChl *a* are termed Q_x (S_2) and Q_y (S_1), respectively. Their transition-dipole moments have a mutually orthogonal polarization and, for monomeric BChl *a* in 7:2 (v/v) acetone:methanol, the corresponding absorption peaks can be found at 590 *nm* (Q_x) and at 772 *nm* (Q_y) (Figure 2.3). Two energetically higher transitions, B_x/B_y (S_3/S_4), give rise to the Soret band below 400 *nm*. The Soret transitions have a mixed polarization. Around 700 *nm* a vibrational overtone transition which couples to the electronic Q_y transition can be observed [28] (Figure 2.3b). Metal-free BChl *a* is called bacteriopheophytin (BPheo) *a*. This

type of chromophore can be found *e.g.* in the RC of purple bacteria.

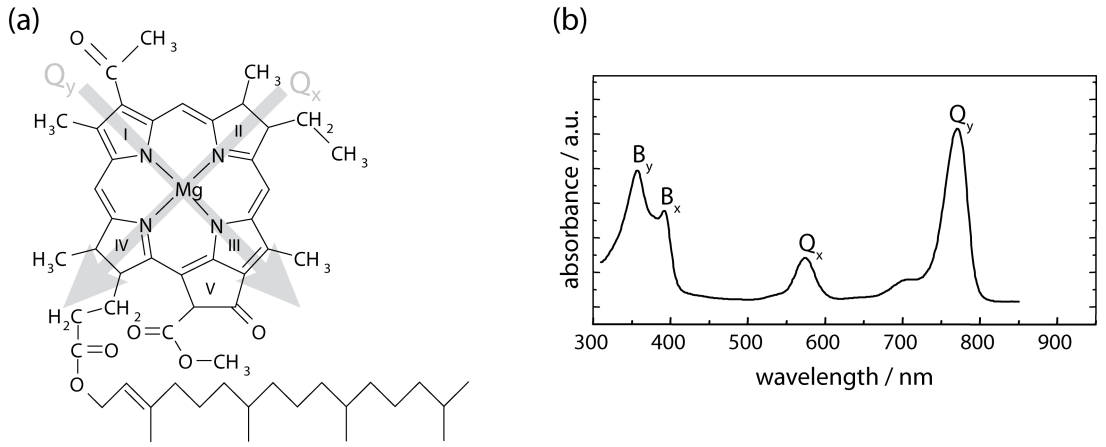

Figure 2.3: *(a) Chemical structure of bacteriochlorophyll (BChl) a, consisting of a bacteriochlorin macrocycle with a central Mg^{2+}-ion and a hydrophobic phytol chain (adapted from [29]). The five rings in the bacteriochlorin macrocycle are numbered according to the Fischer system [4]. The gray arrows indicate the orientations of the Q_y and the Q_x transition-dipole moments. (b) Room-temperature absorption spectrum of monomeric BChl a in 7:2 (v/v) acetone:methanol, where the characteristic BChl a absorption bands are indicated (see text; from [2]).*

In the light-harvesting complexes the BChl *a* molecules are non-covalently bound to the protein scaffold. Interactions of the pigments with the protein environment through dispersive interactions (also known as 'solvent shift') [30], or more specifically, through hydrogen-bonding of the protein residues to the side groups of the bacteriochlorin macrocycle [31], induce shifts of the Q_y transition energy. Furthermore, if on top of these interactions, the BChl *a* molecules in the light-harvesting complexes also interact with each other, the Q_y absorption band of BChl *a* can be red-shifted by more than 100 nm in comparison to the non-solvated pigment [30]. Carotenoids are the other important class of pigments found in the light-harvesting complexes. They are extended molecules with a delocalized π-electron system. The major carotenoid in the RC-LH1 complex from *Rps. acidophila*, which is investigated in this thesis, is spirilloxanthin [32], and this type of carotenoid was also found in the recently published high-resolution crystal structure of the RC-LH1 complex from *T. tepidum* [9]. By absorbing light in the visible range from $400-540$ nm (see *e.g.* Figure 4.2), the carotenoids fill the spectral niche left open by the BChls. These absorption characteristics of the carotenoids are also responsible for the red/brown color of purple bacteria, as, when embedded in the bacteria, the main BChl *a* absorption bands lie in the NIR, outside the visible range [2]. Most importantly however, besides light harvesting and energy transfer to chlorophyll-type pigments, carotenoids in LH complexes function in a process called photoprotection [4, 33].

Thereby, carotenoids rapidly quench triplet excited states of chlorophylls, before they can react with oxygen to form the highly reactive and damaging excited singlet state of oxygen. Additionally, they also quench singlet oxygen if it is somehow formed.

2.3 The LH2 complex from *Rps. acidophila*

The structure of the LH2 complex from *Rps. acidophila* is quite important for this work, although the main objective was the investigation of the structure of the LH1 complex from this bacterial species. For this, amongst others, numerical simulations have been applied. However, since, until recently [9], no high-resolution structure of a RC-LH1 complex was available, for the buildup of LH1 model aggregates for the numerical simulations (chapter 5), it was made use of the detailed structural knowledge available for the LH2 complex from *Rps. acidophila* already since 1995 [34]. In [34] the LH2 structure was determined to a resolution of 2.5 $\mathring{A}$ and an even higher resolved (2.0 $\mathring{A}$) LH2 crystal structure appeared in 2003 [35]. Therefore, the latter structure was chosen as reference point for the construction of the LH1 model aggregates in the numerical simulations of this work. In the present section the overall structural composition of the LH2 complex from *Rps. acidophila* will be briefly described, with a main focus on the arrangement of the BChl *a* pigments. With this, and also taking the following section 2.4 on RC-LH1 complexes into consideration, it will become clear that the BChl *a* arrangement in LH2 and LH1 complexes is in part very similar.
Figure 2.4a shows a side-view of the LH2 complex from *Rps. acidophila*. It is a circular nonamer in which the carotenoids (blue) and the BChl *a* molecules (red/yellow) are non-covalently bound to nine pairs of low-molecular-weight, hydrophobic apoproteins, called α (gray) and β (green). Thereby, each $\alpha\beta$-heterodimer accommodates three BChl *a* molecules and one carotenoid, which is rhodopin glucoside in the case of LH2 *acidophila*. If one would "walk" through the LH2 complex starting from the cytoplasmic side, the first group of BChl *a* pigments one would encounter, are nine monomeric BChl *a* molecules whose bacteriochlorin macrocycles lie flat, parallel to the plane of the membrane (Figure 2.4b). The center-to-center distance between these BChls is about 21 $\mathring{A}$ [2]. They give rise to the 800 *nm* absorption band (Figure 2.1c) and are therefore referred to as B800 molecules. Proceeding further upwards towards the periplasm, one encounters a second group of BChl *a* molecules. In this pigment group 18 BChl *a* molecules can be found, two per each $\alpha\beta$-apoprotein pair (Figure 2.4c). Thereby, the central Mg^{2+}-ions of the BChls are coordinated through histidine residues from the proteins, coming one from the α-apoprotein and one from the β-apoprotein. The BChls in this pigment array are tightly packed and oriented with the planes of their bacteriochlorin rings perpendicular to the membrane plane. Looking from the periplasmic side, the arrangement

of these pigments is reminiscent to the blades of a turbine wheel. The center-to-center separation between the BChls in this group amounts to 9.5 $\AA$ within an $\alpha\beta$-heterodimer and to 8.8 $\AA$ between adjacent BChls of neighboring dimer units [2]. This ring of strongly coupled BChls is collectively responsible for the LH2 absorption at 850 nm (Figure 2.1c) and they are therefore called B850 BChls.

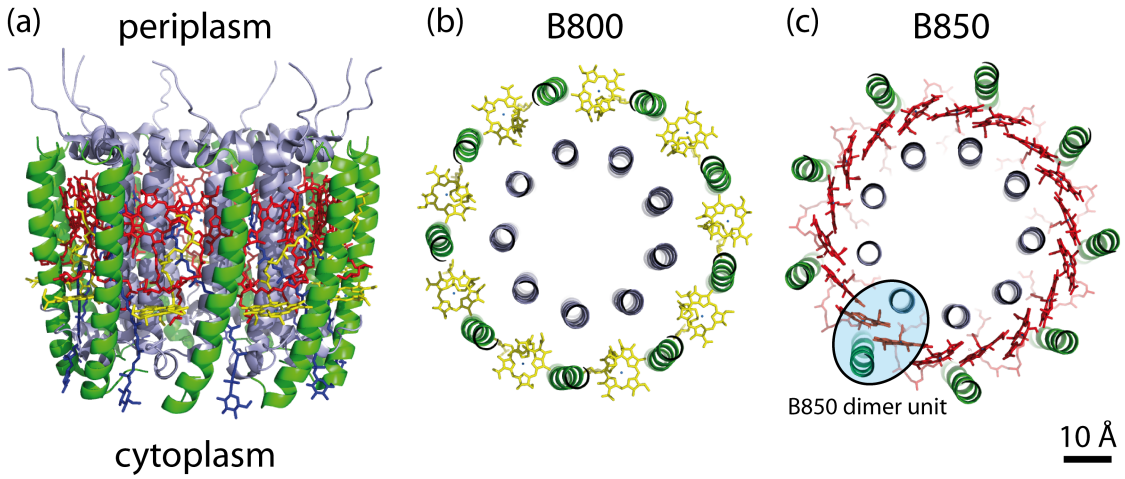

Figure 2.4: *(a) Crystal structure of the LH2 complex from Rps. acidophila viewed along the plane of the membrane ([36], protein database (PDB) file: 2FKW). Color scheme (applies also for the panels (b) and (c)): α/β apoproteins, gray/green; carotenoids (rhodopin glucoside), blue; B800/B850 BChls, yellow/red. (b) The B800 BChl a molecules viewed from the cytoplasmic side, perpendicular to the plane of the membrane. These BChls are located between the β-apoproteins with the planes of their bacteriochlorin rings parallel to the membrane plane. The blue dots represent the central Mg^{2+}-ions of the BChls. For clarity, the carotenoids and the B850 BChl a molecules have been removed. (c) The B850 BChl a molecules viewed from the periplasmic side, perpendicular to the plane of the membrane. These BChls are oriented with the planes of their bacteriochlorin rings perpendicular to the membrane plane. Two B850 BChl a molecules are liganded in each $\alpha\beta$-apoprotein pair, forming a basic B850 modular unit (blue shaded area). For clarity, the carotenoids and the B800 BChl a molecules have been removed. The figure was created with PyMOL; Schrodinger, 2010.*

As in LH1 complexes the BChl a molecules are also arranged in a tightly packed manner, very similar to the B850 pigment array in LH2 (see next section 2.4), the mutual orientation of the two B850 BChl a pigments in an $\alpha\beta$-heterodimer (Figure 2.4c) was used as reference for the basic modular unit in the construction of LH1 model aggregates used for numerical simulations (see chapter 5).

2.4 RC-LH1 complexes

With the recent presentation of the high-resolution (3.0 *Å*) crystal structure of the RC-LH1 complex from *T. tepidum* [9] and the reasonably resolved (4.8 *Å*) structure of the RC-LH1 complex from *Rps. palustris* [24], one can basically distinguish between two types of monomeric core complexes: For the first type (*T. tepidum*) the LH1 complex completely surrounds the RC, but for the second type (*Rps. palustris*) an additional protein out of register with the array of inner LH1 α-apoproteins, creates a gap in the LH1 aggregate (Figure 2.5). Nevertheless, the general construction principle of these two types of LH1 complexes is assumed to be equivalent: Two BChl *a* molecules and one carotenoid (presumably for *Rps. palustris*, *vide infra*) are non-covalently bound between two low-molecular-weight apoproteins α and β. These subunits then oligomerize around the RC, forming a closed array of 16 subunits for *T. tepidum*, whereas for *Rps. palustris* one subunit is replaced by the so called 'W' protein. Thereby, it has to be noted that due to the rather low resolution of the *palustris* structure, the macrocycles of the BChl *a* molecules in the LH1 complex are positioned with low accuracy and it was not possible to locate the carotenoid molecules [24] (Figure 2.5a,c). This was different for the LH1 complex from *T. tepidum* [9] (Figure 2.5b,d). Here, it was shown that the arrangement of the BChl *a* molecules in the LH1 complex is quite analogous to the association of the B850 BChls in LH2, with an average Mg-Mg distance of 9.04 *Å* within a LH1 subunit and 8.46 *Å* between adjacent subunits. As for the LH2 complex, the two BChls in a LH1 $\alpha\beta$-heterodimer are liganded to histidine residues, one coming from the α-apoprotein and one from the β-apoprotein. Additionally, it was possible to locate the positions of the 16 carotenoid molecules (spirilloxanthin) in the LH1 complex, one per each $\alpha\beta$-heterodimer. In both types of LH1 complexes the BChls form a strongly coupled, elliptical array of 30 pigments in the case of *Rps. palustris* and of 32 pigments for *T. tepidum*, giving rise to a single, strong Q_y absorption band in the $870 - 890$ *nm* region, referred to as B880 band (Figure 2.1c). For *T. tepidum*, Ca^{2+}-binding to the LH1 apoproteins (Figure 2.5b) results in a shift of this band to 915 *nm*. Overall, the two RC-LH1 complexes have elliptical structures with comparable dimensions, with the long axis of the ellipse amounting to 110 *Å* for *Rps. palustris* and to 105 *Å* for *T. tepidum*, measured as the distance between the centers of opposing β-apoproteins. The RC of *T. tepidum* has a permanent cytochrome unit, missing for the *Rps. palustris* complex which has a *Rb. sphaeroides*-type RC without this subunit (Figure 2.5a,b).
It has been suggested that the reason for the different types of LH1 complexes is the transfer of ubiquinone/ubiquinol (Q_B/Q_BH_2) through the barrier of the LH1 complex, as part of the cyclic electron transport in purple bacterial photosynthesis [8]. Thereby, for the RC-LH1 complex from *Rps. palustris* it was proposed that the W protein may provide a portal through which Q_BH_2 can traverse the LH1 complex. This notion is reinforced by the specific orientation of the LH1 complex

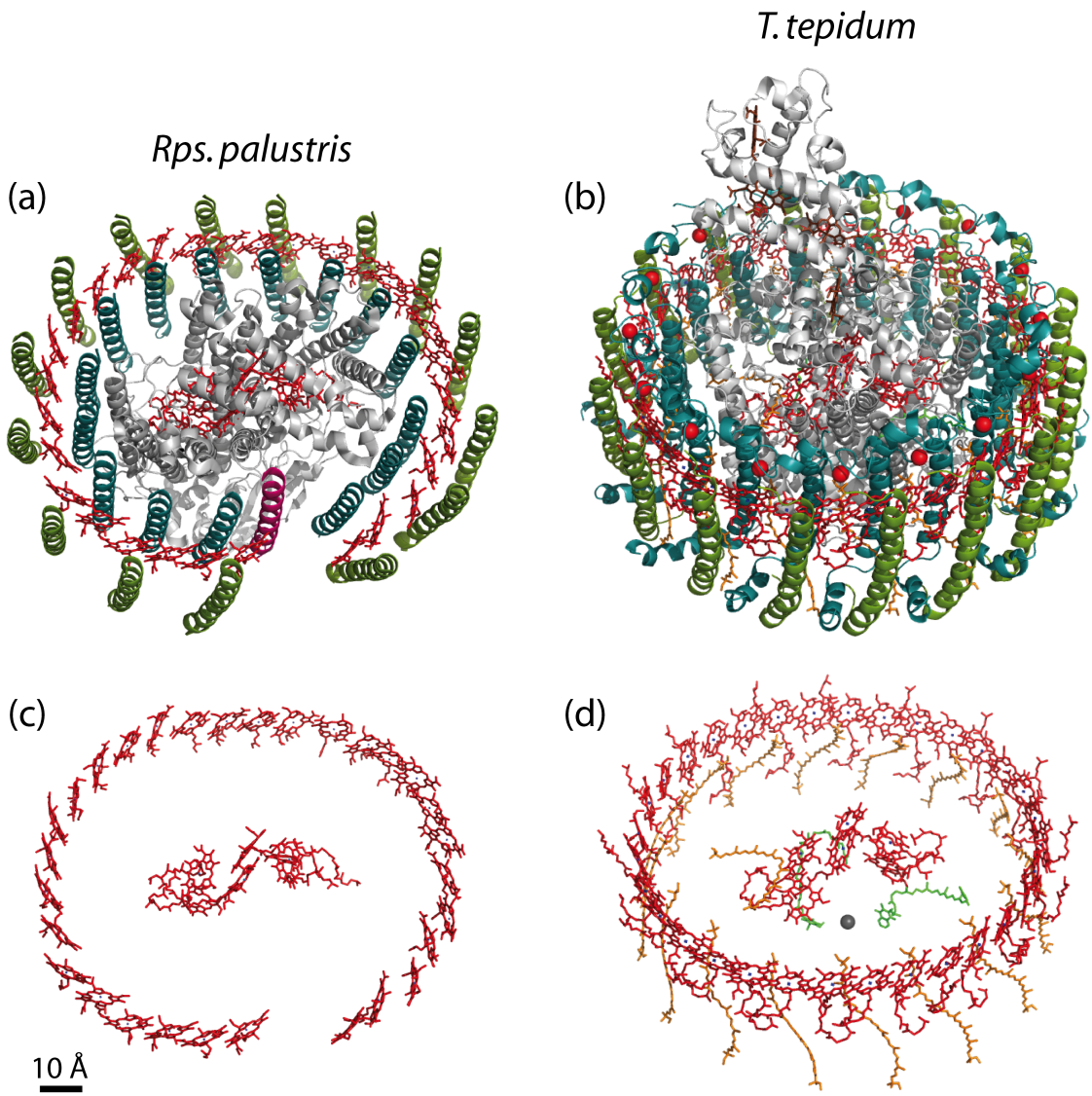

Figure 2.5: *Two types of monomeric core complexes from the photosynthetic purple bacteria. The LH1 complex from the species Rps. palustris (a,c; PDB file: 1PYH) is interrupted by a protein called 'W', whereas the LH1 complex from T. tepidum (b,d; PDB file: 3WMM) completely surrounds the RC. The following color scheme was used in all panels: α-apoproteins, cyan; β-apoproteins, green; W protein, pink; RC proteins, gray; BChls and BPheos, red; Mg^{2+}-ions, blue dots; carotenoids, orange; haems, brown; quinones, light green; Ca^{2+}-ions, red spheres and Fe^{2+}-ion, gray sphere. The top part of the figure (a,b) shows the complete complexes, whereas in the lower part (c,d) the proteins have been removed to allow a closer view on the pigment molecules. (a,b) For the RC-LH1 complex from T. tepidum the RC has a permanent cytochrome subunit which extends into the periplasmic space. Rps. palustris expresses Rb. sphaeroides-type RCs without this subunit. Another peculiarity of the RC-LH1 complex from T. tepidum are the Ca^{2+}-ions bound to the $\alpha\beta$-apoproteins on the periplasmic side. (c,d) In contrast to Rps. palustris, for T. tepidum both the positions of the carotenoids and of the two quinones in the RC are included in the PDB file. The figure was created with PyMOL; Schrodinger, 2010.*

with respect to the RC, such that W is located opposite to the Q_B binding site in the RC, with the hydrophobic tail of Q_B pointing towards the gap in the LH1 aggregate [24] (Figure 2.6). Another bacterial species for which a similar principle for the traffic of Q_B/Q_BH_2 through the LH1 complex was proposed, is *Rb. sphaeroides*. This species forms dimeric RC-LH1 complexes in which a S-shaped LH1 complex surrounds two RCs and two proteins called 'PufX' take over the role of the W protein [37].

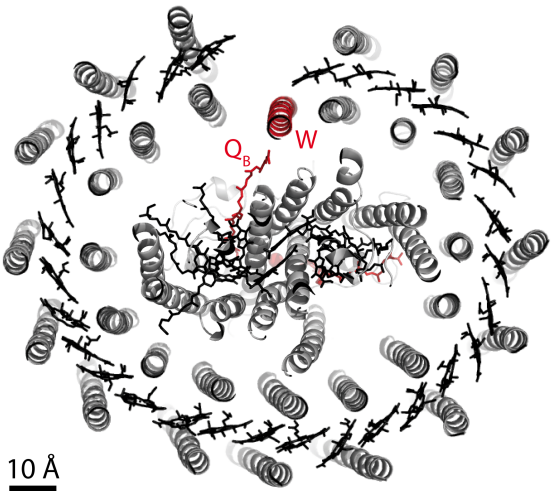

Figure 2.6: *Specific orientation of the LH1 complex from Rps. palustris with respect to the binding site of the secondary electron acceptor, Q_B, in the RC. Color scheme: protein helices, gray; W protein, red; pigment molecules, black; ubiquinones, red; Fe^{2+}-ion, red sphere. Since the ubiquinones are not included in the PDB file: 1PYH of the RC-LH1 complex from Rps. palustris, a RC structure including these molecules had to be found. Thus, the RC structure in this figure was taken from the PDB file: 1PCR [38] and overlaid over the initial RC of the Rps. palustris RC-LH1 structure. It can be seen that the hydrophobic tail of the secondary ubiquinone, Q_B, points towards the W protein which might form a gate, allowing the reduced ubiquinone, Q_BH_2, to escape into the membrane lipid phase. The figure was created with PyMOL; Schrodinger, 2010.*

In the crystal structure of the RC-LH1 complex from *T. tepidum* channels have been revealed in the LH1 complex that may facilitate the shuttling of Q_B/Q_BH_2 through the closed LH1 aggregate [9]. These channels are located on the interface between each pair of adjacent $\alpha\beta$-heterodimers and have an average size approximately equal to the size of the benzoquinone head of an ubiquinone. Based on molecular-dynamics simulations, a similar pathway for Q_B/Q_BH_2 was already proposed earlier for *Rsp. rubrum*, another purple bacterial species with a 'closed' LH1 complex around the RC [22].
The diffusion of Q_B/Q_BH_2 through the LH1 complex, might also be the explanation for the increased structural flexibility of LH1 complexes as compared to LH2,

e.g. observed in AFM studies [20, 39]. While authors in [39] could observe individual LH1 complexes changing their shape from elliptical to circular upon removal of the RC from the RC-LH1 complex, in [20], a large diversity of LH1 structures was found, ranging from circular to elliptical complexes, or even just arcs or open rings. In contrast, equally treated LH2 complexes in [20] displayed homogeneous, circular structures of equal diameter. This was attributed to a differing H-bonding pattern in the two types of light-harvesting complexes: For nonameric LH2 complexes (*e.g.* those from *Rps. acidophila*) it was claimed that H-bonds between the $\alpha\beta$-apoproteins and B850 BChls are not only internal to an $\alpha_1\beta_1\text{BChl}_2$ subunit, but also directed towards the neighboring subunit, thus stabilizing the overall LH2 complex. In contrast, for LH1 complexes it was suggested that all possible H-bonds are internal to an $\alpha_1\beta_1\text{BChl}_2$ subunit, resulting in LH1 aggregates composed of stable $\alpha_1\beta_1\text{BChl}_2$ units, with a certain degree of autonomy within the overall LH1 complex. This notion is corroborated by the fact that LH1 complexes can be readily dissembled into individual $\alpha_1\beta_1\text{BChl}_2$ units, often termed B820 [40, 41], or fractionated into a series of LH1 oligomers varying in size from $(\alpha\beta)_{2-3}$ to $(\alpha\beta)_{10-11}$ [42, 43], but no such subdivision has been reported so far for nonameric LH2 complexes [20]. The differing H-bonding pattern may then also explain the decreased stability of RC-LH1 complexes, as opposed to the LH2 complexes, when they have been detergent-solubilized from their native membrane [2]. This is even more true in the absence of the RC which can otherwise serve as barrier to potential changes of the LH1 shape [20, 44].
The structural information available so far on the RC-LH1 complex from *Rps. acidophila*, which is investigated in this work, is very limited. It is only known that the core complexes from this bacterial species are in all likelihood monomeric (see section 4.1.1). Thus, it will be interesting to find out if *Rps. acidophila* rather forms *palustris*-type or *tepidum*-type RC-LH1 complexes.

2.5 Amphiphiles

Amphiphilic molecules contain both a hydrophilic (polar) and a hydrophobic (non-polar) moiety. Two types of amphiphilic species play a crucial role for the photosynthetic apparatus of purple bacteria: On the one hand, the photosynthetic membrane is composed of phospholipids which are then responsible for the proper organization and stabilization of the different constituents of the photosynthetic apparatus, whereas detergents play a decisive role in photosynthetic research for the isolation of these constituents from their native membrane and for their purification. In the following the detergent and lipid molecules important for this thesis will be presented and a brief overview of the cooperative structures these amphiphilic species form in water is given.

2.5.1 Detergents

Detergents represent an important class of amphiphilic molecules, consisting of a hydrophilic headgroup and a long, hydrophobic hydrocarbon chain (tail). To a certain extent detergent molecules are soluble in water as monomers, loosely integrated into the water structure and lowering the surface tension. Above a critical concentration, the detergent molecules aggregate to form spherical, micellar structures, where the hydrocarbon chains aggregate on the inside of the micelle and are largely protected from interactions with water by the hydrophilic headgroups which are pointing outwards, towards the water (Figure 2.7d). This concentration is known as the so called critical micelle concentration (CMC). The aggregation of the detergent molecules is an entropy driven process, generally referred to as the hydrophobic effect [45, 46]. It can be explained in the following way: If a nonpolar molecule is added to water, a solvate (clathrate)-cage forms around it, forcing the water molecules forming the cage to arrange in an orderly manner. This results in a thermodynamically unfavorable decrease in entropy. To compensate for this loss of entropy, the water molecules induce a clustering of the hydrophobic molecules, with this cluster then having a minimum surface area exposed to water. In this way, the number of water molecules involved in the solvate-cage is minimized as compared to the situation where every hydrophobic molecule is solvated individually, thus adding degrees of freedom to (increasing the entropy of) the entire system.
The CMC varies largely for different types of detergents, depending on the size and nature of the headgroup and the length of the hydrophobic tail. Additionally, environmental conditions such as temperature or the ionic strength of the solution influence the CMC. Figure 2.7a,b shows the chemical structures of the two detergents which are important for this thesis. Dodecyl-β-D-maltoside (DDM) belongs to the nonionic detergents with a CMC of about 0.15 mM at $(20 - 25)\ ^{\circ}C$ [47]. Nonionic detergents are generally considered to be mild and relatively non-denaturating, as they break lipid-lipid interactions and lipid-protein interactions rather than protein-protein interactions [49]. Lauryldimethylamine N-oxide (LDAO) belongs to the zwitterionic detergents, displaying a nonionic character if the pH is above 7 and a cationic character if the pH is below 3 [50]. In general zwitterionic detergents are considered to be more deactivating than nonionic detergents [49]. The CMC of LDAO is approximately 1 mM [47].
The aggregation number (number of molecules in a detergent micelle) is about 100 for both types of detergents, DDM and LDAO, respectively [51, 52]. By molecular-dynamics simulations it was demonstrated that both detergents form ellipsoidal shaped micelles with a radius of gyration of about 25 $\AA$ for DDM and 19 $\AA$ for LDAO [51, 52]. However, the simulations also showed that, due to the larger headgroup of DDM as compared to LDAO, the hydrophobic core in micelles composed of the former detergent is much better protected against contact with water: While for DDM micelles the hydrocarbon surface amounts to only about 10% of the total

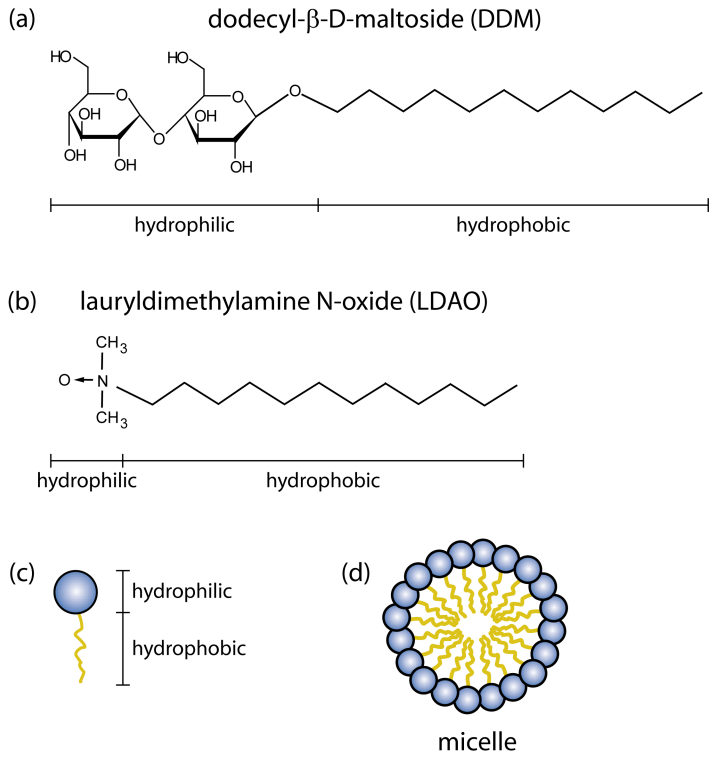

Figure 2.7: *Detergents. (a,b) Chemical structures of dodecyl-β-D-maltoside (DDM) and lauryldimethylamine N-oxide (LDAO) [47]. (c,d) Sketch of a detergent molecule and a thin section of a detergent micelle (redrawn from [48]).*

micelle surface, for LDAO about 50% of the micelle surface consists of hydrocarbon chains. Possible effects of the deviating properties of these two detergents on the stabilization of RC-LH1 complexes from *Rps. acidophila* are discussed in section 4.1 of this thesis.

2.5.2 Lipids

Lipid molecules are the basic constituents of biological membranes. There are three major kinds of membrane lipids, phospholipids, glycolipids and cholesterol, where phospholipids are most abundant in nature [53]. The phospholipid used in this work is 1,2-dioleoyl-*sn*-glycero-3-phosphocholine (DOPC) (Figure 2.8a). It consists of two unsaturated fatty acid chains and a headgroup composed of glycerol and phosphoryl choline.
When exposed to water lipid molecules spontaneously form a bimolecular sheet, the so called lipid bilayer [53] (Figure 2.8c). As for the detergents, the driving force for this process are hydrophobic interactions. However, due to the bulkiness of the two fatty acid chains, phospholipids form lipid bilayers rather than micelles. In the

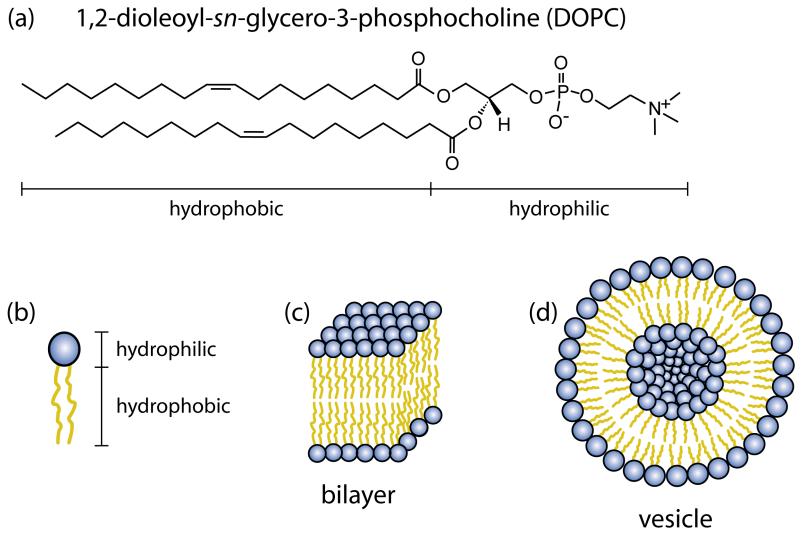

Figure 2.8: *Lipids. (a) Chemical structure of 1,2-dioleoyl-sn-glycero-3-phosphocholine (DOPC) [54]. (b) Sketch of a lipid molecule, (c) a lipid bilayer and (d) a section of a lipid vesicle (redrawn from [48]).*

formation of the lipid bilayer, water molecules are released from the hydrocarbon tails of the membrane lipids and these tails become sequestered in the nonpolar interior of the bilayer. Van der Waals attractive forces acting between the hydrocarbon chains, and electrostatic and hydrogen-bonding interactions between the polar headgroups and to the surrounding water molecules, stabilize the structure of the lipid bilayer.

Lipid vesicles (also known as liposomes) are spherical structures, where a lipid bilayer encloses an aqueous compartment (Figure 2.8d). For their formation a suitable lipid is suspended in water and this solution is then further treated, *e.g.* by sonication or extrusion (see section 3.2). In an ideal case this procedure yields unilamellar vesicles with a homogeneous size distribution.

Schematically, lipid bilayers can be described as two-dimensional solutions of oriented lipids, with a fast lateral diffusion of the lipid molecules in the plane of the membrane [53]. Thereby, the melting temperature, T_C, is a characteristic value for the lipid bilayer, describing the phase transition from the ordered gel phase below T_C, to the disordered fluid phase above T_C. In the gel phase the hydrocarbon chains are fully extended (all trans configuration) and densely packed, whereas in the fluid phase some of the hydrocarbon chains are in gauche configuration, thus preventing a tight packing. There are a number of parameters influencing the phase transition temperature of a certain lipid, such as the hydrocarbon chain length, the number of unsaturated C double bonds and the type of headgroup. With increasing hydrocarbon chain length, van der Waals interactions between the chains become stronger, requiring more energy to disrupt the ordered packing. Accordingly, T_C

would increase for such a lipid. Contrary, the introduction of a cis double bond produces a bend in the hydrocarbon chains. This interferes with a highly ordered packing of the chains, and thus T_C is lowered. For DOPC, due to the one-time unsaturated fatty acid chains, the phase transition temperature is relatively low, $T_C = -17\,^{\circ}C$ [54].

2.6 Spectral properties of chromophores

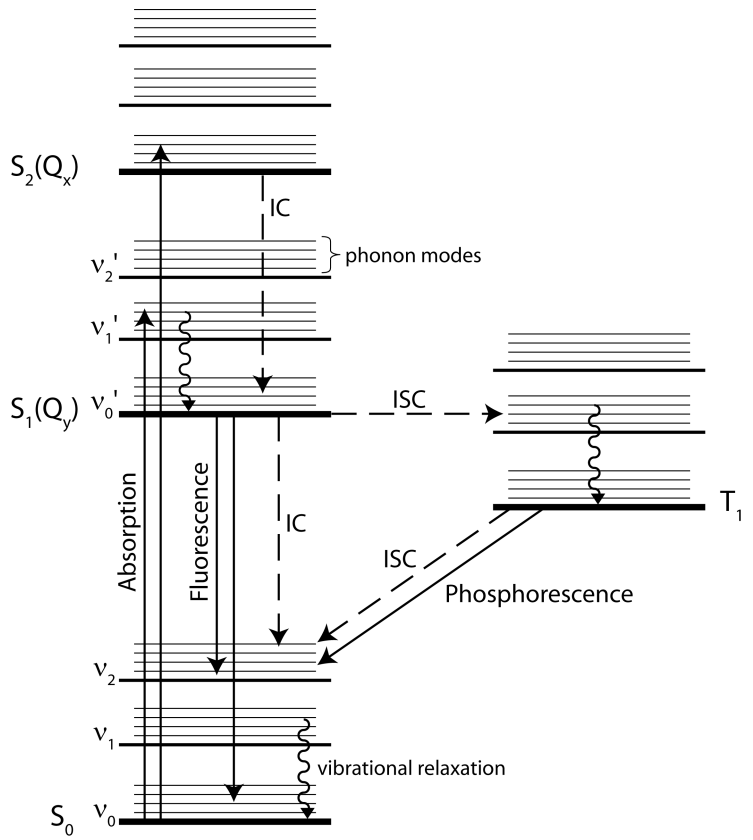

Figure 2.9: *Jablonski diagram of an organic molecule (e.g. BChl a). S_0, $S_{1,2}$ ($Q_{y,x}$) and T_1 denote the electronic ground state, the two lowest singlet excited states and the lowest triplet state, respectively. Vibrational levels that couple to the electronic transitions are denoted as $\nu_i^{(\prime)}$ $(i = 0, 1, 2)$, and phonon modes are indicated by the thin lines on top of the vibrational levels. IC stands for internal conversion and ISC for intersystem crossing. The solid arrows indicate transitions which involve the absorption or emission of a photon, whereas the dashed/wavy arrows indicate non-radiative transitions.*

Figure 2.9 shows the energy level scheme of a BChl a molecule in a so called Jablonski diagram. Thereby, only the two lowest singlet excited states S_1 (Q_y) and S_2

(Q_x), and the lowest triplet state T_1 are depicted. S_0 denotes the electronic ground state which is as well a singlet state. Additionally, vibrational levels, labeled as $\nu_i^{(\prime)}$ ($i = 0, 1, 2$), and phonon levels, that couple to the electronic states, are also shown in Figure 2.9.
If the frequency of the excitation laser is in resonance with an optically allowed transition, the molecule absorbs a photon and will be excited from the electronic ground state S_0 to an excited singlet state $S_{1,(2)}$. The probability for a chromophore to absorb a photon, P_{abs}, is proportional to its absorption cross-section σ. In the dipole approximation, where it is assumed that the wavelength of the excitation laser is much larger than the dimensions of the absorbing chromophore, σ is proportional to the square magnitude of the so called transition-dipole matrix element for a certain electronic transition of the chromophore [55]:

$$P_{abs} \propto \sigma \propto |\langle f|\hat{p}|i\rangle|^2 \ . \tag{2.1}$$

In (2.1) $|i\rangle$ and $|f\rangle$ denote the initial and (excited) final state of the chromophore, respectively, and $\hat{p}$ is the dipole moment operator:

$$\hat{p} = e \cdot \sum_m \vec{r}_m \ , \tag{2.2}$$

where e denotes the elementary unit of charge and the sum runs over the coordinates $\vec{r}_m$ of all electrons in the chromophore. Within the Born-Oppenheimer (BO) approximation, where due to the mass difference between electrons and nuclei ($m_e/m_n \approx 10^{-4}$), it is assumed that electronic dynamics is much faster than nuclear dynamics, the total wavefunctions of the chromophore can be written as direct products of the electronic and nuclear wavefunctions:

$$\left|i\left(\{\vec{r}_m\}, \left\{\vec{R}_n\right\}\right)\right\rangle = \left|e_i\left(\{\vec{r}_m\}, \left\{\vec{R}_n\right\}\right)\right\rangle \cdot \left|\mu\left(\left\{\vec{R}_n\right\}\right)\right\rangle \text{ and} \tag{2.3}$$

$$\left|f\left(\{\vec{r}_m\}, \left\{\vec{R}_n\right\}\right)\right\rangle = \left|e_f\left(\{\vec{r}_m\}, \left\{\vec{R}_n\right\}\right)\right\rangle \cdot \left|\nu\left(\left\{\vec{R}_n\right\}\right)\right\rangle \ , \tag{2.4}$$

where $\{\vec{r}_m\}$ and $\left\{\vec{R}_n\right\}$ denote the sets of electronic and nuclear coordinates, respectively. Thus, the transition-dipole matrix element from equation (2.1) can be written as:

$$\hat{M}_{if} = \langle f|\hat{p}|i\rangle = \langle e_f|\hat{p}|e_i\rangle \cdot \langle \nu|\mu\rangle \ , \tag{2.5}$$

where for clarity electronic and nuclear coordinates have been omitted. The first factor in the product on the rightmost side of equation (2.5) is known as the electronic transition-dipole moment. This integral includes the electronic wavefunctions $|e_i\rangle$ and $|e_f\rangle$ of the electronic ground and excited state, respectively, which depend only parametrically on the set of nuclear coordinates $\left\{\vec{R}_n\right\}$ (*vide infra*). The electronic transition-dipole moment is a measure for the magnitude and the orientation

of the charge displacement during an electronic transition. The square magnitude of the second term in the product on the rightmost side of equation (2.5) is the so called Franck-Condon factor:

$$F_{\mu\nu} = |\langle\nu|\mu\rangle|^2 \ . \tag{2.6}$$

Both integrals in equation (2.5) are evaluated at the same values for the set of nuclear coordinates $\left\{\vec{R}_n\right\}$, as within the BO approximation it is assumed that an electronic transition takes place instantaneously, without a change of the nuclear positions. Then, the Franck-Condon factor describes the direct overlap of the nuclear wavefunctions in the initial and final electronic state, and thus determines the probability for a transition from a vibrational level $|\mu\rangle$ of the electronic ground state to a vibrational level $|\nu\rangle$ of the excited electronic state.
For molecules with a spatially fixed transition-dipole moment (*e.g.* chromophores embedded in a matrix), the following dependency can be found for the transition probability, P_{abs}, on the mutual angle α between the linear polarization of the incident electric field $\vec{E}$ and the orientation of the transition-dipole matrix element $\hat{M}_{if}$:

$$P_{abs} \propto \left|\vec{E} \cdot \hat{M}_{if}\right|^2 = E^2 M_{if}^2 \cdot \cos^2(\alpha) \ . \tag{2.7}$$

Thus, by rotating the polarization of the incident radiation, the absorption signal will display a $\cos^2$-type modulation, thereby enabling one to determine the orientation of the transition-dipole moment of the respective transition, or at least its projection on the plane perpendicular to the optical axis of the incident light.
As already mentioned earlier, the transition energy of the Q_x transition amounts to about $17,000\ cm^{-1}$ and that of the Q_y transition to about $13,000\ cm^{-1}$ [2]. Typically the energy of vibrational modes lies in the range between $400-4000\ cm^{-1}$. For BChl *a* a characteristic vibrational sideband of the Q_y transition can be discerned at about 700 nm, which corresponds to a vibrational energy of about 1300 cm^{-1} [28]. Additionally, the electronic and vibronic levels couple to low-energy vibrations $(10 - 100\ cm^{-1})$ of the surrounding host matrix, the so called phonon modes.
After the chromophore has been excited into a vibrational/phonon level of one of the electronically excited singlet states by absorption of a photon, fast radiationless relaxation into the vibrational ground state of S_1 occurs within about 100 fs. If initially a higher lying singlet level S_n $(n \geq 2)$ is excited, ultra-fast internal conversion (IC) to the lowest excited singlet state S_1, with subsequent vibrational relaxation into the vibrational ground level of S_1 takes place. IC denotes a non-radiative transition between electronic states with the same spin multiplicity. This phenomenon, *i.e.* that emission only takes place from the lowest excited singlet level S_1, independent of the initially excited singlet state, is called Kasha's rule. It only applies to chromophores in a condensed phase, where the energetically higher-lying electronic/vibronic quanta can be transformed into energetically lower-lying

electronic/vibronic quanta, by giving off the excess energy to the local surrounding. Apart from the singlet excited states, BChl *a* also has a triplet system in which the lowest state T_1 lies well below the Q_y (S_1) state. As the transition-dipole moment operator (2.5) conserves the total spin, an electronic transition is only allowed if the total spin quantum number does not change, and therefore singlet - triplet transitions are forbidden. However, the excited Q_y state in BChl *a* can convert with a low probability into the T_1 state via intersystem crossing (ISC) due to spin-orbit coupling. From the T_1 state, the ground state S_0 is reached either via radiationless ISC, or by emission of a photon (phosphorescence). As a result of the weakly allowed transition, the triplet lifetime is in the order of microseconds up to minutes, during which the chromophore cannot absorb another photon. Thus the triplet state may act as a bottleneck in the excitation-relaxation cycle. For BChl *a* in LH-complexes however, rapid energy transfer with close to 100% efficiency occurs from the excited triplet state of BChl *a* to the carotenoid molecules which reduces the lifetime of the BChl *a* triplet by two orders of magnitude [33].
Fluorescence is the radiative transition between electronic levels with the same spin multiplicity. Here the same transition-dipole matrix element (2.5) applies as for the excitation process, which then also defines the polarization of the emitted photon. As emission occurs from the lowest vibronic state of the lowest excited singlet state S_1 (*vide supra*), and transitions into higher vibronic states of the electronic ground state, S_0, are also possible (determined by the Franck-Condon integral (2.6)), the emitted photon usually has a lower energy, than the photon of the excitation process. The resulting shift to lower energies of the fluorescence with respect to the absorption spectrum of a chromophore, is known as Stokes-shift.
Since in this thesis the fluorescence emission of LH complexes is used for their detection and for spectroscopic purposes, the fluorescence quantum yield, Φ_f, of the investigated complex is a decisive parameter. It is defined as the ratio of the number of photons emitted to the number of absorbed photons:

$$\Phi_f = \frac{N_{em}}{N_{abs}} \,. \tag{2.8}$$

With a fluorescence quantum yield of about 10% LH1 complexes can still be considered as quite fluorescent and therefore, well suited for fluorescence-excitation spectroscopy [56].

2.6.1 Homogeneous linewidth, zero-phonon line and phonon side-band

The line shape of a purely electronic transition (*e.g.* $S_1 \leftrightarrow S_0$), both for the emission and the absorption process, is Lorentzian, and its width (full width at half

maximum, $fwhm$) is given by [57]:

$$\Gamma_{hom}(T) = \frac{1}{2\pi\tau_1} + \frac{1}{\pi\tau_2^*(T)} = \frac{1}{\pi\tau_2(T)} \,. \tag{2.9}$$

$\Gamma_{hom}(T)$ is then referred to as the homogeneous linewidth of the transition. τ_1 is the excited state lifetime, $\tau_2^*(T)$ denotes the temperature dependent pure dephasing time and $\tau_2(T)$ stands for the total or effective dephasing time. The pure dephasing processes are caused by interactions with the environment (*e.g.* scattering with phonons), leading to a fluctuation of the energy levels. $\tau_2^*(T)$ then represents the time interval in which the coherence of the electronic transition is lost due to the fluctuating energy gap. As a result, a temperature dependent homogeneous broadening of the absorption and emission lines can be observed. At very low temperatures ($T < 2\ K$), $\tau_2^*(T)$ becomes very long as host phonons and local modes are frozen out, and thus the linewidth of the optical transition will be determined solely by the finite lifetime τ_1 of the electronically excited state. In this limit $\Gamma_{hom}(T)$ represents the lifetime-limited, natural linewidth of the transition. Such an absorption or emission line is also referred to as zero-phonon line (ZPL), since during such a purely electronic transition no creation or destruction of low-energy vibrations in the chromophore or in its local surrounding takes place.

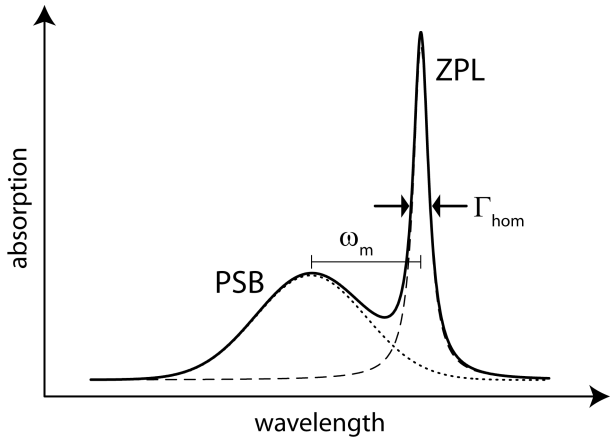

Figure 2.10: *Schematic illustration of the absorption spectrum of a single chromophore embedded in a solid state matrix at low temperatures (thick solid line): The homogeneously broadened* (Γ_{hom}) *zero-phonon line (ZPL, dashed line) is accompanied by a broad phonon side-band (PSB, dotted line) in its high-energy wing.* ω_m *denotes the mean phonon frequency.*

For linear electron-phonon coupling, in combination with the purely electronic transition, a low-energy vibration in the surrounding matrix of the chromophore is simultaneously excited. Therefore, in an absorption spectrum at low temperatures the ZPL is accompanied by a so called phonon side-band (PSB), which is typically shifted to higher energies (smaller wavelengths) by several 10 cm^{-1} with respect

to the maximum of the ZPL (Figure 2.10) [57]. The mean phonon energy ω_m is defined as the energy difference between the peak positions of the ZPL and the PSB. Thereby, ω_m is characteristic for the energy of the phonon mode coupled to the electronic state. The Debye-Waller factor $C_{DW}(T)$ provides a measure for the linear electron-phonon coupling strength [58]:

$$C_{DW}(T) = \frac{I_{ZPL}}{I_{ZPL} + I_{PSB}} = \exp(-S(T)) \,, \tag{2.10}$$

where I_{ZPL} (I_{PSB}) denotes the integrated intensity of the ZPL (PSB). $S(T)$ is the temperature dependent Huang-Rhys parameter, and the second equal sign in (2.10) applies for the low-temperature limit ($T \approx 0\ K$).

2.7 Frenkel-excitons

The quantum mechanical description of excitons in organic crystals and dye aggregates is well established [14, 59–61]. The theory of the so called Frenkel-excitons applies to molecular aggregates in which the electronic wavefunctions of neighboring molecules have no substantial overlap [59]. Here, it should be noted that in general this is only true for the lowest molecular excited singlet state, as higher excited states are expected to have sufficient charge overlap. Upon resonant interaction of the excited states from individual pigments in a molecular aggregate (where generally the strongest contribution to these interactions derives from electrostatic interactions between the transition-dipoles of the individual pigments) excited states are formed that are delocalized over the pigments in the aggregate [48, 59]. These collective excitations are called Frenkel-excitons, where a further prerequisite for the formation of these states is, that the variation of the transition energies of the pigments in the aggregate is much smaller than the interaction strength between adjacent pigments [2]. In such a case, the molecular aggregate can be treated as a single supermolecule of coherently interacting molecules and the excited states of the supermolecule are the exciton states [61]. The optical properties of such strongly coupled molecular aggregates, in particular their absorption spectra, depend crucially on the geometric arrangement of the pigments in the respective aggregates [12, 14].

2.7.1 Pigment-pigment interaction

Bacteriochlorophylls in LH complexes do not only interact with their surrounding protein matrix, but also with each other. Actually, Frenkel-excitons develop by virtue of intermolecular interactions, where electrostatic (Coulomb) interactions are by far the dominant ones [61]. The Coulomb interaction V_{nm} between two

chromophores n and m can be written as:

$$V_{nm} = \frac{1}{4\pi\epsilon\epsilon_0} \sum \frac{q_n q_m}{r_{nm}} \,, \tag{2.11}$$

where ϵ is the dielectric constant of the medium, ϵ_0 the electric permittivity of free space and r_{nm} the relative distance between the electronic or nuclear charges q_n and q_m of the chromophores. If the pigments are not permanently charged and their mutual distance is large compared to their size, the interaction energy, V_{nm}, between them, can be approximated by the dipole-dipole term in the multipole expansion of the Coulomb interaction (higher order terms fall off more rapidly with the mutual distance r_{nm} between the chromophores) [14, 59, 61]:

$$V_{nm} = \underbrace{\frac{\mu^2}{4\pi\epsilon\epsilon_0}}_{V_0} \cdot \frac{1}{r_{nm}^3} \cdot \underbrace{\frac{1}{\mu^2}\left[\vec{\mu}_n \cdot \vec{\mu}_m - 3\frac{(\vec{\mu}_n \cdot \vec{r}_{nm})\,(\vec{\mu}_m \cdot \vec{r}_{nm})}{r_{nm}^2}\right]}_{\kappa_{nm}} \,. \tag{2.12}$$

Here, $\vec{\mu}_n$ and $\vec{\mu}_m$ represent the strength and the orientation of the transition-dipole moments of the molecules n and m, respectively. V_0 defines the coupling strength and, assuming that the interacting chromophores are identical ($|\vec{\mu}_n| = |\vec{\mu}_m| = \mu$), it is, $|\vec{\mu}_n| \cdot |\vec{\mu}_m| = \mu_n \cdot \mu_m = \mu^2$. κ_{nm} is an orientational factor which covers the mutual orientation of the transition-dipole moments by means of normalized vectors. Thus, the dipole-dipole interaction can be divided into a distance dependent part, $1/r_{nm}^3$, and an orientational part, described by κ_{nm}.

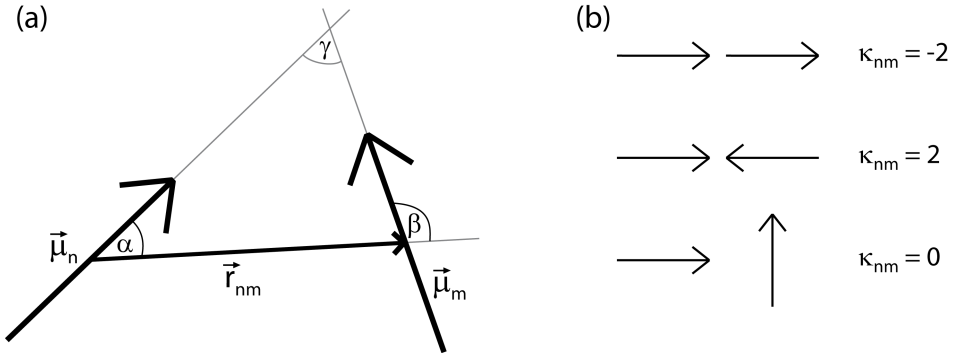

Figure 2.11: *Schematic illustrations of the dipole-dipole interaction. (a) Two dipoles $\vec{\mu}_n$ and $\vec{\mu}_m$ and their connecting vector $\vec{r}_{nm}$ drawn in-plane. α, β and γ indicate the mutual angles between the transition-dipoles and their connecting vector and between each other. (b) Characteristic mutual orientations of the transition-dipole moments and the corresponding values for the orientational parameter κ_{nm} (see text).*

With the angles α, β and γ, defined in Figure 2.11a, it is possible to write down

κ_{nm} in the following way:

$$\begin{aligned}\kappa_{nm} &= \frac{1}{\mu^2}\left[\mu_n\mu_m\cdot\cos(\gamma) - 3\frac{(\mu_n r_{nm}\cdot\cos(\alpha))\,(\mu_m r_{nm}\cdot\cos(\beta))}{r_{nm}^2}\right] = \\ &= \cos(\gamma) - 3\cos(\alpha)\cos(\beta)\,. \end{aligned} \tag{2.13}$$

With this, it is easy to understand that κ_{nm} can adopt the following characteristic values: $\kappa_{nm} = -2\,(2)$ for a collinear head-to-tail (head-to-head) arrangement of the transition-dipoles, and $\kappa_{nm} = 0$ for mutually perpendicular transition-dipoles (Figure 2.11b).

For the B850 aggregate in LH2 complexes and the B880 assembly in LH1 complexes, the dipole-dipole approximation might be questioned, as the distance between neighboring pigments is comparable to their dimensions. Therefore, other approaches to calculate the spectral properties of these pigment assemblies were chosen as well, taking the spatial distribution of the transition-dipole moments [62, 63] or the exchange interaction [64, 65] into account. However, in [64] and [65] it was also shown that the Coulomb coupling between the pigments still dominates over the exchange coupling. Furthermore, it is noteworthy that the dipole-dipole approximation is not only reasonable if the intermolecular distance r_{nm} is larger than the size of the chromophore, but even when r_{nm} is larger than the dipole radius, defined as, $a = \mu_i/e$, where μ_i denotes the magnitude of the transition-dipole moment of the chromophore and e is the elementary unit of charge [61]. For the numerical simulations performed in this work (see chapter 5), a dipole strength of $\mu_i = 8.8\ D$ was assumed for the Q_y transition-dipole moment of the BChl a molecules, corresponding to a dipole radius $a \approx 2\mathring{A}$. Comparing this value to the mutual separation between neighboring BChl a molecules in a LH1 pigment aggregate [9], $r_{nm} \approx 10\mathring{A}$, it can be seen that the prerequisite for the dipole-dipole approximation, $r_{nm} \gg a$, is not perfectly fulfilled in this case. Nevertheless, it can be expected that the dipole-dipole interaction approach provides at least a qualitative description of the processes inside a LH1 complex. Further, to avoid this inaccuracy as much as possible, for the numerical simulations of chapter 5, the effective Hamiltonian approach [66] was adopted in part. In this approach fixed values are assumed for the interaction between neighboring pigments (based on a fit of the resulting exciton spectrum to extensive quantum chemistry calculations) and the dipole-dipole interaction is only applied for pigments which are further apart (second, third, ... neighbors). In [66] it was shown that by means of the effective Hamiltonian the results of extensive quantum chemistry calculations on the B850 aggregate of LH2 complexes, can be reasonably approximated. In chapter 5, due to the fixed positions of the pigments inside a dimer unit, the value of the intradimer interaction is fixed, whereas the interdimer interaction (between neighboring pigments of adjacent dimer units) and the second-neighbor interaction are calculated with the help of the dipole-dipole formula (2.12). Thus, the aforementioned inaccuracy is not completely eliminated for the numerical simulations

in chapter 5, but is still present for the interdimer interaction. Here, a compromise had to be made, since on the one hand, due to the basic construction principle of LH1 complexes, where it is assumed that the dimer units inside the LH1 complex experience a certain degree of conformational freedom with respect to the overall aggregate [20], it is not reasonable to assume a fixed value for the interdimer interaction. On the other hand, the dipole-dipole approach may not be the most accurate way to calculate the varying values for the interdimer interaction around the aggregate. However, for the rather simple numerical simulations of chapter 5, where other approximations are also made (*e.g.* not taking the coupling to phonon modes into account), it is an appropriate solution to use the dipole-dipole formula (2.12) for the calculation of the interdimer interaction, at least to gain a general idea of the excited state properties in LH1 complexes, depending on the mutual arrangement of the dimer units.

2.7.2 Linear aggregate

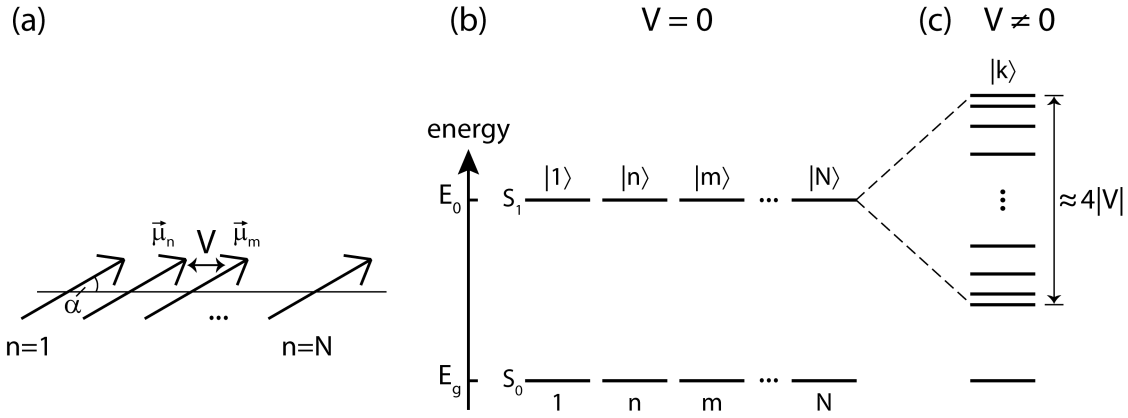

Figure 2.12: *(a) Linear chain of N equidistant two-level pigments with transition-dipoles oriented parallel with respect to each other. V indicates the interaction between nearest-neighbors. (b) Energy level diagram for the case of non-interacting pigments ($V = 0$): The pigments have equal site energy, E_0, and excitations are localized on individual pigments. (c) Energy level diagram for the case of interacting pigments ($V \neq 0$): Formation of exciton states $|k\rangle$ that are delocalized over the pigments in the linear chain. If only nearest-neighbor interactions, V, are taken into account and $N \gg 1$, the width of the exciton band is approximately $4|V|$.*

A linear chain of N identical two-level molecules with their transition-dipole moments oriented parallel with respect to each other is considered (Figure 2.12a,b). Neglecting the influence of phonons and restricting to at most one excitation per chain, the system can be described by the following model Hamiltonian in Heitler-

London approximation:

$$H = \underbrace{\sum_{n=1}^{N} E_0 \left|n\right\rangle \left\langle n\right|}_{diagonal\ elements} + \underbrace{\frac{1}{2}\sum_{n=1}^{N}\sum_{n\neq m} V_{nm} \left|n\right\rangle \left\langle m\right|}_{off-diagonal\ elements}, \tag{2.14}$$

where $|n\rangle$ and $\langle m|$ indicate excitations localized on the pigments n and m, respectively, E_0 denotes the site-energy of pigment n and V_{nm} denotes the interaction between the pigments n and m. If the Hamiltonian is written in matrix representation, the first term corresponds to the diagonal elements of the matrix and the second term to the off-diagonal elements.
For non-interacting pigments ($V = 0$) the excited states ($|1\rangle, \ldots, |N\rangle$) of the pigments are also the eigenstates of the system and excitations are localized on the individual pigments (Figure 2.12b). This is no longer the case if an interaction V is turned on. Diagonalization of the above Hamiltonian (2.14) leads to the eigenstates of the coupled system, the Frenkel-excitons, which can be written as linear combination of the localized eigenstates. If only nearest-neighbor interaction, V, is taken into account and translation symmetry is retained, (2.14) can be solved analytically, leading to the eigenfunctions [59, 67, 68]:

$$\left|k\right\rangle = \sum_{n=1}^{N} a_{kn} \left|n\right\rangle = \sqrt{\frac{2}{N+1}} \sum_{n=1}^{N} \sin\left(\frac{\pi k n}{N+1}\right) \left|n\right\rangle \ , \tag{2.15}$$

where $k = 1, \ldots, N$ is the quantum number of the exciton states. It can be seen that the exciton states, $|k\rangle$, correspond to standing waves of excitation that are delocalized over the complete linear chain, with the k^{th} state having $k - 1$ nodes along the chain. An analogy to the description of the exciton states, $|k\rangle$, can be found in the description of the normal modes of a linear chain consisting of N particles [69]. The corresponding energy eigenvalues of the analytically solved Hamiltonian (2.14) are [59]:

$$E_k = E_0 + 2V \cos\left(\frac{\pi k}{N+1}\right) \ , \tag{2.16}$$

see Figure 2.12c. Thereby, it has to be noted that for a mutual arrangement of transition-dipoles in the linear chain as shown in Figure 2.12a, with $\alpha < 54.7°$, $V < 0$ (determined by the orientation factor, κ_{nm}, in the dipole-dipole formula, *cf.* (2.13)), such that the $k = 1$ exciton state has the lowest eigenenergy. The exciton band described by equation (2.16) extends from $E = E_0 - 2|V|$ to $E = E_0 + 2|V|$ and is symmetric around E_0 (Figure 2.12c).
In the dipole approximation, assuming that the size of the linear aggregate is much

smaller than the excitation wavelength, the coupling of the radiation field to the exciton states $|k\rangle$ leads to the following exciton transition-dipole moments:

$$\vec{\mu}_k = \sum_{n=1}^{N} a_{kn} \cdot \vec{\mu}_n = \sqrt{\frac{2}{N+1}} \sum_{n=1}^{N} \sin\left(\frac{\pi k n}{N+1}\right) \cdot \vec{\mu}_n \,, \tag{2.17}$$

with $\vec{\mu}_n$ denoting the transition-dipole moment of the n^{th} pigment in the aggregate. Thus, in the dipole approximation, the linear chain can be considered as one giant multilevel molecule. From the exciton transition-dipole moments (2.17) the oscillator strength can be calculated as [59, 68]:

$$|\vec{\mu}_k|^2 = \left(\frac{2\mu_{mon}^2}{N+1}\right) \cot^2\left(\frac{\pi k}{2(N+1)}\right) \,, \text{ for } k \text{ odd}, \tag{2.18}$$

$$|\vec{\mu}_k|^2 = 0 \,, \text{ for } k \text{ even}, \tag{2.19}$$

where $\mu_{mon} = |\vec{\mu}_n|$. The latter identity (2.19) can be easily understood from (2.15), as the wavefunctions with an even quantum number k possess point symmetry with respect to the chain center and therefore, the vector summation in (2.17) results in a zero net transition-dipole moment. From (2.18) it can be seen that for a linear aggregate the $k = 1$ state contains the overwhelming part of the total oscillator strength, $N\mu_{mon}^2$, (up to 81% for $N \gg 1$), leading to superradiant emission and domination of the absorption spectrum by this state. The oscillator strengths of higher exciton states drop of as $1/k^2$ for $k \ll N$.
Analytical diagonalization of the linear chain problem with dipolar interactions between all pigments in the aggregate taken into account, instead of only nearest-neighbor couplings, presents a difficult problem [68]. However, straightforward numerical diagonalization of the Hamiltonian (2.14), with all dipolar interactions taken into account, reveals that the resulting wavefunctions are very similar to the $|k\rangle$ states calculated in (2.15). Furthermore, it turns out that the oscillator strength of the lowest band state increases to about 83% of the total (for $N = 250$). And finally, the exciton band now shows a marked asymmetry around E_0, with the lower band-edge to be found at $E = E_0 - 2.403|V|$ and the upper band-edge at $E = E_0 + 1.803|V|$, which also means an increase of the total bandwidth from $4|V|$ to $4.206|V|$.

2.7.3 Circular aggregate

For a ring of N equivalent sites with N-fold symmetry, the Hamiltonian (2.14) has periodic boundary conditions. In this case, the excitonic eigenfunctions $|k\rangle$ are obtained by the Fourier transform of the localized excited states basis as [70]:

$$|k\rangle = \frac{1}{\sqrt{N}} \sum_{n=1}^{N} e^{i2\pi k \frac{n}{N}} |n\rangle \,, \tag{2.20}$$

with the eigenenergies

$$E_k = E_0 + \sum_{n=2}^{N} e^{i2\pi k \frac{n-1}{N}} V_{1,n} \,. \tag{2.21}$$

Thereby, it has to be noted that for aggregates with periodic boundary conditions, an analytical diagonalization of the Hamiltonian is possible even if interactions between all pigments are taken into account. For N odd, the circular symmetry of the Hamiltonian results in a single lowest energy eigenstate with $k = 0$ and pairs of degenerate eigenstates labeled as $k = \pm 1, \ldots, \pm(N-1)/2$. For N even, there is a lowest energy eigenstate with $k = 0$, an uppermost state with $k = N/2$, and, in between, pairs of degenerate eigenstates labeled as $k = \pm 1, \ldots, \pm(N/2-1)$. Again an analogy to the description of the exciton states in (2.20), can be found in the description of the normal modes of N particles positioned on a circle with N-fold symmetry [69].
For a better understanding of the numerical simulations in this work (see chapter 5), some of the peculiarities of a circular aggregate build up from dimeric subunits will be pointed out, where additionally interactions are restricted to nearest- and second-neighbors. In chapter 5 the geometric arrangement of the pigments inside a dimer unit is adopted from the mutual orientation of the pigments in the dimer units of the B850 ring in LH2 complexes from *Rps. acidophila* [35], since, until recently, no high-resolution crystal structure of a RC-LH1 complex was available. (In this regard, it was shown in the recently discovered high-resolution structure of the RC-LH1 complex from *T. tepidum*, that the arrangement of the pigments in the dimer units of the LH1 aggregate, is very similar to the pigment arrangement in the B850 dimer units of LH2 complexes [9].)

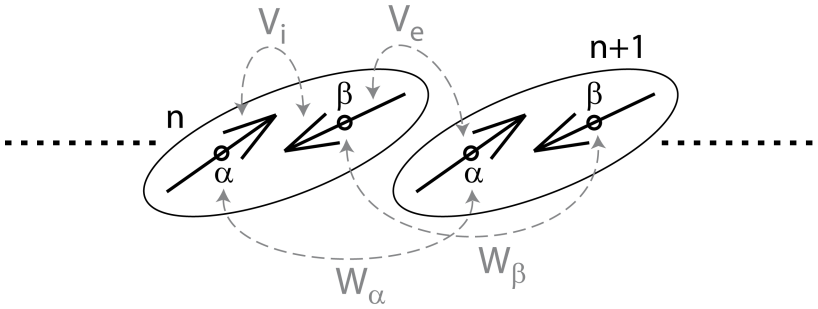

Figure 2.13: *Schematic representation of two adjacent dimer units (n and $n+1$), where the relevant interactions between the pigments are indicated. V_i indicates the nearest-neighbor intradimer interaction, V_e the nearest-neighbor interdimer interaction, W_α the second-neighbor interaction between α-pigments and W_β the second-neighbor interaction between β-pigments. The mutual orientation of the Q_y transition-dipole moments inside the dimer units is adopted from the B850 dimer unit of the LH2 complex from Rps. acidophila.*

Figure 2.13 shows a schematic representation of two adjacent dimer units, n and

$n+1$ (note that from now on the index n applies to a complete dimer unit), where the relevant interactions between the pigments are indicated up to second neighbors. The various interactions are: The nearest-neighbor intradimer interaction $V_i = \langle n_\alpha|V|n_\beta\rangle$, between pigments of the same dimer unit, the nearest-neighbor interdimer interaction $V_e = \langle n_\beta|V|(n+1)_\alpha\rangle$, between neighboring pigments of adjacent dimer units, the second-neighbor interaction $W_\alpha = \langle n_\alpha|W|(n+1)_\alpha\rangle$, between α-pigments of adjacent dimer units and the second-neighbor interaction $W_\beta = \langle n_\beta|W|(n+1)_\beta\rangle$, between β-pigments of adjacent dimer units. It is common practice to define the direction of the Q_y transition-dipole moment as the direction pointing from the N_{III} to the N_I (or from the N_I to the N_{III}) nitrogen atoms in the BChl *a* molecule (Figure 2.3a). Based on this definition and taking the arrangement of the pigments in the LH2 B850 dimer unit into account, adjacent transition-dipoles reside in a head-to-head (tail-to-tail) configuration, while second-neighbor transition-dipoles are in a head-to-tail (tail-to-head) configuration (Figure 2.13). Consequently, the nearest-neighbor interactions have positive values, while the second-neighbor interactions are negative, *i.e.* $V_i, V_e > 0$ and $W_\alpha, W_\beta < 0$. If interactions are considered up to second neighbors, the Hamiltonian for a system of N_d dimers reads as [2]:

$$\begin{aligned} H &= \sum_{n=1}^{N_d} \left(E_\alpha \left|n_\alpha\right\rangle \left\langle n_\alpha\right| + E_\beta \left|n_\beta\right\rangle \left\langle n_\beta\right|\right) + \\ &+ \sum_{n=1}^{N_d} \left(V_i \left(\left|n_\alpha\right\rangle \left\langle n_\beta\right| + H.c.\right) + V_e \left(\left|n_\beta\right\rangle \left\langle (n+1)_\alpha\right| + H.c.\right)\right) + \\ &+ \sum_{n=1}^{N_d} (W_\alpha \left(\left|n_\alpha\right\rangle \left\langle (n+1)_\alpha\right| + H.c.\right) + W_\beta(\left|n_\beta\right\rangle \left\langle (n+1)_\beta\right| + H.c.)). \end{aligned} \tag{2.22}$$

With the assumption that $E_\alpha = E_\beta = E_0$ the eigenvalues of the Hamiltonian (2.22) are given by [14]:

$$\begin{aligned} E_k^j &= E_0 + (W_\alpha + W_\beta)\cos\left(k\frac{2\pi}{N_d}\right) \pm \\ &\pm \sqrt{(W_\alpha - W_\beta)^2\cos^2\left(k\frac{2\pi}{N_d}\right) + V_i^2 + V_e^2 + 2V_iV_e\cos\left(k\frac{2\pi}{N_d}\right)}\ , \end{aligned} \tag{2.23}$$

with the eigenfunctions:

$$\left|k^j\right\rangle = \frac{1}{\sqrt{N_d}} \sum_{n=1}^{N_d} \exp\left(i2\pi k\frac{n}{N_d}\right) \left|n_{\alpha\beta}^j(k)\right\rangle\ . \tag{2.24}$$

$\left|n_{\alpha\beta}^j(k)\right\rangle$ are the symmetric ($j = s$) and antisymmetric ($j = as$) eigenfunctions of the dimer, which contain an additional phase factor that depends on the exciton state quantum number k (*vide infra*). The analytical expression for $\left|n_{\alpha\beta}^j(k)\right\rangle$

is rather longish and not very beneficial for the understanding of this work, the interested reader is therefore referred to the literature [14]. For the eigenenergies of the exciton states (2.23) the '$-$' sign applies to the antisymmetric dimer functions, $j = as$, and the '$+$' sign to the symmetric ones, $j = s$. This connection will also become clear below. As in the above case of the circular aggregate with N-fold symmetry, the quantum number k^j of the exciton states extends from $k^j = 0, \pm 1, \ldots, \pm(N_d - 1)/2$ if N_d is odd and from $k^j = 0, \pm 1, \ldots, N_d/2$ if N_d is even. Thus, due to the dimerization, the exciton band is split in two branches with equal number of exciton states. This phenomenon is commonly referred to as Davydov splitting. Note that for the upper branch the $k^s = 0$ state corresponds to the exciton state with the highest energy, with decreasing energy values for the consecutive states $k^s = \pm 1, \pm 2, ...$, in contrast to the lower branch, where the $k^{as} = 0$ state corresponds to the lowest-energy state, with increasing energy values for the states $k^{as} = \pm 1, \pm 2, ...$ For the construction of a LH1 model aggregate one would chose $N_d = 16$ [9, 71], but naturally the statements made here apply to any circular structure with C_{N_d}-symmetry.
To further simplify the expressions for the eigenvalues and eigenfunctions of the Hamiltonian (2.22), the following settings will be applied: $E_\alpha = E_\beta = E_0$, $V_i = V_e = V_0$ and $W_\alpha = W_\beta = W_0$. Note that this will virtually end the dimerization and correspond to a circular aggregate with C_N-symmetry again, except for the anti-parallel arrangement of neighboring pigments. However, if still treated as dimeric aggregate, some important insights into the excitonic properties of such systems are revealed. With the above settings the eigenvalues and eigenfunctions of the Hamiltonian (2.22) are given by [14]:

$$E_k^j = E_0 + 2W_0 \cos\left(k\frac{2\pi}{N_d}\right) \pm 2V_0 \cos\left(k\frac{\pi}{N_d}\right) , \tag{2.25}$$

and

$$|k^{as}\rangle = \frac{1}{\sqrt{2N_d}} \sum_{n=1}^{N_d} \exp\left(i2\pi k\frac{n}{N_d}\right)\left(-\exp\left(-ik\frac{\pi}{N_d}\right)|n_\alpha\rangle + |n_\beta\rangle\right) , \tag{2.26}$$

$$|k^{s}\rangle = \frac{1}{\sqrt{2N_d}} \sum_{n=1}^{N_d} \exp\left(i2\pi k\frac{n}{N_d}\right)\left(|n_\alpha\rangle + \exp\left(ik\frac{\pi}{N_d}\right)|n_\beta\rangle\right) . \tag{2.27}$$

From the eigenfunctions (2.26) and (2.27) it is now easy to see that the antisymmetric states, $|k^{as}\rangle$, correspond to the low-energy branch of the exciton band ('$-$' sign in (2.25)) and the symmetric states, $|k^s\rangle$, to the high-energy branch ('$+$' sign in (2.25)): As the transition-dipoles in the dimer unit are defined to be anti-parallel, the '$-$' sign in front of the localized $|n_\alpha\rangle$ state in the antisymmetric dimer wavefunctions in equation (2.26), inverts the phase of the n_α transition-dipole moment, such that for the antisymmetric exciton states, $|k^{as}\rangle$, the dimer transition-dipoles have

an energetically favorable head-to-tail configuration [2]. Contrarily, for the symmetric exciton states (2.27), the phase factor in the dimer wavefunctions entails that the dimer transition-dipoles remain in their energetically unfavorable head-to-head arrangement.
With the above assumptions of $E_\alpha = E_\beta = E_0$, $V_i = V_e = V_0$ and $W_\alpha = W_\beta = W_0$, the dimerization in the aggregate with C_{N_d}-symmetry is only based on the antiparallel arrangement of neighboring transition-dipoles, which again only comes from the definition of the transition-dipole moment orientation in the B850 dimer unit of LH2. Thus, ignoring this definition, the treatment of the pigment aggregate as monomeric system with C_N-symmetry, with $N = 2N_d$, yields equivalent results for the eigenvalues and eigenfunctions of the system as those denoted above in (2.25) – (2.27) [14]. In this regard, the phase factors, $\pm\exp\left(\pm ik\frac{\pi}{N_d}\right)$, in the dimer wavefunctions of (2.26) and (2.27) implicate, that the above antisymmetric and symmetric exciton wavefunctions (2.26) and (2.27), as solutions of the dimeric aggregate with C_{N_d}-symmetry, are physically identical to the exciton wavefunctions (2.20) of the monomeric aggregate with C_N-symmetry.
The comparatively simple expression for the exciton energies (2.25) is quite instructive for the derivation of the general properties of the exciton band structure of a circular aggregate. For example, the pairwise degeneracy of the $\pm k$ states can easily be deduced from the axial symmetry of the cos-function in (2.25). Additionally, it can be seen from (2.25) that, as long as interpigment interactions are restricted to nearest neighbors ($W_0 = 0$), the pattern of the exciton energies appears symmetric with respect to the monomer transition energy E_0, with a total width of the exciton band of $4V_0$. This is identical to the previously discussed linear aggregate. Taking second-neighbor interactions into account breaks the symmetry with respect to E_0, since, due to $W_0 < 0$, both the exciton states at the upper and the lower band-edge of the exciton band are shifted to lower energies. This is again similar to the linear aggregate (see section 2.7.2). Generally, it should be noted that due to the $1/r^3$-dependence of the dipole-dipole interaction and, assuming that the distance between second-neighbor pigments is about twice the distance between nearest-neighbors, the magnitude of the second-neighbor interaction is only about 1/8 of the nearest-neighbor interaction. Accordingly, the influence of the second-neighbor interaction on the exciton manifold is limited.
For an optical transition between the ground state and any given exciton state, the exciton transition-dipole moment, $\vec{\mu}\,(k^j)$, can be calculated as follows [2]:

$$\begin{aligned}\vec{\mu}\left(k^j\right) &= \langle g|\,\hat{p}\,|k^j\rangle = \langle g|\,\hat{p}\frac{1}{\sqrt{N_d}}\sum_{n=1}^{N_d}\exp\left(i2\pi k\frac{n}{N_d}\right)|n^j_{\alpha\beta}(k)\rangle \\ &= \frac{1}{\sqrt{N_d}}\sum_{n=1}^{N_d}\exp\left(i2\pi k\frac{n}{N_d}\right)\underbrace{\langle g|\,\hat{p}\,|n^j_{\alpha\beta}(k)\rangle}_{\vec{\mu}\left(n^j_{\alpha\beta}(k)\right)}\end{aligned}$$

$$= \frac{1}{\sqrt{N_d}} \sum_{n=1}^{N_d} \exp\left(i2\pi k \frac{n}{N_d}\right) \cdot \vec{\mu}\left(n^j_{\alpha\beta}(k)\right) \ , \tag{2.28}$$

where $\hat{p}$ is the transition-dipole moment operator and $\vec{\mu}\left(n^j_{\alpha\beta}(k)\right)$ are the dimer transition-dipole moments corresponding to the dimer wavefunctions $\left|n^j_{\alpha\beta}(k)\right\rangle$, respectively. The oscillator strength of the k^{th} exciton state can then be calculated as:

$$\left|\vec{\mu}\left(k^j\right)\right|^2 = \left|\langle g|\,\hat{p}\,\left|k^j\right\rangle\right|^2 \ . \tag{2.29}$$

From (2.28) it can be seen that for a non-vanishing, resulting exciton transition-dipole moment $\vec{\mu}\left(k^j\right)$, a constructive interference is needed in the sum of the individual dimer transition-dipole moments $\vec{\mu}\left(n^j_{\alpha\beta}(k)\right)$. Thus, both the phase factors, which determine the participation of the individual pigments in an exciton state, and the orientation of the pigments, play a decisive role for the resulting selection rules of optical transitions in a circular aggregate.

Due to the circular arrangement of the pigments in the aggregate, only the exciton states $k^j = 0, \pm 1$ have non-vanishing transition-dipole moments [2]. Thereby, the $k^j = 0$ transition-dipole moments are polarized parallel to the C_{N_d}-symmetry axis of the ring, whereas the $k^j = \pm 1$ transition-dipole moments lie within the plane of the ring and have a mutually orthogonal polarization. Since the transition-dipole moments of the individual pigments are oriented mainly parallel to the ring-plane (LH2 B850 dimer unit taken as reference, *vide supra*), rather little of the total oscillator strength is distributed to the $k^j = 0$ states. Furthermore, due to the head-to-tail arrangement of the transition-dipole moments in the dimer wavefunctions of the antisymmetric exciton states (2.26), nearly the complete oscillator strength of the system is concentrated in the states of the energetically lower exciton branch, and more specifically in $k^{as} = \pm 1$. For the symmetric states of the upper exciton branch, the transition-dipole moments in the dimer wavefunctions have a head-to-head arrangement (2.27), and, due to the almost parallel orientation of the transition-dipoles inside the LH2 B850 dimer unit (Figure 2.13), they almost cancel out each other. As a result, the symmetric dimer wavefunctions, $\left|n^s_{\alpha\beta}(k)\right\rangle$, have vanishing transition-dipole moments, and accordingly the oscillator strength of the upper exciton components $k^s = \pm 1$ is almost non-existent in comparison to the oscillator strength of the $k^{as} = \pm 1$ states.

A C_2-modulation of the interpigment interactions, possibly introduced by an elliptic distortion of the pigment assembly, lifts the pairwise degeneracy of the exciton states [12, 14]. Furthermore, as such type of perturbation connects exciton states which differ in quantum number by 2, oscillator strength is transferred from the optically allowed $k^{as} = \pm 1$ states to the $k^{as} = \pm 3$ states. The mutually orthogonal polarization of the $k^{as} = \pm 1$ states is not affected by the C_2-perturbation. Finally, it should be noted that a C_2-type symmetry reduction alone does not give rise to oscillator strength in the lowest exciton state $k^{as} = 0$.

Until now it was assumed that all the molecules in the aggregate have the same transition energy E_0. In the pigment-protein complexes however, stochastic variations of the protein environment lead to differences in the transition energies of individual pigments. These variations of the pigment site energies can be approximated by dressing the mean transition energy, E_0, of the pigments with a Gaussian random distribution (with a width ΔE, $fwhm$), which then describes the probability for a pigment to have a certain transition energy. The Hamiltonian for such a system can be written as:

$$H = \sum_{n=1}^{N} (E_0 + \Delta E_n) \left|n\right\rangle \left\langle n\right| + \frac{1}{2} \sum_{n=1}^{N} \sum_{n \neq m} V_{nm} \left|n\right\rangle \left\langle m\right| \ , \tag{2.30}$$

where ΔE_n reflects the inhomogeneous offset energy of pigment n. Since this type of disorder affects only the diagonal elements of the Hamiltonian it is commonly referred to as diagonal disorder. The main effect of this random diagonal disorder on the exciton manifold is, a mixing of the exciton levels, thereby lifting the pairwise degeneracy of the states and redistributing oscillator strength to nearby states, including the $k^{as} = 0$ state [2, 10].
Depending on the relative magnitude of the mean value for the nearest-neighbor interaction, $V = \frac{V_i + V_e}{2}$, and the width of the Gaussian distribution, ΔE, describing the amount of diagonal disorder in the system, either the site representation, $|n\rangle$, or the exciton representation, $|k\rangle$, is more appropriate for the description of the electronically excited states in the aggregate [2, 72]. Commonly, two limiting cases can be distinguished: In the weak coupling regime, $V/\Delta E \ll 1$, the interaction between neighboring transition-dipoles is much smaller than the site energy difference between the pigments, and the description of the excitations in terms of the localized states, $|n\rangle$, is a good approximation. On the other hand, in the strong coupling limit, $V/\Delta E \gg 1$, the nearest-neighbor interaction between the pigments is much larger than the difference of the site energies and the Frenkel exciton states, $|k\rangle$, provide a reasonable starting point for the description of the excited states in such a system. For the LH1 model structures introduced in chapter 5, the relative magnitude of V and ΔE amounts to $V/\Delta E \approx 6$. Thus, the strong coupling limit applies and the delocalized $|k\rangle$ states are a good approximation for the electronically excited states in the various aggregates.
Striking consequences are expected for the exciton manifold when a symmetry breaking gap is introduced into a circular aggregate [10, 12]. Such a system then comprises the combined properties of a linear and a circular excitonic aggregate. To begin with, the numbering scheme is now equal to the linear aggregate, $k = 1, 2, ...$, indicating that the breaking of the circular symmetry lifts the pairwise degeneracy of the exciton states. Additionally, the oscillator strength is redistributed among the exciton states and, most importantly, the lowest exciton state, $k = 1$, gains considerable oscillator strength (10% of the total oscillator strength for the sim-

ulation of a circular LH1 aggregate with a gap in [10]), even if diagonal disorder is excluded in the calculation of the exciton manifold. Note however, that these 10% are far off the 81% of the total oscillator strength, calculated for the lowest exciton state of a one dimensional linear aggregate (see section 2.7.2). Authors in [10] additionally showed that even for a circular aggregate with a gap, the $k = 2, 3$ states (corresponding to the $k^{as} = \pm 1$ states of a circular aggregate) comprise the main part of the total oscillator strength of the system.
In chapter 5 the exciton manifold of an elliptic aggregate, build up from dimeric subunits and with a gap on the long side of the ellipse, is numerically calculated. Therein, it is also demonstrated how the properties of the exciton manifold can be translated into single-complex spectra, which can then be compared to the experimentally acquired spectra.

3 Materials and methods

Why low-temperature fluorescence-excitation spectroscopy on individual RC-LH1 complexes? - A little bit of history

In 1989 Moerner and Kador were the first to achieve the detection of the optical signal from a single molecule at low temperatures [73]. Thereby, they succeeded in measuring the absorption signal of single pentacene dyes embedded in a host crystal. Since it is clear that the absorption of a single dye molecule will only marginally attenuate the intensity of the incident light beam, a sophisticated double-modulation technique had to be applied, which then resulted in an indirect measurement signal of the pentacene absorption. By measuring fluorescence-excitation spectra of the same system, shortly afterwards in 1990, Orrit and Bernard demonstrated that with this technique the signal-to-noise ratio can be improved significantly [74]. In single-molecule fluorescence-excitation spectroscopy the laser excites a small sample volume in which at most one molecule is present. Subsequently, the frequency of the exciting laser is scanned through the wavelength region of the molecule absorption and only the red-shifted fluorescence from the molecule is collected. In this way, the back-scattered laser light from the sample can be efficiently suppressed with suitable optical filters, and one is able to directly record the fluorescence-detected absorption (excitation) spectrum from an individual molecule. In the present work fluorescence-excitation spectra of individual RC-LH1 complexes from *Rps. acidophila* have been measured.
Temperature has a crucial influence on the homogeneous linewidth of excitation spectra [57]. With rising temperature, low-frequency modes of the matrix or the probe molecule are activated, leading to an increase of dephasing processes and consequently to a broadening of the homogeneous linewidth. For pentacene or terrylene in a *p*-therphenyl host crystal, it was found that this process follows an exponential dependence, such that, *e.g.* the linewidth of a terrylene molecule broadens tremendously upon raising the temperature from 2 to 5 K [57]. Another positive effect of low temperatures is that photobleaching processes are strongly reduced, allowing to study a molecule over a much longer time period compared to room-temperature. Hence, in this thesis individual LH complexes have been studied under cryogenic

conditions, at 1.2 K.
By recording fluorescence-excitation spectra from single LH complexes, spectral details become visible that are otherwise buried under the ensemble average [11, 12]. From these spectral characteristics, amongst other things, conclusions can be drawn on the geometric arrangement of the BChl a molecules in a LH complex [12, 14]. On these grounds, in the present work the currently unknown pigment-distribution in the LH1 complex from *Rps. acidophila* has been investigated by means of low-temperature single-complex fluorescence-excitation spectroscopy.

3.1 Sample and chemicals

The RC-LH1 complexes from *Rps. acidophila*, strain 10050, were obtained from a cooperation partner, Prof. R.J. Cogdell at the University of Glasgow, U.K.. *Rps. acidophila* was grown in Glasgow and the RC-LH1 complexes were prepared as described previously [75] with the exception that, once the RC-LH1 complexes were removed from the sucrose gradient after centrifugation, the detergent was exchanged from 0.1% LDAO to 0.02% DDM. This was carried out by binding the complexes to an anion exchange column, washing the bound complex with five column volumes of detergent buffer containing 0.02% DDM (20 mM Tris/HCl (pH 8), 0.02% DDM) and then the bound complexes were eluted in 200 mM sodium chloride, 20 mM Tris/HCl (pH 8) and 0.02% DDM. The RC-LH1 complexes were stabilized by this detergent exchange and their concentration was adjusted to give an absorption of 100 cm^{-1} at 885 nm (OD_{885}). This stock solution was transferred to Bayreuth, where it was aliquoted, diluted to an OD_{885} of 10 cm^{-1}, and stored in the dark at $-80\ ^{\circ}C$ until use. To eliminate possible damage during transportation, the quality of the sample was checked by recording a room-temperature ensemble absorption spectrum (see Figure 4.2, red line).
Table 3.1 shows a list of the chemicals that were used for sample preparation.

trade name	chemical name	company
DDM	dodecyl-β-D-maltoside	Roth Chemie
Tris	tris-hydroxymethyl-aminomethane	Sigma-Aldrich
PVA	polyvinyl alcohol ($M_W = 124,000-$ $-186,000\ g/mol$)	Sigma-Aldrich
DOPC	1,2-dioleoyl-*sn*-glycero-3-phosphocholine	Avanti Polar Lipids

Table 3.1: *List of the chemicals used for sample preparation.*

For membrane reconstitution 500 μl Slide-A-Lyser dialysis cassettes with a molecular weight cutoff of 3500 Da were purchased from Thermo Scientific (Rockford, U.S.A.).

3.2 Detergent-mediated membrane reconstitution

In order to create a more native-like environment for the detergent stabilized RC-LH1 complexes from *Rps. acidophila*, the complexes were reconstituted into prefabricated lipid vesicles. Thereby, the major 'trick' in the reconstitution protocol is to gradually reduce the detergent concentration in the solution of detergent stabilized RC-LH1 complexes, below the critical micelle concentration (CMC) of the detergent. By doing this, it becomes entropically favorable for the exposed hydrophobic groups of the RC-LH1 complexes to be incorporated into the lipid bilayer of the available lipid vesicles [45, 46]. In this work a detergent-mediated reconstitution procedure was applied, as described in [76–78]. The crucial steps of this procedure are described in the following and sketched in Figure 3.1:

I. As the natural bacterial membrane is too complex for a systematic investigation, the RC-LH1 complexes from *Rps. acidophila* were extracted from their native membrane (see above). From Glasgow a solution of pure RC-LH1 complexes was received, stabilized in detergent buffer (20 mM Tris/HCl (pH 8), 0.02% DDM) to prevent the dissociation/denaturation of the complexes.

II. As a starting point for the preparation of unilamellar lipid vesicles a commercially available stock solution of lipid molecules (DOPC) dissolved in chloroform was used. Initially, to achieve the formation of a lipid film, the solvent had to be removed from the lipid solution. For this, 2 mg of solvated DOPC, were dried under a constant nitrogen flow. Furthermore, to remove all traces of organic solvent, the lipid film was kept under vacuum overnight. In order to avoid chemical oxidation of the lipid hydrocarbon chains, the films were then stored under argon atmosphere at $-20\,°C$ until use.
For vesicle preparation, the lipid films were resuspended in 20 mM Tris buffer (pH 8) at a concentration of 1 mg/ml and vortexed until a complete hydration of the film was achieved. The product of hydration is a large multilamellar vesicle, analogous in structure to an onion, with each lipid bilayer separated by a layer of water. Then, a sequential extrusion of the lipid suspension through polycarbonate membranes (Avanti Polar Lipids, Alabaster, U.S.A.) with decreasing pore size 0.8, 0.2, 0.1 and 0.05 μm, respectively (Avanti protocol), was performed. This procedure yielded unilamellar vesicles with a mean diameter of 64 nm, as determined by dynamic light scattering (DLS).

III. Immediately after preparation the vesicles were used for membrane reconstitution. In order to do so, 250 μl of detergent stabilized RC-LH1 complexes were diluted to either 35 pM (single-complex experiments) or to 650 nM (ensemble experiments), mixed with 250 μl of the liposome suspension, and inserted into a Slide-A-Lyser dialysis cassette (Thermo Scientific) with a molecular weight cutoff

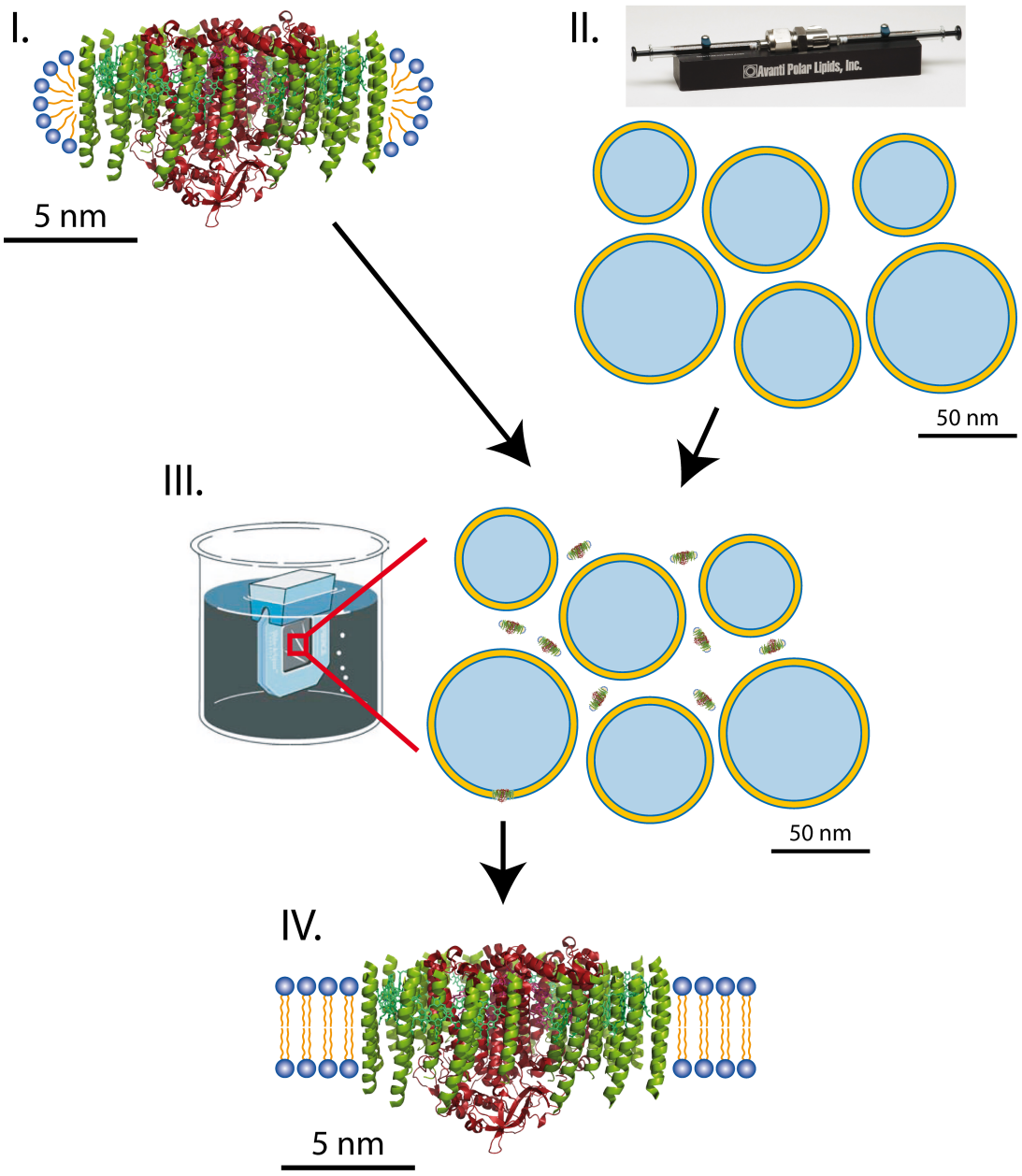

Figure 3.1: *Detergent-mediated membrane reconstitution: I. Initial RC-LH1 complexes from Rps. acidophila stabilized in detergent micelles of the detergent DDM. II. Preparation of unilamellar DOPC vesicles by extrusion. Top: "Avanti mini-extruder" (Avanti Polar Lipids). Bottom: Sketch of the unilamellar vesicles, shown as cross-sections in a two-dimensional representation (mean vesicle diameter: 64 nm). The yellow color indicates the hydrophobic core region of the lipid membrane and the blue color indicates the hydrophilic outer boundaries of the membrane. Water inside the vesicles is indicated by the light blue color. III. Dialysis of the DOPC vesicles together with the detergent stabilized RC-LH1 complexes, against a reservoir of detergent-free buffer. IV. RC-LH1 complexes reconstituted into a lipid bilayer.*

of 3500 Da. This molecular weight cutoff of the dialysis membrane ensures permeability for the detergent molecules, but holds back the lipid vesicles as well as the pigment-protein complexes. The suspension of liposomes with detergent stabilized RC-LH1 complexes was dialyzed against a reservoir of 1.4 l of detergent-free buffer at 5 $°C$ in a dark cold room for 4 days, with exchanging the buffer once at half time. The reconstituted RC-LH1 complexes were then removed from the dialysis cassette and either used immediately for the spectroscopy experiments or stored at 4 $°C$ in the dark for, at most, 9 days until use.

IV. With the end of the dialysis process, the incorporation of the RC-LH1 complexes into a more native-like lipid bilayer environment is complete. For the single-complex samples the average ratio of lipid molecules to RC-LH1 complexes was $(3.5 \times 10^7)/1$ (molar concentration ratio, c/c), which corresponds to about 0.001 RC-LH1 complexes per vesicle [77]. This high dilution ensures that the probability of having two complexes in one vesicle is extremely low (0.0001%). For the samples used for ensemble spectroscopy, the average lipid-to-protein ratio was about 1900/1 (c/c), corresponding to an average of 19 RC-LH1 complexes per vesicle.
In order to test the integrity of the RC-LH1 complexes after the reconstitution process, and to verify whether the protocol was successful, room-temperature absorption spectra were recorded from the ensemble samples using a commercial UV/VIS/NIR-Spectrophotometer (Lambda 750, Perkin Elmer, Waltham, U.S.A.) (see Figure 4.8, red line). The stability of the reconstituted samples was checked by taking a second absorption spectrum from the same sample two weeks later. Both spectra were identical and no indication for a dissociation/denaturation of the RC-LH1 complexes was found.

3.3 Sample preparation

3.3.1 Room-temperature ensemble absorption spectroscopy

Ensemble absorption spectra of bulk samples were recorded with a commercial UV/VIS/NIR-Spectrophotometer (Lambda 750, Perkin Elmer, spectral resolution 1 nm) using quartz cuvettes with an optical path length of 1 mm (Hellma, Müllheim, Germany). The optical density of the samples was adjusted to about 1 cm^{-1} at 885 nm (OD_{885}), which corresponds to a concentration of 265 nM [79].
For ensemble absorption spectroscopy on thin films, a 25 μl drop of sample solution was deposited onto a quartz substrate and left there for adsorption under nitrogen atmosphere, in the dark, for 10 min. Then, the substrate was spun for 10 s at 500 rpm and 60 s at 2000 rpm. The detergent buffer solution containing the RC-LH1 complexes was either used as is, or mixed with 2% (w/w) PVA. In order to detect a signal from the films with a thickness of only about 100 nm, the protein

concentration was adjusted to $OD_{885} = 25\ cm^{-1}$, corresponding to 6.6 μM.

3.3.2 Low-temperature spectroscopy experiments

PVA sample

For single-molecule spectroscopy an aliquot with detergent stabilized RC-LH1 complexes was diluted in several steps in detergent buffer (20 mM Tris/HCl (pH 8), 0.02% DDM) to a protein concentration of about 10 pM (265 nM for ensemble experiments). During the last dilution step 1% (w/w) PVA was added to the sample. These preparations were done at room-temperature in the dark to minimize any photodamage of the sample. Subsequently, a drop (25 μl) of this solution was spin-coated in an inert nitrogen atmosphere onto a quartz substrate, for 10 s at 500 rpm and 60 s at 2000 rpm (model P6700, Specialty Coating System, Indianapolis, U.S.A.). This resulted in an amorphous polymer film with a thickness of about $50 - 70\ nm$. The sample was then mounted into a helium-bath cryostat and precooled to about $-170\ °C$ by slowly adding liquid nitrogen into the cryostat. After pumping out the nitrogen, the cryostat was filled with liquid helium and cooled down to 1.2 K.

Detergent/lipid bilayer sample

A drop (25 μl) of the RC-LH1 solution (either in detergent buffer or in the lipid bilayer) was pipetted under nitrogen atmosphere, in the dark, onto a quartz substrate and left there to adsorb for 10 min. Subsequently, the substrate was spun for 10 s at 500 rpm and 60 s at 2000 rpm. In order to minimize the dissociation of the RC-LH1 complexes stabilized in detergent buffer solution [41], for this sample the above described steps were carried out in a dark cold room at 5 $°C$. For the samples with the reconstituted RC-LH1 complexes the dilution and the spin-coating was done at room-temperature, under dimmed light conditions. Next, the sample was plunged into a cryostat that was prefilled with liquid nitrogen. Then, the nitrogen was pumped out and the cryostat was filled with liquid helium and cooled down to 1.2 K. The concentration of the RC-LH1 complexes was about 265 nM for the ensemble experiments and 10 pM for the single-molecule experiments.

3.4 Experimental setup

For the recording of both fluorescence-excitation and fluorescence-emission spectra a home-built microscope was used that could be operated either in wide-field or in confocal mode. As excitation source served a continuous-wave tunable titanium-sapphire (Ti:Sa) laser (3900S, Spectra Physics, Mountain View, U.S.A.)

that was pumped by a frequency-doubled continuous-wave neodynium:yttrium-vanadate ($Nd:YVO_4$) laser (Millenia Vs, Spectra Physics). Precise changes of the wavelength of the Ti:Sa laser were accomplished by rotating an intracavity birefringent filter with a motorized micrometer screw (Model MM4005, Newport Corporation, Irvine, U.S.A.). In this way, the laser could be tuned continuously within the gain profile of the Ti:Sa crystal, from $770 - 920\ nm$. The accuracy as well as the reproducibility of the laser frequency were tested with a wavemeter and was about $1\ cm^{-1}$ in both cases.

3.4.1 Wide-field imaging

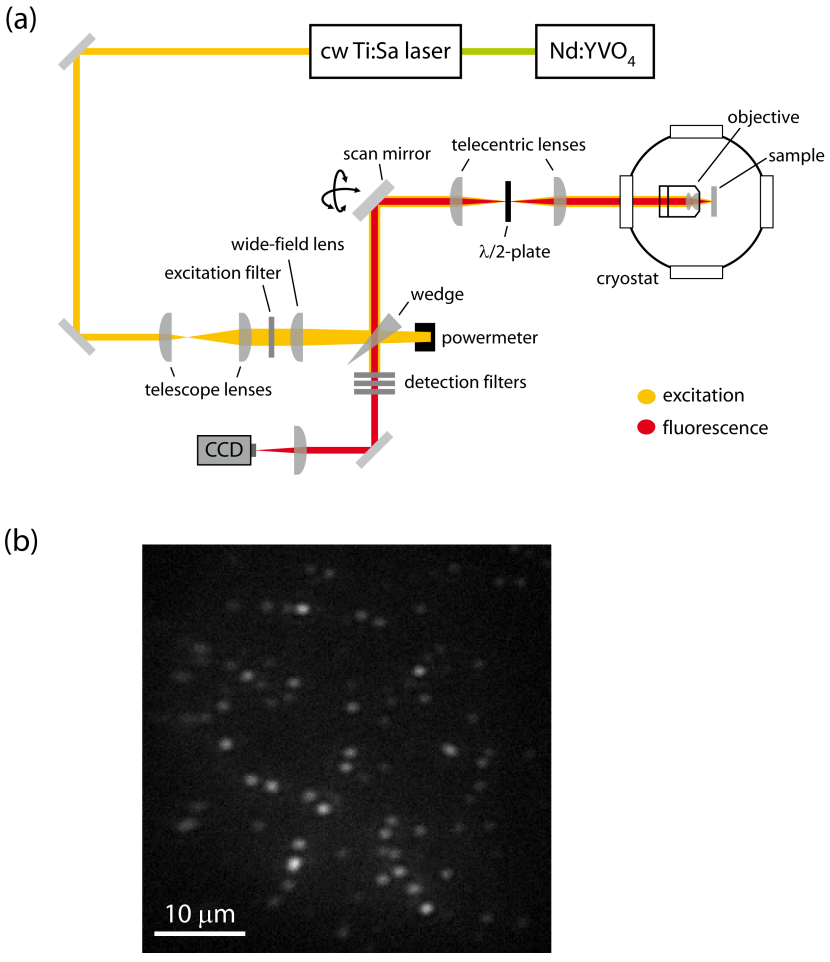

Figure 3.2: *(a) Schematic illustration of the experimental setup when operated in the wide-field imaging mode. The excitation light path is shown in yellow and the detection path in red (for details, see text). (b) Example wide-field image with each bright spot corresponding to the diffraction limited image of an individual RC-LH1 complex.*

For wide-field imaging the sample was aligned in the focal plane of the microscope objective ($f = 2.9\ mm$, NA = 0.85, Microthek, Hamburg, Germany), where both sample and objective were mounted inside the cryostat and immersed in liquid helium (Figure 3.2a). By a biconvex lens ("wide-field lens", focal length, $f = 300\ mm$) the excitation light was focused onto the back-focal plane of the objective, such that a divergent light beam was entering the objective. As a result, the excitation light was only weakly focused on the sample plane, illuminating an area of about $45 \times 45\ \mu m^2$ [80]. The excitation wavelength was 885 nm for the RC-LH1 complexes in PVA and 890 nm for the complexes in detergent buffer/lipid bilayer, in resonance with the respective low-temperature ensemble absorption maxima. Additionally, the exciting laser light passed through an excitation filter (BP 875/50, AHF Analysetechnik, Tübingen, Germany) to suppress residual laser fluorescence. The fluorescence emitted from the sample was collected by the same microscope objective which was used for excitation. The signal was then focused onto a back-illuminated CCD camera (512 SB, Princeton Instruments, Trenton, U.S.A. or Ikon-M 934 BR-DD, Andor Technology, Belfast, U.K.), after passing a set of suitable bandpass filters that blocked back-scattered excitation light (BP 925/40 for the PVA/detergent samples and BP 935/40 for the lipid bilayer samples; AHF Analysetechnik). An example wide-field image, where the fluorescence signal from the sample was integrated for 20 s, is shown in Figure 3.2b. Each bright spot corresponds to the diffraction limited image of an individual RC-LH1 complex. From the wide-field image, a spatially well-isolated complex was then selected for the confocal studies.

3.4.2 Confocal fluorescence-excitation spectroscopy

Single-complexes

To record a fluorescence-excitation spectrum from the selected complex, the setup was switched to the confocal mode (Figure 3.3a). In this mode, the excitation laser was guided through an excitation pinhole to optimize the beam profile, and the parallel laser beam entering the objective was then tightly focused on the sample plane, creating a diffraction-limited excitation volume. This confocal volume could be made to coincide with the complex by a well-controlled deflection of the excitation beam with the help of a gimbal mounted scan mirror. A pair of telecentric lenses ensured a precise displacement of the focus within the sample plane, while maintaining alignment with the back-aperture of the objective. The fluorescence emitted from the sample was collected by the same objective and focused onto a single-photon counting avalanche photodiode (APD) (SPCM-AQR-16, Perkin Elmer, Vaudreuil, Canada) after passing a set of four bandpass filters (BP 925/40 for the PVA/detergent samples and BP 935/40 for the lipid bilayer samples; AHF Analysetechnik). Thereby, the finite size of the detector-diode ($\varnothing \approx 170\ \mu m$) served

also as detection pinhole in the confocal setup.

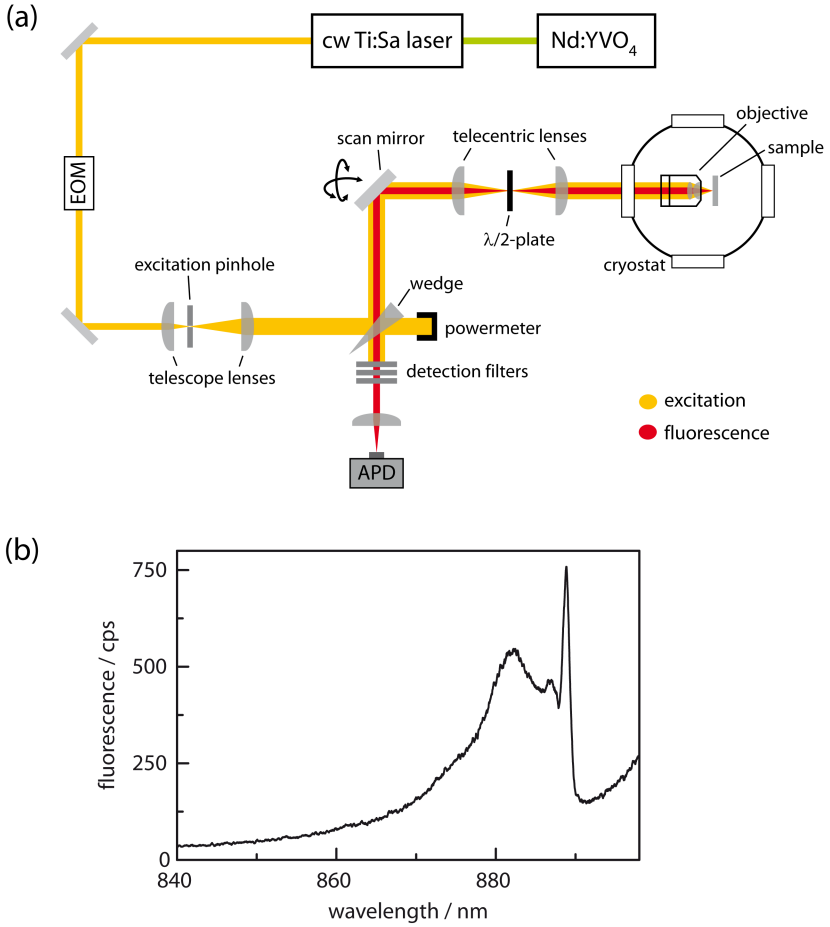

Figure 3.3: *(a) Schematic illustration of the experimental setup when operated in the confocal mode. The excitation light path is shown in yellow and the detection path in red (for details, see text). (b) Typical fluorescence-excitation spectrum of an individual RC-LH1 complex from Rps. acidophila, averaged over all incident polarizations.*

The laser was scanned repetitively between $836-899\ nm$ for the RC-LH1 complexes stabilized in PVA/detergent buffer and from 850 to 910 nm for the complexes in the lipid bilayer. Thereby, each recorded trace was stored separately in computer memory. The scan speed was $2\ nm/s$ ($\approx 26\ cm^{-1}/s$) and the acquisition time was $10\ ms$, which yields a nominal resolution of about $0.26\ cm^{-1}$, ensuring that the spectral resolution is limited by the spectral bandwidth of the laser, *i.e.* $1\ cm^{-1}$. In order to examine the polarization dependence of the optical transitions of the complexes, a $\lambda/2$-plate was inserted in the excitation path. This plate was rotated by 3.1° between successive scans, changing the linear polarization of the excitation light by twice this value. The stability of the laser power was ensured by a feed-

back loop controlled electro-optical modulator (EOM). In this way, a stabilization of the incident laser power to a variation of only about 10% over the detected spectral range ($836 - 899$ or $850 - 910$ nm, respectively) could be achieved. During the measurement of fluorescence-excitation spectra, this remaining variation of the laser power as a function of the excitation wavelength was recorded with a powermeter and all spectra were corrected for this variation. The superior ability of confocal microscopy for background suppression [81], can be observed in Figure 3.3b, where the fluorescence-excitation spectrum of a single RC-LH1 complex from *Rps. acidophila* features a high signal-to-noise ratio (which is additionally improved by averaging over many spectra with different polarizations of the incident radiation). Typically the excitation intensity for the acquisition of single-complex fluorescence-excitation spectra was about 200 W/cm^2 and measurements were conducted at 1.2 K.

Ensemble

For the acquisition of fluorescence-excitation spectra from ensembles of RC-LH1 complexes, the same measurement principle as above was applied. However, in these measurements the quartz substrate was evenly covered by a thin layer of RC-LH1 complexes, such that in the wide-field mode the whole illuminated area was fluorescing. Fluorescence-excitation spectra were then recorded from arbitrary confocal volumes within the displacement range of the scan mirror. The scanning range amounted to $780 - 900$ nm, and a pair of bandpasses (BP 925/40, AHF Analysetechnik) was used as detection filters. The typical excitation intensity for the ensemble fluorescence-excitation spectra was about 5 W/cm^2.

3.4.3 Ensemble fluorescence-emission spectroscopy

For the acquisition of fluorescence-emission spectra from thin-film ensembles of RC-LH1 complexes, the setup was used in the confocal mode. The detection unit, consisting of a spectrometer (SpectraPro-150, 300 lines/mm, Acton Research Corporation, Acton, USA) with a CCD camera (Luca-R 604M-OM, Andor Technology) attached to it, was positioned opposite to the CCD camera for wide-field imaging (Figure 3.2a). The emission signal from the sample was then deflected into the direction of the spectrograph by means of a flip mirror [82]. The sample was excited at 800 nm through an excitation bandpass filter (BP 805/60, AHF Analysetechnik). The emission from the sample passed through a pair of longpass filters (LP 830, AHF Analysetechnik), was dispersed in the spectrometer and imaged onto the CCD chip. The spectral resolution of the combined spectrograph/camera system amounted to 1.5 nm (20 cm^{-1}) and all emission spectra have been corrected for the spectral sensitivity of the combined system. The exposure time for the measurement of the ensemble fluorescence-emission spectra amounted to 15 s and the excitation intensity was 14 kW/cm^2.

4 Spectroscopy on RC-LH1 complexes from *Rps. acidophila*

In the first part of this chapter the RC-LH1 complex from *Rps. acidophila* has been revisited for single-molecule spectroscopy. Thereby, the pigment-protein complexes were stabilized in the detergent buffer solution using a relatively mild detergent dodecyl-β-D-maltoside (DDM), instead of lauryldimethylamine N-oxide (LDAO) which was applied in a previous study [10]. This leads to a significant reduction of the fraction of broken/dissociated RC-LH1 complexes with respect to [10] and thus, it was possible to investigate a sufficiently large sample of individual RC-LH1 complexes. For most of the complexes the fluorescence-excitation spectra exhibit a narrow spectral feature at the red end of the spectrum. Analysis of the statistics of the spectral properties yields a close resemblance with the results obtained on RC-LH1 complexes from *Rps. palustris* for which a low-resolution x-ray structure is available. Based on this comparison the conclusion is gained that for both species the LH1 complex can be described by the same structural model, *i.e.* an overall elliptical assembly of pigments that features a gap.
In the second part of this chapter RC-LH1 complexes from *Rps. acidophila* stabilized in detergent buffer solution and reconstituted into a phospholipid bilayer have been investigated, and the results were compared with the outcome of the first part, conducted on RC-LH1 immobilized in polyvinyl alcohol (PVA). The aim of this study was to test whether the immobilization of the complexes in a PVA matrix might lead to a deterioration of the proteins and thereby limit the accessible information that can be obtained from optical spectroscopy. It has been found that the complexes dissolved in a detergent buffer solution, without stabilization in a PVA matrix, are subject to fast spectral dynamics preventing any meaningful application of single-molecule spectroscopy. Furthermore, for the complexes reconstituted into a lipid bilayer it is revealed that the reconstitution process results in a significantly larger fraction of broken complexes with respect to the preparation of the complexes in a PVA film. However, it is also found that for the intact complexes the statistics of the key spectral features, such as the spectral separations of the bands and the mutual orientation of their transition-dipole moments, show

no difference as a function of using either a bilayer or PVA as a matrix. Given the additional effort involved in the reconstitution process, the lower amount of intact RC-LH1 complexes, and, concerning the decisive spectral details, the identical results with respect to embedding the complexes in a PVA matrix, led to the conclusion that the immobilization of these proteins in a PVA matrix is a good choice for conducting low-temperature experiments on individual light-harvesting complexes.

4.1 Spectroscopy on RC-LH1 complexes stabilized in the detergent DDM

4.1.1 The RC-LH1 complex from *Rps. acidophila*

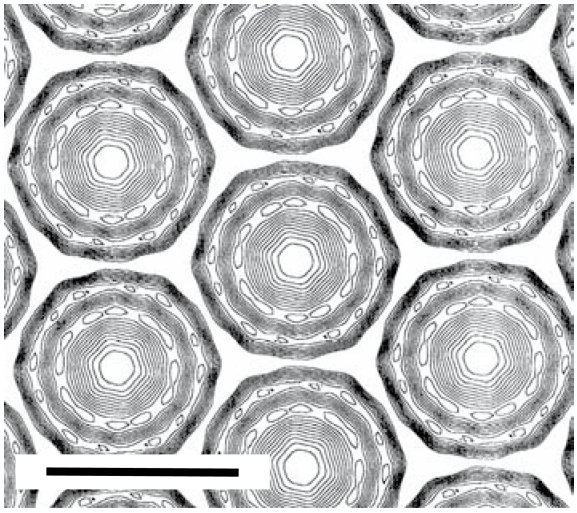

Figure 4.1: *19 Å resolution projection map of negatively stained two-dimensional crystals of RC-LH1 complexes from Rps. acidophila, strain 7750 (from [2]). The length of the scale bar corresponds to* 12 nm.

So far structural information on the RC-LH1 complex from *Rps. acidophila* is very limited. There is only a projection map of negatively stained two-dimensional crystals of RC-LH1 complexes from the strain 7750 of *Rps. acidophila* available (in contrast to strain 10050 investigated in this work), however with a very poor resolution of only 19 $\AA$ (Figure 4.1). From this projection map one could infer that the LH1 complexes from this bacterial species are circular and completely surround their corresponding RC. Then again the projection map originates from a time (1994), where such a type of LH1 model was dogma and actually the map was created by assuming a six-fold symmetry for a complete LH1 ring [2]. Therefore,

given also the very low resolution of the projection map, the only information that can be extracted from it, is that the RC-LH1 complexes from *Rps. acidophila* are monomeric, but neither the precise shape (circular *vs.* elliptical) of the LH1 complex, nor if the LH1 aggregate has a gap or not, are revealed.
It is now well established that the spatial arrangement of the pigments determines to a large extent the spectroscopic features of the complexes and that in these systems collective effects have to be considered in order to appropriately describe their electronically excited states [2, 5, 12, 14, 15, 61, 62, 64, 70, 83–88]. This leads to the so called Frenkel excitons, which arise from the interactions of the transition-dipole moments of the individual pigments, and which correspond to delocalized electronically excited states. The presence of a gap in the chromophore arrangement has severe consequences for the electronic structure of the complex and the photophysical parameters of the exciton states. Firstly, degeneracies between the exciton states are lifted and following common practice the exciton states are numbered $k = 1, 2, \ldots, N$ [59], with N being the total number of pigments in the aggregate. Secondly, significant oscillator strength is shifted to the lowest exciton state, *i.e.* $k = 1$, in marked contrast to a closed-ring BChl *a* arrangement, as for example for LH2, where nearly all oscillator strength is accumulated in the next higher exciton states [11, 12, 14, 85]. Since the fluorescence lifetime of the $k = 1$ state is in the order of 600 ps [56, 89] which is rather long with respect to the relaxation of the higher exciton states, that takes place on a 100 fs timescale [27, 90], this leads to the occurrence of a relatively narrow spectral feature at the red-edge of the absorption spectrum. Exploiting single-molecule spectroscopy those features could be made visible and not only confirmed the presence of the gap in LH1 from *Rps. palustris*, but also gave rise to a refinement of details of the x-ray structure [12, 15].
The first single-molecule experiments on RC-LH1 complexes were conducted by Ketelaars et al. [10] on those from the species *Rps. acidophila*. This study was a follow up of the experiments on LH2 complexes from the same species [11, 13, 14]. Unfortunately, the resulting spectra revealed a large degree of spectral heterogeneity and it was argued that in some of the complexes the LH1 rings were not fully intact or might even be decomposed. The spectral signature of those LH1 complexes which were considered intact, was interpreted as originating from a closed ring structure. However, this interpretation was based upon the work performed on the LH2 complexes [13, 14] for which such a structural composition is well known. This raises the question if the conclusions drawn from the early LH1 spectra for the buildup of their structures were really correct.
By means of simple room-temperature ensemble absorption experiments clear evidence was already found for a partial dissociation of the RC-LH1 complexes from *Rps. acidophila* if they were stabilized in the detergent lauryldimethylamine N-oxide (LDAO), as it was used in the previous study [10] (see following section 4.1.2). Thus, given the remaining structural uncertainties for the RC-LH1 complex from *Rps. acidophila* and the encouraging results obtained on RC-LH1 from

Rps. palustris [12, 15], in this work the RC-LH1 complex from *Rps. acidophila* was revisited for single-molecule spectroscopy, now using the milder detergent dodecyl-β-D-maltoside (DDM) for the stabilization of the complexes in the buffer solution.

4.1.2 Results and Discussion

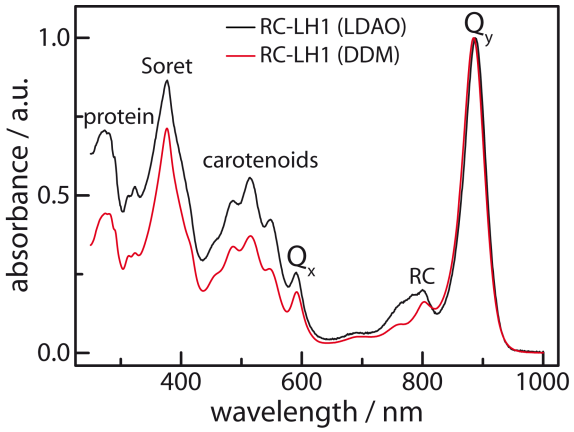

Figure 4.2: *Room-temperature ensemble absorption spectra of RC-LH1 complexes from Rps. acidophila solubilized in LDAO (black line, data taken from [10]) and DDM (red line). The assignments of the various bands are given in the figure. For better comparison the spectra have been normalized to the peaks of the Q_y absorption bands.*

Figure 4.2 shows a comparison of the room-temperature ensemble absorption spectra of RC-LH1 from *Rps. acidophila* obtained from complexes that were either stabilized in the detergent LDAO (black line, from [10]) or in DDM (red line). Both spectra feature the known BChl *a* absorption bands (Q_y: 885/887.5 nm, DDM/LDAO; Q_x: 591.5/591 nm; Soret: 376.5/377 nm) as well as bands that can be attributed to the RC (803/799 nm), the carotenoids (515/514.5 nm, main peak), and the proteins' aromatic residues (274/273 nm) [4]. A commonly accepted measure for the purity of the sample is given by the ratio of the optical densities at 885 nm and at 280 nm, OD_{885}/OD_{280}, which amounts to 2.26 for the sample stabilized in DDM (Figure 4.2, red line) and 1.43 for the one in LDAO (Figure 4.2, black line), indicating the higher quality of the DDM sample. Another hint that the LDAO-stabilized RC-LH1 complexes might be partly broken is provided by the pronounced shoulder of the RC absorption band around 783 nm. This shoulder probably originates from free BChl *a* which absorbs around 770 nm [4], and is not observed for the DDM-stabilized sample.
The low-temperature (1.2 K) fluorescence-excitation spectra from individual RC-LH1 complexes were recorded as a function of the polarization of the excitation light. The laser was scanned repetitively between 836 and 899 nm and between

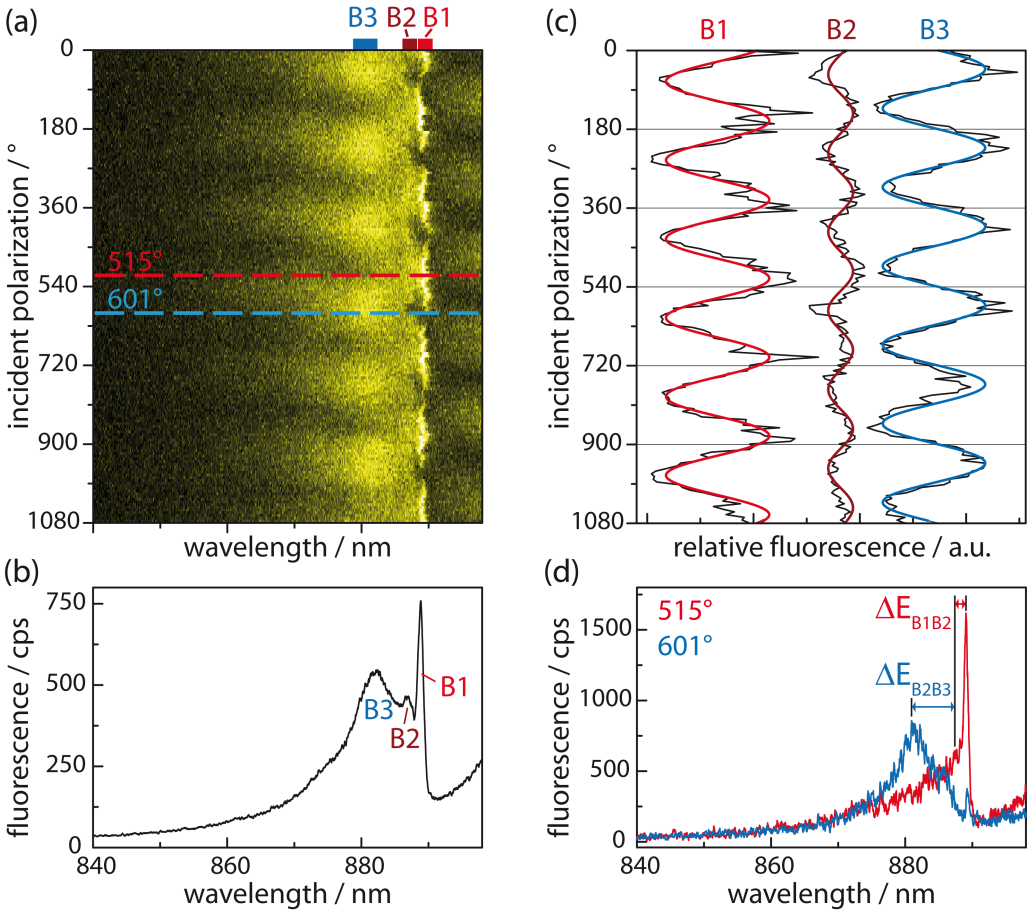

Figure 4.3: *Low-temperature* $(1.2\ K)$ *fluorescence-excitation spectrum from an individual RC-LH1 complex from Rps. acidophila as a function of the polarization of the excitation light. (a) Stack of 174 consecutively recorded individual spectra. Between two successive spectra the polarization of the incident radiation has been rotated by* $6.2°$*. The horizontal axis corresponds to the excitation wavelength, the vertical axis to the scan number or equivalently to the polarization angle and the intensity is given by the color code. The excitation intensity was* $300\ W/cm^2$*. (b) Spectrum that corresponds to the average of the 174 consecutively recorded spectra. (c) Integrated fluorescence intensity of the three spectral intervals B1-B3 that are indicated at the top of the panel in part (a), as a function of the polarization of the incident radiation (black lines). The colored lines correspond to* $\cos^2$*-type functions that have been fitted to the data. (d) Average of 3 adjacent spectra that have been recorded for polarizations where the distinct spectral features B1 (red) and B3 (blue) are most pronounced. The positions of the spectra within the stack displayed in part (a) are indicated by the dashed lines. To improve the signal-to-noise ratio the spectra in (b) and (d) have been smoothed by averaging over five adjacent data points.*

two successive scans the polarization of the incident radiation was rotated by 6.2°. An example for this protocol is shown in Figure 4.3. The resulting spectra are shown in Figure 4.3a in a two-dimensional representation, where 174 individual scans have been stacked on top of each other. The horizontal axis corresponds to wavelength, the vertical axis to the polarization of the excitation laser, and the detected fluorescence intensity is given by the color code. Averaging all individual spectra yields the sum spectrum displayed in Figure 4.3b. It shows three spectral features denoted as B1-B3 that peak at 889 nm, 887 nm, and 882 nm, respectively. Subsequently, in each individual spectrum the intensity of the bands B1-B3 was integrated over a small wavelength interval as indicated by the bars on top of Figure 4.3a, and the result is displayed in Figure 4.3c as a function of the polarization (black lines). For all three bands the intensity shows a modulation that is consistent with a $\cos^2$-dependence (colored lines). From this procedure the mutual angle between the transition-dipole moments of the bands is obtained, that amounts to $\Delta\alpha_{B1B2} = 17°$ for B1 and B2, and $\Delta\alpha_{B2B3} = 79°$ for B2 and B3, respectively. Finally, Figure 4.3d displays two spectra that have been recorded for those polarizations where the bands B1 (red) and B3 (blue) feature the maximum intensity. In order to improve the signal-to-noise ratio, each spectrum in Figure 4.3d corresponds to the average of three consecutive individual laser scans, indicated by the dashed lines in Figure 4.3a. This approach provides the energetic separations between the spectral bands which are $\Delta E_{B1B2} = 26\ cm^{-1}$, and $\Delta E_{B2B3} = 60\ cm^{-1}$ for this example.

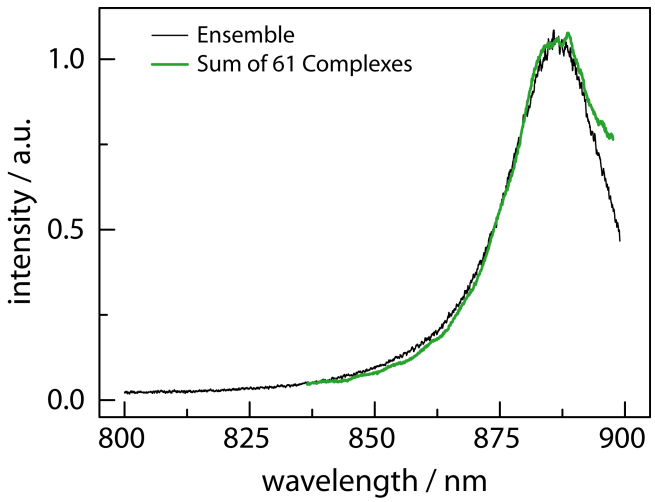

Figure 4.4: *Low-temperature (1.2 K) ensemble fluorescence-excitation spectra of RC-LH1 complexes from Rps. acidophila. The black spectrum was recorded for an ensemble of RC-LH1 complexes embedded in a thin polymer film with an excitation intensity of about 5 W/cm^2. The green line corresponds to the sum of 61 spectra recorded for individual RC-LH1 complexes. For easier comparability the two spectra have been peak normalized.*

In total, fluorescence-excitation spectra have been recorded from 61 individual, DDM-stabilized RC-LH1 complexes from *Rps. acidophila*. Figure 4.4 shows a comparison between the sum of all 61 spectra, averaged over all incident polarizations (green line), and a low-temperature (1.2 K) ensemble fluorescence-excitation spectrum of DDM-stabilized RC-LH1 complexes embedded in a PVA matrix (black line). The ensemble spectrum has its maximum at about 886.4 nm and a width of 306 cm^{-1} (full width at half-maximum, $fwhm$). The sum spectrum is slightly red shifted with respect to the ensemble spectrum and also has a slightly broader linewidth (887.1 nm/323 cm^{-1}; peak/$fwhm$). Overall the ensemble spectrum is quite well reproduced by the spectrum that results from the summation of the single-complex spectra (in contrast to the precursor study, where only 24 complexes were measured [10]), indicating that in this work the selected complexes are a fair statistical representation of the ensemble.
Generally, the excitation spectra featured a few broad bands with linewidths ($fwhm$) varying between 100 cm^{-1} and 290 cm^{-1}. Most of the complexes (49/61 corresponding to 80%) featured in addition at least one narrow absorption line. The widths of these lines varied between 3 and 12 cm^{-1} for different complexes. However, it is worth noting that the widths of the narrow lines do not reflect the homogeneous linewidths, but are determined by unresolved spectral diffusion. For the narrow line B1 depicted in Figure 4.5 spectral diffusion can be observed on two timescales, where both diffusion types lead to a broadening of the apparent linewidth of B1. Within the time span of the measurement, which should be assumed here as the time needed for the acquisition of the 58 spectra shown in Figure 4.5a, comparatively large spectral jumps (red arrow in Figure 4.5a) and gradual spectral drifts of the transition frequency of the narrow line can be seen. As a result, the apparent linewidth of a narrow line is considerably broadened in a spectrum averaged over many scans. Thus, to circumvent the large spectral drifts occurring on a slow timescale, one should try to determine the homogeneous linewidth of B1 within a single scan (Figure 4.5b). This relationship is demonstrated in Figure 4.5. Panel (a) of the Figure shows a selected part of the two-dimensional representation of the measurement protocol of the complex in Figure 4.3. In panel (b) an individual scan is shown, where the spectrum has been smoothed by averaging over five adjacent data points to improve the signal-to-noise ratio. Panels (c) and (d) show an expanded view around the narrow line B1 of the spectrum in (b). Thereby, in panel (c) the spectrum is still shown in its smoothed form, making the narrow line appear as a double peak with peak positions at 889.46 and 889.83 nm, respectively. Panel (d) shows the same spectral range as in (c) without smoothing of the spectrum and finally panel (e) shows the gray shaded region of panel (d) on a further expanded wavelength scale. The black dots indicate the data points which are separated by about 0.02 nm ($\approx 0.26\ cm^{-1}$) and the black line connecting the points is shown as a guide for the eyes. The spectral region marked in red is an educated guess for the spectral diffusion range of the narrow line within the shown scan. The green

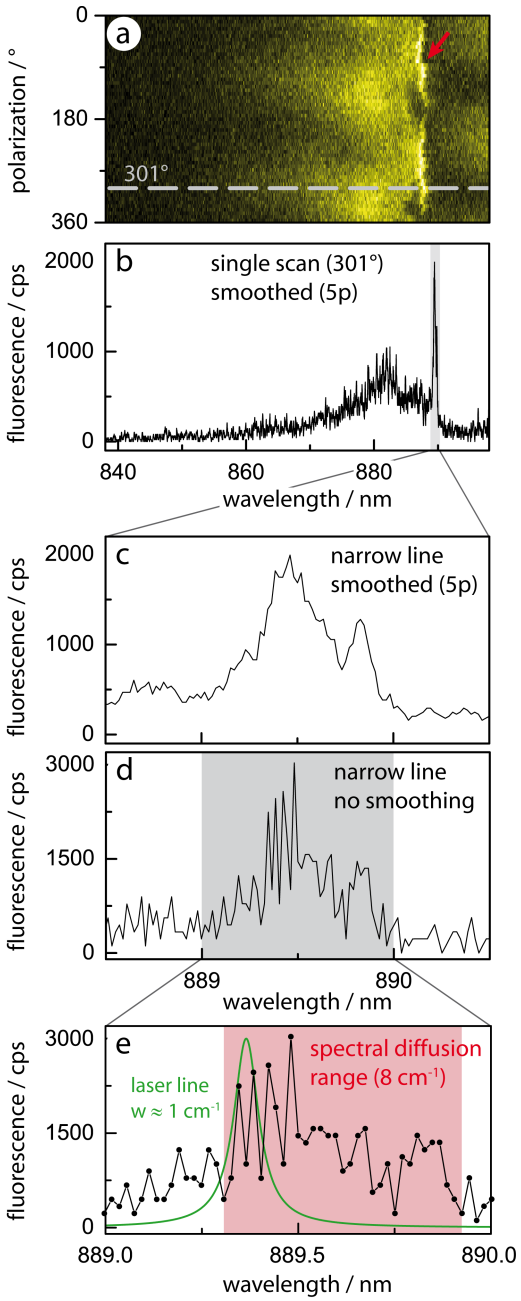

Figure 4.5: *Spectral diffusion of the narrow absorption line. (a) Stack of 58 consecutively recorded spectra. The spectra correspond to a selected region of the complex shown in Figure 4.3. The red arrow indicates a large spectral jump of the narrow line between successive scans. (b) Single scan which corresponds to the dashed line in panel (a). The spectrum has been smoothed by averaging over five adjacent data points. (c) Narrow line of the spectrum in (b) shown on an extended wavelength scale. (d) Spectrum (c) without averaging of adjacent data points. (e) Expanded view of the gray shaded region of panel (d). The black dots indicate the data points and the black line is shown to guide the eyes. The spectral region marked in red is an educated guess for the spectral diffusion range of the narrow line within one scan. For illustration the green line indicates the spectral bandwidth of the laser of* $\approx 1\ cm^{-1}$.

line is a simulated Lorentzian line ($fwhm = 1\ cm^{-1}$). It is shown for illustration, indicating the spectral bandwidth of the excitation laser of $\approx 1\ cm^{-1}$. In the course of the experimental protocol the frequency of the laser line is shifted from one data point to the next.
When the linewidth of a narrow line is determined within a single scan, one should not be misled by the effect of spectral smoothing: While the narrow line appears as a broad peak with a narrow side peak to longer wavelength in Figure 4.5c, the corresponding spectrum in Figure 4.5d, where no smoothing was applied, looks rather jagged, displaying multiple peaks in the spectral region of the main peak in Figure 4.5c. The following explanation for the resulting spectrum is proposed (Figure 4.5e): During the time in which the laser is scanned over the spectral region of interest, the transition frequency of the narrow line undergoes fast changes within the spectral range shaded in red. Thus, if by chance the transition frequency of the narrow line overlaps with the spectral bandwidth of the excitation laser, a high fluorescence signal can be observed (peaks in the left part of the indicated spectral diffusion range). Here however it can also be seen that between two measurement points (separated by about $0.26\ cm^{-1}$ and a time period of $10\ ms$) the transition frequency of the narrow line can jump out of the spectral overlap with the relatively broad laser line, leading to the pronounced dips between the four maxima in the left part of the spectral diffusion range. Thus, it can be learned that fast spectral diffusion occurring on the ms-timescale prevents the determination of the homogeneous linewidth of the narrow line, which however should be considerably smaller than the spectral diffusion range defined in Figure 4.5e.
The values given above for the linewidths of the narrow lines were determined in spectra corresponding to the average over 3 adjacent scans in which the transition frequency of the narrow line was spectrally stable, and additionally the resulting spectra have been smoothed by averaging over 5 adjacent data points. Therefore, the linewidths determined in this way, can be regarded as a measure for the range of the fast spectral diffusion of the narrow lines for the individual complexes.
Naturally, the fast diffusion of the transition frequency of the narrow line also affects its fluorescence intensity. A maximum of the detected fluorescence is only to be expected for a perfect agreement of the narrow line transition frequency with the frequency of the excitation laser, and every deviation between these two frequencies will result in a decrease of the observed fluorescence intensity of the narrow line. Furthermore, as the spectra have been smoothed by averaging over five adjacent data points to improve the signal-to-noise ratio, the resultant narrow line fluorescence intensity in these spectra is significantly lowered in comparison to the non-smoothed spectra (see y-axis scale in Figure 4.5c and d). Finally, the excitation of the narrow line, for which, according to the LH1 fluorescence lifetime [56, 89], a linewidth of about $0.02\ cm^{-1}$ can be estimated, with a broadband laser (spectral bandwidth $\approx 1\ cm^{-1}$), might lead to a further decrease of its fluorescence intensity [91]. A systematic investigation of this phenomenon however failed, due to the

fast spectral diffusion of the narrow line [92]. Nevertheless, taken together, all of the three above-mentioned processes (spectral diffusion, smoothing and broadband-excitation) should then at least in part be responsible for the observed deviation of the fluorescence intensity of the narrow line, B1, which is considerably smaller than the absorbance calculated for the lowest exciton state $k = 1$ in the numerical simulations (see chapter 5).
Returning to the single-complex spectra, according to their spectral characteristics, the RC-LH1 complexes could be grouped into three categories, referred to as A - C, hereafter. A typical example for each category is shown in Figure 4.6. For each category the top panel displays a stack of 58 consecutively recorded fluorescence-excitation spectra as a function of the polarization of the excitation. Below these patterns the sum spectrum (black line) is shown together with example spectra (colored lines), each corresponding to the average of three consecutive scans, that feature the characteristic spectral details of each category.

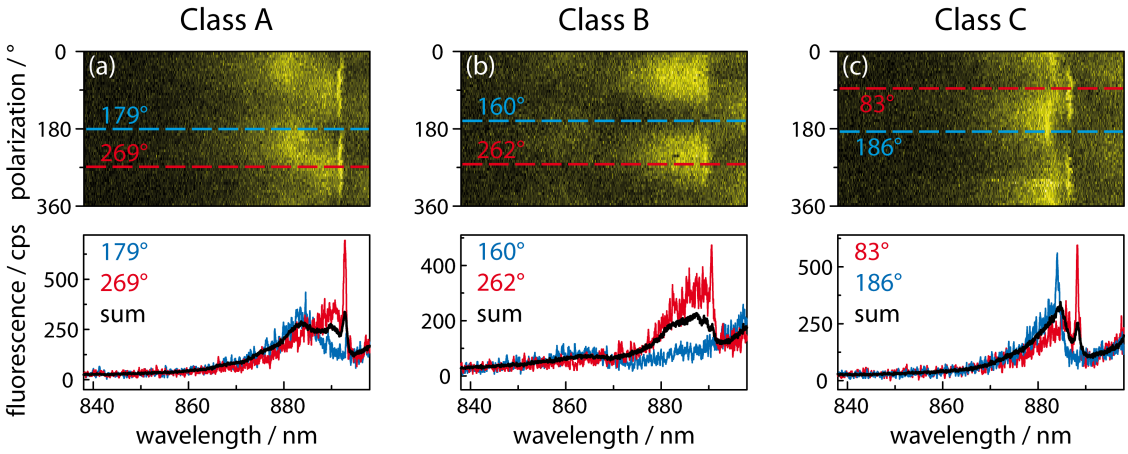

Figure 4.6: *Classes of fluorescence-excitation spectra obtained from different RC-LH1 complexes from Rps. acidophila. The upper panels (a), (b) and (c) show stacks of consecutively recorded fluorescence-excitation spectra that have been restricted to 58 spectra each for brevity. Between two individual fluorescence-excitation spectra the polarization of the incident radiation has been rotated by* $6.2°$*, and the fluorescence intensity is indicated by the color code. The spectra displayed at the bottom of each panel correspond either to the sum of the full stack of spectra (black lines), or to the average over three adjacent individual spectra (blue/red) that have been recorded for a distinct polarization of the excitation (indicated by the dashed colored lines in the top panels). Additionally, all spectra have been smoothed by averaging over five adjacent data points. In each case the vertical axis of the lower panels is valid for all three traces. The spectra were recorded at* $1.2\ K$ *and the excitation intensity was typically about* $250\ W/cm^2$*.*

The complexes attributed to category A (50 of 61 complexes) featured two broad bands with distinctly different orientation of their transition-dipole moments (Fig-

ure 4.6a). For 38 of these complexes a narrow spectral feature was observed at the low-energy side of the fluorescence-excitation spectra. For the other 12 complexes the spectrum overlaps with the detection window, possibly masking a narrow line at the red end of the spectrum. The complexes assigned to class B (4/61) feature a single, linear polarization of the whole spectrum (Figure 4.6b). For all four complexes the registered fluorescence-excitation spectra exhibit a broad band with a narrow line at the low-energy wing. Finally, in category C (7/61) the complexes featured either two narrow lines, each one on the red wing of a broad absorption band, or a broad band on the red side of a narrow line extending into the detection window which presumably masks a second narrow line (Figure 4.6c).
Given that the majority of the RC-LH1 complexes featured category A spectra, in the following the focus will be on this type of spectra. In Figure 4.7 the distributions of the separations of the spectral bands and the mutual orientations of the associated transition-dipole moments, determined as described before for Figure 4.3, are summarized. The histograms differ from each other in the number of entries, which reflects the fact that for some complexes the spectra were red-shifted to an extent that they overlapped with the detection window, thus preventing the observation of all spectral bands. In particular, for 23 complexes only was the narrow feature at the red end of the spectrum observable and spectrally sufficiently stable to allow a reliable fit of the relative phase angle. Only these complexes were considered for the histogram shown in Figure 4.7c. Similarly, for 11 of the category A complexes the energetic separation between B2 and B3 was so small that a reliable determination of the relative phase angle of the associated transition-dipole moments was impossible, which reduced the number of entries in the histogram shown in Figure 4.7d from 50 to 39. For the energy difference between the bands B1 and B2 (B2 and B3) a variation between 2 cm^{-1} and 68 cm^{-1} (3 cm^{-1} and 236 cm^{-1}) is found, with a mean value of 33 cm^{-1} (85 cm^{-1}), Figure 4.7a,b. To restrict the scale for the relative orientations of the transition-dipole moments to values between 0° and 90°, the phase differences were calculated as $\Delta\alpha_{B_iB_j} = \left|\alpha_{B_i} - \alpha_{B_j}\right|$ if the result was less than 90° or as $\Delta\alpha_{B_iB_j} = 180° - \left|\alpha_{B_i} - \alpha_{B_j}\right|$ otherwise. Accordingly, the distribution of the relative orientations of the transition-dipole moments that are associated with B1 and B2 displays a maximum at about 0° and a steep decrease for larger angles (Figure 4.7c). For the bands B2 and B3 the respective distribution for the mutual orientation of the transition-dipole moments increases from 15° to a maximum at about 90° (Figure 4.7d).
The insets in Figure 4.7a,c show the distributions for the energy splitting, ΔE_{B1B2}, and the mutual angle between the corresponding transition-dipole moments, $\Delta\alpha_{B1B2}$, for the bands B1 and B2 of RC-LH1 from *Rps. palustris* and were taken from [15]. Given the similarity of these distributions with the data from *Rps. acidophila*, it can be concluded that the *palustris* model described in [15] also grasps the essential features of the RC-LH1 structure from *Rps. acidophila* (see however chapter 5). In [15] the experimental data were compared with results from numer-

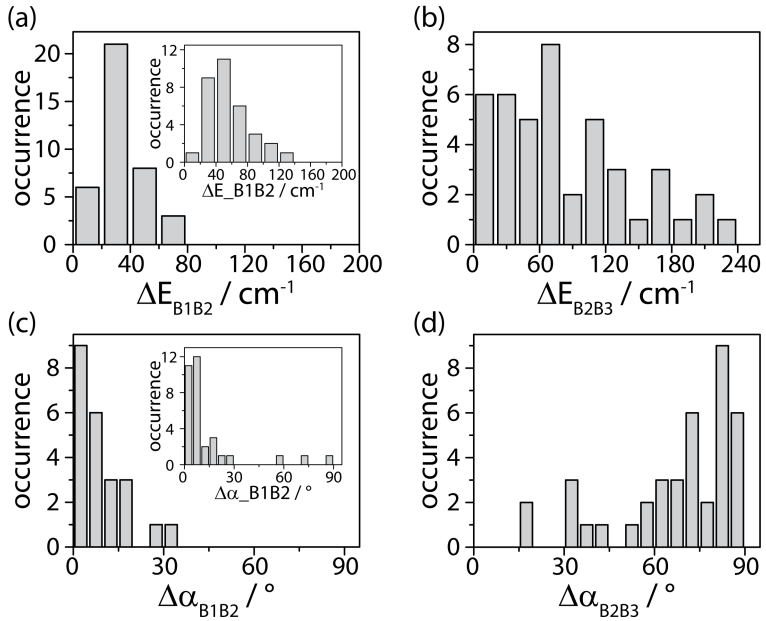

Figure 4.7: *Distributions of the energetic separations ΔE observed between (a) B1 and B2, and (b) B2 and B3, and of the mutual angles $\Delta\alpha$ between the transition-dipole moments that are associated with (c) B1 and B2, and (d) B2 and B3. The insets in (a) and (c) display the corresponding data for RC-LH1 from Rps. palustris and have been taken from [15].*

ical simulations based on a simple model Hamiltonian using the Heitler-London approximation and it was found that the RC-LH1 complexes from *Rps. palustris* can be adequately modeled by 15 BChl *a* dimers that are distributed equidistantly around an ellipse that features a gap adjacent to the RC Q_B binding site. In analogy with the *palustris* study the observed spectral bands B1, B2, B3 are assigned to the exciton states $k = 1, 2, 3$, respectively, where B3 may have additional contributions from exciton states $k > 3$ depending on the specific realization of the diagonal disorder. In chapter 5 a LH1 model structure with more realistic simulation parameters than those used in [15] is presented. However, therein and also regarding the outlook in chapter 6, it becomes clear that a more profound statement about further structural details of the LH1 aggregates of the bacterial species *Rps. palustris* and *Rps. acidophila* or differences between them requires on the one hand a better resolved crystal structure as a starting point (here, the new structure from *T. tepidum* [9] may provide some new insights). On the other hand, a more sophisticated theoretical approach than Heitler-London and a dipole-dipole interaction between the pigments is needed, for obtaining better information about the site energies of the individual BChl *a* molecules and the intermolecular interaction strengths, respectively [93]. In particular those BChl *a* molecules adjacent to the gap are expected to have distinctly different site energies with respect to the other

BChl *a* molecules in the assembly, due to their differing protein environment. Unfortunately the distributions for the energy separations ΔE_{B2B3} and the mutual angles $\Delta\alpha_{B2B3}$ of the associated transition-dipole moments for the bands B2 and B3 are not available for the *Rps. palustris* study, and so the corresponding distributions from this work have been compared with the results from the study of Ketelaars et al. [10] on RC-LH1 from *Rps. acidophila*, where the focus was predominantly on these two broad bands. In that study four types of spectra (I-IV) were distinguished that correspond to the classes A-C that are used here, as given in Table 4.1.

detergent DDM (present work)		detergent LDAO [10]	
class	relative fraction (number of complexes)	type	relative fraction (number of complexes)
A	82% (50)	I + II	46% (7 + 4)
B	6.5% (4)	III	16.5% (4)
C	11.5% (7)	IV	37.5% (9)

Table 4.1: *Influence of the type of detergent on the occurrence of RC-LH1 complexes from Rps. acidophila with distinct spectral features.*

The analysis of the spectra presented in Ketelaars et al. [10], was based on work performed on LH2 complexes from the same species [13, 14]. In LH2 the B850 BChl *a* molecules form a closed ring, that, in first approximation (omitting dimerization), gives rise to a (circular) exciton structure with pairwise degenerate exciton states $k^{circ} = \pm 1, \pm 2, \ldots$ and two non-degenerate states $k^{circ} = 0, 9$. Appreciable oscillator strength is found only for the states $k^{circ} = \pm 1$ which feature mutually orthogonal transition-dipole moments. Ketelaars et al. interpreted the two broad spectral features (here denoted as B2 and B3) as the $k^{circ} = \pm 1$ exciton states of a closed ring structure in analogy with the LH2 case. The more frequent observation of a narrow spectral feature for RC-LH1 with respect to LH2 (interpreted to stem from $k^{circ} = 0$) was ascribed to the fact that in RC-LH1 the structural heterogeneity leads to a more pronounced mixing of the exciton levels and subsequent redistribution of oscillator strength, due to the higher density of exciton states in LH1 with respect to LH2. As a consequence of this, they classified spectra that featured both a narrow spectral line at the red end of the spectrum, as well as a mutual angle between the transition-dipole moments of the two following, red shifted, broad bands around 90° (here denoted as $\Delta\alpha_{B2B3}$) as type I, and spectra where these bands featured a phase difference between 30° and 65° as type II. However, single-molecule work on RC-LH1 from *Rps. palustris* and on mutants from *Rb. sphaeroides*, *i.e.* an open ring and a closed ring structure, has revealed that the frequent occurrence of the narrow spectral feature at the red end of the spectrum is a strong indication for a pigment arrangement with a gap [12]. For the

current study, therefore the distinction between type I and type II spectra has been omitted and all spectra that featured two broad bands with distinctly differently oriented transition-dipole moments were classified as category A. Merging the data for type I and type II spectra in [10] yields for the energy separation (mean ± sdev) $\Delta E_{B2B3} = (122 \pm 64)\ cm^{-1}$ and for the mutual angle of the transition dipole moments $\Delta\alpha_{B2B3} = (71 \pm 22)^\circ$ which can be compared with $(85 \pm 60)\ cm^{-1}$ and $(67 \pm 20)^\circ$ found here. Within their error margins the energetic separations roughly agree with each other, and the limited statistics of the previous study, where only 11 complexes contributed to the type I and type II spectra, should be kept in mind. The mutual orientations of the transition-dipole moments between the bands B2 and B3 are consistent with the previous work and, as stated already in [10], the observed strong deviation from a mean around 90° (in contrast to what has been observed for $k^{circ} = \pm 1$ for LH2 complexes from *Rps. acidophila* [77, 94]) might reflect an orientational distribution of the RC-LH1 complexes with respect to the plane of the polymer film. For the LH2 complexes it is believed that the electrostatic interaction between the complexes and the substrate in combination with the laminar flow induced by the spin-coating process entails a planar alignment of the LH2 complexes on the substrate [10]. In RC-LH1 however the RC protrudes by about 20 $\mathring{A}$ from the N-terminal side of the LH1 ring [95] which might tilt the plane of the LH1 ring with respect to the substrate. As a result only the projections of the exciton transition-dipole moments on the plane perpendicular to the optical axis can be observed.

Finally, the complexes that featured spectra classified as category B and C will be briefly addressed. Class B spectra would be consistent with RC-LH1 complexes that are tilted so far that they are oriented with the plane of the BChl *a* ring perpendicular to the substrate. The smaller relative fraction of complexes attributed to this class in this study in comparison to the work of Ketelaars et al. [10], might be related to the much larger sizes reported for DDM-micelles as compared to LDAO-micelles, $72,000$ *vs.* $21,500$ *Da* [96]. The greater micelle size will increase the planar area of the RC-LH1-detergent construct and thereby promote a parallel alignment with respect to the substrate plane. Class C spectra could originate from two molecular aggregates in close proximity to each other. A probable explanation for this is that these spectra stem from broken RC-LH1 complexes that were in the process of dissociation prior to cooling them down to cryogenic temperatures. For RC-LH1 complexes sustained in LDAO, traces for such dissociation processes were already observed in the room-temperature absorption spectrum of the stock solution, see Figure 4.2. Here, the specific aggregation of the detergent molecules in the detergent micelles might play an important role for the dissociation of the RC-LH1 complexes. While for DDM-micelles it was found that the hydrophobic core of the micelle is sturdily protected from interaction with water (only about 10% of the micelle surface consists of water exposed hydrocarbon tails) [52], for LDAO-micelles, presumably due to the smaller headgroups of the detergent molecules, a hydration

level of the hydrophobic core of almost 50% was found [51]. Thus, it is conceivable that for LDAO stabilized RC-LH1 complexes water molecules might intrude into the hydrophobic regions of the RC-LH1 complexes, thereby destabilizing them.
If the interpretation of the spectral properties for the different classes is correct, the fraction of broken/dissociated RC-LH1 complexes (here class C, type IV in [10]) from *Rps. acidophila* can be significantly reduced by using DDM instead of LDAO as detergent, namely from 37.5% to 11.5%. Due to the higher quality of the stock solution, it was possible to perform polarization-resolved fluorescence-excitation spectroscopy, and to determine the distributions of the spectral properties with an improved statistics. It is found that the spectra of RC-LH1 from *Rps. acidophila* resemble in shape and statistical properties those obtained on RC-LH1 from *Rps. palustris* in an earlier study [12, 15] and one comes to the conclusion that both structures can be described by the same structural LH1 model, namely an elliptical arrangement of BChl *a* molecules comprising a gap (see also chapters 5 and 6). This is in particular interesting in view of the new RC-LH1 crystal structure from *T. tepidum*, revealing a LH1 complex with a completely closed, elliptical structure [9]. Regarding the electron density map (Figure 4.1) and the results from the previous single-molecule study [10], such a type of LH1 complex was also expected for the species *Rps. acidophila*. However, the results of the present section show that a completely closed ring structure almost certainly can be excluded for the LH1 complex from *Rps. acidophila*, but the LH1 complexes from this bacterial species should rather be attributed to the *palustris*-type LH1 complexes, defined by monomeric aggregates with a gap in their overall structure.

4.2 Influence of the environment on the spectra of the RC-LH1 complexes

4.2.1 Motivation

Single-molecule spectroscopy has proven to be a powerful tool with which to investigate the details of the spectroscopic properties in relation to the structure of photosynthetic pigment-protein complexes [7, 11–15, 18, 44, 94, 97–117]. However, many of the single-molecule experiments, as well as many ensemble studies, have been performed on detergent-solubilized complexes and involved immobilization of the complexes in a matrix, preferentially in a thin film that was placed onto a surface, usually either directly or by spin-coating [11–13, 100, 103, 105, 110]. It has been questioned whether this then deforms the structure of these antenna complexes and, therefore, introduces, *per se*, significant changes in their spectroscopic behavior that would not be reflected in their native membrane environment, since it is generally assumed that the LH complexes are more stable and fully native when housed in their host biological membrane [17–19]. Supporting evidence for

this conjecture was also obtained by single-molecule spectroscopic investigations on the LH1 complex from the purple bacterium *Rsp. rubrum*, which revealed significant spectroscopic differences on the single-molecule level between membrane-reconstituted and detergent-solubilized complexes. The results of this study were interpreted in terms of a narrowed statistical distribution of conformational states for the membrane-reconstituted LH1 complexes [16]. A similar conclusion has been drawn for photosystem I (PS I) from *Thermosynechoccocus elongatus* that was studied in buffer solution, glycerol-buffer mixtures, and polyvinyl alcohol (PVA) [118]. It was found that the degree of observed inhomogeneity for the complexes increased in the matrices in the order glycerol-buffer, buffer solution, and PVA. Moreover, in PVA the low-temperature optical spectra of the complexes showed a remarkable blue-shift with respect to the other two matrices, and it was argued that conclusions drawn from PS I in PVA are of questionable value.
In the group of Prof. J. Köhler, in which also this work was performed, the light-harvesting complexes from purple bacteria have been studied by single-molecule techniques in great detail [12, 15, 94, 103, 108, 115]. However, for (most of) the experiments the detergent-solubilized LH complexes were immobilized in a PVA matrix, and thin films were prepared by spin-coating a small amount of this solution onto a quartz substrate. Concerning LH2 the issue whether the sample preparation conditions have a significant influence on the optical spectra was addressed some years ago [77]. In that study the spectroscopic properties of individual LH2 complexes embedded in the usual spin-coated PVA film were compared with those from individual LH2 complexes reconstituted into a 1,2-dioleoyl-*sn*-glycero-3-phosphocholine (DOPC) lipid bilayer, which was considered as the closest approximation to the natural membrane. A detailed analysis of the spectra showed that the distributions of the key spectral features, *i.e.* the splitting of the $k = \pm 1$ exciton states, and the mutual orientation of the corresponding transition-dipole moments, showed no significant differences for the two environments. Moreover, the single complexes immobilized in PVA did not display a more pronounced structural disorder than when in a phospholipid membrane. Generally, the RC-LH1 complexes are considered to be more fragile compared to LH2 [20]. Indeed, as was shown in the previous section 4.1, the type of detergent used for stabilizing RC-LH1 in the buffer solution, *i.e.* lauryldimethylamine N-oxide (LDAO) *vs.* dodecyl-β-D-maltoside (DDM), has already a significant influence on the stability of the proteins. The experiments of the present section were performed, in order to test whether the immobilization of RC-LH1 complexes in a PVA matrix might lead to a deterioration of the proteins and thereby limit the accessible information from optical spectroscopy. Overall, the present section is organized into two parts. In the first part, details of the optical spectra from ensembles of RC-LH1 complexes are compared as a function of the matrix and as a function of temperature. For the room-temperature experiments, the complexes were either stabilized in DDM micelles in buffer solution, in lipid vesicles, or in thin films of DDM buffer and DDM/PVA. For

the experiments at low temperatures, the experimental results obtained from thin-film samples of RC-LH1 complexes stabilized in DDM micelles in buffer solution, RC-LH1 complexes immobilized in DDM/PVA, and RC-LH1 complexes reconstituted into a DOPC lipid bilayer are compared to each other. The second part of this section is devoted to the comparison of the results obtained from single-molecule spectroscopy at low temperatures. Therefore, spectra were recorded from individual complexes in thin films of DDM buffer solution and from those reconstituted into the lipid bilayer, and the results are compared with the data from the previous section 4.1 that were acquired for RC-LH1 complexes immobilized in a DDM/PVA thin-film matrix. The general finding is that the distributions of the spectral features, *i.e.* the separation of the absorption bands and their relative polarization properties are identical for the RC-LH1 complexes in DDM/PVA and the lipid bilayer (within the statistical accuracy). Moreover, it is argued that the blue-shift observed for the ensemble spectra in the DDM/PVA matrix with respect to the other two matrices upon cooling, reflects a thermal expansion of the PVA film.

4.2.2 Results

Ensemble spectroscopy

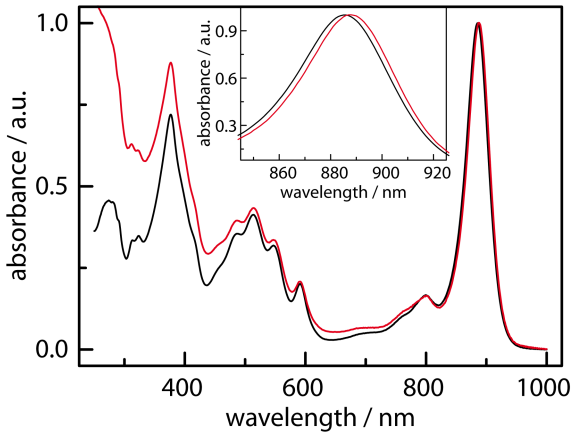

Figure 4.8: *Room-temperature absorption spectra of RC-LH1 complexes from Rps. acidophila stabilized in DDM micelles in buffer solution (black line) or reconstituted into a DOPC bilayer (red line). The increase of the absorbance below* $500\ nm$ *for the reconstituted sample is due to Rayleigh scattering of the vesicles. The inset shows an expanded view of the BChl a* Q_y *absorption bands, peaking at* $885.5\ nm$ *for the detergent stabilized complexes and at* $887.5\ nm$ *for the reconstituted complexes. For better comparison the spectra were peak normalized to the maxima of their* Q_y *absorptions.*

Figure 4.8 shows a comparison of the room-temperature absorption spectra of ensembles of RC-LH1 complexes from *Rps. acidophila* in detergent buffer solution (DDM, black line) and reconstituted into a lipid bilayer (DOPC, red line). The main absorption at about 885 nm (B885 band) is due to the Q_y transition of the BChl a molecules, whereas the band at around 600 nm reflects the absorption from the Q_x transition of the BChl a molecules. These bands are clearly separated from the absorption bands caused by the reaction center (around 800 nm), the carotenoids (around 500 nm), the Soret band of the BChl a molecules (around 400 nm), and the protein matrix in the near UV spectral region. Upon reconstitution of the pigment-protein complexes into a lipid bilayer the B885 absorption band is slightly red-shifted by 2 nm with respect to the same band obtained from complexes that were stabilized in detergent buffer solution, see inset Figure 4.8. This spectral shift indicates that the reconstitution process was successful [17, 77, 119].

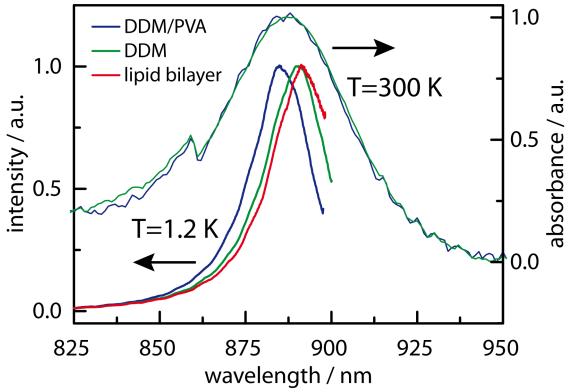

Figure 4.9: *Top, room-temperature absorption spectra of ensembles of RC-LH1 complexes from Rps. acidophila ($OD_{885} = 25\ cm^{-1}$) embedded in a thin layer of DDM/PVA (blue) or DDM buffer solution (green). Bottom, low-temperature fluorescence-excitation spectra of RC-LH1 ($OD_{885} = 1\ cm^{-1}$) in DDM/PVA (blue), DDM buffer solution (green), or reconstituted into a DOPC lipid bilayer (red). For clarity, all spectra are peak normalized and correspond to averages over all polarizations of the incident radiation as well as over 40 adjacent data points. The excitation intensity was* $5\ W/cm^2$.

In Figure 4.9 the thin-film absorption/fluorescence-excitation spectra of RC-LH1 ensembles are compared for three different matrices at two different temperatures. The top two traces feature the room-temperature B885 absorption band of RC-LH1 sustained either in a PVA layer or in a film of detergent buffer solution. The two spectra closely overlap and feature about the same spectral peak position and linewidth. At low temperatures (1.2 K) fluorescence-excitation spectra were recorded from thin films that contained RC-LH1 complexes (i) in DDM micelles in PVA, (ii) in DDM micelles in buffer solution, and (iii) in a DOPC lipid bilayer. At the bottom of Figure 4.9 the corresponding fluorescence-excitation spectra are shown for RC-LH1 complexes embedded in the three different environments. All

details of the spectral features shown in Figures 4.8 and 4.9 are summarized in Table 4.2.

	T (K)	peak of the absorption*/ fluorescence-excitation band (nm)	spectral width ($fwhm$) (cm^{-1})
Bulk RC-LH1 Sample (Figure 4.8)			
DDM	300	885.5*	571
lipid bilayer	300	887.5*	562
Thin-film RC-LH1 Sample (Figure 4.9)			
DDM/PVA	300	886.5*	555
DDM	300	887.0*	565
DDM/PVA	1.2	885.5	272
DDM	1.2	889.9	287
lipid bilayer	1.2	891.8	293

Table 4.2: *Spectral properties of the main Q_y absorption band of bulk/thin-film ensembles of RC-LH1 complexes from Rps. acidophila as a function of temperature and environment.*

For the samples embedded in DDM or DDM/PVA, the width ($fwhm$) of the B885 absorption band decreases from about 560 cm^{-1} at room-temperature to about 280 cm^{-1}, upon cooling the samples to low temperatures. Interestingly, the peak position of the absorption band shifts differently for the two matrices: A red-shift from 887.0 to 889.9 nm is observed for DDM and a smaller blue-shift from 886.5 to 885.5 nm for DDM/PVA, which is within the resolution of the instrument. For the RC-LH1 complexes reconstituted into a lipid bilayer a similar temperature dependent reduction of the linewidth is observed as for RC-LH1 in the two other environments, here from 562 to 293 cm^{-1}, and a red-shift of the peak position from 887.5 nm at room-temperature to 891.8 nm at cryogenic temperatures. Hence, the slight difference of 2 nm between the spectral peak positions for RC-LH1 in DDM and reconstituted into a lipid bilayer is conserved when the temperature is lowered.

Figure 4.10 shows the low-temperature fluorescence-emission spectra of the thin-film ensembles stabilized in the three different environments, together with the fluorescence-excitation spectra from Figure 4.9. The color code is the same as in Figure 4.9. The characteristic parameters of the spectra in Figure 4.10, *i.e.* peak positions, linewidths and Stokes-shifts, are summarized in Table 4.3.
It can be seen that the widths of all spectra are comparable and amount to about 280 cm^{-1} ($fwhm$). Interestingly, a distinctly larger Stokes-shift is observed for RC-LH1 complexes sustained in the lipid bilayer in comparison to the two other matrices, which is probably due to excitation energy transfer within a network of RC-LH1 complexes (*vide infra*).

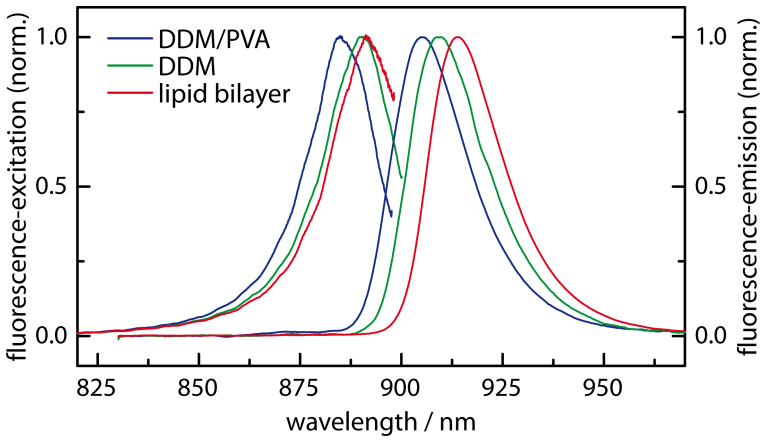

Figure 4.10: *Low-temperature (1.2 K) fluorescence-excitation and -emission spectra of ensembles of RC-LH1 complexes from Rps. acidophila stabilized in thin films in three different environments (blue: detergent (DDM) micelles in a PVA matrix; green: detergent (DDM) micelles in buffer solution; red: lipid (DOPC) bilayer membrane). The fluorescence-excitation spectra are those from Figure 4.9. For clarity, a gliding average over 20 (40) data points has been applied for the display of the emission (excitation) spectra and all spectra have been peak normalized. The excitation intensity for the emission-spectra amounted to 14 kW/cm^2.*

	fl.-excitation peak/nm ($fwhm/cm^{-1}$)	fl.-emission peak/nm ($fwhm/cm^{-1}$)	Stokes-shift/cm^{-1}
DDM/PVA	885.5 (272)	905.0 (279)	244
DDM	889.9 (287)	909.1 (282)	237
lipid bilayer	891.8 (293)	913.9 (270)	271

Table 4.3: *Parameters of the low-temperature (1.2 K) fluorescence-excitation and fluorescence-emission spectra from ensembles of RC-LH1 complexes from Rps. acidophila embedded in three different thin-film environments.*

Single-complex spectroscopy

An example of a fluorescence-excitation measurement for a single RC-LH1 complex stabilized in detergent buffer solution is shown in Figure 4.11. Figure 4.11b displays a stack of 87 consecutively recorded spectra, where the polarization of the incident radiation has been rotated by 6.2° after each individual scan. From this pattern it is obvious that the optical signal strongly fluctuates, with extended periods that prohibit the recording of any signal from the complex. But also during the bright periods the signal strength shows strong variations. For some individual scans the signal level remains sufficiently stable to allow the recording of a fluorescence-excitation spectrum that features the typical characteristics of a RC-LH1 complex with an interrupted LH1 aggregate: A broad band is followed by a narrow line on

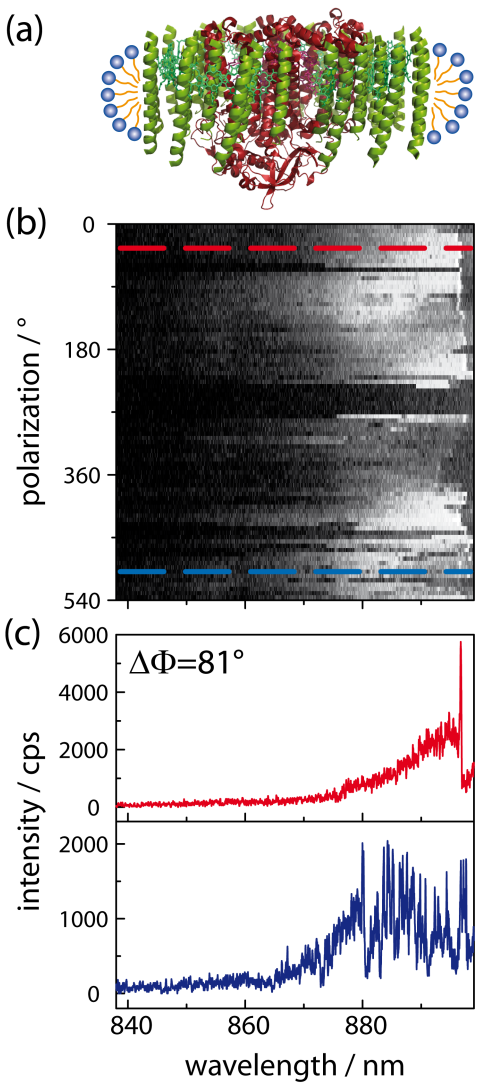

Figure 4.11: *(a) Sketch of a RC-LH1 complex stabilized inside a detergent micelle (red: RC; green: LH1; yellow/blue: hydrophobic tail/hydrophilic head group of DDM). (b) Two-dimensional representation of 87 consecutively recorded fluorescence-excitation spectra from a RC-LH1 complex from Rps. acidophila stabilized in detergent buffer solution. The horizontal axis corresponds to wavelength, the vertical axis to the polarization of the incident radiation and the fluorescence intensity is given by the gray scale, where white denotes high intensity. Between two successive scans the polarization of the excitation light has been rotated by* $6.2°$*. (c) Examples of two individual fluorescence-excitation spectra that were recorded for a mutual phase difference of* $\Delta\Phi = 81°$ *for the polarization of the excitation light. The dashed horizontal lines in (b) indicate the positions of these spectra within the stack. Both spectra have been smoothed by averaging over five adjacent data points. The temperature of the sample was* $1.2\ K$*, and the excitation power was* $678\ W/cm^2$*.*

its red side ([12] and previous section 4.1), see Figure 4.11c red spectrum. However, for about half of the individual spectra the signal level is affected significantly by blinking and/or spectral diffusion, which prevents the recording of a meaningful spectrum, see Figure 4.11c blue line. Such a behavior was found for the majority of the RC-LH1 complexes in detergent buffer solution. For this preparation method it was therefore impossible to obtain detailed information from the fluorescence-excitation spectra, such as the number of bands, their energetic separation, or the mutual orientation of the corresponding transition-dipole moments.
The situation is different for RC-LH1 complexes that were reconstituted into a lipid bilayer. For this preparation method the vast majority of the 83 studied complexes featured a stable signal level. Typically the fluorescence-excitation spectra of these complexes featured a few broad bands with widths ($fwhm$) varying between 100 and 240 cm^{-1}, and at least one narrow absorption line with widths ($fwhm$) mostly between 1 and 2 cm^{-1}. As was demonstrated in the preceding section 4.1, the widths of the narrow lines do not reflect their homogeneous linewidths but are determined by unresolved spectral diffusion. In a few exceptional cases with very strong spectral diffusion the widths of these lines increased up to about 7 cm^{-1}.
The recorded fluorescence-excitation spectra could be grouped into the same three classes as observed in the previous section 4.1, for the RC-LH1 complexes from *Rps. acidophila* in DDM micelles in PVA.
Briefly, the spectra assigned to class A (49 of 83 complexes) featured two dominant broad bands with distinctly different polarizations and a narrow spectral feature at the low-energy wing, those assigned to class B (4/83) featured (predominantly) a single linear polarization of the whole spectrum, and finally the complexes grouped in class C (30/83) featured multiple narrow lines in the spectrum. A typical example for a fluorescence-excitation measurement from each class is shown in Figure 4.12. The patterns in Figure 4.12b-d display each a stack of 87 consecutively recorded spectra in a two-dimensional representation similar to that of Figure 4.11. Between two successive scans the polarization of the excitation light was rotated by 6.2°. The spectra underneath the patterns correspond to averages of three consecutive scans, and display the spectral features that are characteristic for the class assignment.
The distribution of the complexes across the classes A-C is given in Table 4.4 together with the distribution obtained in the preceding section 4.1, where the RC-LH1 complexes from *Rps. acidophila* were immobilized in DDM micelles in a PVA matrix. In section 4.1, only the class A spectra were attributed to stem from intact RC-LH1 complexes. The class B spectra were considered as RC-LH1 complexes that were tilted so far that they were oriented with the plane of the BChl *a* ring perpendicular to the substrate, and class C spectra were ascribed to fragments from broken RC-LH1 complexes that were in the process of dissociation/denaturation prior to cooling them to low temperatures. Following the reasoning of the previous section the reconstitution process described in this work leads to a reduction of the fraction of intact complexes from 82% (DDM/PVA) to 59% (lipid bilayer), whereas

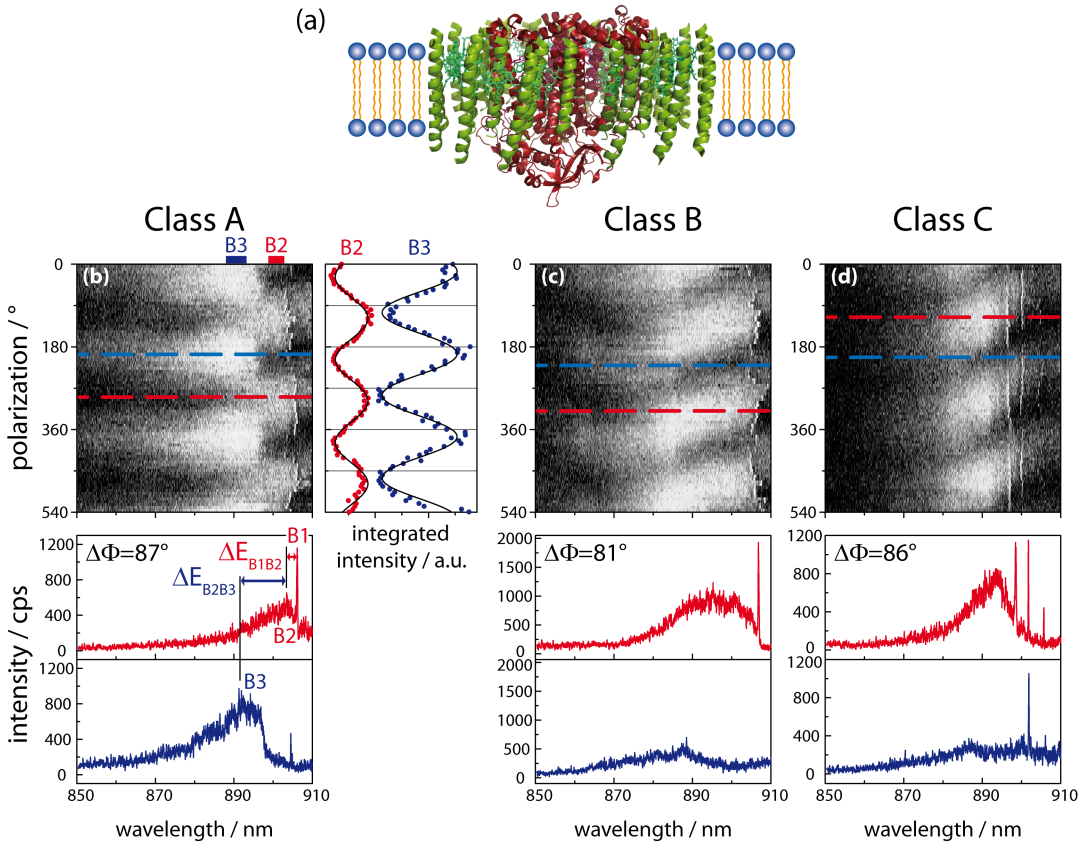

Figure 4.12: *Classes of fluorescence-excitation spectra obtained from different RC-LH1 complexes from Rps. acidophila reconstituted into a lipid bilayer. (a) Sketch of a RC-LH1 complex reconstituted into a DOPC lipid bilayer. The color code is the same as in Figure 4.11. The upper panels in (b-d) show stacks of 87 consecutively recorded fluorescence-excitation spectra. Between two individual fluorescence-excitation spectra the polarization of the incident radiation has been rotated by* $6.2°$*, and the fluorescence intensity is indicated by the gray scale. The spectra displayed at the bottom of each panel correspond to the average over 3 adjacent, individual spectra (red/blue) that have been recorded for a distinct polarization of the excitation (indicated by the dashed colored lines in the top panels). For clarity, all spectra have been smoothed by averaging over five adjacent data points. The relative phase difference between the red/blue example spectra is given by* $\Delta\Phi$*, respectively. The sample-temperature was* $1.2\ K$ *and the excitation intensity amounted to about* $140\ W/cm^2$*. For the class A example the energetic separations between the bands B1 and B2,* ΔE_{B1B2}*, and between the bands B2 and B3,* ΔE_{B2B3}*, are indicated in the figure. The graph on the right-hand side of panel (b) shows the variation of the fluorescence intensity, that is integrated over the spectral intervals denoted as B2 and B3 at the top of pattern (b), as a function of the polarization of the incident radiation. The dots correspond to the experimental data and the black lines correspond to* $\cos^2$*-type functions fitted to the data.*

the fraction of broken complexes increases from 11.5 to 36%. This indicates that the reconstitution procedure is probably a rather harsh treatment for the RC-LH1 complexes.

	lipid bilayer (present section)	DDM/PVA (previous section 4.1)
class	relative fraction (number of complexes)	relative fraction (number of complexes)
A	59% (49)	82% (50)
B	5% (4)	6.5% (4)
C	36% (30)	11.5% (7)

Table 4.4: *Relative fractions (total numbers) of RC-LH1 complexes from Rps. acidophila assigned to the three classes A, B, and C in the lipid bilayer and in the DDM/PVA environment.*

Accordingly, in the following the focus of the analysis will be on the class A type spectra from which the spectral separations of the observed bands were extracted and the mutual orientations of the associated transition-dipole moments. For the example shown in Figure 4.12b, the energetic separation between the bands B1 and B2, ΔE_{B1B2}, amounts to 35 cm^{-1} and between the bands B2 and B3, ΔE_{B2B3}, to 75 cm^{-1}. Integration of the intensity of the bands B2 and B3 over the spectral regions that are indicated by the bars on top of the spectral diffusion plot, Figure 4.12b, yields the modulation of the signal as a function of the polarization of the excitation light. The results are shown next to the pattern in Figure 4.12b together with $\cos^2$-type fit functions from which the mutual angle between the respective transition-dipole moments is obtained as $\Delta\alpha_{B2B3} = 77°$. Similarly $\Delta\alpha_{B1B2} = 2°$ is found (data not shown).
Figure 4.13 shows the distributions of the parameters ΔE_{B1B2}, ΔE_{B2B3}, $\Delta\alpha_{B1B2}$ and $\Delta\alpha_{B2B3}$ for all complexes that featured class A spectra. The red entries refer to the current section, while the gray entries are valid for RC-LH1 in DDM/PVA and have been taken from the preceding section 4.1. The scale for the phase angles has been restricted to values between 0 and 90° by using $\Delta\alpha_{BiBj} = |\alpha_{Bi} - \alpha_{Bj}|$, if the result was less than 90°, or $\Delta\alpha_{BiBj} = 180° - |\alpha_{Bi} - \alpha_{Bj}|$ otherwise. The number of entries for the histograms differs, because some spectra did not allow the determination of all parameters. Visual inspection of the histograms reveals already that the distributions for the two sample environments are very similar. This is quantified in Table 4.5, which provides the statistical parameters, mean and standard deviation (sdev), for each histogram. This testifies that, within statistical accuracy, the results of the current section are equivalent to those obtained on RC-LH1 complexes embedded in a PVA matrix (section 4.1).

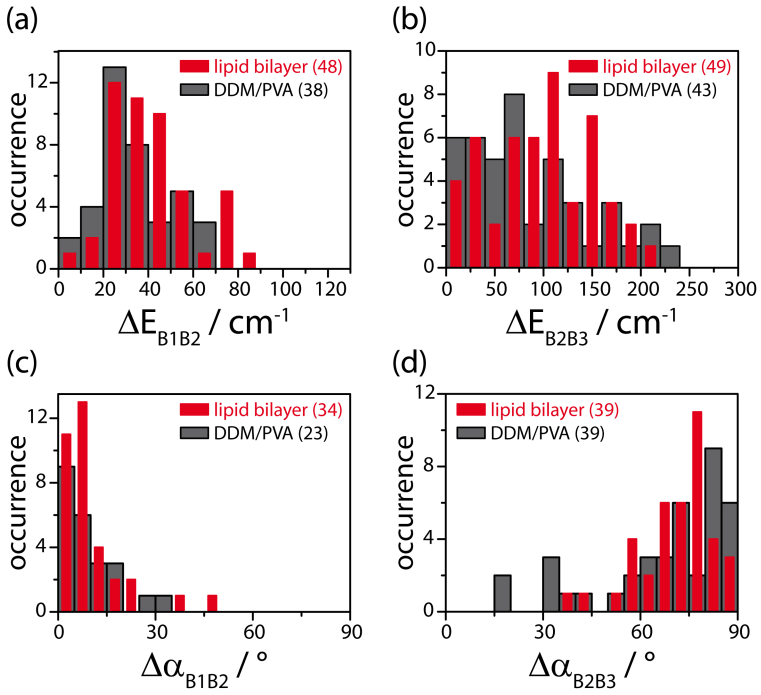

Figure 4.13: *Distributions of the energetic separations between the bands (a) B1 and B2, and (b) B2 and B3, and of the mutual angles between the transition-dipole moments associated with (c) B1 and B2, and (d) B2 and B3. The gray bars refer to RC-LH1 complexes from Rps. acidophila that have been embedded in a DDM/PVA matrix and have been taken from section 4.1. The red bars refer to the current section. For both cases the number of RC-LH1 complexes that contributed to a histogram is given in the legend.*

	ΔE_{B1B2} (mean $\pm$ sdev)/cm^{-1}	ΔE_{B2B3} (mean $\pm$ sdev)/cm^{-1}	$\Delta\alpha_{B1B2}$ (mean $\pm$ sdev)/°	$\Delta\alpha_{B2B3}$ (mean $\pm$ sdev)/°
lipid bilayer (this section)	40 ± 18	98 ± 55	9.4 ± 9.8	71 ± 11
DDM/PVA (section 4.1)	33 ± 17	85 ± 60	8.5 ± 7.8	67 ± 20

Table 4.5: *Energetic separations ΔE_{B1B2} (ΔE_{B2B3}) of the bands B1 and B2 (B2 and B3) and mutual angles $\Delta\alpha_{B1B2}$ ($\Delta\alpha_{B2B3}$) between the corresponding transition-dipole moments for the class A RC-LH1 complexes stabilized in a lipid bilayer and in DDM/PVA.*

The distribution of the spectral peak position of the narrow band B1 is shown in Figure 4.14 (red bars) together with the sum of all individual spectra that were assigned to class A. The histogram is centered at 902 nm (mean) in the red wing of the sum spectrum and has a width (sdev) of 40 cm^{-1}. For comparison the gray entries in Figure 4.14 show the corresponding data for the class A type spectra from

RC-LH1 complexes of *Rps. acidophila* embedded in DDM/PVA (section 4.1). For this environment the distribution of the spectral position of the narrow peak (gray bars) is centered at 892 nm (mean) and features a width (sdev) of 48 cm^{-1}.

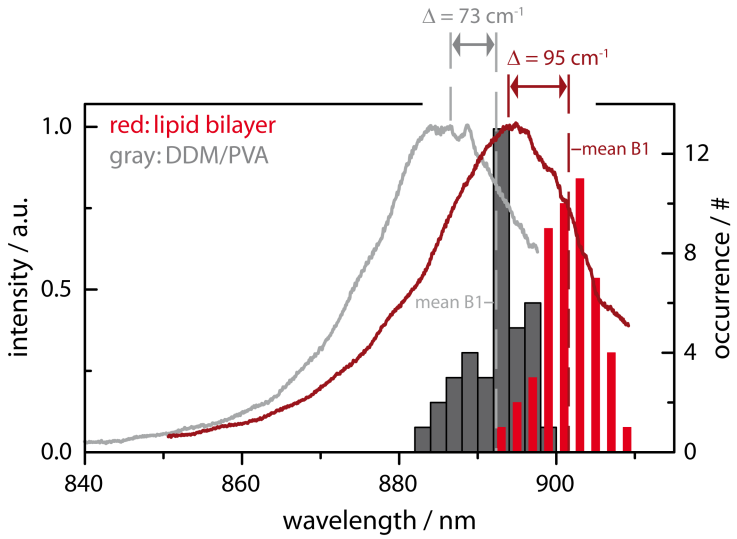

Figure 4.14: *Distribution of the spectral peak position of the band B1 for RC-LH1 complexes from Rps. acidophila reconstituted into a lipid bilayer (red bars) or embedded in a DDM/PVA matrix (gray bars). For comparison, the respective sum spectra of all individual complexes assigned to class A are shown by the full lines (for DDM/PVA only those 38 complexes were considered from section 4.1, where a narrow absorption line could be detected). The energetic separation between the mean of the histogram and the peak of the sum spectrum amounts to* 95 cm^{-1} *for the lipid bilayer and to* 73 cm^{-1} *for the DDM/PVA matrix.*

It is obvious from Figure 4.14 that the narrow spectral feature appears on the low-energy wing of the sum spectrum for both sample preparation conditions. The energy displacement between the mean of the histogram and the peak of the sum spectrum is 95 cm^{-1} for the lipid bilayer and 73 cm^{-1} for the DDM/PVA matrix, respectively. The slightly broader distribution for the B1 spectral peak position of the RC-LH1 complexes stabilized in detergent micelles inside the PVA matrix, with respect to those reconstituted into a lipid bilayer, provides a first hint that the packing of the complexes in the polymer matrix is not as tight as in the lipid bilayer, giving rise to more conformational freedom (*vide infra*).
Interestingly, both the values for the widths of the B1 distributions and the energetic separations with respect to the sum spectra, in both environments, are slightly smaller than the corresponding values determined in zero-phonon hole (ZPH) action spectra [120, 121]. This might reflect the different sample preparation conditions applied: Spatially well-isolated, individual RC-LH1 complexes deposited in thin films on quartz substrates in the experiments of this work, in contrast to bulk-ensemble samples stabilized in buffer/glycerol mixtures in [120, 121].

4.2.3 Discussion

At room-temperature, the ensemble absorption spectra from RC-LH1 complexes reconstituted into a DOPC lipid bilayer feature a 2 nm red-shift of the B885 band with respect to the complexes that are stabilized in DDM detergent and dissolved in buffer solution, see Figure 4.8. This red-shift probably reflects a slight compression of the RC-LH1 complexes in the lipid bilayer (*vide infra*) and/or an aggregation of the complexes as was shown in [17, 119, 122]. The latter is corroborated by the strong Stokes-shift that is observed for the reconstituted RC-LH1 complexes with respect to those in the other matrices (Figure 4.10, Table 4.3) and which is a clear indication for excitation energy transfer towards the lowest energy states within a network of complexes.
In order to compare the influence of temperature on the peak position of the B885 absorption band of RC-LH1 complexes that are embedded in thin-film samples, two different setups have been used: Namely, a commercial spectrometer for the room-temperature experiments, and a home-built single-molecule confocal microscope for the experiments under cryogenic conditions. Due to the different sensitivities of the detectors in the two setups a sample with a protein concentration of about 6 μM (corresponding to $OD_{885} = 25\ cm^{-1}$) had to be used for the room-temperature experiment. This is in contrast to the low-temperature work where a protein concentration of about 250 nM ($OD_{885} = 1\ cm^{-1}$) was used. Therefore, first it had to be verified whether for the high-concentration sample aggregation of the RC-LH1 complexes might play a role [123, 124].
Indeed, a red-shift of 1.5 nm is observed for the B885 band in the thin-film sample with respect to the monodispersed RC-LH1 complexes in DDM bulk-buffer solution. This shift is small, yet not negligible, which has to be kept in mind for the comparison between room-temperature and low-temperature experiments. Nevertheless, the two top traces in Figure 4.9 clearly demonstrate that the addition of PVA leaves the spectral position and the shape of the B885 absorption band unaffected.
For RC-LH1 complexes embedded in a lipid bilayer or (thin films of) DDM buffer solution, the peak of the B885 absorption band features a red-shift of 4.3 or 2.9 nm, respectively, upon cooling the samples to cryogenic temperatures. This is in contrast to samples immobilized in DDM/PVA, where a small blue-shift of 1 nm, which is within the resolution of the spectrometer, is observed. It is well known that the DOPC bilayer undergoes a phase transition at $T_C = -17\ ^\circ C$ [54], from a two-dimensional liquid crystalline phase above T_C to a highly ordered, and densely packed gel phase below T_C [53]. Hence, it is conceivable that the phase transition leads to a compression of the RC-LH1 complexes that are embedded in the lipid bilayer. In [125] the authors ascribed the main contribution of the observed pressure-induced red-shift to pigment-pigment interactions, because it was shown that a change of the local pressure had only minor influence on the protein binding

pockets and the conformation of the BChl *a* molecules in LH1 complexes. A putative compression of the LH1 complexes by the lipid bilayer results in an increase of the dispersive interactions that yields a lowering of the BChl *a* site energies [126, 127]. At the same time it causes an increase in the excitonic interaction between the pigments and results in a larger width of the exciton band. Since the main oscillator strength is associated with the states at the bottom of the exciton band this yields as well a lowering of the LH1 Q_y transition energy. Likewise, for the samples in DDM buffer an increase of the local pressure may be induced by crystalline bulk water [118] and similar effects as above may lead to the observed red-shift of 2.9 nm. In contrast to the other two environments, immobilization of the RC-LH1 complexes in the DDM/PVA matrix yields no significant spectral shift of the B885 absorption band upon cooling. This is consistent with the finding that thin polymer films exhibit a negative thermal expansion coefficient below the glass transition temperature T_g [128]. For pure PVA T_g amounts to 80 $°C$, and an expansion rather than a contraction of the polymer film upon cooling is conceivable.
Next the focus will be on the single-complex, low-temperature fluorescence-excitation spectra. The complexes have been embedded in three different environments, namely in DDM micelles in buffer, in a DOPC lipid bilayer, and in a DDM/PVA matrix. The data for the latter guest/host configuration have been taken from the previous section 4.1. The RC-LH1 complexes sustained in DDM micelles in buffer feature a pronounced blinking of the emitted intensity that prohibits any quantitative analysis of the spectra (Figure 4.11). This is in clear contrast to the RC-LH1 complexes embedded in the other two environments, where the majority of complexes showed stable emission characteristics during the more than one hour experimental time.
In literature varying explanations for the dark/quenched state of a LH complex can be found: In a very recent publication authors argue that a state of reduced fluorescence intensity for a LH complex might be reached by a photoactivated local conformational change in the LH complex [117]. This conformational change might increase vibronic coupling or coupling between intramolecular and protein vibrations, such that most of the photoenergy is dissipated non-radiatively. (Here, one should remember that already without this conformational change the fluorescence quantum yield of LH complexes is only about 10% [56].) Adapting this explanation to the experiments in this work, it remains an open question why such conformational changes should occur more frequently in the DDM/buffer environment as compared to the other two matrices, in particular, since it is assumed that the RC-LH1 complexes in the DDM/PVA environment experience increased conformational freedom, as compared to the complexes in DDM/buffer or the lipid bilayer. Thus, photoinduced transitions of a RC-LH1 complex to a quenched state, should be expected most frequently in DDM/PVA, which is definitely not the case.
An alternative explanation for the dark/quenched state of a LH complex is, analogous to semiconductor nanocrystals [129], to assign this state to the ionized state,

LH^+, of the complex [97, 130, 131]. For LH complexes it is assumed that during excitation of *e.g.* a LH1 complex, an electron is ejected from one of the B885 chromophores into the matrix. This chromophore then forms a radical cation which acts as a trap for the excitation energy [97, 130, 131]. According to [129] the ejected electron will induce a reaction field in the surrounding matrix which stabilizes the charge against fast recombination with the ionized $LH1^+$ complex. Further, the authors in [129] define the so called stabilization energy, E_{st}, which needs to be overcome to regain the electron from the matrix. E_{st} increases with increasing static dielectric constant ϵ of the matrix. This then results in higher probabilities for long off-times for emitters embedded in environments with large dielectric constants. In this work a marked difference is observed in the blinking behavior for the detergent stabilized RC-LH1 complexes embedded either in a PVA film (section 4.1) or in a film of buffer solution. It is therefore assumed that in this case not the direct surrounding (DDM micelle) of the pigment-protein complex is responsible for the differing behavior, but the matrices in which the detergent stabilized complexes are embedded. Thus, the three static dielectric constants that need to be compared are $\epsilon_{water} \approx 80$ [132], $\epsilon_{PVA} \approx 14$ [129] and $\epsilon_{lipid\,bilayer} \approx 4$ [133]. From this comparison a distinctly larger value of ϵ is discerned for the water environment, possibly indicating that in a water matrix the ejected electron can be most effectively shielded against the Coulomb potential of the $LH1^+$ complex. This might then explain the extended off-times for most of the complexes in the detergent-buffer environment (Figure 4.11), but only very rarely observed for the complexes in the PVA matrix or in the lipid bilayer.
That water molecules can actually intrude into the hydrophobic regions of detergent micelles, was demonstrated by Abel et al. [52], who showed in molecular dynamics simulations of DDM micelles that about 10% of the micelle's hydrophobic core is exposed to water (with respect to the total micelle surface). Moreover, the authors in [17] describe how, under high pressure, water intruding into the detergent micelles, disrupts part of the LH complexes. In contrast to that the equivalent pressure experiment performed on LH complexes stabilized in a lipid membrane showed no disruption of the pigment-protein complexes, meaning that the tighter packing of the lipid membrane avoids water intrusion. For the PVA matrix it is assumed that most of the water is expelled from the polymer network during the spin-coating process.
Finally, it should be noted that although the above explanation seems quite plausible, it is nothing more than an educated guess where, for confirmation, a systematic investigation of the dependency of the blinking process on the matrix material is required, taking also the presumable charge-separation in the bacterial RC into account [131], which was not discussed here for brevity.
For the RC-LH1 complexes reconstituted into a DOPC bilayer the same characteristic features are found that led to the grouping of the complexes into three distinct classes, A-C, as observed previously for the complexes immobilized in DDM/PVA

(section 4.1). Interestingly, the fraction of complexes that were associated with broken RC-LH1 complexes, *i.e.* those assigned to class C, increases significantly for the lipid bilayer environment with respect to the DDM/PVA matrix. Most likely, this reflects that the dissociation/denaturation of the RC-LH1 complexes is more pronounced during the reconstitution process. This interpretation is supported by the following observations. In [123] and in [124], in particular for the detergent DDM, it was shown that LH complexes tend to aggregate even in a detergent environment at high enough protein concentrations, while authors in [17] demonstrated that aggregated pigment-protein complexes in a detergent environment are more resilient against pressure induced dissociation than isolated ones. Likewise, for RC-LH1 complexes from *Rsp. rubrum* it was found that dissociation becomes more effective upon increasing the detergent concentration [40, 41], which is equivalent to a decrease of the protein concentration for the single-complex experiments as in this work. Therefore, as a rule, the RC-LH1 bulk samples are stored as aliquots at $OD_{885} = 10\ cm^{-1}$, corresponding to a detergent-protein-ratio of about 150/1 (c/c), which, according to [17], should lead to aggregated RC-LH1 complexes. As a matter of fact for the single-complex experiments on reconstituted RC-LH1 complexes the protein concentration in the detergent buffer solution has been lowered to a detergent-protein-ratio of about (1.1×10^7) /1 (c/c), before it is joined with the vesicle solution. Subsequently, for dialysis, this mixture is kept in a cold room at 5 $°C$ for four days. Given the results of the above references [17, 40, 41] it can be expected that some of those RC-LH1 complexes that are still in the detergent environment will tend to dissociate during this time, *i.e.* before they are incorporated into the vesicles. This is consistent with the larger fraction of intact RC-LH1 complexes in the DDM/PVA environment, *i.e.* those assigned to class A, because these samples are cooled down to cryogenic temperatures immediately after the dilution process, which reduces the time interval between preparation and observation tremendously. Yet, it is worth to note that once the RC-LH1 complexes have been reconstituted into a lipid bilayer the samples can be kept without a loss of quality in the refrigerator for more than a week, which is impossible for complexes stabilized in a detergent buffer solution at single-complex concentrations. This testifies that the stability of the RC-LH1 complexes once reconstituted into the lipid bilayer is generally higher than in a detergent micelle [19].
A detailed evaluation of the data was performed only for those spectra that were assigned to class A, which are interpreted to stem from intact RC-LH1 complexes. These spectra display the general characteristic features that have been found for monomeric RC-LH1 complexes including a gap, in previous studies [10, 12, 15]. Signatures for an increase of the interaction strength between the BChl *a* molecules in RC-LH1 in the lipid bilayer with respect to those embedded in the DDM/PVA matrix, as have been found in the ensemble spectra, can also be found in the single-molecule data. For example, the slightly larger mean values for the energy displacements ΔE_{B1B2} and ΔE_{B2B3} in the lipid bilayer as compared to DDM/PVA

(Table 4.5), indicate a larger splitting between the lowest exciton states, which presumably results from an increase of the interpigment interactions in the lipid bilayer. Similarly, in Figure 4.14 the larger spectral separation of 95 cm^{-1} between the lowest exciton state and the maximum of the sum spectrum for the reconstituted complexes with respect to the separation of 73 cm^{-1} for the RC-LH1 complexes embedded in DDM/PVA, again indicates elevated intermolecular interaction strengths between the BChl *a* molecules within the RC-LH1 complexes that are reconstituted into the lipid bilayer. Finally, in the lipid bilayer the width of the band B1 is distributed between 1 and 2 cm^{-1}, whereas the same distribution covers the range from $3 - 12$ cm^{-1} in the DDM/PVA matrix (section 4.1). From this observation it can be concluded that structural fluctuations that give rise to spectral diffusion [103], are more pronounced in the polymer matrix, which might reflect a larger degree of conformational freedom for the RC-LH1 complexes in this environment.
In summary, RC-LH1 complexes from *Rps. acidophila* immobilized in different environments have been studied. The ensemble absorption spectra show spectral shifts as a function of the matrix as well as, as a function of temperature. The latter effect can be explained consistently with variations of the local pressure that are induced by the matrix material upon cooling the sample. Application of single-molecule techniques reveals that the reconstitution process results in a significantly larger fraction of broken complexes with respect to embedment in a DDM/PVA film. In single-molecule spectroscopy these complexes can be treated separately and the intact complexes overall feature the same spectral signatures as their intact counterparts that have been immobilized in DDM/PVA. However, given the extra effort of reconstitution, the increased fraction of broken complexes, and the fact that the intact complexes feature the same decisive spectral details as those prepared in DDM/PVA, it can be concluded that, at least for the experiments conducted at low temperatures, using PVA as a matrix is a good choice. Additionally, as the polymer matrix seems to provide more conformational freedom to the LH complexes under cryogenic conditions, as compared to the other two environments, one might even argue that, from the three investigated environments, at low temperatures, the PVA matrix might represent the best approximation of the natural, room-temperature conditions of the RC-LH1 complexes (*i.e.* pigment site energy, pigment-pigment interaction strength, structural diversity of the LH complexes).

5 Numerical simulations - proposal of a *Rps. acidophila* LH1 aggregate

5.1 Motivation - Why refining the refined LH1 model of *Rps. palustris*?

In section 4.1 it has been shown that the spectral properties of the RC-LH1 complexes from *Rps. acidophila* are very similar to those of the RC-LH1 complexes from *Rps. palustris*. Therefore, it was concluded that the refined structural model presented for the LH1 complex of *Rps. palustris* in [15] should also apply for the LH1 complex of *Rps. acidophila*. However, some of the assumptions made for the solving *palustris* model in [15] are rather simplifying, concerning both the coupling strength between the BChl *a* molecules and the construction of the pigment aggregate. Therefore, in the following some of the deficits of the simulations in [15] will be named, which make a refinement of the refined LH1 model from *Rps. palustris* necessary in this work.

As a first rather rough simplification in [15] only interactions between neighboring pigments were taken into account. Furthermore, the parameter for the coupling strength, V_0, in the dipole-dipole interaction term (2.12) was chosen quite small, such that the resulting values for the interaction strength were only, $V_i = 218\ cm^{-1}$, for the interaction between pigments of the same dimer unit (intradimer interaction) and, $V_e = 126\ cm^{-1}$, for the interaction between pigments of neighboring dimer units (interdimer interaction). These figures are significantly smaller than the mean values of the nearest-neighbor coupling, V ($V = \frac{V_i+V_e}{2}$), in LH1 complexes, determined in recent studies [134, 135]. Therein authors deduced the width of the exciton state manifold, δE, resulting from the strongly coupled array of BChl *a* pigments in LH1 complexes, by means of fluorescence-anisotropy excitation spectra and found $\delta E \approx 1900\ cm^{-1}$. Knowing that, in a crude approximation, $\delta E \approx 4V$ [136], this results in a value for the mean nearest-neighbor interaction of

$V \approx 475\ cm^{-1}$, which is more than double the coupling strength applied in [15].
As a consequence of the small next-neighbor interactions in the simulations in [15], an implausibly small value had to be chosen for the average site energy, E_0, of the pigments, $E_0 = 11,570\ cm^{-1} \hat{=} 864.3\ nm$, for the simulated single-complex spectra to be in a spectral region comparable to the experiment. There are several reasons making this value for E_0 unlikely. Firstly, for the LH1 complex of the bacterial species *Rsp. rubrum* it was shown that the dissociation of this complex first leads to dimeric subunits, consisting of a BChl *a* dimer and two polypeptides, absorbing at 820 *nm*. Subsequently monomeric subunits, of one BChl *a* molecule non-covalently bound to an apoprotein, are formed, absorbing at 777 *nm* [41]. This indicates that, as a consequence of the protein environment the transition energy, E_0, of the BChl *a* molecules is slightly red-shifted from about 770 *nm*, for free BChl *a* in solution [4], to 777 *nm* for protein-bound BChl *a*, and that the additional red-shift from 777 *nm* to 820 *nm* results from pigment-pigment interactions [137]. Taking the similarities of the structural subunits of the LH1 complexes from *Rsp. rubrum* [138] and *Rps. palustris* and their similar room-temperature ensemble absorption spectra [32, 138], into account, the site energies of the BChl *a* pigments in the LH1 complex from *Rps. palustris* should also be expected around 777 *nm*, which would correspond to $E_0 = 12,870\ cm^{-1}$. However, comparing this figure to $E_0 = 11,570\ cm^{-1}$, used in [15], a discrepancy of more than 1000 cm^{-1} can be discerned.
Another possibility to gain more realistic values for the BChl *a* site energies, would be to take the LH2 complex from *Rps. acidophila* as reference, especially since the B850 BChl *a* dimer unit of this complex, served as a basis for the arrangement of the pigments in the LH1 *palustris* structural model [15]. In this case, the site energy for a protein-bound BChl *a* molecule, could be directly adopted from the B800 BChl *a* molecules in a LH2 complex, where, due to the weak coupling between the pigments, excitations are mainly localized on individual sites. As the transition energies for the individual pigments in the B800 aggregate of LH2 complexes are mainly spread around $E_0 = 12,500\ cm^{-1} \hat{=} 800\ nm$, this could then be another measure for the pigment site energies in a LH1 complex. Again this number for E_0 is by far larger than E_0 applied in [15].
Regarding the structural composition, two shortcomings can be identified for the *palustris* model in [15]. To begin with, the dimerization of the BChl *a* pigments in the LH1 structural model in [15] is based on the placement of the pigments on two separate ellipses with different circumferences. As a consequence of this construction principle, the mutual orientation and distance between the Q_y transition-dipole moments varies for different dimer units around the ellipse. This can be well observed in Figure 4, Model C, in [15], especially in the representation with exaggerated eccentricity. The inhomogeneity of the different dimer units along the LH1 aggregate is problematic both for the simulations and from a biochemical point of view. For the simulations, the B850 dimer unit from the LH2 complex of *Rps.*

acidophila could only serve as a rough structural guide, with many dimer units of the model in [15] clearly deviating from this given standard. This then creates a large set of free parameters for the simulations which cannot be confirmed experimentally. From the biochemical point of view the varying dimer units of the LH1 model in [15] could pose a problem, since observations made by atomic force microscopy (AFM) [20], led the authors to the conclusion that the building principle of a LH1 complex bases upon stable dimer subunits, consisting of, amongst others, two protein-bound BChl *a* molecules with fixed mutual orientation and distance, where, on the other hand, each dimer unit experiences a certain degree of conformational freedom within the overall LH1 complex. The notion of stable LH1 subunits was additionally corroborated in biochemical studies, where the dissociation of LH1 aggregates first led to dimeric subunits, which were then further decomposed into monomeric ones [40, 41].

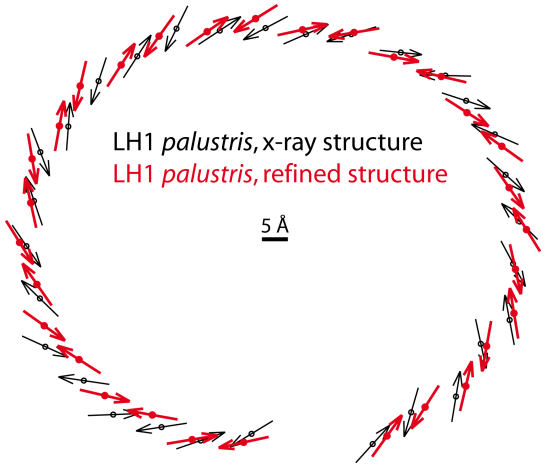

Figure 5.1: *Comparison of the arrangement of the BChl a molecules in the LH1 complex from Rps. palustris, for the x-ray structure as deposited in the protein database ([24], PDB file: 1PYH; black arrows) and the refined structural model from [15] (red arrows). The small circles indicate the positions of the central Mg^{2+} ions of the BChl a molecules and the arrows indicate the corresponding Q_y transition-dipole moments. The scale bar shows approximately the resolution of the x-ray structure of* 4.8 *Å.*

In Figure 5.1 the BChl *a* assembly of the LH1 complex from *Rps. palustris* is shown for the x-ray structure ([24], PDB file: 1PYH; black arrows) and for the refined structural model proposed in [15] (red arrows). In the depicted representation the small circles indicate the positions of the central magnesium ions inside the bacteriochlorin macrocycles of the BChl *a* molecules and the orientation of the BChl *a* Q_y transition-dipole moments is indicated by the arrows. An accurate inspection of the superposition of the pigments in the two structures of Figure 5.1, reveals considerable deviations between them, in particular observable in the lower left

and top left "corners" of the aggregates. These deviations may not be of any importance, since the positions of the BChl *a* molecules in the crystal structure of the RC-LH1 complex from *Rps. palustris* have a low accuracy (4.8 *Å* resolution, [24]). Additionally, numerical simulations in [15] have shown that the LH1 model in which the distinct arrangement of the BChl *a* molecules was adopted from the RC-LH1 *palustris* crystal structure, failed to reproduce the spectral characteristics observed in the single-complex fluorescence-excitation spectra. On the other hand, in the RC-LH1 *palustris* crystal structure [24] the BChl *a* molecules were still modeled into the resulting electron density map and one may therefore speculate if the arrangement of the BChl *a* molecules as proposed in [24], still has a certain significance. In this regard, AFM studies have revealed specific interactions between the RC and its surrounding LH1 complex, where actually it was shown that the elliptic conformation is imposed on the LH1 complexes by the asymmetric shape of the RCs and that the LH1 complexes reassumed a circular conformation, when the RCs were removed from their center [39, 139]. Thus, it could be that the seemingly irregular orientation of certain LH1 BChl *a* pigments in the crystal structure is not just an artifact of the modeling routine [24], but may be induced by interactions between the LH1 complex and the RC, although a specific experimental evidence for this notion is lacking. Another aspect in favor of a particular interplay between LH1 complex and associated RC, is the unique orientation of the RC with respect to the LH1 complex, resulting in the UQ_B binding site in the RC pointing directly towards the gap within the LH1 aggregate [24]. Thus, despite the specific arrangement of the pigments in the LH1 complex as proposed in the crystal structure [24] should not be regarded as the ultimate solution, this structure still is the most detailed experimental evidence for the positioning of the BChl *a* molecules in a LH1 complex with a gap in its overall structure, available so far. Therefore, for the design of a LH1 model it should still be desirable, to be as similar to the LH1 *palustris* crystal structure as possible, with the additional requirement for the model structure that it should be able to reproduce the spectral features observed in the single-complex fluorescence-excitation spectra.
For the numerical simulations in the following section 5.2 it was tried to eliminate some of the simplifications made for the LH1 model in [15], getting a step closer towards, what is assumed to be the native situation in purple bacteria LH1 complexes. The ultimate goal of the numerical simulations performed in this thesis was to find a structural model for the assembly of the BChl *a* molecules in a LH1 complex which satisfactorily reproduces the spectral features found experimentally in single-complex fluorescence-excitation spectra of the intact RC-LH1 complexes from *Rps. acidophila*. Due to the good agreement of the spectral characteristics in the fluorescence-excitation spectra of the RC-LH1 complexes from *Rps. acidophila* and *Rps. palustris* (section 4.1), a successful model structure for the LH1 complex of *Rps. acidophila* would naturally also serve as a model for the LH1 complex from *Rps. palustris*, thereby constituting an alternative to the structural model proposed

in [15].

5.2 Numerical simulations based on various LH1 model structures

In this section the optical properties of various LH1 model aggregates are simulated and compared to the spectroscopic data recorded for the class A RC-LH1 complexes from *Rps. acidophila*. Thereby, it is sought to gain a more profound knowledge about the specific organization of the BChl *a* molecules inside the LH1 complex of this bacterial species. The crystal structure of the RC-LH1 complex from *Rps. palustris* [24] serves as structural reference for all LH1 model structures presented in this work, meaning that all models have a gap in their BChl *a* assembly and are comparable to the LH1 complex from *Rps. palustris* within the 4.8 *Å* resolution of the crystal structure. This procedure is still reasonable in view of the new highly resolved crystal structure of the RC-LH1 complex from *T. tepidum* [9], as the LH1 complex of this bacterial species was shown to have a completely closed structure. The single-complex measurements on the RC-LH1 complexes from *Rps. acidophila* however (section 4.1), indicate that the LH1 complexes from this species have a gap in their strongly coupled pigment assembly. Thus, it is justified to take the interrupted LH1 structure from *Rps. palustris* [24] as benchmark for a structural model of the LH1 complex from *Rps. acidophila*.

5.2.1 Characterization of initial LH1 model structures

In this paragraph three basic LH1 structures will be introduced and the specific aggregation of their BChl *a* pigments will be characterized by the nearest-neighbor interactions being effective between them. To begin with, the first LH1 model structure (Structure 1) will be described and, by means of this structure, it will also be explained how more realistic values for the nearest-neighbor interactions are achieved in the simulation. Thereafter, the two remaining LH1 models, Structure 2 and 3, will be presented.

Structure 1

The basic geometry of Structure 1 is an ellipse (Figure 5.2a). The semi-major axis a and the semi-minor axis b of the ellipse were calculated as $a = r_0 \cdot (1 + \delta)$ and $b = r_0 \cdot (1 - \delta)$, with a radial deformation, $\delta = 7.3$ % and a radius $r_0 = 43$ *Å*. Then, in line with the idea of the modular building principle for LH1 complexes [20], 16 dimer units with fixed mutual orientation and distance between the two BChl *a* pigments constituting the dimer, were equidistantly (constant segment ds of the ellipse's circumference) distributed on the elliptic basic structure. Subsequently,

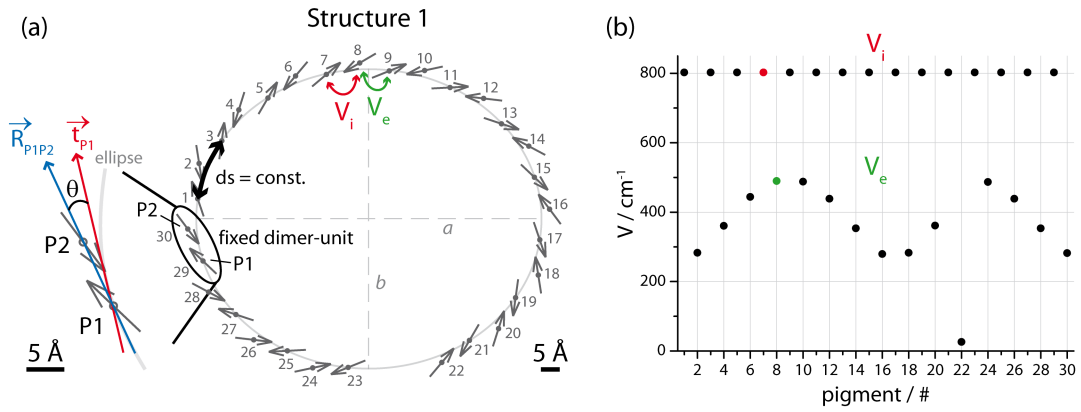

Figure 5.2: *Arrangement of the BChl a Q_y transition-dipole moments and nearest-neighbor interactions in Structure 1. The arrows in (a) indicate the orientation of the Q_y transition-dipole moments and the dots show the positions of the central Mg^{2+} ions of the BChl a molecules in Structure 1. 15 identical dimer units, with their structural parameters adopted from the LH2 complex of Rps. acidophila (see text), were distributed with equidistant step size ds on the circumference of an ellipse, with a semi-major axis $a = 46.14$ Å and a semi-minor axis $b = 39.86$ Å. The dimer units are tilted by a constant angle $\theta = 6.7°$ with respect to the ellipse, determined between the connection-vector of the two pigments $\vec{R}_{P1P2}$ and the local tangent of the ellipse $\vec{t}_{P1}$ (extended view, on the left). The individual pigments are numbered consecutively to facilitate the assignment of the nearest-neighbor interactions, whereby exemplary, V_i indicates the intradimer interaction between pigments 7 and 8 and V_e indicates the interdimer interaction between pigments 8 and 9, respectively. The scale bar to the left applies to the enlarged view and the one to the right to the overall structure. (b) Nearest-neighbor interactions between the pigments in Structure 1. The interaction values assigned to the respective pigment numbers describe the interaction strength between the indicated pigment and the next following one in clockwise direction. The value of the intradimer interaction, V_i, remains constant along the ellipse ($V_i = 803\ cm^{-1}$), whereas the value of the interdimer interaction, V_e, undergoes a modulation. Marked as red and green dots are the interaction values highlighted in (a).*

one dimer unit was removed from the BChl *a* assembly to mimic the gap in the LH1 aggregate. The mutual arrangement of the two BChl *a* molecules inside the dimer units of the LH1 model structures was taken to be homologous to the B850 dimer units in LH2 complexes from *Rps. acidophila* ([35], PDB file: 1NKZ). This is in line with the recent publication of the high-resolution crystal structure of the RC-LH1 complex from *T. tepidum* [9], which revealed that the arrangement of the BChl *a* molecules in the dimer units of a LH1 aggregate is very similar to the arrangement in the dimer units of LH2 complexes. In a rather simple approach to calculate the interaction strength between the pigments, which is nevertheless sensitive to changes in the mutual orientation and distance between the pigments,

a dipole-dipole type function was applied [62]:

$$V_{nm} = V_0 \frac{\kappa_{nm}}{r_{nm}^3} \ , \tag{5.1}$$

where V_0 denotes the coupling strength, κ_{nm} is the usual orientation factor and r_{nm} denotes the mutual distance between the pigments n and m. For Structure 1, as it consists of fixed dimer units, one can generally distinguish between two types of next-neighbor interactions, V, acting between adjacent pigments in the aggregate: V_i for the intradimer interaction and V_e for the interdimer interaction (Figure 5.2a). Seeking to draw a more realistic picture of the processes inside a LH1 complex it was decided to use values of $V_i = 806\ cm^{-1}$ for the intradimer interaction and $V_e = 377\ cm^{-1}$ for the interdimer interaction, as a reference point [60, 140]. These figures are significantly larger than the interaction strengths used in [15]. Yet, the values for V_i and V_e in [60, 140] were determined based on a fit of the resulting exciton spectrum to extensive quantum chemistry calculations [66] and therefore, these values seem to be more reliable than those used in [15]. In order to achieve a value compatible to $V_i = 806\ cm^{-1}$ for the intradimer interaction, using the dipole-dipole interaction approach, the coupling strength V_0 is the only free parameter in equation (5.1), as the parameters κ_{nm} and r_{nm} are predetermined due to the fixed mutual orientation and distance between the pigments inside a dimer unit. Setting V_0 to $387,626\ \mathring{A}^3\, cm^{-1}$, which corresponds to a dipole strength of the Q_y transition-dipole moments of 8.8 D if one assumes an optical density $n_{opt} = 1$, results in a value for the intradimer coupling strength, $V_i = 803\ cm^{-1}$, which is very close to the above value of $806\ cm^{-1}$. The dipole strength of 8.8 D chosen in this work is very similar to the 8.3 D applied in [141] to model the processes in a vesicle-scale PSU, but somewhat larger than the 6.3 D determined in [142] for dimer units of LH1 complexes.

In contrast to the simulations in [60, 140], in this work the value for the interdimer interaction V_e was not assumed as fixed, but V_e varied along the ellipse depending on the mutual distance and orientation of adjacent dimer units. With this type of modeling the idea from the basic construction principle of LH1 complexes is included, which proposes stable dimer subunits with a certain degree of structural freedom within the LH1 complexes [20]. The structural parameter which allows for the adjustment of V_e, seeking to achieve a value close to the aforementioned value in [60, 140], is the tilt angle θ of the dimer units with respect to the local tangents of the ellipse (Figure 5.2a). Choosing $\theta = 6.7°$ results in a mean value of $V_e = 381\ cm^{-1}$ (the interaction strength at the gap was omitted in the calculation of the mean, to make V_e comparable to V_i and to the literature values), which is again in good agreement with V_e in [60, 140].

For the simulation procedure of this thesis a crucial characteristic for a given LH1 model is the modulation of the nearest-neighbor interaction along the aggregate. For Structure 1, with the given construction prerequisites, naturally the intradimer

interaction adopts a fixed value, $V_i = 803\ cm^{-1}$, whereas the interdimer interaction, V_e, shows a C_2 modulation along the ellipse if the decreased interaction at the gap is neglected (Figure 5.2b). The maxima of the interdimer interaction, V_e, can be found on the long sides of the ellipse, where the pigments of neighboring dimer units have the most parallel orientation with respect to the vector connecting them and contrary, the minima of V_e are located on the short sides of the ellipse.
As a further improvement with respect to the simulations in [15], interactions up to second neighbors (*i.e.* $m = n + 2$ in equation (5.1)) were included in this thesis. The mean value for the second-neighbor interactions in Structure 1 was calculated to $W = -92\ cm^{-1}$, where again, for comparability reasons, the interaction values at the gap were excluded.
Since the simulation results of Structure 1 failed to reproduce the single-complex data of the intact RC-LH1 complexes from *Rps. acidophila* (see next section 5.2.2), two further LH1 model structures were introduced. In Figure 5.3, for comparison, all three LH1 models are shown in a common representation. Additionally the nearest-neighbor interactions, constituting a characteristic fingerprint of the respective BChl *a* assembly, are shown to the right of each structure.
Initially, Structure 1 is redrawn in Figure 5.3a (gray arrows) and compared to the structural model of the LH1 complex from *Rps. palustris* as deposited in the protein database (file: 1PYH [24]; green, transparent arrows). It can be seen that, despite all the structural prerequisites considered for Structure 1, on the one hand, to diminish the number of free parameters in the simulation (stable BChl *a* dimer units) and on the other hand, to realize a plausible value for the interdimer interaction V_e (tilt angle θ of the dimer units), Structure 1 still is within the resolution of 4.8 $\mathring{A}$ of the LH1 *palustris* crystal structure.

Structure 2

For Structure 2 (Figure 5.3b) the positions of the LH1 BChl *a* pigments were adopted from the crystal structure of the *Rps. palustris* RC-LH1 complex [24]. This kind of LH1 model was already applied in the numerical simulations in [15], where it could not successfully describe the measured single-complex data of RC-LH1 complexes from *Rps. palustris*. However, applying a much higher coupling parameter $V_0 = 347,353\ \mathring{A}^3\ cm^{-1}$ corresponding to a dipole strength of the Q_y transition-dipole moments of 8.3 D (an explanation why V_0 deviates from the value used in Structure 1 will follow in section 5.2.2), in this work one resides in a totally different energy regime as compared to [15]. It is clear that the stronger coupling between the pigments in Structure 2 as compared to the corresponding LH1 model in [15], despite the equal structural buildup, will result in differing excitonic properties, which then again makes Structure 2 a plausible structural model for the LH1 complex from *Rps. acidophila*. The irregular arrangement of the BChl *a* pigments in Structure 2 is best visualized by the variation of the nearest-neighbor

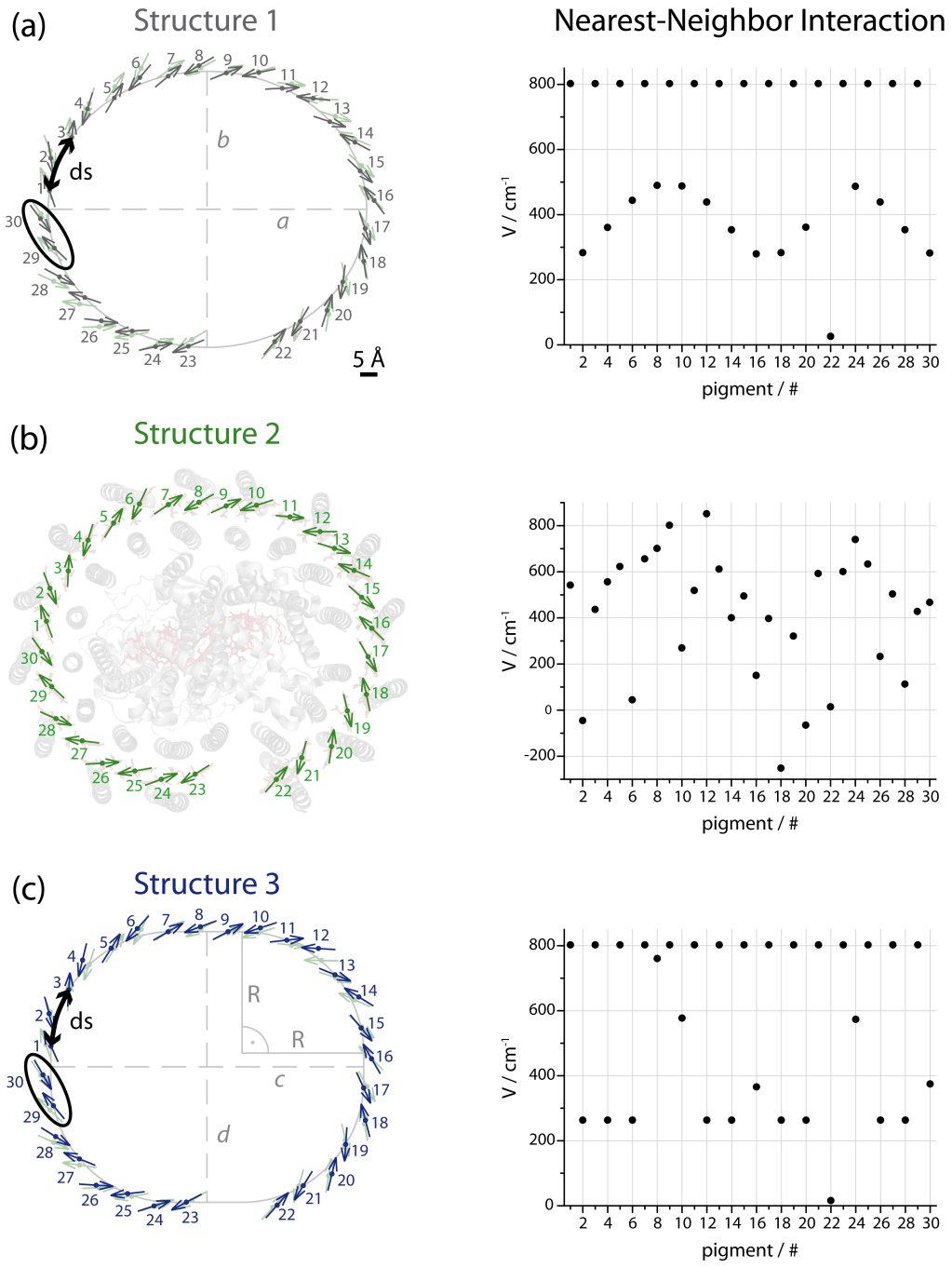

Figure 5.3: *Basic LH1 model structures (left) with corresponding nearest-neighbor interactions (right). The representation is equivalent to Figure 5.2. (a) Structure 1 (gray arrows), same as Figure 5.2. (b) Structure 2 (green arrows): Distribution of the LH1 BChl a pigments as in the RC-LH1 palustris crystal structure (PDB file: 1PYH [24]), which is underlaid for illustration. (c) Structure 3 (blue arrows): Distribution of fixed dimer units on a rectangle with rounded corners. Structures 1 and 3 are underlaid with Structure 2 (green, transparent arrows), respectively, which served as the benchmark LH1 model in this work.*

dipole-dipole interaction, $V_{n,n+1}$ (n denoting the pigment number), along the structure, with $-252\ cm^{-1} \leq V_{n,n+1} \leq 852\ cm^{-1}$ (mean: $411\ cm^{-1}$) (Figure 5.3b, *right*). With regard to the interaction-diagram of Structure 2 it also becomes apparent that a differentiation between an intradimer interaction, V_i, and an interdimer interaction, V_e, is clearly not possible for Structure 2. For the second-neighbor interaction, $W_{n,n+2}$, in Structure 2 a variation between $-99\ cm^{-1} \leq W_{n,n+2} \leq -4\ cm^{-1}$ (mean: $-58\ cm^{-1}$) can be observed.

Structure 3

As a third basic LH1 model Structure 3 is introduced (Figure 5.3c). The main intent in the buildup of Structure 3 was to create a LH1 aggregate which is in better agreement with the benchmark LH1 structure, Structure 2 (as it represents the pigment arrangement of the RC-LH1 *palustris* crystal structure), than Structure 1. Here, especially in the "corners" of Structure 1 (pigment numbers: 5, 6; 11-15 and 25-28) systematic deviations with respect to Structure 2 can be observed (Figure 5.3a). Since the pigment positions of Structure 1 and 2 agree at the vertices of the ellipse, but the pigments of Structure 1 are shifted inwards with respect those of Structure 2 for the segments in between the vertices, the impression is gained that the overall geometric shape of Structure 2 might be better described by a rectangle with rounded corners. Therefore, exactly this basic geometry was chosen for Structure 3 (Figure 5.3c). The length of the long half-axis c in the rectangle of Structure 3 amounts to 45.33 $\AA$ and to 39.17 $\AA$ for the short half-axis d. The radius R of the four circles used for rounding the corners amounts to 35.25 $\AA$. For the placement of the pigment molecules in Structure 3 the identical principle was applied as for Structure 1, meaning that 15 dimer units, each taken to be homologous to a B850 BChl *a* dimer in the LH2 complex from *Rps. acidophila* [35], were distributed at equal distance *ds* on the rounded rectangle and each dimer unit had a constant tilt angle $\theta = 6.7°$ with respect to the local tangent of the rounded rectangle. As a result of the new underlying conformation of Structure 3, the overall agreement with Structure 2 is now much more pronounced in comparison to Structure 1 (Figure 5.3a, c). Additionally it might be of importance that Structure 3 is consistent with the basic LH1 building principle of stable dimer subunits which is definitely not the case for Structure 2.
Since the same coupling strength V_0 was used in Structure 3 as in Structure 1, one receives equivalent values for the intradimer interaction $V_i = 803\ cm^{-1}$ in the two structures. However, due to the deviant basic geometries, a different modulation of the interdimer interaction, V_e, can be observed in Structure 3 as compared to Structure 1 (Figure 5.3a, c, *right*). For Structure 3 one recognizes constant values of about $260\ cm^{-1}$ for V_e, between neighboring dimer units that are both located on one of the four quadrants in the corners of the rectangle. For neighboring dimer units, where one or both units are located on a straight line of the circumference

of the rectangle, V_e increases significantly. The mean value of V_e in Structure 3 amounts to 359 cm^{-1} and the mean value for the second-neighbor interaction, W, amounts to -85 cm^{-1}, where in both cases the values at the gap were omitted for comparability reasons. It can be seen that, as for Structure 1, the mean value of V_e in Structure 3, is in reasonable agreement with the expensively computed value of $V_e = 377$ cm^{-1} from [60, 140].
The coordinates of the central Mg^{2+} ions of the BChl *a* molecules and the unit vectors, $\hat{n}$, of their corresponding Q_y transition-dipole moments in the structures 1, 2 and 3 are listed in the Appendix, part A.

5.2.2 Numerical simulations based on the initial LH1 models

In this section first it will be described how, from numerical calculations of the excitonic properties of the structures 1, 2 and 3, it is possible to generate simulated data which can be compared to the spectral characteristics of the bands B1-B3 of the intact RC-LH1 complexes from *Rps. acidophila*. Subsequently, from the comparison of the simulated data with the statistical distributions of the spectral properties of the bands B1-B3, one wanted to find out if one of the three proposed models can better describe the spectral characteristics of the RC-LH1 complexes and therefore may provide hints towards the structural buildup of the LH1 complex from *Rps. acidophila*. In this regard it should be noted that it is legitimate to compare the low-temperature spectroscopic data of the RC-LH1 complexes with data from numerical simulations basing upon LH1 aggregates only, since at cryogenic temperatures, for RCs which have been cooled down in the dark, electron transfer from the primary electron acceptor Q_A to the secondary acceptor Q_B is blocked [143, 144]. Therefore, once Q_A has been reduced following the first excitation of the special pair, no further photochemistry and concomitant quenching of the LH1 fluorescence by the RC can occur, which makes the spectral signature of the low-temperature fluorescence-excitation spectra from RC-LH1 complexes solely dependent on the structure of the LH1 complexes.

Simulation of a single-complex spectrum

The spectral characteristics of a LH1 aggregate, are determined by its electronic structure. In the limit of strong coupling between the pigments in the aggregate, its electronic structure can be described by the following Hamiltonian in Heitler-London approximation, in which interactions up to second neighbors have been

taken into account [13]:

$$H = \sum_{n=1}^{30} E_{0,n} \left|n\right\rangle \left\langle n\right| \quad + \quad \sum_{n=1}^{30} V_{n,n+1} \left(\left|n\right\rangle \left\langle n+1\right| + H.c.\right) + \quad \sum_{n=1}^{30} W_{n,n+2} \left(\left|n\right\rangle \left\langle n+2\right| + H.c.\right) \ , \tag{5.2}$$

with $n = 1, 2, \ldots, 30$ denoting the pigment number in the respective LH1 complex, $E_{0,n}$ indicating the individual site energy of pigment n, $\left|n\right\rangle$, $\left|n+1\right\rangle$ and $\left|n+2\right\rangle$ corresponding to excitations localized on the pigments n, $n+1$ and $n+2$, respectively and $V_{n,n+1}$ and $W_{n,n+2}$ denoting the nearest-neighbor and second-neighbor interactions. Numerical diagonalization of the above Hamiltonian (5.2) leads to the excitonic eigenenergies E_k and eigenstates $\left|k\right\rangle$ of the strongly coupled pigment assembly, with:

$$\left|k\right\rangle = \sum_{n=1}^{30} a_{n,k} \left|n\right\rangle \ . \tag{5.3}$$

Due to the gap in the LH1 aggregates, they can be treated as linear excitonic systems and therefore, following common practice [59], the exciton states are numbered consecutively $k = 1, 2, \ldots, 30$. The coefficient $a_{n,k}$ indicates the amplitude of the exciton wavefunction of the k^{th} exciton state at pigment n and thereby denotes the participation of this pigment in the k^{th} exciton state. The exciton transition-dipole moments are then given as:

$$\vec{\mu}\left(k\right) = \sum_{n=1}^{30} a_{n,k} \, \vec{\mu}\left(n\right) \ , \tag{5.4}$$

where $\vec{\mu}\left(n\right)$ denotes the transition-dipole moment of an individual BChl a molecule, and finally the oscillator strengths of the exciton states can be derived from:

$$\left|\vec{\mu}\left(k\right)\right|^2 = \left|\sum_{n=1}^{30} a_{n,k} \, \vec{\mu}\left(n\right)\right|^2 = \mu_{mon}^2 \left|\sum_{n=1}^{30} a_{n,k} \, \hat{\mu}\left(n\right)\right|^2 \ , \tag{5.5}$$

where $\mu_{mon} = \left|\vec{\mu}\left(n\right)\right|$ is the dipole strength and $\hat{\mu}\left(n\right)$ the unit vector of an individual BChl a molecule. With these expressions at hand it is demonstrated, using Structure 1 as example, on the one hand, how the structural composition of an aggregate affects its resulting exciton manifold and on the other hand, how this exciton manifold can then be translated into a single-complex spectrum. In doing so, this procedure will then also provide one with the means to extract data from simulated spectra that can be compared with the experimental data. The numerically calculated excited state manifold and the corresponding single-complex spectra of

Structure 1 are depicted in Figure 5.4. Thereby, the site energy for all pigments in Structure 1 was set to $E_0 = 12,590\ cm^{-1} \stackrel{\wedge}{=} 794.3\ nm$, where the explicit procedure for the determination of E_0 in the various structures will be described further below.
In part (a) of Figure 5.4 a pictorial representation of the wavefunctions and the resulting transition-dipole moments for the 3 lowest exciton states of the Structure 1 is shown. Thereby, the length of the small vectors is given by the exciton coefficients $a_{n,k}$ in equation (5.4) and the large vector in the middle of the aggregates represents the exciton transition-dipole moment, $\vec{\mu}\,(k)$, resulting from the summation of the small vectors, respectively. The position and orientation of the small vector arrows corresponds to the arrangement of the Q_y transition-dipole moments in Structure 1. All vectors are shown as projections to the xy-plane. According to the specific modulation of the interdimer interaction, V_e, in Structure 1 (Figure 5.2b) it can be seen that the amplitude of the exciton wavefunction for the $k = 1$ state is largest in that region of Structure 1, where the interdimer interaction, V_e, has its maximum, namely on the long side of the ellipse (Figure 5.4a). This is similar to excitonic systems dominated by static energy disorder, where the lowest exciton state was found to localize on pigments with significantly lowered site energies [104, 145]. The $k = 2$ exciton state of Structure 1 localizes predominantly on the pigments adjacent to the gap (Figure 5.4a), which is again an area in Structure 1 with large values for the interdimer interaction, and finally the wavefunction of the $k = 3$ exciton state has a node on the long side of the ellipse, between two areas with large amplitudes of the wavefunction.
The representation in Figure 5.4a is instructive for two reasons: Firstly, one can easily understand how the mutual angles between the different exciton transition-dipole moments come about. Secondly, it helps in the understanding of the interplay between the structural buildup of the LH1 complexes and the specific localization of the exciton wavefunctions, resulting in certain lengths of the exciton transition-dipole moment vectors, $\vec{\mu}\,(k)$. Subsequently, the oscillator strength, $|\vec{\mu}\,(k)\,|^2$, of the respective exciton states can be calculated with the help of equation (5.5). The resulting distribution of the oscillator strength among the lowest exciton states of Structure 1 is shown in Figure 5.4b. In this representation the x-axis corresponds to oscillator strength in monomer units and the y-axis represents the energy scale given as wavelength in nm. The exciton states are shown at the positions of their eigenenergies E_k on the y-axis, and their oscillator strength is given by the length of the black bars, respectively. It can be observed that almost the total oscillator strength, amounting to 30 monomer units in a system comprising 30 pigments as Structure 1, is shared among the exciton states $k = 1, 2, 3$ and 5, where the oscillator strength of the latter is somewhat smaller than that of the three lowest states. For a determination of the energy splitting between the different spectral bands comparable to the experiment, the calculated exciton manifold of Structure 1, first of all needed to be transduced into single-complex absorption spectra (Figure 5.4c).

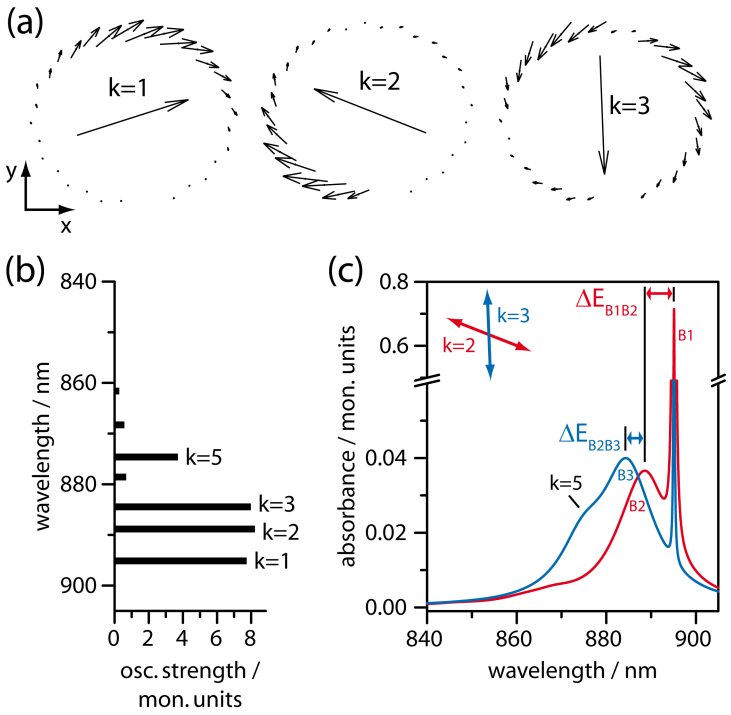

Figure 5.4: *Illustration of the numerically calculated exciton manifold of Structure 1 and two single-complex spectra derived from it. (a) Pictorial representation of the amplitudes of the exciton wavefunctions and the resulting transition-dipole moments of the three lowest exciton states $k = 1, 2, 3$ in Structure 1. The small arrows indicate the amplitude of the exciton wavefunctions at the respective pigment positions and the large arrows in the middle of the aggregates, indicate the resulting exciton transition-dipole moments. (b) "Exciton ladder" indicating the energy and the oscillator strength of the exciton states in the low-energy part of the Structure 1 exciton manifold. The y-axis represents the energy scale given as wavelength in nm and the oscillator strength of the respective exciton states, given in monomer units, is represented by the length of the black bars. (c) Single-complex spectra derived from the numerically calculated Structure 1 exciton manifold. The red spectrum corresponds to an excitation polarization parallel to the $k = 2$ exciton transition-dipole moment and for the blue spectrum the polarization is assumed to be parallel to the $k = 3$ transition-dipole moment. In the spectra, the higher exciton states, $k > 1$, are assigned broad Lorentzian lines ($fwhm = 190\ cm^{-1}$), while the lowest exciton state, $k = 1$, is assigned a narrow line B1 ($fwhm = 5\ cm^{-1}$). The oscillator strength of the exciton states is reflected by the area under the respective Lorentzians. The peak positions of the broad bands are denoted as B2 (red spectrum) and B3 (blue spectrum), respectively. The energy displacement between the simulated bands B1 and B2 amounts to $\Delta E_{B1B2} = 83\ cm^{-1}$ and to $\Delta E_{B2B3} = 53\ cm^{-1}$ between the bands B2 and B3. The $k = 5$ exciton state is visible as a shoulder at shorter wavelength within the B3 band.*

For the linewidth of the higher exciton states, $k > 1$, in the simulation both the fast relaxation between these states on the 100 fs time scale [27, 90] and the mean linewidth determined for the broad bands in the single-complex experiments (section 4.1) was considered. As a result, in the simulated single-complex spectra the higher exciton states, $k > 1$, were dressed with broad Lorentzian lines with a width of 190 cm^{-1} ($fwhm$). Accordingly, since the fluorescence lifetime of the $k = 1$ exciton state was found to be in the range of several hundred ps [56, 89] and again also taking the measurement results of section 4.1 into account, the $k = 1$ state was dressed with a narrow line ($fwhm = 5\ cm^{-1}$) in the simulated single-complex spectra. The oscillator strength of a given exciton state is represented by the area under the corresponding Lorentzian line.
The two spectra shown in Figure 5.4c simulate two specific polarizations of the excitation light, once the polarization is parallel to the $k = 2$ exciton transition-dipole moment (red spectrum) and once parallel to the $k = 3$ transition-dipole moment (blue spectrum). In such a representation the two simulated spectra are compatible with the red and blue spectra from the experiment, used there for the determination of the energy splittings ΔE_{B1B2} and ΔE_{B2B3} (section 4.1). Yet in the simulations, since the lowest exciton state is dressed with a narrow line, its spectral position is unbiased by the broad bands of the higher exciton states and therefore the energetic position of the B1 band was determined directly from the transition energy of the $k = 1$ exciton state. However, the broad bands B2 and B3 in the simulations cannot solely be assigned to the exciton states $k = 2$ and $k = 3$, respectively. On the one hand, if the mutual polarization of their corresponding transition-dipole moments deviates from 90°, they will contribute in part to the spectrum of the other band. On the other hand, higher exciton states ($k > 3$) may also contribute to the bands B2 and B3. This becomes apparent in the blue spectrum of Figure 5.4c, where the $k = 5$ state appears as a pronounced shoulder in the high-energy wing of the B3 band. Thus, the spectral positions of B2 and B3 had to be determined from the simulated single-complex spectra, as maxima of the red and blue spectrum, respectively (Figure 5.4c). With these presettings the energetic separations in Figure 5.4c were determined to $\Delta E_{B1B2} = 83\ cm^{-1}$ between the bands B1 and B2 and to $\Delta E_{B2B3} = 53\ cm^{-1}$ between the bands B2 and B3.
The mutual phase angles between the bands B1 and B2 (B2 and B3) in the simulated spectra, were deduced from the mutual orientations of the transition-dipole moments of the exciton states predominantly contributing to the intensity of these bands. Thus $\Delta\alpha_{B1B2}$ in the experiment corresponds to the mutual angle $\Delta\alpha_{k1k2}$, between the $k = 1$ and $k = 2$ exciton transition-dipole moments in Structure 1, and $\Delta\alpha_{B2B3}$ corresponds to $\Delta\alpha_{k2k3}$, denoting the mutual angle between the $k = 2$ and $k = 3$ transition-dipole moments. In the experimental spectra it might be that higher exciton states, $k > 3$, with a polarization deviating from that of the $k = 3$ state, additionally contribute to the B3 band. This however would become visible

by a curvature of the intensity profile of this band in the two dimensional representation of the experimental protocol. Yet, for the determination of the phase angle of the B3 band, only the intensity region energetically closest associated to the B2 band was taken into account. Thus, in the simulation it is reasonable to determine the polarization of the B3 band based only on the orientation of the $k = 3$ exciton transition-dipole moment. For Structure 1 the mutual angle between the $k = 1$ and $k = 2$ transition-dipole moments amounts to $\Delta\alpha_{k1k2} = 39°$ and the angle between the $k = 2$ and $k = 3$ transition-dipole moments to $\Delta\alpha_{k2k3} = 66°$.
Before going on with the presentation of the simulation results from the structures 1, 2 and 3, a general discrepancy between simulation and experiment, already visible in Figure 5.4, will be briefly discussed. Presumably, due to the excitation of the B1 band which has an estimated linewidth of 0.02 cm^{-1} [56, 89], with a multi-mode laser with a broad spectral bandwidth of ≈ 1 cm^{-1} and the fast spectral diffusion of B1, the fluorescence intensity of B1 in the experimental spectra is significantly lower than indicated by the corresponding oscillator strength of the $k = 1$ exciton state in the numerical simulations [91]. The rather simple simulation approach may additionally contribute to this deviation. Thus, since otherwise the $k = 1$ absorption would dominate the simulated single-complex spectra, they are shown on an interrupted y-axis scale, which is both adapted to the lower absorbances of the broad bands in the high-energy region of the spectrum and to the high absorbance of the narrow line on the low-energy end (Figure 5.4c).

Diagonal disorder

In order to compare the statistical data of the spectral characteristics of the bands B1, B2 and B3 in the single-complex fluorescence-excitation spectra, with the data from numerical simulations of the structures 1, 2 and 3, at first, a more realistic scenario for the numerical simulations needs to be created. Static disorder in the surrounding matrix of the LH complexes induces local variations in the protein environment of the pigment binding sites, thereby causing shifts of the pigment site energies [103, 108, 146]. To account for this phenomenon in the simulations, from now on, the pigment site energies, $E_{0,n}$, in the Hamiltonian (5.2), were taken randomly from a Gaussian distribution centered at E_0 with a width $\Delta = 100$ cm^{-1} $(fwhm)$. Since this variation of the site energies affects only the diagonal elements of the Hamiltonian, it is also referred to as diagonal disorder. The chosen width, $\Delta = 100$ cm^{-1}, of the Gaussian distribution, characterizing the degree of the diagonal disorder, is in good agreement with $\Delta \approx 125$ cm^{-1}, extracted from the width of the B800 ensemble absorption band of LH2 complexes from *Rps. acidophila* [11], where, due to the excitations localized on individual pigments, the variation of the pigment site energies can be directly monitored. Additionally, small values for the diagonal disorder in combination with large values for the nearest-neighbor interactions V_i and V_e, are corroborated by [147], where authors found the best accordance

between experimental results and simulations on LH1 complexes of the purple bacterial species *Rb. sphaeroides*, for values of the mean nearest-neighbor couplings of $V_i = 600\ cm^{-1}$ and $V_e = 370\ cm^{-1}$, respectively, combined with a comparatively small value of $\Delta \approx 71\ cm^{-1}$, for the diagonal disorder.

Comparison of the simulated spectral properties of the structures 1, 2 and 3 with the experimental data

In Figure 5.5 the spectral characteristics of the simulated absorption spectra from the structures 1, 2 and 3 are compared to the experimental data of the intact RC-LH1 complexes from *Rps. acidophila* stabilized in detergent micelles and embedded in a PVA matrix (section 4.1). The simulations in Figure 5.5 were run 1000 times for each structure, where in each run a particular set of site energies for the pigments in the respective aggregates was randomly generated with the above described Gaussian distribution. For each realization of the pigment site energies the values for the energy displacement, ΔE_{B1B2} (ΔE_{B2B3}), between the bands B1 and B2 (B2 and B3) and the mutual angle, $\Delta\alpha_{k1k2}$ ($\Delta\alpha_{k2k3}$), between the $k = 1$ and $k = 2$ ($k = 2$ and $k = 3$) transition-dipole moments were determined as described in Figure 5.4, and the resulting distributions for the three structure were compared with the experimental data (Figure 5.5b). The mean site energies, E_0, in the simulations, were set to $12,590\ cm^{-1} \hat{=} 794.3\ nm$ in Structure 1, $12,500\ cm^{-1} \hat{=} 800\ nm$ in Structure 2 and $12,680\ cm^{-1} \hat{=} 788.6\ nm$ in Structure 3. The criterion for the choice of E_0 was to achieve a satisfying overlap of the experimental distribution of the spectral positions of B1, with the distributions of the energetic positions of the lowest exciton state, $k = 1$, in the simulations (see Appendix, part B).
For the structures 1 and 3, with their fixed BChl *a* dimer units, the coupling constant, V_0, in equation (5.1) was chosen such that the desired value for the intradimer interaction, V_i, was achieved (section 5.2.1). Accordingly, the mean site energies, E_0, of the pigments in these two structures come as a result in order to satisfy the aforementioned agreement between the spectral positions of B1 in the experiment and $k = 1$ in the simulation. Therefore, the values for E_0 resembling those of isolated protein-bound BChl *a* molecules either in LH1 [41] or in LH2 complexes [11], are a corroboration for the increased inter-pigment couplings applied in the simulations of this thesis. Since fixed dimer units are not available in Structure 2, the parametrization was contrary in this case: Initially the site energy of the pigments was set to the reasonable value of $E_0 = 12,500\ cm^{-1}$ and in a successive step the coupling constant, V_0, was adapted such that the criterion of overlapping distributions for the B1 band in the experiment and the $k = 1$ exciton state energy in the simulation was satisfied.
Part (a) of Figure 5.5 shows the exciton manifold with the calculated oscillator strength for the 11 lowest exciton states and an example single-complex absorption spectrum for each of the structures 1, 2 and 3, respectively. In the exciton

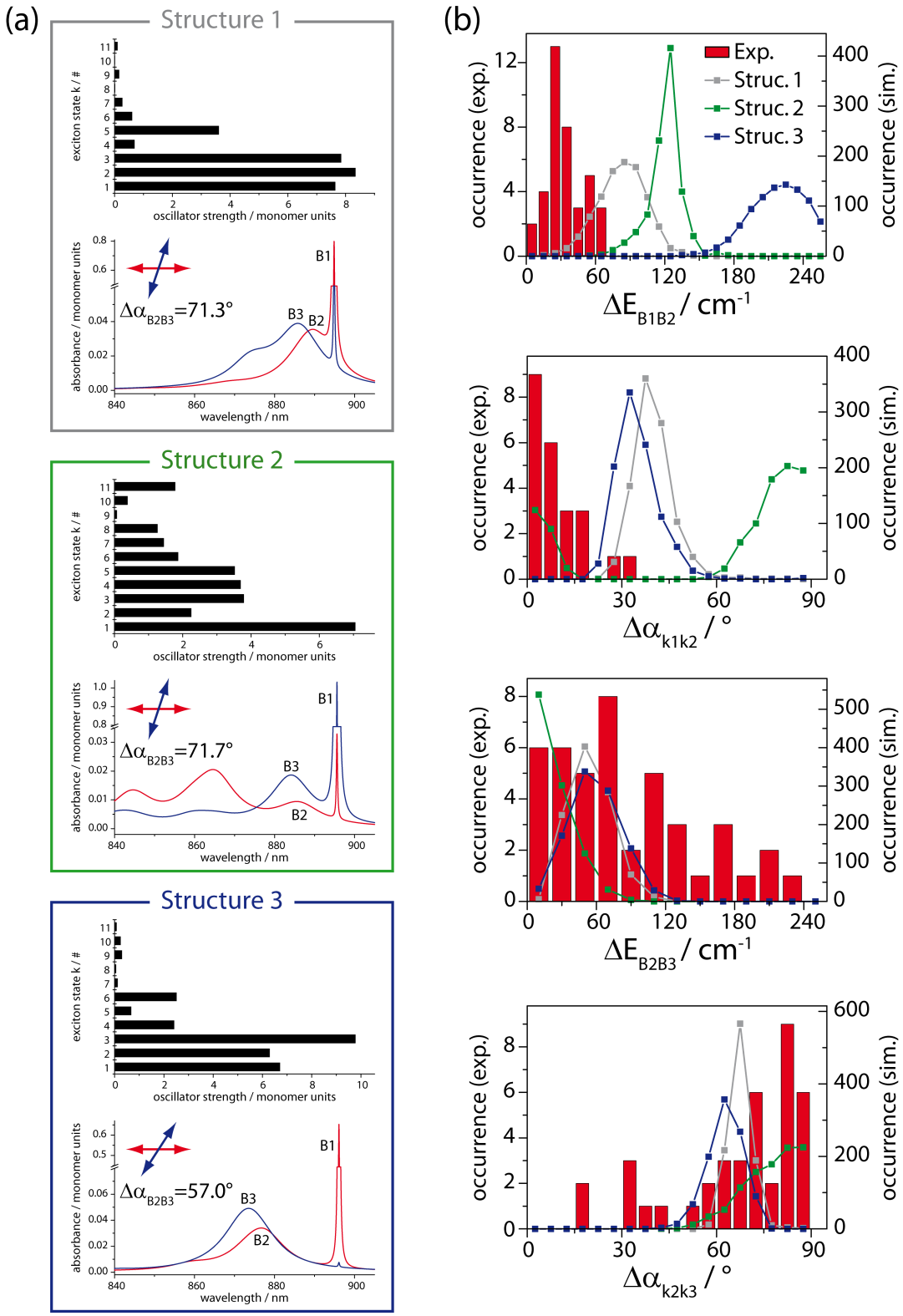

Figure 5.5: *Numerical simulations based upon the structures 1, 2 and 3, respectively. (a) Exciton manifold and example single-complex spectra. (b) Comparison with experimental data. For details see text.*

manifolds the oscillator strengths of the respective exciton states correspond to the mean values resulting from 1000 individual realizations of the pigment site energies, whereas the simulated single-complex spectra are depicted for one particular realization of the pigment site energies in each structure, respectively. Therefore, the information comprised in the depicted excitonic manifolds can be regarded as more general for the respective model aggregates, while the single-complex spectra are predominantly shown for illustrative reasons, and allow only a limited insight into the spectral characteristics of the given structures for one particular realization of the pigment site energies. The polarizations of the two spectra were chosen along the $k = 2$ (red spectrum) and $k = 3$ (blue spectrum) transition-dipole moments, respectively, as described in Figure 5.4 for Structure 1. For each structure the mutual polarization of the two example spectra is indicated by the red and blue arrows and specified as $\Delta\alpha_{B2B3}$. The spectral range for the representation of the simulated single-complex spectra ($840 - 905\ nm$) is compatible to the experimental range for the acquisition of single-complex fluorescence-excitation spectra from RC-LH1 complexes embedded in DDM/PVA ($836 - 899\ nm$).
With regard to the specific characteristics of the calculated exciton manifold and the resultant single-complex spectra of Structure 1 in Figure 5.5a, *top*, it can be seen that the introduction of diagonal disorder does not change the optical properties of this aggregate significantly, in comparison to the situation with constant site energy, E_0, for the pigments (Figure 5.4). This is a first hint that for Structure 1 the modulation of the interdimer interaction, V_e, dominates over the diagonal disorder, Δ, in determining the spectral characteristics of this model aggregate. In the middle panel of Figure 5.5a it can be seen that the irregular arrangement of the pigments in Structure 2 results in the higher exciton states, $k > 3$, gaining considerable oscillator strength. In the simulated single-complex spectra this is reflected by an increased number of bands in the high-energy spectral range. Since this clearly contradicts the experimental observation, this would already constitute a reason to discard Structure 2 as model aggregate for the LH1 complex of *Rps. acidophila*, no matter if the simulated spectral properties of the bands B1, B2 and B3 match the experimental ones, or not (see below). For Structure 3, comparable to Structure 1, again the lowest three exciton states, $k = 1, 2, 3$, receive the prominent part of the total oscillator strength (Figure 5.5a, *bottom*). However, the most striking feature of Structure 3 is the large energy displacement between the narrow line B1 and the following broad bands B2 and B3 in the depicted example spectra. This again represents a discrepancy with respect to the measurement results, making also Structure 3 an improbable candidate for a structural model of the LH1 complex from *Rps. acidophila*. Thus, considering the example spectra of all three model structures, it seems that only Structure 1 displays spectral properties compatible with the measured single-complex spectra, thereby representing the most promising model for the pigment arrangement in the LH1 complex of *Rps. acidophila*. Nevertheless, for the comparison of the spectral properties of the bands

B1, B2 and B3 with the corresponding experimental distributions, structures 2 and 3 were also taken into account for the sake of completeness, and in the end this provided valuable information in the process of finding a structural model which satisfactorily reproduced the experimental results (see following section 5.2.3).
Figure 5.5b shows the comparison of the spectral characteristics of the class A complexes embedded in a DDM/PVA matrix (red bars) with the results of the numerical simulations basing upon the structures 1, 2 and 3 (gray, green and blue squares, respectively). Overall the comparison reveals that, while the simulated distributions of the three structures are at least in partial agreement with the experimental distributions of the spectral properties of the bands B2 and B3, none of the three structures is able to mimic the spectral characteristics measured for the bands B1 and B2.
For the energy displacement between the bands B1 and B2, ΔE_{B1B2}, the simulated distributions have their peak positions at 85, 125 and 225 cm^{-1} for the structures 1, 2 and 3, respectively. All three distributions clearly deviate from the experimental histogram which covers much smaller energy values, with a peak at 25 cm^{-1}. For the mutual orientation between the $k = 1$ and $k = 2$ transition-dipole moments, $\Delta\alpha_{k1k2}$, the distributions of the structures 1 and 3 have their peak positions at 37.5 and 32.5°, respectively. Both distributions are shifted significantly from the experimental histogram which has its peak around 0°, with a steep decrease towards larger values. The distribution of $\Delta\alpha_{k1k2}$ for Structure 2 has a bimodal shape with peak positions around 0 and 88°, thus at least partially agreeing with the experimental data. The distributions for the energetic separation between the bands B2 and B3, ΔE_{B2B3}, for the structures 1 and 3 are very similar, both peaking at 50 cm^{-1} and displaying a width ($fwhm$) of about 60 cm^{-1}. With these properties they coincide only with the low-energy part of the experimental distribution which is spread over a much wider energy-range ($0 - 240$ cm^{-1}), and has its maximum at 70 cm^{-1}. The distribution of ΔE_{B2B3} for Structure 2 peaks at 10 cm^{-1} and decreases rapidly towards larger values, thereby also only partially agreeing with the experimentally determined data. The distributions for the mutual orientation of the $k = 2$ and $k = 3$ transition-dipole moments, $\Delta\alpha_{k2k3}$, for the structures 1 and 3 have their peak positions at 67.5 and 62.5°, respectively. Thereby, they display only a partial concordance with the experimental histogram which has some entries around 30°, followed by a steady increase of entries starting from 50° to a maximum around 90°. The distribution of $\Delta\alpha_{k2k3}$ for Structure 2 shows the same behavior as the latter part of the experimental histogram.

Interpretation of the simulated data for the structures 1, 2 and 3

In the distributions of the spectral characteristics of Structure 1 in Figure 5.5b it can be recognized that, owing to the inclusion of diagonal disorder in the simulation, the "ideal" values of $\Delta E_{B1B2} = 83$ cm^{-1}, $\Delta\alpha_{k1k2} = 39°$, $\Delta E_{B2B3} = 53$ cm^{-1} and

$\Delta\alpha_{k2k3} = 66°$, determined above with constant site energy, E_0, for the pigments, are now somewhat scattered over a wider range, meaning that, besides the modulation of the interdimer interaction, V_e, the distinct realization of the pigment site energies is an additional criterion affecting the specific localization patterns of the exciton states. Thus, for example, the $k = 1$ exciton state in Structure 1 will still localize on the long side of the ellipse (Figure 5.4a, *left*), where V_e is strongest, but only on those pigments in this localization area which have a lowered site energy with respect to their neighboring ones [104, 145]. In this way diagonal disorder influences both the energy of the $k = 1$ exciton state and its transition-dipole moment. Since this is also valid for the two higher exciton states $k = 2$ and $k = 3$, it is clear that such processes will lead to a spread of the calculated values for ΔE_{B1B2}, $\Delta\alpha_{k1k2}$, ΔE_{B2B3} and $\Delta\alpha_{k2k3}$, respectively. However, all four distributions of the aforementioned values for Structure 1 are still centered at the values calculated for the case without taking diagonal disorder into account (Figure 5.5b). This shows that, with the applied simulation parameters, the modulation of the interdimer interaction, V_e, still plays the decisive role for the determination of the specific localization areas of the exciton states in Structure 1 and not the diagonal disorder. As the distributions of the simulated spectral properties for Structure 3 resemble those of Structure 1, not necessarily with respect to their peak positions, but regarding their width and overall shape, a similar dependence for the localization of the exciton states in this structure is indicated.
In Figure 5.6 the exciton wavefunctions and the resulting transition-dipole moments of the three lowest states $k = 1, 2, 3$ are shown for the structures 2 and 3, respectively. Thereby, the two exciton localization patterns in Structure 2 are depicted for two different realizations of the pigment site energies, whereas diagonal disorder was not taken into account in the calculation of the exciton wavefunctions for Structure 3.
For Structure 2 it can be seen that depending on the specific realization of the pigment site energies, the $k = 2$ and $k = 3$ exciton wavefunctions interchange their localization areas on the aggregate. This phenomenon can be understood by recalling that the distribution of ΔE_{B2B3} for Structure 2 peaks at 10 cm^{-1} (Figure 5.5b), thereby indicating a negligible energy difference between the $k = 2$ and $k = 3$ exciton states of Structure 2. Consequently, diagonal disorder plays a decisive role for the localization of these two states in Structure 2. In the majority of cases, if the site energies of the pigments in the aggregate do not show significant deviations from the mean value E_0, the localization patterns of the exciton states $k = 1, 2, 3$ are similar to the left illustration, Δ_1, for Structure 2 in Figure 5.6: As the $k = 1$ exciton wavefunction, the $k = 2$ state localizes in the top right corner of the aggregate, where the nearest-neighbor interaction is strongest in Structure 2 (Figure 5.3), but with a node in the middle of its localization area. The $k = 3$ exciton wavefunction localizes in the bottom left corner of the aggregate, where the nearest-neighbor interaction in Structure 2 has its second maximum. However, if by

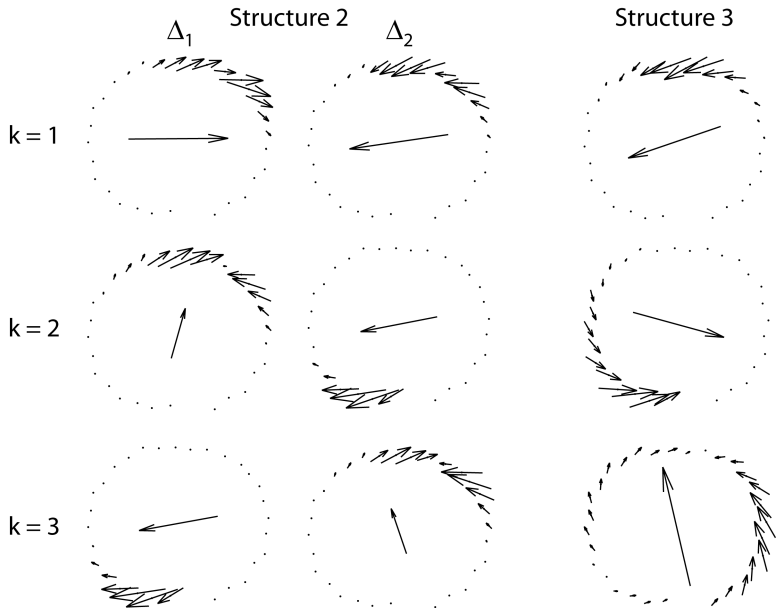

Figure 5.6: *Pictorial representation of the exciton wavefunctions and the resulting transition-dipole moments of the three lowest exciton states $k = 1, 2, 3$ (top down) for the structures 2 and 3, respectively. The display is analogous to Figure 5.4a. The two differing localization patterns for Structure 2 correspond to two individual realizations of the pigment site energies Δ_1 and Δ_2, respectively. The Structure 3 exciton wavefunctions were calculated without the inclusion of diagonal disorder. See text for details.*

chance the pigments in the bottom left corner of the structure exhibit significantly lowered site energies, this will also lower the eigenenergy of the exciton state in this localization area and, recalling the marginal energy difference between the $k = 2$ and $k = 3$ exciton states in Structure 2, this will ultimately result in a smaller eigenenergy for the exciton state in the bottom left localization area, in comparison to the energy of the exciton state localizing in the top right corner of the aggregate with a node in the middle of its wavefunction. As a result, the $k = 2$ exciton state will now be attributed to the wavefunction in the bottom left corner of Structure 2 and the $k = 3$ state is assigned to the wavefunction in the top right corner of the aggregate (Figure 5.6, Structure 2, Δ_2). For the resulting exciton transition-dipole moments this means that, due to the permanent localization of the $k = 1$ exciton state in the top left corner of Structure 2, the $k = 1$ and $k = 2$ transition moments will be mostly parallel to each other, if the $k = 2$ state localizes in the bottom left corner of the aggregate (Figure 5.6, Structure 2, Δ_2) and mostly perpendicular to each other for the alternative localization pattern (Figure 5.6, Structure 2, Δ_1). Thus, the interchanging localization areas of the $k = 2$ and $k = 3$ exciton wavefunctions in Structure 2 serve both as explanation for the bimodal distribution of $\Delta\alpha_{k1k2}$, and for the comparatively broad distribution of $\Delta\alpha_{k2k3}$ for Structure 2 in

Figure 5.5b.
On the right-hand side of Figure 5.6, the exciton wavefunctions of the states $k = 1, 2, 3$ of Structure 3 are depicted. Thereby, in the calculation of the excitonic wavefunctions diagonal disorder was not taken into account, since, as already discussed above, the influence of diagonal disorder on the localization of the exciton states in Structure 3 is limited. For the $k = 1$ exciton wavefunction in Structure 3 it can be seen that it localizes predominantly in the top part of the aggregate, where the dimer units are arranged on a straight line, thereby inducing a maximum of the interdimer interaction, V_e, in this region of the aggregate (Figure 5.3). The exceptionally large values for V_e in the area of the $k = 1$ localization for Structure 3 also explain the comparatively large energy gap between the B1 band and the bands B2 and B3 in Structure 3 (Figure 5.5). The $k = 2$ exciton wavefunction in Structure 3 localizes in the lower left corner of the aggregate, where the interdimer interaction, V_e, has a second maximum for Structure 3 (Figure 5.3). Finally, the $k = 3$ exciton wavefunction has a large amplitude on the right part of the aggregate and a smaller amplitude on the pigments in the left part of the aggregate. Due to the buildup of Structure 3 the amplitudes interfere constructively, such that the resulting $k = 3$ transition-dipole moment is larger than the $k = 1$ and $k = 2$ transition-dipole moments, which is also reflected in the higher oscillator strength of the $k = 3$ exciton state in comparison to the two lower exciton states of Structure 3 (Figure 5.5, Structure 3).
To sum up, the results of this section have demonstrated that none of the initial structures 1, 2 and 3 is able to reproduce the data acquired on the intact RC-LH1 complexes from *Rps. acidophila* stabilized in a DDM/PVA matrix. While for Structure 1 the simulated single-complex absorption spectrum still showed some resemblance with the measurement data, this impression could not be maintained for the simulated distributions of the spectral properties of the bands B1, B2 and B3. The very reverse case was found for Structure 2: While the simulated single-complex spectrum was clearly deviating from the experimental spectra, two of the simulated distributions of the spectral properties ($\Delta\alpha_{k1k2}$ and $\Delta\alpha_{k2k3}$) coincided at least in part with the experimental data. Finally, for Structure 3 neither in the simulated single-complex spectrum, nor in the simulations of the spectral characteristics of the bands B1, B2 and B3, an accordance with the experimental results could be identified.

5.2.3 Designing a LH1 model structure that reproduces the experimental results

In this section it will be described how the arrangement of the pigments in a given LH1 model structure can be modified in such a way that numerical simulations, based upon this new structure, will then satisfactorily reproduce the experimental

distributions of the spectral characteristics of the bands B1, B2 and B3. As initial LH1 model, for the modifications to be applied on, Structure 3 was chosen. The reason for this was on the one hand that Structure 3 is more closely related to the LH1 aggregate gained from the crystal structure of the RC-LH1 complex from *Rps. palustris* [24] (Structure 2) than Structure 1 (see section 5.2.1). On the other hand, consisting of stable dimer units, Structure 3 conforms to the basic construction principle proposed for LH1 complexes in [20] which is definitely not the case for Structure 2. Furthermore, to remain consistent with the LH1 building principle, structural modifications on the initial LH1 model were restricted to the realignment of dimer units as a whole, keeping the mutual distance and orientation of the pigments inside a dimer unit unchanged.

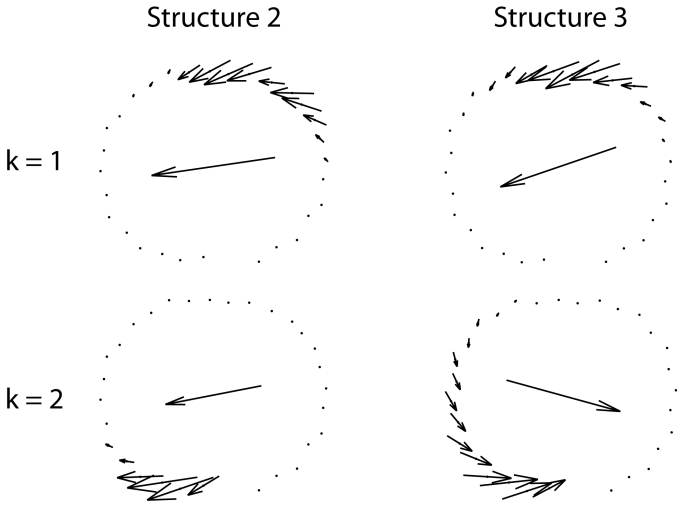

Figure 5.7: *Pictorial representation of the exciton wavefunctions and the resulting transition-dipole moments of the exciton states $k = 1$ and $k = 2$ (top down) of the structures 2 and 3, respectively. The depicted wavefunctions are those from Figure 5.6, where for Structure 2 the wavefunctions to the right in Figure 5.6 are shown (Δ_2).*

Thinking about ways how Structure 3 could be modified to match the experimental histograms, the exciton localization patterns depicted on the right-hand side for Structure 2 in Figure 5.6 were particularly interesting, since there the desired parallel orientation of the $k = 1$ and $k = 2$ transition-dipole moments can be observed that has also been found in the experimental single-complex spectra. For clarity, the relevant wavefunctions of the exciton states $k = 1$ and $k = 2$ of the structures 2 and 3 from Figure 5.6 are redrawn in Figure 5.7. It can be seen that for Structure 3 the localization area of the $k = 2$ exciton state, though more delocalized, is quite similar to the localization of the $k = 2$ state in Structure 2. Thus, taking the localization pattern of the $k = 1$ exciton state in Structure 2 as an example, one possibility to achieve parallel transition-dipole moments for the $k = 1$ and $k = 2$

exciton states in a modified Structure 3 aggregate, would be to rearrange the dimer units in the top right corner of Structure 3 in such a way that the localization area of the $k = 1$ state expands around this corner in the new structure. It is obvious from Figure 5.7 that the resulting $k = 1$ transition-dipole moment of such a localization pattern would then be more or less parallel with respect to the $k = 2$ transition-dipole moment. Practically, the new localization of the $k = 1$ exciton state can be accomplished by a rearrangement of the dimer units located on the top long axis of Structure 3, such that the interdimer interaction, V_e, decreases in this region, and a concomitant modification of the dimer units in the top right corner, such that V_e increases here. A further positive effect entailed by the lowering of the exceptionally high interdimer interactions, V_e, along the long axis of Structure 3 (Figure 5.3c) would be the resultant increase of the eigenenergy of the $k = 1$ exciton state, thus reducing the large energy splitting observed before between the $k = 1$ and $k = 2$ exciton states in Structure 3 (Figure 5.5). From a physiological point of view the outlined structural modifications could be justified by specific interactions between the RC and the LH1 complex, as already denoted in the motivation (section 5.1) for the LH1 complex from the *Rps. palustris* x-ray structure (Structure 2). Additionally, by adopting the specific exciton localization patterns from Structure 2 for the pigment rearrangements to be performed in Structure 3, it is sought to extract that information from the excitonic properties of Structure 2 that might be physiologically relevant.

Modification of Structure 3 - Structure 3'

In Figure 5.8 the modified Structure 3, denoted as Structure 3' from now on, is depicted together with a diagram of the corresponding nearest-neighbor interactions between the BChl *a* Q_y transition-dipole moments. In total, the arrangement of four dimer units in Structure 3' has been changed with respect to Structure 3 (Figure 5.8a, *top*). The two dimer units comprising the pigments 7, 8 and 13, 14, respectively, both remained at their original positions and were each rotated by 2° with respect to the local tangents of these dimer units, once away from the tangent (pigments 7, 8) and once towards the tangent (pigments 13, 14). The protomer units containing the pigments 9, 10 and 11, 12, respectively, were each shifted by 2 $\AA$ along the circumference of the rounded rectangle, where subsequently the alignment of the two dimer units in their new positions followed the protocol described earlier for the structures 1 and 3. Since the dimer units were rearranged as a whole and as the coupling constant for the dipole-dipole interaction, V_0, in equation (5.1), was adopted from Structure 3, the intradimer interaction, $V_i = 803\ cm^{-1}$, in Structure 3' remained equivalent as in the structures 1 and 3 (Figure 5.8b). The effects of the performed rearrangements in Structure 3' become apparent by comparison of the interdimer interaction values, V_e, for the structures 3 and 3', respectively. Here the coupling strengths with changed values with respect to Structure 3 are marked

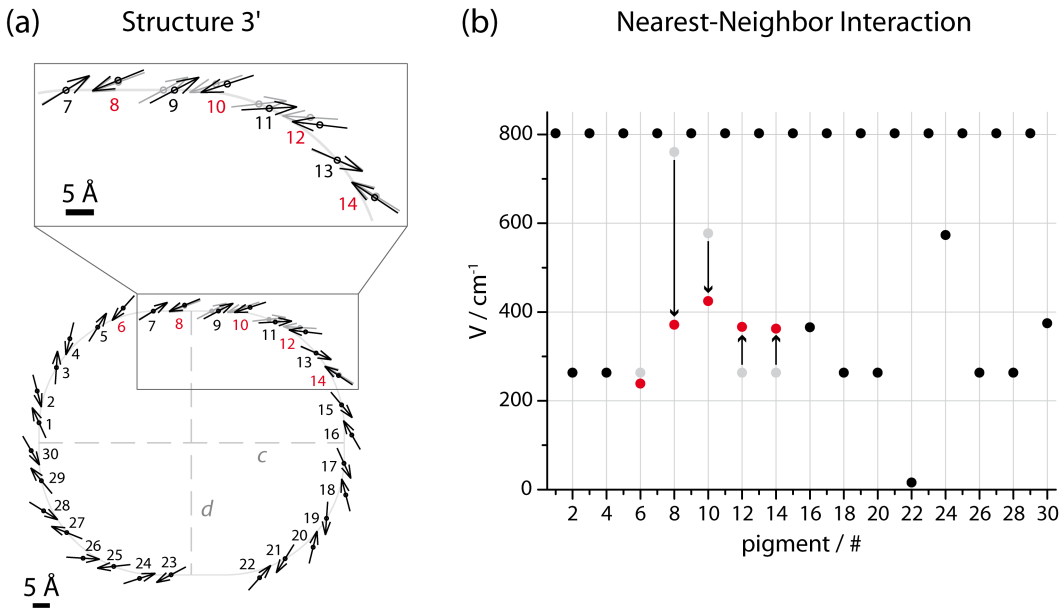

Figure 5.8: *Arrangement of the BChl a pigments and nearest-neighbor interactions, $V_{n,n+1}$, in Structure 3'. The representation is equivalent to Figure 5.2. (a) Top, extended scale: Four dimer units which are positioned differently in Structure 3' with respect to Structure 3 (see text for details). The orientation of the respective dimer units in Structure 3 is depicted in light gray for comparison. Bottom: Complete Structure 3', with c and d indicating the long and short half-axis of the basis rectangle adopted from Structure 3. The red figures indicate those pigments in Structure 3' for which the interdimer interaction, V_e, has changed with respect to Structure 3. (b) Nearest-neighbor interactions in Structure 3', with constant intradimer interaction, $V_i = 803\ cm^{-1}$, and varying interdimer interaction, V_e. The interdimer interactions with changed values in Structure 3' in comparison to Structure 3 are marked in red, while the respective values for Structure 3 are again shown in light gray. The arrows denote the change of the interaction strength when replacing Structure 3 by Structure 3'.*

in red in Figure 5.8b and the corresponding values of Structure 3 are shown in light gray. The changes of the interaction strength in Structure 3' as compared to Structure 3 can be understood easily from the above-described structural modifications and the equation (5.1) for the dipole-dipole couplings: Naturally, the coupling strength V_e between the pigments 8 and 9 (12 and 13) decreases (increases) as the distance between them increases (decreases). The orientation parameter κ_{nm} is responsible for the remaining changes of V_e, leading to an increase of V_e if, after their reorientation, the interacting dipoles are more parallel with respect to their connection-vector (pigments 12, 13 and 14, 15) and to a decrease if the respective pigments are rotated away from a beforehand more parallel orientation with respect to their connection-vector (pigments 6, 7; 8, 9 and 10, 11).
Overall, the performed modifications in Structure 3' have entailed the desired

change of the modulation of the interdimer interaction, V_e, in Structure 3, namely the formerly punctually high interaction values found on the long axis of Structure 3, are now compensated by a set of increased interaction values around the top right corner of Structure 3'. The mean value for the interdimer interaction, V_e, in Structure 3' is 333 cm^{-1} which is slightly smaller than the corresponding value in Structure 3 ($V_e = 359\ cm^{-1}$), where in both cases the interactions across the gap were omitted for comparability reasons. For the second-neighbor interaction, W, a mean value of $-86\ cm^{-1}$ was calculated for Structure 3' which is almost identical to the value in Structure 3 ($W = -85\ cm^{-1}$) and again the coupling strengths across the gap were not considered in the calculations of the mean values.

Numerical simulations based on Structure 3'

Figure 5.9 shows the numerically calculated exciton manifold of Structure 3' together with the resulting single-complex absorption spectrum. Furthermore, Figure 5.9 shows a comparison of the simulated with the experimental distributions of the spectral properties from the bands B1-B3 for Structure 3' and the intact RC-LH1 complexes from *Rps. acidophila*.
Part (a) of Figure 5.9 shows a pictorial representation of the exciton wavefunctions of the lowest three exciton states $k = 1, 2, 3$ in Structure 3'. Diagonal disorder was not considered in the calculation, since also in Structure 3' the modulation of the interdimer interaction, V_e, dominates over the influence of energetic disorder, in the determination of the localization sites for the three lowest exciton states. Regarding the wavefunction distribution of the $k = 1$ exciton state it can be seen that the accomplished rearrangements of the four dimer units in Structure 3' have lead exactly to the desired delocalization of the $k = 1$ wavefunction around the top right corner of Structure 3'. Since the localization area of the $k = 2$ wavefunction in Structure 3' basically remains unchanged with respect to Structure 3, the resulting transition-dipole moments of the $k = 1$ and $k = 2$ exciton states in Structure 3' are now more or less parallel to each other. For the $k = 3$ exciton state it can be observed that the specific amplitude distribution of the wavefunction of this state, together with the alignment of the pigments in Structure 3', result in a comparatively large $k = 3$ transition-dipole moment for Structure 3'. This feature is also reflected in the diagram for the mean oscillator strength of the eleven lowest exciton states, $k = 1 - 11$, in Structure 3', resulting from the average over 1000 individual realizations of the pigment site energies (diagonal disorder, $\Delta = 100\ cm^{-1}$), where the mean oscillator strength of the $k = 3$ state significantly sticks out (Figure 5.9b, *top*). Furthermore, the diagram of the excitonic manifold shows that the essential part of the total oscillator strength of Structure 3' is accumulated in the three lowest exciton states $k = 1, 2, 3$.
In Figure 5.9b, *bottom* two absorption spectra of Structure 3' are depicted which were calculated for one particular realization of the pigment site energies. Each

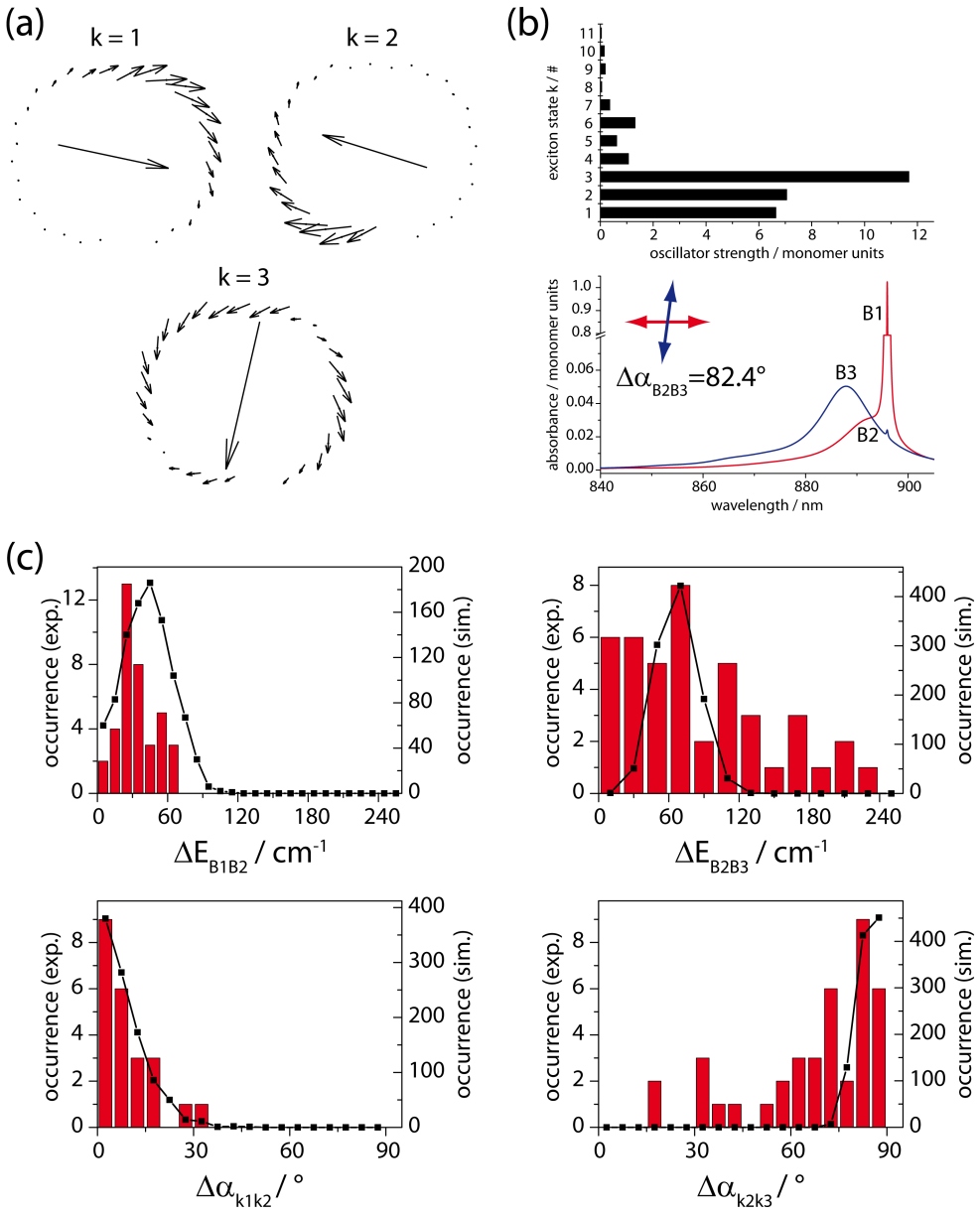

Figure 5.9: *Numerically calculated spectral characteristics of Structure 3' and comparison with the corresponding experimental data of the intact RC-LH1 complexes from Rps. acidophila. (a) Pictorial representation of the excitonic wavefunctions and transition-dipole moments for the lowest three exciton states $k = 1, 2, 3$ in Structure 3', calculated without diagonal disorder. (b) Mean oscillator strength of the exciton states $k = 1 - 11$ determined from the average of 1000 individual realizations of the pigment site energies (top) and example single-complex spectra, calculated for one particular realization of the pigment site energies (bottom). The red and blue arrows indicate the mutual polarization of the respective spectra. The representation in (a) and (b) is adopted from the Figures 5.4 and 5.5. (c) Comparison of the simulated distributions of the spectral properties of the bands B1-B3 for 1000 individual realizations of the pigment site energies in Structure 3' (black squares) with the corresponding experimental data from the intact RC-LH1 complexes of Rps. acidophila (red bars).*

spectrum simulates one particular polarization of the excitation light. Thereby, the red spectrum corresponds to an excitation polarization parallel to the $k = 2$ transition-dipole moment and the blue spectrum to a polarization parallel to the $k = 3$ transition-dipole moment. For the distinct realization of the pigment site energies in Structure 3' for which the two absorption spectra were calculated, the mutual angle between the $k = 2$ and $k = 3$ transition-dipole moments amounted to $\Delta\alpha_{B2B3} = 82.4°$. The value for the mean site energy in Structure 3' was set to $E_0 = 12,510\ cm^{-1} \hat{=} 799.4\ nm$, again obeying the criterion that the simulated distribution of the $k = 1$ exciton energies has to coincide with the experimental distribution of the spectral peak positions of the B1 band (see Appendix, part B). Thus, similar to the other three structures, the comparatively large value for the coupling parameter, V_0, and the alignment of the pigments in Structure 3', together with the aforementioned criterion for the $k = 1$ exciton state energy, result in a reasonable value for the mean site energy, E_0, of the pigments in Structure 3', in the range of the uncoupled B800 BChl *a* molecules in LH2. From the simulated red spectrum of Structure 3' (Figure 5.9b) it already becomes clear that the energetic separation between the bands B1 and B2 now bears much more resemblance with the experimental spectra than it was the case for Structure 3.
Figure 5.9c displays the comparison of the distributions from the simulated spectral characteristics of the bands B1-B3 (black squares) with the experimental distributions of the corresponding data from the intact RC-LH1 complexes stabilized in a DDM/PVA environment (red bars). Thereby, the spectral properties were calculated for 1000 individual realizations of the pigment site energies in Structure 3', chosen randomly from a Gaussian distribution centered at E_0, and with a width $\Delta = 100\ cm^{-1}$ $(fwhm)$. As already described above, the mutual polarizations between the bands B1 and B2 (B2 and B3) in the simulations, were chosen equivalent to the mutual orientations of the $k = 1$ and $k = 2$ ($k = 2$ and $k = 3$) exciton state transition-dipole moments, respectively.
For the distributions of the simulated spectral properties for the bands B1 and B2 (exciton states $k = 1$ and $k = 2$) of Structure 3', now a good accordance with the experimental distributions can be observed. This proves on the one hand that, by the performed rearrangements on Structure 3, the $k = 1$ and $k = 2$ transition-dipole moments have been parallelized in Structure 3'. On the other hand, due to the lowering of the average interdimer interaction, V_e, in the localization area of the $k = 1$ exciton state in Structure 3' (Figure 5.8), the eigenenergy of the $k = 1$ state (B1) has increased that much, that the simulated energetic separations with respect to the B2 band (predominantly $k = 2$), are now in good agreement with the experimental data.
In the comparison of the distributions for the energetic splittings between the bands B2 and B3, ΔE_{B2B3}, for the experimental spectra and the simulation, a coincidence of the two maxima at 70 cm^{-1} can be discerned. However, the experimental histogram is distributed over a much wider range of energy-values for, ΔE_{B2B3}, than

the corresponding distribution resulting from the numerical simulations. This might be related to minor structural distortions of dimer units in the localization area of the $k = 3$ wavefunction for the experimental samples, which were not accounted for in the simulations. The same effect could partly be responsible for the deviation between the distribution resulting from the numerical simulations for the mutual orientation of the $k = 2$ and $k = 3$ exciton transition-dipole moments, $\Delta\alpha_{k2k3}$, and the respective data of the bands B2 and B3 determined in the single-complex fluorescence-excitation experiments. Here, the simulation produces a distribution peaking at about 90° with a steep decrease for smaller angles, $\Delta\alpha_{k2k3}$, whereas the experimental histogram shows a distinctly larger spread, starting with first entries for $\Delta\alpha_{B2B3}$ just above 15° and an increasing number of entries for larger values of $\Delta\alpha_{B2B3}$, until at 82.5° the maximum of the experimental distribution is reached. A further phenomenon, certainly contributing to the discrepancy between the distributions of $\Delta\alpha_{k2k3}$ ($\Delta\alpha_{B2B3}$) for simulation and experiment, respectively, is the non-planar alignment of the RC-LH1 complexes on the substrate, for which clear evidence has been found in the single-complex experiments, but which was not taken into account in the simulations. Namely in the experiment, the apparent angle between two transition-dipole moments actually corresponds to the angle between the projections of these transition-dipole moments on the substrate plane. Thus, *e.g.* two mutually orthogonal transition-dipole moments would only appear as such, for a complex lying flat on the substrate, but, with increasing out-of-plane tilt of the complex, the apparent angle between the transition-dipole moments will decrease, in this way possibly explaining the smaller values in the experimental distribution of $\Delta\alpha_{k2k3}$ ($\Delta\alpha_{B2B3}$), as compared to the distribution resulting from the numerical simulations.

After having shown that Structure 3' can reasonably reproduce the measurement data, in Figure 5.10 the arrangement of the pigments in Structure 3' is compared to the arrangement of the LH1 pigments in the x-ray structure of the RC-LH1 complex from *Rps. palustris* [24]. The two vectors depicted in the center of the LH1 structures indicate the Q_y transition-dipole moments of the RC special pair BChl *a* molecules, where their position and orientation with respect to the *palustris* LH1 complex was adopted from the PDB, file: 1PYH. The two LH1 aggregates in Figure 5.10 show a remarkable agreement in the arrangement of their pigments, naturally within the 4.8 $\AA$ resolution of the crystal structure and, furthermore, the agreement is much more pronounced than between the refined *palustris* structure and the x-ray structure shown in Figure 5.1.

The coordinates of the central Mg^{2+} ions of the BChl *a* molecules and the unit vectors, $\hat{n}$, of their corresponding Q_y transition-dipole moments in Structure 3' are again listed in the Appendix, part A.

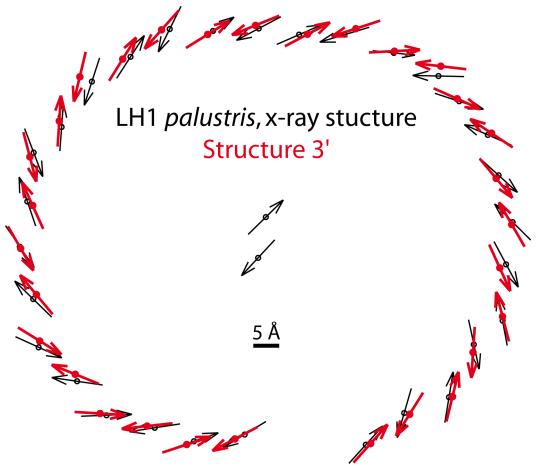

Figure 5.10: *Comparison of the arrangement of the BChl a molecules in the crystal structure of the RC-LH1 complex from Rps. palustris ([24], PDB file: 1PYH; black arrows) with the BChl a arrangement in Structure 3' (red arrows). The small circles indicate the positions of the central Mg^{2+} ions in the BChl a molecules and the small vector arrows indicate the orientation of the BChl a Q_y transition-dipole moments. The two vectors in the middle of the LH1 aggregates indicate the position and orientation of the special pair Q_y transition-dipole moments in the RC, as deposited in the PDB for the palustris RC-LH1 complex. The scale bar shows approximately the resolution of the x-ray structure of* 4.8 *Å.*

5.3 Conclusion

From the numerical simulations performed in this chapter, first of all, it can be learned that using significantly increased values for the nearest-neighbor couplings between the pigments, in comparison to previous simulations on LH1 *palustris* [15], results in very plausible values for the pigment site energies, E_0, for all proposed LH1 models in this work. Vice versa, this can be interpreted as a confirmation for the magnitude of the interaction strength applied here, which then should also be a good mimicry of the natural situation. However, it was also found that, due to the change to more realistic simulation parameters with respect to the simulations in [15] (site energy, coupling strength, inclusion of second-neighbor interactions and dimeric building principle), both the structures with an equidistant placement of fixed dimer aggregates onto basic geometric structures (structures 1 and 3) and Structure 2, with the placement of the BChl *a* molecules equivalent to the x-ray structure of the RC-LH1 complex from *Rps. palustris* [24], fail to reproduce the experimental data. Thereby, the LH1 models with a regular positioning of BChl *a* dimer units on an ellipse and a rectangle with rounded corners, structures 1 and 3, respectively, are superior to Structure 2, in reproducing at least the general features of the single-complex spectra, namely a restricted number of spectral bands (only the lowest exciton states gain considerable oscillator strength), whereas the

irregular arrangement of the pigments in Structure 2, results in a large number of broad bands in the high-energy region of the detected spectral range (distribution of the total oscillator strength over many exciton states), clearly deviating from the experimental observations. This leads to the conclusion that the pigment arrangement in the LH1 complex of *Rps. acidophila* must also be rather regular, thereby accumulating the main part of the total oscillator strength in the lowest exciton states of the aggregate.
In the search for a structure able to reproduce the experimental distributions of the spectral characteristics of the intact RC-LH1 complexes from *Rps. acidophila*, the excitonic wavefunctions calculated for the various structures were analyzed in more detail, thereby recognizing that the two lowest exciton states $k = 1$ and $k = 2$ each localize in characteristic areas of the LH1 aggregates, with significantly increased values for the nearest-neighbor interactions between the pigments. Taking advantage of this knowledge, it was possible to modify a regular LH1 model based on a rectangle with rounded corners (Structure 3), thereby still obeying the dimeric LH1 building principle [20] by readjusting only complete dimer units, in such a way that the spectral characteristics of the resulting LH1 aggregate (Structure 3') showed a satisfying agreement with the data of the single-complex measurements on the intact RC-LH1 complexes from *Rps. acidophila*. At this, it should be noted that the minimal structural changes performed on Structure 3' with respect to Structure 3 (Figure 5.8), have a huge impact on the resultant spectral properties. The localization patterns of the lowest exciton states in Structure 3' were motivated by the localization patterns in Structure 2 which corresponds to the RC-LH1 *palustris* crystal structure. Thus, with the modifications in Structure 3' it was sought to approach the native structure of a LH1 complex, with the described structural rearrangements possibly induced by specific interactions of the LH1 complex with the RC. However, comparing the orientation of the $k = 1$ transition-dipole moment in Structure 3' (Figure 5.9a) with the orientation of the special pair Q_y transition-dipole moments (Figure 5.10), it can be seen that the mutual angle between them is not optimal for an effective energy transfer from the LH1 complex to the RC. Here a parallel orientation of the interacting dipoles would be ideal. However, given the remaining structural uncertainties (see below), at this point it would be too early to start a detailed discussion about possible implications of the specific localization areas of the exciton states.
Since the spectroscopic data acquired on individual RC-LH1 complexes from *Rps. palustris* are very similar to the *acidophila* data (see section 4.1), Structure 3' could very well also serve as a structural model for the LH1 complex from *Rps. palustris*, in particular taking the superiority of this model in comparison to the refined LH1 *palustris* model in [15] into account, on the one hand with respect to the simulation parameters and on the other hand with respect to the better structural overlap with the *palustris* x-ray structure (Figure 5.1 *vs.* Figure 5.10).
However, it is also clear that, by means of the method described in the previous

section 5.2.3, various LH1 model structures can be built within the resolution limit of the LH1 *palustris* x-ray structure which will as well reproduce the spectral properties of the intact RC-LH1 complexes from *Rps. acidophila*. This makes Structure 3' rather questionable as unique structural model for the LH1 complex of *Rps. acidophila*. Still, the modifications in Structure 3' were restricted on the one hand, by readjusting only complete dimer units and on the other hand, by adopting the exciton localization patterns from Structure 2, thereby seeking to create a LH1 model closely associated to the native situation. Nevertheless, it remains highly uncertain if the very specific pigment rearrangements performed on Structure 3 to achieve Structure 3' can be taken for granted. Additionally, an alternative, more comprehensive interpretation of the spectral properties observed in the single-complex fluorescence-excitation spectra might be possible. Therein, the effect of the specific overlap between the excitonic wavefunctions for the exciton relaxation dynamics, and accordingly, for the observed linewidths is considered. This new interpretation however, favors Structure 1 over Structure 3' as structural model for the *Rps. acidophila* LH1 complex (see chapter 6), thereby further weakening the status of Structure 3' as exclusive solution for the LH1 complex from *Rps. acidophila*. Finally, in the recently discovered high-resolution crystal structure of the RC-LH1 complex from *T. tepidum* [9] the BChl *a* dimer units seem to be evenly distributed on an ellipse. Increased interactions between the RC and the LH1 complex which might lead to a deterioration of the LH1 pigment arrangement were only observed on the short sides of the ellipse for this structure. This again speaks against the rearrangements performed in Structure 3', where however, it also has to be kept in mind that (in contrast to Structure 3') the LH1 complex from *T. tepidum* has a completely closed LH1 ring. Thus, the alignment of the pigments in a LH1 complex comprising a gap might differ.
In summary, also given the limitations of the quite simple simulation approach (Hamiltonian in Heitler-London approximation and dipole-dipole interactions between the pigments), it is not claimed that in Structure 3' the one and only structural model for the LH1 complex from *Rps. acidophila* has been found, but certainly Structure 3' presents a LH1 model aggregate that can clearly compete with, if not outperform the refined *palustris* LH1 model described in [15]. However, the more important result of this chapter is that, in excitonic systems dominated by the modulation of the nearest-neighbor interaction rather than by diagonal disorder, the localization areas of the lowest exciton states in the aggregate coincide with the maxima of the nearest-neighbor interaction. This information could be of general interest and might be useful, *e.g.* when considering the influence of the structural buildup of any LH1 complex on the energy transfer to the RC.

6 Outlook - alternative interpretation of the single-complex spectra?!

In a recent study Kunz et al. recorded low-temperature fluorescence-excitation and emission spectra of the same individual LH2 complexes from *Rps. acidophila* and thereby, were able to identify the lowest exciton state of the strongly coupled B850 pigment assembly [148]. In the excitation spectra this state appeared as a broad band on the low-energy end of the detected spectral region, displaying a significantly reduced fluorescence intensity in comparison to the neighboring bands in the spectra which were shifted to higher energies and were therefore attributed to the higher exciton states of the B850 aggregate. The criterion for an unambiguous identification of the lowest exciton state was a fluorescence-emission spectrum emerging directly from the spectral region, where the lowest exciton state was detected in the corresponding fluorescence-excitation spectrum, for an individual LH2 complex (see also [115], Figure 1a therein). After a careful reinspection of the measurement data of the class A RC-LH1 complexes from *Rps. acidophila*, also in these spectra a broad, low-intensity band (B0), red-shifted with respect to the B1 band was discovered. In terms of its spectral characteristics the B0 band is quite similar to the lowest exciton state found for the LH2 complexes in [148]. Due to its strongly reduced fluorescence intensity with respect to the accompanying high-energy bands, the significance of B0 was neglected so far. However, given the results presented in [148], this view might be reconsidered.

Altogether, a band B0 could be discerned for 28 out of the 38 class A RC-LH1 complexes displaying a narrow line B1 in a DDM/PVA environment and for 42 out of the 49 class A complexes embedded in a lipid bilayer. For the remaining complexes in each environment the spectra were red-shifted to such an extent that a potential band B0 would be hidden in the detection window of the band-pass filters. In Figure 6.1 single-complex fluorescence-excitation spectra are shown for class A RC-LH1 complexes in each of the two stabilizing environments DDM/PVA

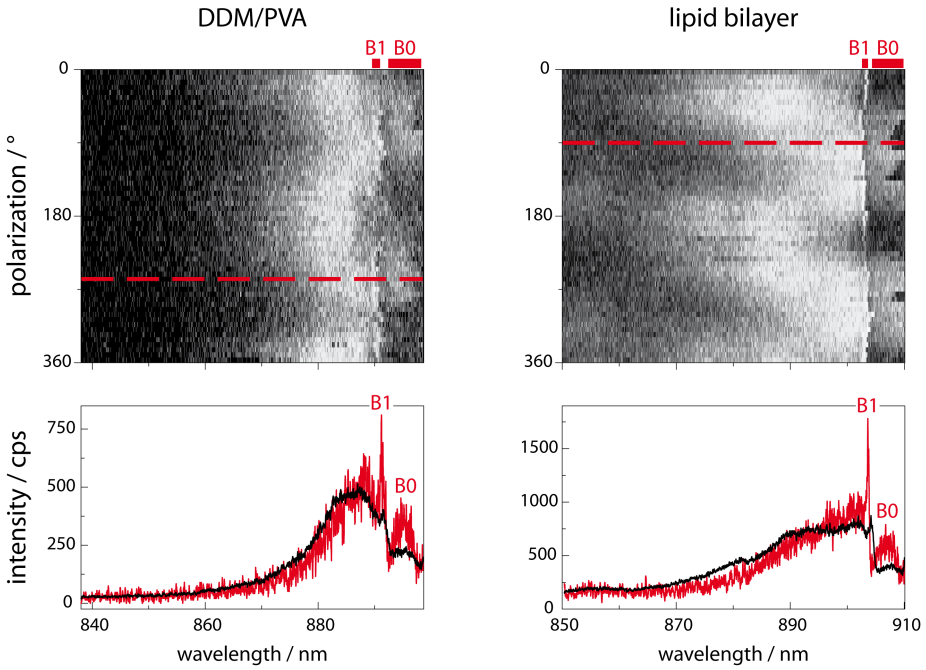

Figure 6.1: *Fluorescence-excitation spectra of two class A complexes displaying a band B0 red-shifted with respect to the B1 band stabilized in a DDM/PVA matrix (left) and in a lipid bilayer (right), respectively. The top panel, for each complex, shows a stack of 58 consecutively recorded spectra (spectral diffusion plot), where after each scan the polarization of the excitation laser has been rotated by* $6.2°$*. The vertical axis corresponds to the polarization of the incident laser light and the horizontal axis to wavelength. The selected spectral regions were adapted to the two environments in which the complexes were embedded. The fluorescence intensity is coded by the gray scale, white denoting high intensities. The red bars on top of the panels indicate the spectral intervals for the occurrence of B1 and B0, respectively. The black spectra in the lower panels correspond to an average over all 58 scans in the top panels, respectively. The red spectra are averages of three adjacent, individual scans with the central scans marked by the dashed lines in the top panels, respectively. The positions of the red spectra within the spectral diffusion plots were chosen such that the spectrally diffusing B0 band lay completely within the detected spectral region. The excitation intensity amounted to about* $250\ W/cm^2$ *for the RC-LH1 complex in DDM/PVA and* $140\ W/cm^2$ *for the RC-LH1 complex in the lipid bilayer.*

and lipid bilayer, respectively. For both complexes a low-intensity band B0 can be observed on the low-energy end of the spectra. In the upper panels 58 consecutively recorded fluorescence-excitation spectra are shown, where after each scan the polarization of the incident radiation was rotated by 6.2°. The red bars on top of the panels denote the spectral intervals for the occurrence of B1 and B0, respectively, where B0 appears as a broad, low-intensity band red-shifted with respect to B1. In the two-dimensional representation of the recorded spectra, also referred

to as spectral diffusion plot, it can be well observed that for both complexes B0 is subjected to spectral diffusion, leading to a partial overlap of B0 with the detection window of the band-pass filters in some of the spectra. The red spectra displayed below the spectral diffusion plots are averages of three adjacent, individual scans, where the positions of the central scans are indicated by the red, dashed lines in the top panels, respectively. The red scans were selected at positions within the spectral diffusion plots, where the B0 bands are entirely within the detectable spectral regions. The black spectra in the lower panels correspond to the averages of all 58 scans depicted in the top panels, respectively. It can be seen that due to the aforementioned spectral diffusion of B0, its spectral profile almost disappears in the averaged spectra. For the particular complexes chosen as examples in Figure 6.1, at least temporarily, the B0 band is completely within the detectable spectral region. However, a B0 band is also discernable for the class A complexes shown in chapter 4, yet with the constraint that due to red-shifted spectra, only the high energy shoulder of B0 is visible (see *e.g.* Figure 4.3a and Figure 4.12b).
The abrupt disappearance of the fluorescence intensity of the B0 band in some of the spectra of the RC-LH1 complex to the right in Figure 6.1, might represent a further confirmation that the B0 band indeed represents the fluorescence-emitting, lowest exciton state for the studied LH1 complexes. In [148] a similar behavior was observed for the lowest exciton state of a distinct LH2 complex and it was shown that the fluorescence-emission spectra of this complex featured large spectral "jumps" by as much as 16 nm. It was argued that such "jumps" can lead to a significant change of the spectral overlap of the emission spectrum from an individual LH complex with the spectral transmission window of the detection band-pass filters and that the emission spectrum can even "jump" out of the transmission window, thus leading to a disappearing fluorescence signal in the corresponding excitation spectrum.
A further indication that B0 might represent the lowest exciton state of the LH1 aggregates instead of B1, will be demonstrated by means of Figure 6.2. Therein histograms of the spectral peak positions of the bands B1 (gray bars) and B0 (red bars) are shown, together with an ensemble spectrum of RC-LH1 complexes stabilized in a DDM/PVA environment. The distributions of the bands B1 and B0 are both located in the red wing of the ensemble spectrum, where the ensemble spectrum is taken from Figure 4.4 and the B1 distribution was already shown in Figure 4.14. The distribution of the B0 band is centered at 895.5 nm (mean) and has a width (sdev) of 27 cm^{-1}. Here, it has to be noted that only 17 of the 28 complexes displaying a B0 band for the DDM/PVA environment were considered in the histogram, as for the remaining complexes the peak of the B0 band was hidden in the detection window of the bandpass filters. Consequently, the complete B0 histogram will be broader and maybe also the peak position will be further red-shifted. The spectral separation between the peak of the ensemble spectrum and the mean of the histogram amounts to 75.4 cm^{-1} for the B1 distribution and

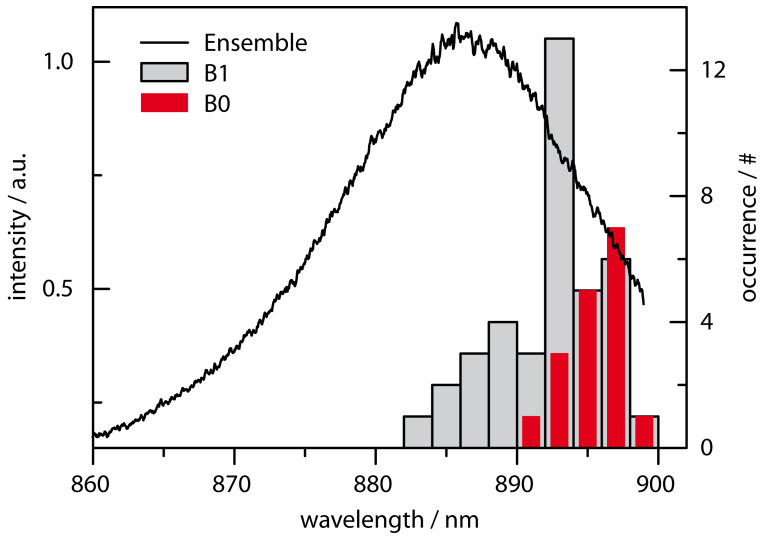

Figure 6.2: *Distributions of the spectral peak positions of the bands B1 and B0, together with an ensemble fluorescence-excitation spectrum of RC-LH1 complexes from Rps. acidophila embedded in a DDM/PVA matrix. The energetic separation between the peak of the ensemble spectrum and the mean of the histogram amounts to* $75.4\ cm^{-1}$ *for the B1 distribution and to* $115.4\ cm^{-1}$ *for the B0 distribution, respectively.*

to $115.4\ cm^{-1}$ for the B0 distribution, respectively. The latter value shows a much better agreement with the corresponding values determined in zero-phonon hole (ZPH) action spectra, where energy displacements in the range of $130\ cm^{-1}$ were found [120, 121]. Thus, the smaller values for the energetic separation of the B1 distribution found in the single-complex measurements as compared to the values from the zero-phonon hole (ZPH) action spectra, might not be related to the different sample preparation conditions, as reasoned in section 4.2, but, as the values should describe the energy displacement of the lowest exciton state with respect to the peak of the ensemble spectrum, to a wrong assignment of the bands in the single-complex spectra to the exciton states of a LH1 aggregate. According to this reasoning, B0 rather than B1 should represent the lowest exciton state of a LH1 aggregate in the single-complex spectra.
However, the unambiguous experimental proof uncovering B0 as the lowest exciton state in RC-LH1 complexes remains missing in this work, since no fluorescence-emission spectra from single RC-LH1 complexes were recorded. Yet, in the following some ideas will be presented, how the spectral characteristics of the RC-LH1 complexes could be interpreted, now with the inclusion of the B0 band.
First of all the question will be asked, if B0 was really assigned to the lowest exciton state, $k = 1$, of a LH1 aggregate, instead of B1, then what would be a plausible explanation for the narrow linewidth of B1? For this, one has to recall the measurement principle for the acquisition of fluorescence-excitation spectra, where the

fluorescence intensity of the higher exciton states is monitored through their relaxation to the lowest exciton state and subsequent fluorescence-emission from this state [115, 148]. Thus, the fast relaxation (*fs* timescale) of a higher exciton state ($k > 1$) to the lowest exciton state $k = 1$ in a LH1 complex, will be reflected by a broad band in the corresponding fluorescence-excitation spectrum, while a slowly relaxing (*ps* timescale), higher exciton state will appear as a narrow line in the excitation spectrum. The relaxation between the exciton states is induced by exciton-phonon scattering and a crucial parameter, determining the relaxation rate, is the spatial overlap between the exciton wavefunctions [149–151].
In Figure 6.3 the wavefunctions of the six lowest exciton states, $k = 1 - 6$, for Structure 1 are depicted, beginning with the lowest-energy state, $k = 1$, at the bottom of the figure. Thereby, diagonal disorder was not included in the calculation of the excitonic eigenstates. In the left part of Figure 6.3 the excitonic wavefunctions are shown in an extended representation, where the parameter, $a_{n,k}^2$, for the squared wavefunction amplitudes, indicates the participation of pigment n in the exciton state k, respectively. Interestingly, it can be observed that despite the elliptic geometry and the inclusion of only correlated, off-diagonal disorder in the calculation of the exciton wavefunctions, the localization behavior of the exciton states in Structure 1, is very similar to that of linear J-aggregates, where only diagonal (energetic) disorder was included in the calculation of the exciton states' wavefunctions [149, 150]: While for the higher exciton states the corresponding wavefunctions are delocalized over a large part of the aggregate, the lowest exciton states ($k = 1$ and $k = 2$ in Figure 6.3) localize on finite segments of the strongly coupled pigment assembly, displaying wavefunctions without nodes in their respective localization area. For illustration, in Figure 6.3, *right*, the wavefunctions and resulting transition-dipole moments of the exciton states are also shown in a pictorial representation, with Structure 1 as underlying geometry. Thereby, the length of the small arrows is proportional to the wavefunction amplitude, $a_{n,k}$, of the k^{th} exciton state on the n^{th} pigment, respectively. The inverse participation ratio, $I_k = 1/\sum_{n=1}^{30} (a_{n,k})^4$, is a measure for the delocalization length of the wavefunction of the exciton state k, or equivalently, the approximate number of pigments participating in the k^{th} exciton state [151].
The spatial overlap between the wavefunctions of the exciton states k and k' can be calculated as $C_{k,k'} = \sum_{n=1}^{N} (a_{n,k})^2 (a_{n,k'})^2$, where N denotes the total number of pigments in the aggregate. Thereby, the overlap between the wavefunctions of the exciton states $k = 1$ and $k = 2$ in Figure 6.3 can be calculated to $C_{1,2} \approx 0.0018$ and to $C_{1,3} \approx 0.0442$ for the states $k = 1$ and $k = 3$. $C_{1,2}$ and $C_{1,3}$ differ by a factor of 25. Thus, it would be conceivable that, due to the large overlap between their wavefunctions, the $k = 3$ exciton state is subjected to a fast relaxation to the $k = 1$ state, resulting in a broad band (B3) in the corresponding excitation spectrum. Accordingly, the nearly vanishing overlap between the wavefunctions associated with the exciton states $k = 2$ and $k = 1$, would result in a comparatively slow relaxation

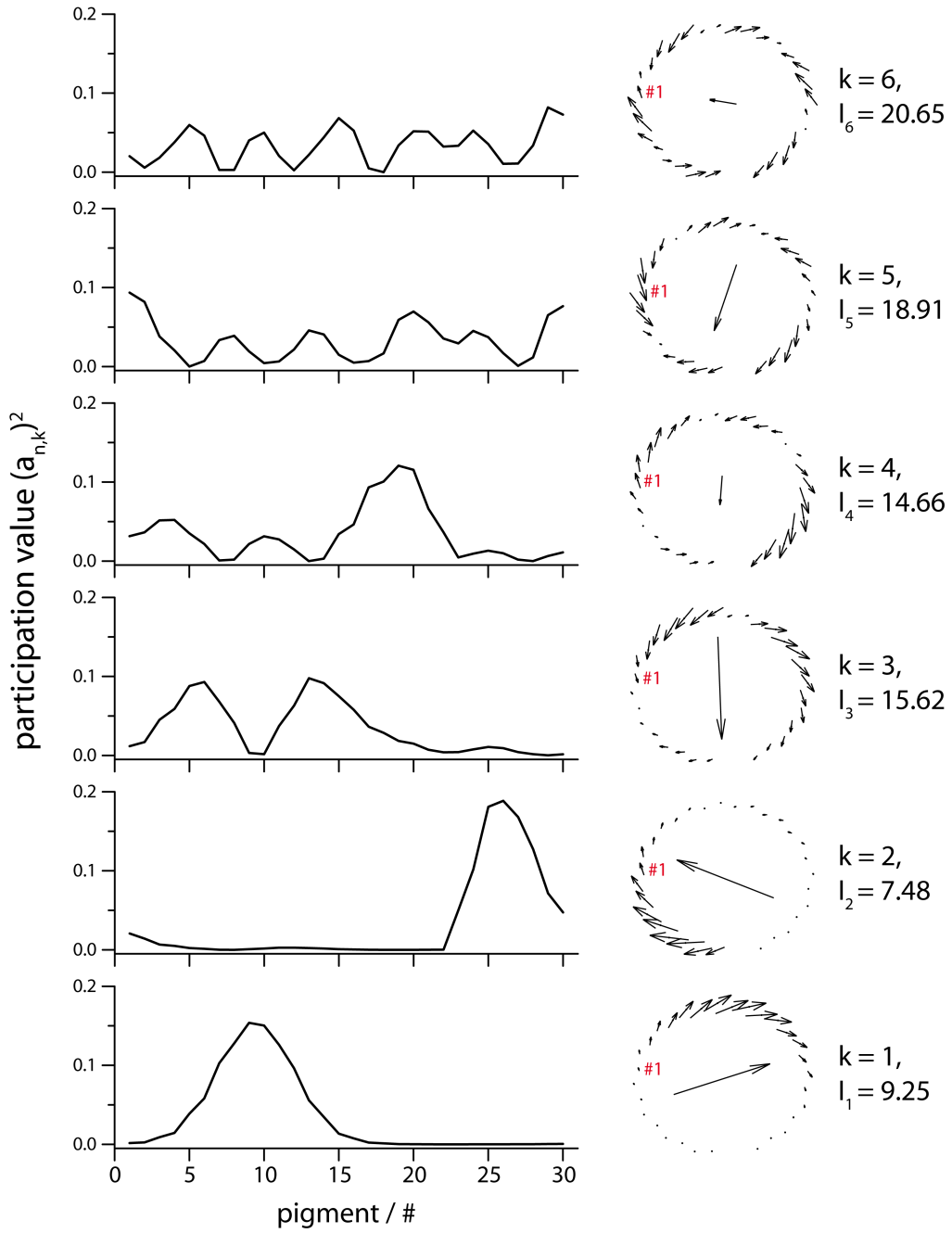

Figure 6.3: *Wavefunctions of the exciton states $k = 1 - 6$ in Structure 1, calculated without the inclusion of diagonal disorder. The states are sorted with respect to their eigenenergies, starting with $k = 1$ at the bottom. Left: Elongated representation of the wavefunctions. The participation value $a^2_{n,k}$ (y-axis) corresponds to the squared wavefunction amplitude of the exciton state k on pigment n (x-axis), respectively. Right: Pictorial representation of the excitonic wavefunctions and the resulting transition-dipole moments (central arrows), with Structure 1 as underlying geometry. The length of the small arrows is proportional to the wavefunction amplitude $a_{n,k}$, respectively. "#1" denotes pigment #1 for the representation in the left panel, and further pigments in the structure are numbered in clockwise direction. I_k denotes the inverse participation ratio of the k^{th} exciton state (see text).*

of the $k = 2$ state to $k = 1$ and thus a narrow line for the band B1 (now associated with the $k = 2$ exciton state) in the corresponding excitation spectrum. This notion is corroborated by a recent work of Novoderezhkin et al. [151], where the authors calculated relaxation times of up to 20 ps between exciton states localized on opposite sides of a LH2 complex. Such a relaxation time would translate into a linewidth of about 0.5 cm^{-1} for the band associated with the energetically higher exciton state, which is reasonable agreement with the linewidths observed for the B1 bands in the excitation spectra (in spite of the remaining uncertainties regarding the homogeneous linewidth of B1, see section 4.1).
In [149] it was claimed for J-aggregates that at low temperatures the relaxation of spatially localized exciton states to energetically lower-lying states should be hindered due to the missing overlap between their wavefunctions and therefore these states will decay radiatively. Taken together with the conclusions from the above section, for the relaxation of the $k = 2$ exciton state in a LH1 complex, this would then result in a competing process between its direct, radiative decay to the electronic ground state and its non-radiative relaxation to the $k = 1$ exciton state. Given the typical time scales for these processes, ≈ 600 ps for the ensemble fluorescence decay of LH1 complexes [56, 89] and ≈ 20 ps for the relaxation between exciton states localized on opposite sides of a circular LH complex [151], the latter process should dominate. However, a definite proof for this behavior can again only be gained by recording fluorescence-excitation and -emission spectra of the same individual RC-LH1 complexes. It would be very interesting in such measurements, to observe if the complete fluorescence emission arises from the B0 band, or if part of the emission also results from the band B1.
With this new explanation for the occurrence of the narrow line B1 the question arises, why such a band is almost constantly observed in the low-temperature fluorescence-excitation spectra of RC-LH1 complexes with an interrupted LH1 aggregate (this thesis and [10, 12]), but only very rarely for RC-LH1 complexes with a completely closed circular LH1 aggregate [12, 44], or for LH2 complexes [11, 13]. Here, it is conceivable that the symmetry of the investigated, strongly interacting pigment assemblies might play a crucial role. For systems with a broken symmetry due to a gap in the pigment assembly, it could be that the resultant exciton localization patterns fulfill the prerequisites for a slow relaxation of the $k = 2$ exciton state to the $k = 1$ state (*vide supra*), which then would be reflected by a narrow line for the $k = 2$ state in the corresponding excitation spectra. In contrast, for completely closed pigment assemblies with circular or elliptical aggregates, also different localization patterns are to be expected for the lowest exciton states as compared to the complexes with a broken symmetry. For example, model calculations on elliptically deformed LH2 aggregates revealed largely overlapping wavefunctions for the lowest ($k^{circ} = 0$) and the second lowest exciton state ($k^{circ} = +1$) [14]. According to the above argumentation this would then lead to a fast relaxation of $k^{circ} = +1$ to $k^{circ} = 0$, and consequently to a broad band for the $k^{circ} = +1$ state in

the corresponding fluorescence-excitation spectrum. In this regard, it is clear that disorder can significantly influence the exciton localization patterns. In the model calculations in [14] diagonal disorder was omitted, whereas in [151], where the room-temperature case was simulated for LH2, a large value for the diagonal disorder, for some realizations of the pigment site energies, lead to the above mentioned localization of the exciton wavefunctions of $k^{circ} = +1$ and $k^{circ} = 0$ on opposite sides of a circular LH2 complex. Disorder might also be responsible for the rare occasions when a narrow line is observed in single-complex fluorescence-excitation spectra of LH complexes with completely closed, circular or elliptical aggregates. Here it could be that both structural distortions in the pigment aggregates (off-diagonal disorder) or shifts in the pigment site energies (diagonal disorder) might lead to a localization of the exciton wavefunctions in question, and thus to a reduction in their spatial overlap. As a result, the respective higher exciton state can relax only slowly to the lowest exciton state in the manifold and consequently a narrow line will occur for this state in the corresponding single-complex spectra. However, the lack of narrow lines in the majority of the fluorescence-excitation spectra for LH complexes with closed, circular/elliptical structures, indicates largely delocalized, overlapping wavefunctions in these aggregates for low-temperature conditions, and therefore mostly broad bands are visible in these spectra, reflecting the fast relaxation of the higher exciton states to the lowest one.
Returning to the RC-LH1 spectra of this work, one might ask how, with the new interpretation of the spectral bands, in particular assigning the band B1 to the $k = 2$ exciton state, the occurrence of the band B2 can be explained, since, according to the simulations of chapter 5, the polarization behavior of B2 does not allow the straightforward attribution of this band to the next higher exciton state $k = 3$. Therefore, as B2 always occurs more or less in phase with B1 and is shifted towards higher energies, one could alternatively interpret B1 as the zero-phonon line (ZPL) of the transition to the $k = 2$ exciton state and B2 as its associated phonon side-band (PSB). A measure for the electron-phonon coupling strength can be gained by determining the relative intensity of the ZPL with respect to the total intensity of the transition, $C_{DW} = \frac{I_{ZPL}}{I_{ZPL}+I_{PSB}}$, where C_{DW} is the so called Debye-Waller factor and I_{ZPL} (I_{PSB}) refers to the integrated intensity of the ZPL (PSB), respectively. Thus a prominent PSB, as observed by comparison of the intensity of the B2 band with respect to B1 in the fluorescence-excitation spectra of the class A RC-LH1 complexes, would indicate strong electron-phonon coupling for the transition to the $k = 2$ exciton state. So far, with the help of fluorescence-excitation spectra of individual LH complexes, the electron-phonon coupling strength could only be determined for the localized excitations in the B800 band of LH2 complexes and the coupling for this kind of excitations was found to be weak [152, 153]. This however, does not have to be contradictory to the aforementioned strong coupling for the $k = 2$ state in LH1 complexes, since authors in [121] described a similar effect: While they found large electron-phonon coupling strengths for the

fluorescence-emission from the delocalized states in the strongly coupled B850 and B875 aggregates of LH2 and LH1 complexes, respectively, electron-phonon coupling was discovered to be weak for the fluorescence-emission from the states localized on individual BChl *a* molecules in the Fenna-Matthews-Olson (FMO) complex. Additionally, the notion of strong electron-phonon couplings for systems of strongly interacting BChl *a* molecules was corroborated by the emission spectra recorded from individual LH2 complexes [115, 154]. However, it has to be noted that in all the above mentioned studies [115, 121, 154] the electron-phonon coupling for strongly interacting pigment assemblies was probed for the relaxed, fluorescence-emitting states. Due to an intrinsic problem occurring in the measurement principle of fluorescence-excitation spectra of strongly coupled systems (*vide infra*), up to now, it was not possible to probe the electron-phonon coupling strength directly upon excitation of the higher exciton states ($k > 1$, for the RC-LH1 complexes of this work).

In the measurement of fluorescence-excitation spectra of strongly coupled pigment aggregates, due to the fast relaxation of the higher exciton states to the fluorescence-emitting, lowest exciton state, potential PSBs of the higher states generally would be hidden under their broad, overall line shapes. Thus, owing to the comparatively slow relaxation of the $k = 2$ exciton state to $k = 1$, it might be possible for the first time to separately detect the ZPL and the PSB of a higher exciton state in a fluorescence-excitation experiment and thereby, to determine the electron-phonon coupling strength of this state upon its excitation. Here, it should be noted that the electron-phonon coupling strength determined for the transition to the $k = 2$ exciton state would then be a specific parameter of this transition. Thereby, an additional factor which might contribute to an increased electron-phonon coupling strength of the $k = 2$ exciton state in comparison to the other states, could be its delocalization length, where it is common knowledge that the strength of the electron-phonon coupling grows with decreasing delocalization length for a given exciton state [104, 155, 156]. In Figure 6.3 it can be observed that the $k = 2$ exciton state displays the smallest delocalization length, described by inverse participation ratio, I_k, and accordingly this should lead to a stronger electron-phonon coupling for this state, in comparison to the other exciton states. Concluding, the comparability of the intensity ratios of the bands B1 and B2 in the fluorescence-excitation spectra of the intact RC-LH1 complexes from *Rps. acidophila* with the intensity ratios of the ZPLs and PSBs in the emission spectra of individual LH2 complexes from *Rps. acidophila* in [115, 154], could indicate a similar electron-phonon coupling strength for the absorbing $k = 2$ exciton state in LH1 and the fluorescence-emitting state in LH2. This might be related to the comparatively small delocalization length predicted for the $k = 2$ exciton state in LH1 which then should be similar to the delocalization length of the relaxed, fluorescence-emitting state in LH2.

For completeness, it should also be mentioned that with this new interpretation of B1 and B2, the energy displacement between these bands, ΔE_{B1B2}, would cor-

respond to the mean phonon energy of the phonon modes accompanying the pure electronic transition to the $k = 2$ exciton state. In this respect, it is satisfying to observe that the distributions of ΔE_{B1B2} in Figure 4.13a, for RC-LH1 complexes in two different environments, are in good agreement with the distributions of the mean phonon energies for the localized excitations in the B800 band of LH2 complexes [153]. Furthermore, the slightly larger values for ΔE_{B1B2} in the lipid bilayer environment might be attributed to the higher pressures to which the complexes are subjected in this environment as compared to the DDM/PVA matrix, going along with an increase of the mean phonon frequencies [157, 158].
With the new interpretation of the band B1 also the multiple narrow lines in the fluorescence-excitation spectra of the class C complexes would gain a new meaning. While in chapter 4 these lines were interpreted as the lowest exciton states of individual pigment aggregates located in close proximity, according to the new interpretation of the spectral characteristics in fluorescence-excitation spectra, the blue-shifted narrow lines could also result from localized, higher exciton states in the same LH1 complex, where the fluorescence-emission from this complex would result from a broad band energetically located near the transmission window of the band-pass filters. The latter interpretation seems more probable, since, if the narrow lines in the middle of the spectral range would really belong to the fluorescence-emitting, lowest exciton states of separated pigment aggregates, the phonon side-bands in the emission spectra from these states would have to be quite prominent and extend into the detection window of the band-pass filters, thus making the recording of a fluorescence signal possible. By comparison with the fluorescence-excitation and emission spectra from individual LH2 complexes [115, 148], this does not seem very likely, but, for confirmation, this again calls for the simultaneous recording of fluorescence-excitation and emission spectra from individual RC-LH1 complexes.
The class C complex in Figure 4.6 serves as a nice example on which this new interpretation of the spectral features will be briefly demonstrated. Overall, the spectral characteristics of this complex are very similar to those of a class A complex, however with the significant difference that the B3 band also displays a narrow feature on its low-energy wing. Here it is assumed that, presumably due to structural distortions of the pigment array in the localization area of the $k = 3$ wavefunction, the delocalization length of this state decreases, thereby reducing its overlap with the $k = 1$ wavefunction. As a result, the relaxation time of $k = 3$ will increase which is reflected by the narrow line in the red wing of B3. Interestingly, the narrow line associated with B3 ($fwhm = 16.3\ cm^{-1}$) is approximately two times broader than the narrow line visible red-shifted with respect to B2 ($fwhm = 7.6\ cm^{-1}$) for the same complex, possibly indicating a still faster relaxation of $k = 3$ in comparison to $k = 2$. However, given the discussion on the fast spectral diffusion of the narrow lines in section 4.1, one should be cautious with a direct conversion of the measured linewidths into lifetime values. A careful inspection of the spectral diffusion plot of the class C complex in Figure 4.6 reveals a broad, low-intensity band attached to

the transmission window of the band-pass filters which, according to the argumentation in this chapter, should correspond to the fluorescence-emitting $k = 1$ exciton state of this complex.
Regarding the comparatively long fluorescence lifetime of LH1 complexes ($\approx 600\ ps$ [56, 89]), one might ask why the $k = 1$ exciton state appears as the broad band B0 in the fluorescence-excitation spectra, since, given the lifetime, the linewidth of B0 should be about $0.02\ cm^{-1}$. In [148] authors argued that the broad linewidth associated with the lowest exciton state might result from fast spectral diffusion of this state, thereby smearing out the spectral profile observed for the associated band in the fluorescence-excitation spectra. Additionally, the linewidth of B0 may be broadened because of the predicted, comparatively small delocalization length of the $k = 1$ state (Figure 6.3). Therefore, increased electron-phonon coupling should also be expected for this state, giving rise to a pronounced phonon side-band.
With the above said, it is clear that the relatively simple simulation approach used in chapter 5 could then not account for all spectral features observed for the RC-LH1 complexes. Thus, *e.g.* the band B2 which according to the new interpretation of the spectral characteristics could be ascribed to electron-phonon couplings, would not appear in those simulations, as such couplings are not included therein (Hamiltonian in Heitler-London approximation). Here, it should be noted however, that also in more elaborated simulation approaches the eigenvalues (exciton energy levels) and the eigenstates (exciton wavefunctions) of the one exciton Hamiltonian are calculated taking only static energy disorder of the pigment site energies (diagonal disorder) into account [104, 151, 159]. The coupling of the electronic transitions to phonon modes (dynamic disorder) then determines the spectral profiles of the exciton states, defined by parameters like the exciton-phonon coupling strength or the ultrafast relaxation between the higher exciton states induced by the dynamic disorder (Redfield relaxation theory) [104, 151, 159]. Thus, if the comparison between simulation and experimental results is restricted to the energetic separation between spectral bands, that can be attributed to specific exciton states, and the mutual orientation between their corresponding transition-dipole moments, these values are well determinable through the diagonalization of the Hamiltonian (5.2) in chapter 5. Therefore, it is reasonable to compare the spectral characteristics of the RC-LH1 complexes from *Rps. acidophila*, now in the framework of the new interpretation of the bands B1 and B0, with the results of the numerical simulations for the various LH1 model structures introduced in chapter 5, even if the coupling to phonon modes is not included in that approach.
This comparison was performed in order to find out if the structural LH1 models and also the simulation parameters introduced in chapter 5 are still applicable with the new interpretation of the spectral characteristics for the class A RC-LH1 complexes and if one of the models stands out. Thereby, the focus was on the analysis of the spectral properties of the bands B0 and B1 in the experiment and respectively, on the exciton states $k = 1$ and $k = 2$ in the simulations. Additionally, Structure

2 was excluded from the analysis, since on the one hand the simulated spectra for this structure clearly deviate from the experimental ones, and on the other hand, for most realizations of the diagonal disorder, Structure 2 does not fulfill the requirement of the $k = 1$ and $k = 2$ wavefunctions localizing on opposite sides of the LH1 aggregate, mandatory for the assignment of B1 to the $k = 2$ exciton state. All three remaining structures (1, 3 and 3') conform to the latter requirement.
When applying the simulations, it should be noted however, that, similar to chapter 5, the oscillator strength of the exciton states $k = 1$ and $k = 2$ in the simulations does not match the experimentally determined fluorescence intensities of the bands B0 and B1, respectively. For both spectral bands the measured fluorescence intensities are considerably smaller than predicted by the oscillator strength of the corresponding exciton states in the simulations. The experimental shortcomings which could lead to this deviation between measured and simulated spectral intensities of the narrow line B1 were already outlined in chapter 5, and since, according to [148], B0 also results from a narrow line undergoing fast spectral diffusion, the same reasoning would apply here.

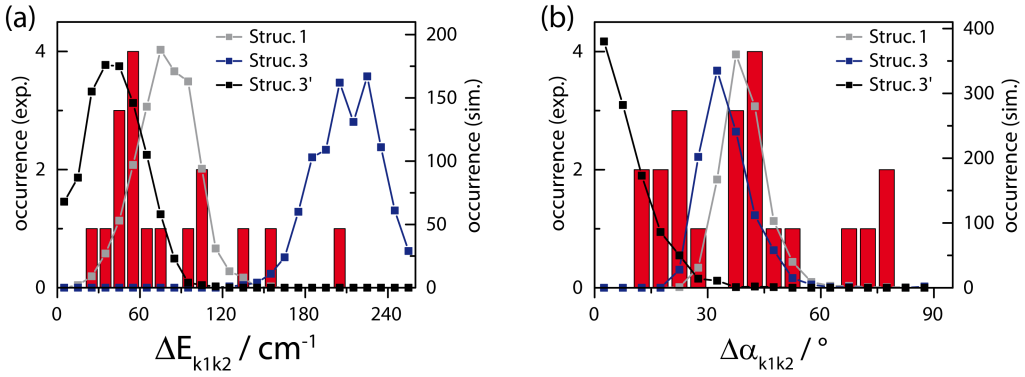

Figure 6.4: *Comparison of the distributions of the energy splittings between the bands B0 and B1 (a, red bars) and the mutual orientations of the associated transition-dipole moments (b, red bars), with the calculated distributions of the corresponding values for exciton states $k = 1$ and $k = 2$ of the structures 1, 3 and 3' (squares), respectively. The experimental histograms comprise 17 class A RC-LH1 complexes from Rps. acidophila for the energy splittings between B0 and B1 (a) and 21 complexes for the mutual phase angles between these bands (b). The simulated distributions correspond to 1000 individual realizations of the pigment site energies for each structure, respectively.*

In Figure 6.4 the distributions of the mutual energy displacements between the bands B0 and B1, ΔE_{k1k2}, and the mutual angles between the corresponding transition-dipole moments, $\Delta\alpha_{k1k2}$, are compared to the respective data of the exciton states $k = 1$ and $k = 2$ in the numerical simulations of the structures 1, 3 and 3', respectively. In analogy to chapter 5 only the class A complexes stabilized in DDM/PVA were considered, as the simulation parameters in chapter 5 were es-

pecially adjusted to RC-LH1 complexes in this environment. Deviating from the procedure in chapter 5, here the experimental data for the energetic separations between B0 and B1, were directly compared to the energy splittings between the calculated excitonic eigenenergies of the states $k = 1$ and $k = 2$, since, due to the assignment of the narrow line B1 to the $k = 2$ exciton state, the influence of higher exciton states on the values determined for the energy splittings can be excluded. The simulated data for the mutual angles between the transition-dipole moments associated with the exciton states $k = 1$ and $k = 2$ were adopted from chapter 5. The number of entries in both histograms of Figure 6.4 deviates from the total number of class A spectra displaying a B0 band (28), because the determination of ΔE_{B0B1} and $\Delta\alpha_{B0B1}$ was not possible in all of these spectra.
For the energetic separations between B0 and B1 the best agreement with the experimental data is found for Structure 3' (Figure 6.4a). The distribution of ΔE_{k1k2} determined for Structure 1 is shifted to slightly larger energy displacements compared to the maximum of the experimental histogram, while the energy splittings between the $k = 1$ and $k = 2$ exciton states calculated for Structure 3, are by far larger, than the experimentally determined energetic separations between B0 and B1. The distribution of the mutual orientations of the transition-dipole moments associated with the exciton states $k = 1$ and $k = 2$, $\Delta\alpha_{k1k2}$, for Structure 1 covers the range from 25 to 60°, corresponding to the region where for the experimental histogram the maximum number of entries can be found. The distribution for Structure 3 is shifted to slightly smaller angle values in comparison to the Structure 1 distribution, and the simulated distribution for Structure 3' has its peak position at about 0°, showing a steep decrease for larger angles, clearly deviating from the experimental distribution. Interestingly however, none of the three LH1 model aggregates is able to reproduce the wide spread of mutual phase angles found in the experimental histogram.
The comparison of the experimental data with the data from the numerical simulations first of all reveals that for none of the three structures a perfect agreement with both experimental distributions can be achieved. In particular the experimentally observed wide spread of the angle values, $\Delta\alpha_{B0B1}$, which cannot be reproduced by the numerical simulations (Figure 6.4b), might indicate that the parameter for the diagonal disorder in the simulations of chapter 5 ($\Delta = 100\ cm^{-1}$) was chosen too small. Additionally, structural heterogeneity (small rearrangements of dimer units) probably occurring among the studied RC-LH1 complexes from *Rps. acidophila* [20], but not taken into account in the simulations, would as well broaden the experimental distribution of $\Delta\alpha_{B0B1}$ with respect to the simulations.
Despite these shortcomings, the comparison of the simulated spectral properties of the bands B0 and B1 (exciton states $k = 1$ and $k = 2$) for all three structures with the experimental ones reveals that, if the distributions of the energy splittings and the mutual phase angles are taken together, the calculated distributions of Structure 1 display the closest agreement with the experimental histograms. This

is interesting from the point of view that Structure 1 bases upon a comparatively simple construction principle, where 15 BChl *a* dimer units are equidistantly distributed on an ellipse comprising a gap. Thus, it might be that the structural adjustments which needed to be accomplished on Structure 3' to reproduce the experimental distributions in chapter 5, are the result of a misinterpretation of the spectral characteristics of the class A RC-LH1 complexes, instead of providing an improved insight into the specific arrangement of the BChl *a* molecules in the LH1 complex of *Rps. acidophila*.
The remaining deviations between simulation and experiment, still observable for Structure 1 in Figure 6.4 and, as mentioned above, for the diagonal disorder and the oscillator strength of the exciton states $k = 1$ and $k = 2$, might indicate that the simulation parameters still need further optimization. This would refer both to the parameters defining the interpigment coupling and the diagonal disorder, and also to the arrangement of the pigments in the LH1 complex. For the latter, the recently found high-resolution crystal structure of the RC-LH1 complex from *T. tepidum* [9] might be of great help, yet with one dimer unit removed to mimic the presumable gap in the LH1 complex from *Rps. acidophila*. During the optimization process however, one should pay attention that the key feature for the new interpretation of the spectral properties, namely the localization of the $k = 1$ and $k = 2$ exciton state wavefunctions on opposite sides of the LH1 aggregate, is still met. That this is the case for Structure 1 and also the simulated spectral characteristics for the exciton states $k = 1$ and $k = 2$ are quite similar to the experimental results (Figure 6.4), might indicate that Structure 1 and also the chosen simulation parameters (at least for the interaction strength) are close to the native situation. Furthermore, this would again be a confirmation of the notion that the modulation of the interdimer interaction is a crucial parameter that necessarily needs to be taken into consideration for the determination of the localization sites of the exciton states (see chapter 5).
To sum up, in this chapter it was shown that instead of the narrow line B1, the lowest exciton state $k = 1$ in LH1 complexes, might be associated with a broad, low-intensity band (B0), occurring red-shifted with respect to B1. In future work this new interpretation of the spectral characteristics could be confirmed experimentally by acquiring fluorescence-excitation and emission spectra from the same individual RC-LH1 complexes, similar to [148]. In an attempt for an explanation of the spectral properties in the fluorescence-excitation spectra of the RC-LH1 complexes from *Rps. acidophila*, now with the new assignment of the spectral bands, it was suggested that the localization of the $k = 2$ exciton state on the opposite side of the LH1 aggregate, with respect to the $k = 1$ state, might be responsible for the narrow line B1 which, according to the new interpretation, is assigned to the $k = 2$ exciton state. This type of localization for the exciton states $k = 1$ and $k = 2$ is permanently observed in three out of the four LH1 model structures presented in this work. From these three structures, Structure 1, which is based on

an interrupted ellipse with equidistantly distributed dimer units, best reproduces the experimental results of the bands B1 and B0. However, in this outlook also the shortcomings of the simulation approach in chapter 5 have been revealed. On the one hand, given the experimental proof that the assignment of B0 and B1 to $k = 1$ and $k = 2$, respectively, is correct, both the simulation parameters and the pigment arrangement in Structure 1 could be refined in the future, for a better agreement with the experimental results. In general, it could be regarded as a rough simplification in the numerical simulations of this work, to neglect the specific couplings of the exciton states to phonon modes [104, 121, 151, 159] and to assign linewidths to the exciton states basing solely on general results for the exciton relaxation dynamics. In particular, not considering the explicit spatial overlap between the exciton wavefunctions for their intraband relaxation to the lowest exciton state [149–151], might have led to a wrong assignment of the experimentally determined spectral bands to the respective exciton states of a LH1 complex comprising a gap. Therefore, it would be very interesting in the future, to observe if the application of more sophisticated simulation approaches, including exciton-phonon couplings, will satisfactorily reproduce the fluorescence-excitation spectra from individual RC-LH1 complexes with an interrupted pigment aggregate.

7 Summary

The topic of this thesis was the investigation of the specific arrangement of the bacteriochlorophyll (BChl) *a* molecules in the light-harvesting 1 (LH1) complex from *Rhodopseudomonas (Rps.) acidophila*. In purple bacteria the LH1 complex forms an interconnected unit with a reaction-center (RC) complex, where the LH1 complex directly surrounds the RC to form the so called RC-LH1 core complex. As part of a cyclic electron transport pathway in bacterial photosynthesis, reduced ubiquinone molecules, Q_BH_2, have to leave the RC and pass through the LH1 complex into the membrane space. By now, it is well established that for some purple bacterial species the LH1 complex has a gap, presumably to facilitate the shuttling of Q_BH_2, whereas for other species, with a completely closed LH1 ring, channels in the LH1 aggregate might enable the transfer of Q_BH_2. Before this work, it was not known to which of these two types of RC-LH1 complexes (interrupted *vs.* closed LH1 ring), the RC-LH1 complex from *Rps. acidophila* belonged, let alone an idea of the exact arrangement of the BChl *a* molecules in the LH1 aggregate. In the following a short summary of the results achieved in this thesis will be presented.

In a first series of experiments the RC-LH1 complex from *Rps. acidophila* was revisited for single-molecule spectroscopy. Thereby, the pigment-protein complexes were stabilized in the relatively mild, non-denaturating detergent dodecyl-β-D-maltoside (DDM), instead of the more deactivating detergent lauryldimethylamine N-oxide (LDAO) which was used in a previous study. In total, low-temperature (1.2 K) fluorescence-excitation spectra have been recorded from 61 individual RC-LH1 complexes stabilized in DDM, in comparison to only 24 complexes measured in the precursor study. According to their spectral characteristics, the complexes were either considered as intact or broken. The fraction of broken (dissociated) RC-LH1 complexes could be reduced significantly by using DDM instead of LDAO as detergent, namely from 37.5% in the precursor work to 11.5% in this thesis. Due to the enhanced quality of the stock solution, it was possible to perform polarization-resolved fluorescence-excitation spectroscopy, and to determine the distributions of the spectral properties for the intact RC-LH1 complexes with an improved statistics. Both these distributions and characteristic spectral features, such as a narrow line oc-

curring on the red end of the spectra for most of the complexes, show a remarkable resemblance with the data obtained on RC-LH1 complexes from *Rps. palustris* in an earlier study. For the *Rps. palustris* RC-LH1 complex a low-resolution crystal structure is available. Hence, taking also the aforementioned similarity of the spectral characteristics into account, it is concluded that the LH1 complexes from *Rps. acidophila* and *Rps. palustris* can be described by the same structural model, namely an elliptical arrangement of BChl *a* molecules interrupted by a gap. Thus, by successfully applying low-temperature single-molecule spectroscopy as a tool for structural investigation, it was revealed for the first time that the RC-LH1 complex from *Rps. acidophila* rather belongs to the RC-LH1 complexes with an interrupted LH1 aggregate, than to those with a completely closed LH1 ring.

In a second experimental series the influence of the environment on the spectra of the RC-LH1 complexes from *Rps. acidophila* was investigated. Thereby, the complexes were stabilized in detergent (DDM) buffer solution and reconstituted into a phospholipid bilayer, and the results were compared with the outcome of the first experimental series (*vide supra*), conducted on DDM stabilized RC-LH1 immobilized in a polyvinyl alcohol (PVA) matrix (DDM/PVA). The aim of these experiments was to test whether the immobilization of the RC-LH1 complexes in PVA might lead to a deformation of the LH1 structure, thereby limiting the significance of the results obtained from optical spectroscopy.
In ensemble absorption and fluorescence-excitation spectra, spectral shifts were observed both as a function of the matrix as well as, as a function of temperature. Regarding the latter, varying spectral shifts were observed in the three environments upon cooling the sample. This could be explained consistently with an increase of the local pressure exerted on the complexes in the lipid bilayer and the DDM buffer solution, whereas for DDM/PVA a decrease of the local pressure is conceivable, since, due to a negative thermal expansion coefficient for thin polymer films below the glass transition temperature, an expansion rather than a contraction of the PVA-film is expected upon temperature reduction. In low-temperature single-molecule measurements it was found that the complexes dissolved in DDM buffer solution, without stabilization in a PVA matrix, are subjected to fast spectral dynamics preventing the extraction of meaningful data from single-molecule spectroscopy. Furthermore, for the complexes reconstituted into a lipid bilayer it was revealed that the reconstitution process results in a significantly larger fraction of broken complexes with respect to the preparation of the complexes in a PVA film. However, it was also found that for the intact complexes the statistics of the key spectral features, such as the spectral separation of the bands and the mutual orientation of their transition-dipole moments, show no difference as a function of using either a lipid bilayer or PVA as a matrix. Given the additional effort involved in the reconstitution process, the lower amount of intact RC-LH1 complexes, and, concerning the decisive spectral details, the identical results with respect to embed-

ding the complexes in a PVA matrix, led to the conclusion that the immobilization of these pigment-protein complexes in a PVA matrix is a good choice for conducting low-temperature experiments on individual light-harvesting complexes.

Next, the statistical distributions of the spectral features from the intact RC-LH1 complexes were compared with the corresponding data from numerical simulations of various LH1 model structures. Thereby, it was sought to learn more about the specific arrangement of the BChl *a* molecules in the LH1 complex from *Rps. acidophila*. All proposed LH1 model structures were within the resolution limit of the *Rps. palustris* RC-LH1 crystal structure and consequently all models had a gap in their BChl *a* arrangement. In comparison to an earlier simulation study on the RC-LH1 complex from *Rps. palustris*, more realistic simulation parameters were applied in this thesis, both with respect to the structural buildup of the LH1 models and regarding the coupling strength between the pigments.
Initially three different LH1 model structures were tested. In two of these models fixed BChl *a* dimer units were placed equidistantly on an ellipse or a rectangle with rounded corners, whereas in the third model the placement of the BChl *a* molecules was equivalent to the irregular arrangement of the pigments in the *Rps. palustris* crystal structure. As a first result of the significantly increased interaction strengths in the simulations of this work, the site energy of the pigments in all proposed LH1 models adopts plausible values. However, it was also found that none of the three initial structures is able to reproduce the experimental distributions of the spectral features of the RC-LH1 complexes from *Rps. acidophila*. A careful analysis of the localization patterns of the LH1 exciton states, $k = 1$ and $k = 2$, each localize in characteristic areas of the LH1 aggregates, where the values for the nearest-neighbor interactions between the pigments are significantly increased. With this knowledge it was possible, by slightly rearranging only four dimer units in one of the regular LH1 models (rectangle with rounded corners), to create a new LH1 model whose spectral properties are in satisfying agreement with the experimental single-molecule data. The structural modifications were inspired by the RC-LH1 *palustris* crystal structure and it could be argued that they are due to specific interactions between the RC and the LH1 complex. The final LH1 model clearly outperforms the refined *Rps. palustris* LH1 model introduced in an earlier study, since for the present model both more realistic simulation parameters were applied and it shows a much better structural overlap with the *Rps. palustris* RC-LH1 crystal structure.
However, it has to be noted that in the only high-resolution crystal structure available for a RC-LH1 complex so far, no evidence can be found for the specific modifications performed on the regular LH1 structure. Additionally, it should be clear that similar structural modifications, as the one described above, can also lead to a LH1 model within the resolution of the *palustris* x-ray structure, being able to reproduce the experimental spectra. Therefore, it will not be claimed that in the final

LH1 model the 'one and only' structural solution for the LH1 complex from *Rps. acidophila* has been found, but it was shown how, in the limits of a rather simple simulation approach (Heitler-London approximation and dipole-dipole interaction between the pigments), a LH1 model with a regular placement of the pigments can be modified, to achieve a satisfying reproduction of the experimental distributions of the spectral features. Consequently, the more important result of this part is, that in excitonic systems which are dominated by the modulation of the nearest-neighbor interaction rather than by the diagonal disorder, the two lowest exciton states localize in specific areas of the LH1 aggregates, coinciding with the maxima of the nearest-neighbor interaction. This finding might be of general interest for any strongly coupled pigment array.

Finally, triggered by a recent work on LH2 complexes from *Rps. acidophila*, a careful reinspection of the spectra from the individual RC-LH1 complexes considered as intact, revealed that, instead of the narrow line on the low-energy end of the spectra, a broad low-intensity band, occurring red-shifted with respect to the narrow line, might represent the lowest exciton state, $k = 1$, of the LH1 complexes. In future work this new interpretation could be tested, by acquiring fluorescence-excitation and emission spectra from the same individual RC-LH1 complexes. According to the work on LH2, in these spectra the criterion for the identification of the lowest exciton state should be, that the emission spectrum has to emerge directly from the spectral region of the lowest exciton state in the excitation spectrum. Referring to the numerical simulations from the previous part, it is argued that not the long excited state lifetime of the $k = 1$ exciton state in comparison to the higher exciton states might be responsible for the characteristic narrow line in the RC-LH1 fluorescence-excitation spectra, but the localization of the $k = 1$ and $k = 2$ exciton states on opposite sides of the LH1 aggregate. This would affect the relaxation of the $k = 2$ state, now attributed to the narrow line, to $k = 1$, as the rate for this process is amongst others determined by the spatial overlap between the corresponding exciton wavefunctions. Accordingly, due to the negligible overlap between the $k = 2$ and $k = 1$ exciton wavefunctions, it might be, that the narrow line reflects the comparatively slow relaxation of the $k = 2$ state to $k = 1$. In contrast, much more extended spatial overlaps with the $k = 1$ exciton wavefunction were found for the higher exciton states ($k \geq 3$), making a fast relaxation to $k = 1$ plausible and explaining the broad bands observed for these states in the excitation spectra.
If this new interpretation of the spectral characteristics turns out to be true, on the one hand this would prove the necessity of acquiring, at the same time, fluorescence-excitation and emission spectra from individual LH complexes to ensure the completeness of the excitation spectra for these complexes. On the other hand, this would call for a reinterpretation of the spectra not only from the preceding parts of this work, but also from previous single-molecule studies on RC-LH1 complexes.

Appendix - numerical simulations

A Coordinates of the LH1 model structures

Coordinates (x, y, z) of the positions of the central Mg^{2+} ions of the BChl *a* molecules and unit vectors, $\hat{n}$, of their corresponding Q_y transition-dipole moments of the LH1 model structures in this thesis. All entries are given in $\mathring{A}$.

Structure 1

Pigm.	x	y	z	n_x	n_y	n_z
1	-45.706	5.451	0.000	-0.318	0.937	-0.146
2	-45.317	14.886	-0.109	0.154	-0.978	-0.138
3	-39.268	20.929	0.000	0.133	0.980	-0.146
4	-34.717	29.203	-0.109	-0.298	-0.945	-0.138
5	-26.944	32.358	0.000	0.500	0.854	-0.146
6	-19.562	38.247	-0.109	-0.638	-0.758	-0.138
7	-11.327	38.641	0.000	0.756	0.638	-0.146
8	-2.401	41.725	-0.109	-0.854	-0.501	-0.138
9	5.486	39.578	0.000	0.918	0.369	-0.146
10	14.928	39.712	-0.109	-0.968	-0.208	-0.138
11	21.730	35.164	0.000	0.988	0.053	-0.146
12	30.708	32.239	-0.109	-0.984	0.116	-0.138
13	35.478	25.484	0.000	0.939	-0.310	-0.146
14	42.777	19.493	-0.109	-0.874	0.466	-0.138
15	44.280	11.200	0.000	0.718	-0.681	-0.146
16	48.337	2.673	-0.109	-0.593	0.793	-0.138
17	45.700	-5.483	0.000	0.317	-0.937	-0.146
18	45.303	-14.917	-0.109	-0.154	0.978	-0.138
19	39.248	-20.956	0.000	-0.134	-0.980	-0.146
20	34.690	-29.227	-0.109	0.298	0.944	-0.138
21	26.921	-32.372	0.000	-0.500	-0.854	-0.146
22	19.536	-38.257	-0.109	0.638	0.757	-0.138
23	-5.514	-39.575	0.000	-0.918	-0.369	-0.146
24	-14.956	-39.704	-0.109	0.968	0.208	-0.138
25	-21.762	-35.148	0.000	-0.988	-0.052	-0.146

Structure 1

Pigm.	x	y	z	n_x	n_y	n_z
26	-30.739	-32.217	-0.109	0.984	-0.116	-0.138
27	-35.502	-25.459	0.000	-0.939	0.311	-0.146
28	-42.796	-19.462	-0.109	0.874	-0.466	-0.138
29	-44.291	-11.169	0.000	-0.717	0.681	-0.146
30	-48.339	-2.638	-0.109	0.592	-0.794	-0.138

Structure 2

Pigm.	x	y	z	n_x	n_y	n_z
1	-46.295	6.801	1.369	-0.321	0.947	-0.030
2	-45.070	16.267	1.005	0.351	-0.930	-0.110
3	-39.658	21.231	1.142	0.069	0.931	-0.358
4	-33.789	30.013	0.277	-0.298	-0.920	-0.256
5	-26.302	34.810	0.125	0.536	0.829	-0.159
6	-18.719	40.166	-0.861	-0.440	-0.884	0.157
7	-10.329	39.814	-0.608	0.821	0.540	-0.184
8	-1.462	40.285	-1.049	-0.860	-0.456	-0.228
9	6.385	39.106	-0.503	0.871	0.380	-0.311
10	15.173	39.091	-2.029	-0.958	-0.287	0.025
11	24.749	35.565	-0.336	0.818	-0.085	-0.568
12	33.372	31.090	-1.256	-0.997	0.022	-0.074
13	37.405	26.199	-0.284	0.940	-0.308	-0.145
14	42.966	19.698	1.558	-0.911	0.395	-0.114
15	45.049	11.866	1.062	0.729	-0.659	-0.185
16	47.756	2.827	2.030	-0.700	0.697	-0.158
17	46.514	-5.370	-0.099	0.472	-0.881	0.017
18	45.810	-16.249	-0.244	-0.183	0.968	-0.174
19	40.255	-20.869	-0.526	0.205	-0.956	-0.210
20	35.431	-31.101	-0.353	0.162	0.984	-0.079
21	26.754	-34.157	-1.503	-0.275	-0.952	-0.130
22	19.307	-40.285	-1.264	0.656	0.726	-0.207
23	-4.186	-38.312	-1.831	-0.827	-0.503	-0.250
24	-14.009	-39.616	-2.028	0.945	0.323	-0.058
25	-21.625	-37.009	-1.787	-0.984	-0.150	-0.097
26	-30.955	-34.586	-1.614	0.983	0.037	-0.177
27	-36.644	-28.006	-0.493	-0.985	0.145	-0.092
28	-44.114	-21.425	-0.713	0.898	-0.408	-0.166
29	-45.169	-12.088	0.522	-0.717	0.697	-0.020
30	-47.755	-1.951	1.295	0.554	-0.813	-0.181

Structure 3

Pigm.	x	y	z	n_x	n_y	n_z
1	-45.273	6.000	0.000	-0.409	0.901	-0.146
2	-45.821	15.427	-0.109	0.251	-0.958	-0.138
3	-40.114	22.375	0.000	0.065	0.987	-0.146
4	-36.145	30.943	-0.109	-0.232	-0.963	-0.138
5	-27.833	34.371	0.000	0.524	0.839	-0.146
6	-20.287	40.048	-0.109	-0.659	-0.739	-0.138
7	-11.341	39.143	0.000	0.858	0.492	-0.146
8	-2.008	40.582	-0.109	-0.930	-0.340	-0.138
9	6.001	39.166	0.000	0.875	0.462	-0.146
10	15.380	40.271	-0.109	-0.942	-0.307	-0.138
11	23.034	36.701	0.000	0.983	0.108	-0.146
12	32.162	34.284	-0.109	-0.989	0.061	-0.138
13	36.985	26.696	0.000	0.918	-0.370	-0.146
14	43.889	20.253	-0.109	-0.843	0.520	-0.138
15	44.555	11.286	0.000	0.634	-0.759	-0.146
16	47.597	2.347	-0.109	-0.497	0.857	-0.138
17	45.269	-6.055	0.000	0.408	-0.901	-0.146
18	45.803	-15.483	-0.109	-0.249	0.959	-0.138
19	40.086	-22.421	0.000	-0.067	-0.987	-0.146
20	36.104	-30.983	-0.109	0.233	0.963	-0.138
21	27.786	-34.398	0.000	-0.525	-0.839	-0.146
22	20.232	-40.064	-0.109	0.660	0.738	-0.138
23	-6.055	-39.166	0.000	-0.875	-0.462	-0.146
24	-15.433	-40.271	-0.109	0.942	0.307	-0.138
25	-23.084	-36.681	0.000	-0.984	-0.106	-0.146
26	-32.208	-34.250	-0.109	0.988	-0.062	-0.138
27	-37.020	-26.655	0.000	-0.917	0.371	-0.146
28	-43.913	-20.201	-0.109	0.842	-0.522	-0.138
29	-44.566	-11.234	0.000	-0.633	0.760	-0.146
30	-47.594	-2.289	-0.109	0.496	-0.857	-0.138

Structure 3'

Pigm.	x	y	z	n_x	n_y	n_z
1	-45.273	6.000	0.000	-0.409	0.901	-0.146
2	-45.821	15.427	-0.109	0.251	-0.958	-0.138
3	-40.114	22.375	0.000	0.065	0.987	-0.146
4	-36.145	30.943	-0.109	-0.232	-0.963	-0.138
5	-27.833	34.371	0.000	0.524	0.839	-0.146
6	-20.287	40.048	-0.109	-0.659	-0.739	-0.138
7	-11.341	39.143	0.000	**0.840**	**0.522**	-0.146
8	**-2.064**	**40.907**	-0.109	**-0.918**	**-0.373**	-0.138
9	**8.001**	39.166	0.000	0.875	0.462	-0.146
10	**17.380**	40.271	-0.109	-0.942	-0.307	-0.138
11	**24.872**	**35.914**	0.000	**0.988**	**0.052**	-0.146
12	**33.849**	**32.983**	-0.109	**-0.984**	**0.116**	-0.138
13	36.985	26.696	0.000	**0.904**	**-0.401**	-0.146
14	**43.660**	**20.016**	-0.109	**-0.824**	**0.549**	-0.138
15	44.555	11.286	0.000	0.634	-0.759	-0.146
16	47.597	2.347	-0.109	-0.497	0.857	-0.138
17	45.269	-6.055	0.000	0.408	-0.901	-0.146
18	45.803	-15.483	-0.109	-0.249	0.959	-0.138
19	40.086	-22.421	0.000	-0.067	-0.987	-0.146
20	36.104	-30.983	-0.109	0.233	0.963	-0.138
21	27.786	-34.398	0.000	-0.525	-0.839	-0.146
22	20.232	-40.064	-0.109	0.660	0.738	-0.138
23	-6.055	-39.166	0.000	-0.875	-0.462	-0.146
24	-15.433	-40.271	-0.109	0.942	0.307	-0.138
25	-23.084	-36.681	0.000	-0.984	-0.106	-0.146
26	-32.208	-34.250	-0.109	0.988	-0.062	-0.138
27	-37.020	-26.655	0.000	-0.917	0.371	-0.146
28	-43.913	-20.201	-0.109	0.842	-0.522	-0.138
29	-44.566	-11.234	0.000	-0.633	0.760	-0.146
30	-47.594	-2.289	-0.109	0.496	-0.857	-0.138

The highlighted data indicate those entries for Structure 3', with changed values with respect to Structure 3.

B Simulated $k = 1$ exciton state energies - comparison with the experiment

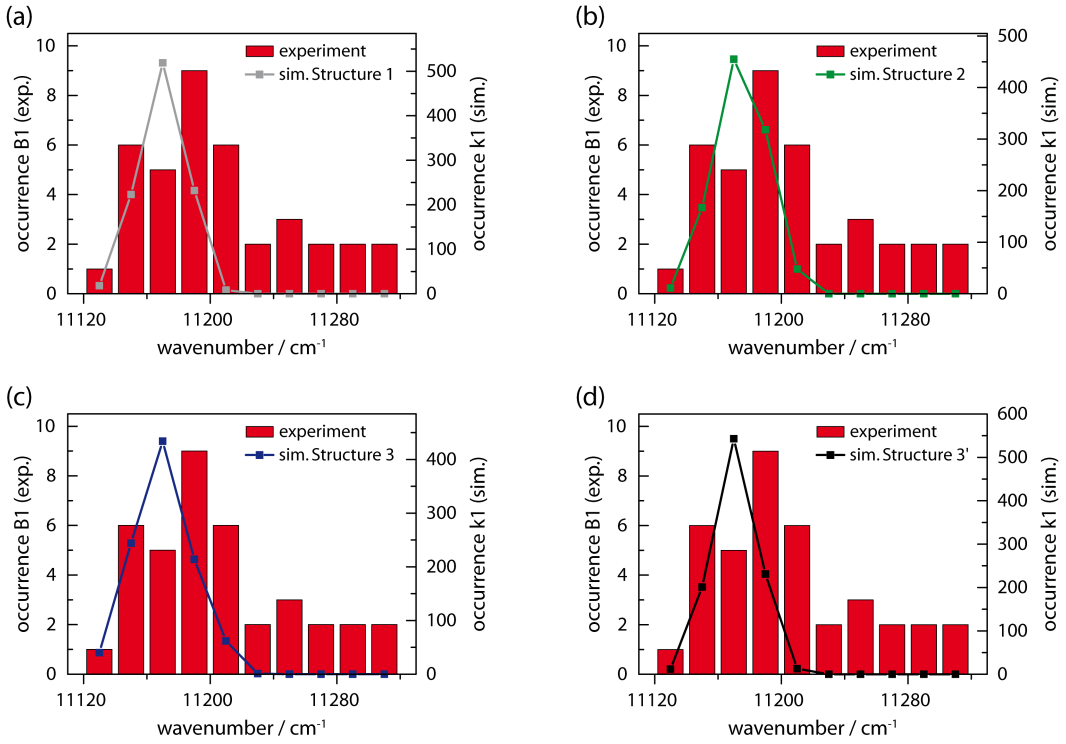

Figure B.1: *Comparison of the distribution of the spectral positions of the B1 band for the intact RC-LH1 complexes from Rps. acidophila embedded in a DDM/PVA matrix (red bars, 38 complexes) with the distributions of the $k = 1$ exciton state energies, calculated numerically for the four LH1 model structures (colored squares). For each model structure the numerical simulation was run for 1000 individual realizations of the pigment site energies (diagonal disorder, $\Delta = 100\ cm^{-1}$). Panel (a) shows the distribution of the $k = 1$ exciton state energies for Structure 1, (b) for Structure 2, (c) for Structure 3 and (d) for Structure 3'.*

In Figure B.1 the distribution of the spectral positions of the B1 band for the intact RC-LH1 complexes from *Rps. acidophila* stabilized in a DDM/PVA environment (red bars) is compared to the distributions of the $k = 1$ exciton state energies, calculated for the four LH1 model structures of this thesis (colored squares). Thereby, the mean site energy, E_0, of the pigments in the four LH1 models was adjusted individually for each structure, in order to achieve overlapping distributions for the spectral occurrence of the band B1 in the experiment and the calculated $k = 1$ exciton state energies. The resultant values for the mean site energy, E_0, were $12,590\ cm^{-1} \hat{=} 794.3\ nm$ in Structure 1, $12,500\ cm^{-1} \hat{=} 800\ nm$ in Structure 2, $12,680\ cm^{-1} \hat{=} 788.6\ nm$ in Structure 3 and $12,510\ cm^{-1} \hat{=} 799.4\ nm$ in Struc-

ture 3'. With these figures for E_0 all numerically calculated distributions of the $k = 1$ exciton state energies show a satisfying overlap with the low-energy part of the experimental B1 distribution, comprising the majority of the intact RC-LH1 complexes from *Rps. acidophila*.

Bibliography

[1] E. Romero, R. Augulis, V.I. Novoderezhkin, M. Ferretti, J. Thieme, D. Zigmantas and R. van Grondelle Quantum coherence in photosynthesis for efficient solar-energy conversion. *Nat. Phys.* **10** 676–682 (2014).

[2] R.J. Cogdell, A. Gall and J. Köhler The architecture and function of the light-harvesting apparatus of purple bacteria: from single molecules to *in vivo* membranes. *Q. Rev. Biophys.* **39** 227–324 (2006).

[3] S. Scheuring and J.N. Sturgis Chromatic Adaption of Photosynthetic Membranes. *Science* **309** 484–487 (2005).

[4] R.E. Blankenship Molecular Mechanisms of Photosynthesis. *Blackwell Science: Oxford* (2008).

[5] J. Strümpfer, M. Şener and K. Schulten How Quantum Coherence Assists Photosynthetic Light-Harvesting. *J. Phys. Chem. Lett.* **3** 536–542 (2012).

[6] G.S. Engel, T.R. Calhoun, E.L. Read, T.K. Ahn, T. Mancal, Y.C. Cheng, R.E. Blankenship and G.R. Fleming Evidence for wavelike energy transfer through quantum coherence in photosynthetic systems. *Nature* **446** 782–786 (2007).

[7] R. Hildner, D. Brinks, J.B. Nieder, R.J. Cogdell and N.F. van Hulst Quantum Coherent Energy Transfer over Varying Pathways in Single Light-Harvesting Complexes. *Science* **340** 1448–1451 (2013).

[8] R.J. Cogdell and A.W. Roszak The purple heart of photosynthesis. *Nature* **508** 196–197 (2014).

[9] S. Niwa, L.J. Yu, K. Takeda, Y. Hirano, T. Kawakami, Z.Y. Wang-Otomo and K. Miki Structure of the LH1-RC complex from *Thermochromatium tepidum* at 3.0 Å. *Nature* **508** 228–232 (2014).

[10] M. Ketelaars, C. Hofmann, J. Köhler, T.D. Howard, R.J. Cogdell, J. Schmidt and T.J. Aartsma Spectroscopy on Individual Light-Harvesting 1 Complexes of *Rhodopseudomonas acidophila*. *Biophys. J.* **83** 1701–1715 (2002).

[11] A.M. van Oijen, M. Ketelaars, J. Köhler, T.J. Aartsma and J. Schmidt Unraveling the Electronic Structure of Individual Photosynthetic Pigment-Protein Complexes. *Science* **285** 400–402 (1999).

[12] M.F. Richter, J. Baier, T. Prem, S. Oellerich, F. Francia, G. Venturoli, D. Oesterhelt, J. Southall, R.J. Cogdell and J. Köhler Symmetry matters for the electronic structure of core complexes from *Rhodopseudomonas palustris* and *Rhodobacter sphaeroides* PufX^{-}. *Proc. Natl. Acad. Sci. U. S. A.* **104** 6661–6665 (2007).

[13] M. Ketelaars, A.M. van Oijen, M. Matsushita, J. Köhler, J. Schmidt and T.J. Aartsma Spectroscopy on the B850 Band of Individual Light-Harvesting 2 Complexes of *Rhodopseudomonas acidophila*: I. Experiments and Monte-Carlo Simulations. *Biophys. J.* **80** 1591–1603 (2001).

[14] M. Matsushita, M. Ketelaars, A.M. van Oijen, J. Köhler, T.J. Aartsma and J. Schmidt Spectroscopy on the B850 Band of Individual Light-Harvesting 2 complexes of *Rhodopseudomonas acidophila*: II. Exciton states of an elliptically deformed ring aggregate. *Biophys. J.* **80** 1604–1614 (2001).

[15] M.F. Richter, J. Baier, J. Southall, R.J. Cogdell, S. Oellerich and J. Köhler Refinement of the x-ray structure of the RC-LH1 core complex from *Rhodopseudomonas palustris* by single-molecule spectroscopy. *Proc. Natl. Acad. Sci. U. S. A.* **104** 20280–20284 (2007).

[16] U. Gerken, F. Jelezko, B. Götze, M. Branschädel, C. Tietz, R. Ghosh and J. Wrachtrup Membrane Environment Reduces the Accessible Conformational Space Available to an Integral Membrane Protein. *J. Phys. Chem. B* **107** 338–343 (2003).

[17] L. Kangur, K. Timpmann and A. Freiberg Stability of Integral Membrane Proteins under High Hydrostatic Pressure: The LH2 and LH3 Antenna Pigment - Protein Complexes from Photosynthetic Bacteria. *J. Phys. Chem. B* **112** 7948–7955 (2008).

[18] D. Uchiyama, H. Hoshino, K. Otomo, T. Kato, K.i. Onda, A. Watanabe, H. Oikawa, S. Fujiyoshi, M. Matsushita, M. Nango et al. Single-protein study of photoresistance of pigment-protein complex in lipid bilayer. *Chem. Phys. Lett.* **511** 135–137 (2011).

[19] A. Freiberg, L. Kangur, J.D. Olsen and C.N. Hunter Structural Implications of Hydrogen-Bond Energetics in Membrane Proteins Revealed by High-Pressure Spectroscopy. *Biophys. J.* **103** 2352–2360 (2012).

[20] S. Bahatyrova, R.N. Frese, K.O. van der Werf, C. Otto, C.N. Hunter and J.D. Olsen Flexibility and Size Heterogeneity of the LH1 Light Harvesting Complex Revealed by Atomic Force Microscopy. *J. Biol. Chem.* **279** 21327–21333 (2004).

[21] W. Kühlbrandt Many wheels make light work. *Nature* **374** 497–498 (1995).

[22] A. Aird, J. Wrachtrup, K. Schulten and C. Tietz Possible Pathway for Ubiquinone Shuttling in *Rhodospirillum rubrum* Revealed by Molecular Dynamics Simulation. *Biophys. J.* **92** 23–33 (2007).

[23] S. Scheuring and J. Sturgis Atomic force microscopy of the bacterial photosynthetic apparatus: plain pictures of an eleborate machinery. *Photosynth. Res.* **102** 197–211 (2009).

[24] A.W. Roszak, T.D. Howard, J. Southall, A.T. Gardiner, C.J. Law, N.W. Isaacs and R.J. Cogdell Crystal structure of the RC-LH1 core complex from *Rhodopseudomonas palustris*. *Science* **302** 1969–1971 (2003).

[25] S. Scheuring, D. Lévy and J.L. Rigaud Watching the components of photosynthetic bacterial membranes and their in situ organisation by atomic force microscopy. *Biochim. Biophys. Acta* **1712** 109–127 (2005).

[26] S. Scheuring AFM studies of the supramolecular assembly of bacterial photosynthetic core-complexes. *Curr. Opin. Chem. Biol.* **10** 387–393 (2006).

[27] V. Sundström, T. Pullerits and R. van Grondelle Photosynthetic Light-Harvesting: Reconciling Dynamics and Structure of Purple Bacterial LH2 Reveals Function of Photosynthetic Unit. *J. Phys. Chem. B* **103** 2327–2346 (1999).

[28] I.P. Mercer, I.R. Gould and D.R. Klug A Quantum Mechanical/Molecular Mechanical Approach to Relaxation Dynamics: Calculation of the Optical Properties of Solvated Bacteriochlorophyll-a. *J. Phys. Chem. B* **103** 7720–7727 (1999).

[29] C. Hofmann Pigment-Pigment Interactions and Protein Dynamics in Light-Harvesting Complexes: a Single-Molecule Study. *Ph.D. Thesis: Universität Bayreuth* (2004).

[30] I. Renge and K. Mauring Spectral shift mechanisms of chlorophylls in liquids and proteins. *Spectrochim. Acta A* **102** 301–313 (2013).

[31] G. Uyeda, J.C. Williams, M. Roman, T.A. Mattioli and J.P. Allen The Influence of Hydrogen Bonds on the Electronic Structure of Light-Harvesting Complexes from Photosynthetic Bacteria. *Biochemistry* **49** 1146–1159 (2010).

[32] A. Gall, S. Henry, S. Takaichi, B. Robert and R.J. Cogdell Preferential incorporation of coloured-carotenoids occurs in the LH2 complexes from non-sulphur purple bacteria under carotenoid-limiting conditions. *Photosynth. Res.* **86** 25–35 (2005).

[33] R.J. Cogdell and H.A. Frank How carotenoids function in photosynthetic bacteria. *Biochim. Biophys. Acta* **895** 63–79 (1987).

[34] G. McDermott, S.M. Prince, A.A. Freer, A.M. Hawthornthwaite-Lawless, M.Z. Papiz, R.J. Cogdell and N.W. Isaacs Crystal structure of an integral membrane light-harvesting complex from photosynthetic bacteria. *Nature* **374** 517–521 (1995).

[35] M.Z. Papiz, S.M. Prince, T. Howard, R.J. Cogdell and N.W. Isaacs The Structure and Thermal Motion of the B800-850 LH2 Complex from *Rps. acidophila* at 2.0 ÅResolution and 100 K: New Structural Features and Functionally Relevant Motions. *J. Mol. Biol.* **326** 1523–1538 (2003).

[36] V. Cherezov, J. Clogston, M.Z. Papiz and M. Caffrey Room to Move: Crystallizing Membrane Proteins in Swollen Lipidic Mesophases. *J. Mol. Biol.* **357** 1605–1618 (2006).

[37] P. Qian, M.Z. Papiz, P.J. Jackson, A.A. Brindley, I.W. Ng, J.D. Olsen, M.J. Dickman, P.A. Bullough and N.C. Hunter Three-Dimensional Structure of the *Rhodobacter sphaeroides* RC-LH1-PufX Complex: Dimerization and Quinone Channels Promoted by PufX. *Biochemistry* **52** 7575–7585 (2013).

[38] U. Ermler, G. Fritzsch, S.K. Buchanan and H. Michel Structure of the photosynthetic reaction centre from *Rhodobacter sphaeroides* at 2.65 Å resolution: cofactors and protein-cofactor interactions. *Structure* **2** 925–936 (1994).

[39] S. Scheuring, J. Seguin, S. Marco, D. Lévy, B. Robert and J.L. Rigaud Nanodissection and high-resolution imaging of the *Rhodopseudomonas viridis* photosynthetic core complex in native membranes by AFM. *Proc. Natl. Acad. Sci. U. S. A.* **100** 1690–1693 (2003).

[40] J.F. Miller, S.B. Hinchigeri, P.S. Parkes-Loach, P.M. Callahan, J.R. Sprinkle, J.R. Riccobono and P.A. Loach Isolation and Characterization of a Subunit form of the Light-Harvesting Complex of *Rhodospirillum rubrum*. *Biochemistry* **26** 5055–5062 (1987).

[41] A. Pandit, R.W. Visschers, I.H.M. van Stokkum, R. Kraayenhof and R. van Grondelle Oligomerization of Light-Harvesting I Antenna Peptides of *Rhodospirillum rubrum*. *Biochemistry* **40** 12913–12924 (2001).

[42] W.H.J. Westerhuis, C.N. Hunter, R. van Grondelle and R.A. Niederman Modeling of Oligomeric-State Dependent Spectral Heterogeneity in the B875 Light-Harvesting Complex of *Rhodobacter sphaeroides* by Numerical Simulation. *J. Phys. Chem. B* **103** 7733–7742 (1999).

[43] W.H.J. Westerhuis, J.N. Sturgis, E.C. Ratcliffe, C.N. Hunter and R.A. Niederman Isolation, Size Estimates, and Spectral Heterogeneity of an Oligomeric Series of Light-Harvesting 1 Complexes from *Rhodobacter sphaeroides*. *Biochemistry* **41** 8698–8707 (2002).

[44] U. Gerken, D. Lupo, C. Tietz, J. Wrachtrup and R. Ghosh Circular Symmetry of the Light-Harvesting 1 Complex from *Rhodospirillum rubrum* is Not Perturbed by Interaction with the Reaction Center. *Biochemistry* **42** 10354–10360 (2003).

[45] R. Winter and F. Noll Methoden der Biophysikalischen Chemie. *Teubner: Stuttgart* (1998).

[46] P.W. Atkins Physikalische Chemie. *Wiley-VCH: Weinheim* (2001).

[47] Sigma-Aldrich. *Product Catalog* (2014).

[48] M.F. Richter Symmetry Matters for the Electronic Structure of Light-Harvesting Complexes. *Ph.D. Thesis: Universität Bayreuth* (2008).

[49] A.M. Seddon, P. Curnow and P.J. Booth Membrane proteins, lipids and detergents: not just a soap opera. *Biochim. Biophys. Acta* **1666** 105–117 (2004).

[50] T.C. Kaufmann, A. Engel and H.W. Rémigy A Novel Method for Detergent Concentration Determination. *Biophys. J.* **90** 310–317 (2006).

[51] F. Sterpone, G. Marchetti, C. Pierleoni and M. Marchi Molecular Modeling and Simulation of Water near Model Micelles: Diffusion, Rotational Relaxation and Structure at the Hydration Interface. *J. Phys. Chem. B* **110** 11504–11510 (2006).

[52] S. Abel, F.Y. Dupradeau, E.P. Raman, A.D. MacKerell Jr. and M. Marchi Molecular Simulations of Dodecyl-β-maltoside Micelles in Water: Influence of the Headgroup Conformation and Force Field Parameters. *J. Phys. Chem. B* **115** 487–499 (2011).

[53] L. Stryer Biochemistry. *H. W. Freeman and Company: New York* (2000).

[54] Avanti Polar Lipids. *Product Catalog* (2014).

[55] H. Haken and H.C. Wolf Molekülphysik und Quantenchemie. *Springer: Berlin* (2005).

[56] R. Monshouwer, M. Abrahamson, F. van Mourik and R. van Grondelle Superradiance and Exciton Delocalization in Bacterial Photosynthetic Light-Harvesting Systems. *J. Phys. Chem. B* **101** 7241–7248 (1997).

[57] T. Basché, S. Kummer and C. Bräuchle Excitation and Emission Spectroscopy and Quantum Optical Measurements, in "Single-Molecule Optical Detection, Imaging and Spectroscopy" Ed. T. Basché, W.E. Moerner, M. Orrit and U.P. Wild *VCH: Weinheim* pp. 31–67 (1996).

[58] R. Jankowiak, M. Reppert, V. Zazubovich, J. Pieper and T. Reinot Site Selective and Single Complex Laser-Based Spectroscopies: A Window on Excited State Electronic Structure, Excitation Energy Transfer, and Electron-Phonon Coupling of Selected Photosynthetic Complexes. *Chem. Rev.* **111** 4546–4598 (2011).

[59] J. Knoester and V.M. Agranovich Frenkel and charge-transfer excitons in organic solids, in "Thin Films and Nanostructures" Ed. V.M. Agranovich and G.F. Bassani *Elsevier: Amsterdam* pp. 1–96 (2003).

[60] X. Hu, T. Ritz, A. Damjanovic and K. Schulten Pigment Organization and Transfer of Electronic Excitation in the Photosynthetic Unit of Purple Bacteria. *J. Phys. Chem. B* **101** 3854–3871 (1997).

[61] H. van Amerongen, L. Valkunas and R. van Grondelle Photosynthetic Excitons. *World Scientific: Singapore* (2000).

[62] K. Sauer, R.J. Cogdell, S.M. Prince, A.A. Freer, N.W. Isaacs and H. Scheer Structure Based Calculations of the Optical Spectra of the LH2 Bacteriochlorophyll-Protein Complex from *Rhodopseudomonas acidophila*. *Photochem. Photobiol.* **64** 564–576 (1996).

[63] B.P. Krueger, G.D. Scholes and G.R. Fleming Calculation of Couplings and Energy-Transfer Pathways between the Pigments of LH2 by the ab Initio Transition Density Cube Method. *J. Phys. Chem. B* **102** 5378–5387 (1998).

[64] R.G. Alden, E. Johnson, V. Nagarajan, W.W. Parson, C.J. Law and R.J. Cogdell Calculations of Spectroscopic Properties of the LH2 Bacteriochlorophyll-Protein Antenna complex from *Rhodopseudomonas acidophila*. *J. Phys. Chem. B* **101** 4667–4680 (1997).

[65] G.D. Scholes, I.R. Gould, R.J. Cogdell and G.R. Fleming *Ab Initio* Molecular Orbital Calculations of Electronic Couplings in the LH2 Bacterial Light-Harvesting Complex of *Rps. Acidophila*. *J. Phys. Chem. B* **103** 2543–2553 (1999).

[66] M.G. Cory, M.C. Zerner, X. Hu and K. Schulten Electronic Excitations in Aggregates of Bacteriochlorophylls. *J. Phys. Chem. B* **102** 7640–7650 (1998).

[67] R.M. Hochstrasser and J.D. Whiteman Exciton Band Structure and Properties of a Real Linear Chain in a Molecular Crystal. *J. Chem. Phys.* **56** 5945–5958 (1972).

[68] H. Fidder, J. Knoester and D.A. Wiersma Optical properties of disordered molecular aggregates: A numerical study. *J. Chem. Phys.* **95** 7880–7890 (1991).

[69] C. Kittel Einführung in die Festkörperphysik. *Oldenbourg: München* (2006).

[70] S.E. Dempster, S. Jang and R.J. Silbey Single molecule spectroscopy of disordered circular aggregates: A perturbation analysis. *J. Chem. Phys.* **114** 10015–10023 (2001).

[71] S. Karrasch, P.A. Bullough and R. Ghosh The 8.5 Å projection map of the light harvesting complex I from *Rhodospirillum rubrum* reveals a ring composed of 16 subunits. *EMBO J.* **14** 631–638 (1995).

[72] C. Hofmann, M. Ketelaars, M. Matsushita, H. Michel, T.J. Aartsma and J. Köhler Single-Molecule Study of the Electronic Couplings in a Circular Array of Molecules: Light-Harvesting-2 Complex from *Rhodospirillum molischianum*. *Phys. Rev. Lett.* **90** 013004 (2003).

[73] W.E. Moerner and L. Kador Optical Detection and Spectroscopy of Single Molecules in a Solid. *Phys. Rev. Lett.* **62** 2535–2538 (1989).

[74] M. Orrit and J. Bernard Single Pentacene Molecules Detected by Fluorescence Excitation in a *p*-Terphenyl Crystal. *Phys. Rev. Lett.* **65** 2716–2719 (1990).

[75] T.D. Howard, K. McAuley and R.J. Cogdell Crystallization of Membrane Proteins, in "Membrane Transport" Ed. S. Baldwin *Oxford University Press: Oxford* pp. 269–307 (2000).

[76] A. Stamouli, S. Kafi, D.C.G. Klein, T.H. Oosterkamp, J.W.M. Frenken, R.J. Cogdell and T.J. Aartsma The Ring Structure and Organization of Light Harvesting 2 Complexes in a Reconstituted Lipid Bilayer, Resolved by Atomic Force Microscopy. *Biophys. J.* **84** 2483–2491 (2003).

[77] M.F. Richter, J. Baier, R.J. Cogdell, J. Köhler and S. Oellerich Single-Molecule Spectroscopic Characterization of Light-Harvesting 2 Complexes Reconstituted into Model Membranes. *Biophys. J.* **93** 183–191 (2007).

[78] T.J. Pflock, S. Oellerich, L. Krapf, J. Southall, R.J. Cogdell, G.M. Ullmann and J. Köhler The Electronically Excited States of LH2

Complexes from *Rhodopseudomonas acidophila* Strain 10050 Studied by Time-Resolved Spectroscopy and Dynamic Monte Carlo Simulations. II. Homo-Arrays Of LH2 Complexes Reconstituted Into Phospholipid Model Membranes. *J. Phys. Chem. B* **115** 8821–8831 (2011).

[79] R.K. Clayton and B.J. Clayton B850 pigment-protein complex of *Rhodopseudomonas sphaeroides*: Extinction coefficients, circular dichroism, and the reversible binding of bacteriochlorophyll. *Proc. Natl. Acad. Sci. U. S. A.* **78** 5583–5587 (1981).

[80] S. Oellerich and J. Köhler Low-temperature single-molecule spectroscopy on photosynthetic pigment-protein complexes from purple bacteria. *Photosynth. Res.* **101** 171–179 (2009).

[81] E. Lang, J. Baier and J. Köhler Epifluorescence, confocal and total internal reflection microscopy for single-molecule experiments: a quantitative comparison. *J. Microsc.* **222** 118–123 (2006).

[82] R.E. Kunz Spectroscopic Investigations of Light-Harvesting 2 Complexes from *Rps. acidophila* - Fluorescence-Excitation and Emission Spectroscopy on Ensembles and Individual Complexes. *Ph.D. Thesis: Universität Bayreuth* (2014).

[83] H.M. Wu, M. Rätsep, I.J. Lee, R.J. Cogdell and G.J. Small Exciton Level Structure and Energy Disorder of the B850 Ring of the LH2 Antenna Complex. *J. Phys. Chem. B* **101** 7654–7663 (1997).

[84] L.D. Bakalis, M. Coca and J. Knoester Optical line shapes of dynamically disordered ring aggregates. *J. Chem. Phys.* **110** 2208–2218 (1999).

[85] M.V. Mostovoy and J. Knoester Statistics of Optical Spectra from Single-Ring Aggregates and its Application to LH2. *J. Phys. Chem. B* **104** 12355–12364 (2000).

[86] X. Hu, T. Ritz, A. Damjanovic, F. Autenrieth and K. Schulten Photosynthetic apparatus of purple bacteria. *Q. Rev. Biophys.* **35** 1–62 (2002).

[87] S. Jang and R.J. Silbey Single complex line shapes of the B850 band of LH2. *J. Chem. Phys.* **118** 9324–9336 (2003).

[88] S. Jang, R.J. Silbey, R. Kunz, C. Hofmann and J. Köhler Is There Elliptic Distortion in the Light Harvesting Complex 2 of Purple Bacteria?. *J. Phys. Chem. B* **115** 12947–12953 (2011).

[89] A. Freiberg and K. Timpmann Picosecond fluorescence spectroscopy of light-harvesting antenna complexes from *Rhodospirillum rubrum* in the 300-4 K

temperature range. Comparison with the data on chromatophores. *J. Photochem. Photobiol. B: Biol.* **15** 151–158 (1992).

[90] S.I.E. Vulto, J.T.M. Kennis, A.M. Streltsov, J. Amesz and T.J. Aartsma Energy Relaxation within the B850 Absorption Band of the Isolated Light-Harvesting Complex LH2 from *Rhodopseudomonas acidophila* at Low Temperature. *J. Phys. Chem. B* **103** 878–883 (1999).

[91] E. Lang, R. Hildner, H. Engelke, P. Osswald, F. Würthner and J. Köhler Comparison of the Photophysical Parameters for Three Perylene Bisimide Derivatives by Single-Molecule Spectroscopy. *Chem. Phys. Chem.* **8** 1487–1496 (2007).

[92] M. Richter, J. Baier, J. Southall, R. Cogdell, S. Oellerich and J. Köhler Spectral diffusion of the lowest exciton component in the core complex from *Rhodopseudomonas palustris* studied by single-molecule spectroscopy. *Photosynth. Res.* **95** 285–290 (2008).

[93] L. Janosi, I. Kosztin and A. Damjanović Theoretical prediction of spectral and optical properties of bacteriochlorophylls in thermally disordered LH2 antenna complexes. *J. Chem. Phys.* **125** 014903 (2006).

[94] C. Hofmann, T.J. Aartsma and J. Köhler Energetic disorder and the B850-exciton states of individual light-harvesting 2 complexes from *Rhodopseudomonas acidophila*. *Chem. Phys. Lett.* **395** 373–378 (2004).

[95] D. Fotiadis, P. Qian, A. Philippsen, P.A. Bullough, A. Engel and C.N. Hunter Structural Analysis of the Reaction Center Light-Harvesting Complex I Photosynthetic Core Complex of *Rhodospirillum rubrum* Using Atomic Force Microscopy. *J. Biol. Chem.* **279** 2063–2068 (2004).

[96] P. Strop and A.T. Brunger Refractive index-based determination of detergent concentration and its application to the study of membrane proteins. *Protein Sci.* **14** 2207–2211 (2005).

[97] M.A. Bopp, Y. Jia, L. Li, R.J. Cogdell and R.M. Hochstrasser Fluorescence and photobleaching dynamics of single light-harvesting complexes. *Proc. Natl. Acad. Sci. U. S. A.* **94** 10630–10635 (1997).

[98] L. Ying and S. Xie Fluorescence Spectroscopy, Exciton Dynamics, and Photochemistry of Single Allophycocyanin Trimers. *J. Phys. Chem. B* **102** 10399–10409 (1998).

[99] M.A. Bopp, A. Sytnik, T.D. Howard, R.J. Cogdell and R.M. Hochstrasser The dynamics of structural deformations of immobilized single light-harvesting complexes. *Proc. Natl. Acad. Sci. U. S. A.* **96** 11271–11276 (1999).

[100] C. Tietz, O. Cheklov, A. Dräbenstedt, J. Schuster and J. Wrachtrup Spectroscopy on Single Light-Harvesting Complexes at Low Temperature. *J. Phys. Chem. B* **103** 6328–6333 (1999).

[101] F. Jelezko, C. Tietz, U. Gerken, J. Wrachtrup and R. Bittl Single-Molecule Spectroscopy on Photosystem I Pigment-Protein Complexes. *J. Phys. Chem. B* **104** 8093–8096 (2000).

[102] C. Tietz, F. Jelezko, U. Gerken, S. Schuler, A. Schubert, H. Rogl and J. Wrachtrup Single Molecule Spectroscopy on the Light-Harvesting Complex II of Higher Plants. *Biophys. J.* **81** 556–562 (2001).

[103] C. Hofmann, T.J. Aartsma, H. Michel and J. Köhler Direct observation of tiers in the energy landscape of a chromoprotein: A single-molecule study. *Proc. Natl. Acad. Sci. U. S. A.* **100** 15534–15538 (2003).

[104] V.I. Novoderezhkin, D. Rutkauskas and R. van Grondelle Dynamics of the Emission Spectrum of a Single LH2 Complex: Interplay of Slow and Fast Nuclear Motions. *Biophys. J.* **90** 2890–2902 (2006).

[105] D. Rutkauskas, J. Olsen, A. Gall, R.J. Cogdell, C.N. Hunter and R. van Grondelle Comparative Study of Spectral Flexibilities of Bacterial Light-Harvesting Complexes: Structural Implications. *Biophys. J.* **90** 2463–2474 (2006).

[106] D. Rutkauskas, R.J. Cogdell and R. van Grondelle Conformational Relaxation of Single Bacterial Light-Harvesting Complexes. *Biochemistry* **45** 1082–1086 (2006).

[107] Y. Berlin, A. Burin, J. Friedrich and J. Köhler Low temperature spectroscopy of proteins. Part II: Experiments with single protein complexes. *Phys. Life Rev.* **4** 64–89 (2007).

[108] J. Baier, M.F. Richter, R.J. Cogdell, S. Oellerich and J. Köhler Determination of the Spectral Diffusion Kernel of a Protein by Single-Molecule Spectroscopy. *Phys. Rev. Lett.* **100** 018108 (2008).

[109] H. Oikawa, S. Fujiyoshi, T. Dewa, M. Nango and M. Matsushita How Deep Is the Potential Well Confining a Protein in a Specific Conformation? A Single-Molecule Study on Temperature Dependence of Conformational Change between 5 and 18 K. *J. Am. Chem. Soc.* **130** 4580–4581 (2008).

[110] M. Brecht, V. Radics, J.B. Nieder, H. Studier and R. Bittl Red Antenna States of Photosystem I from *Synechocystis* PCC 6803. *Biochemistry* **47** 5536–5543 (2008).

[111] T.P.J. Krüger, V.I. Novoderezhkin, C. Ilioaia and R. van Grondelle Fluorescence Spectral Dynamics of Single LHCII Trimers. *Biophys. J.* **98** 3093–3101 (2010).

[112] S. Tubasum, R.J. Cogdell, I.G. Scheblykin and T. Pullerits Excitation – Emission Polarization Spectroscopy of Single Light Harvesting Complexes. *J. Phys. Chem. B* **115** 4963–4970 (2011).

[113] S. Furumaki, F. Vacha, S. Habuchi, Y. Tsukatani, D.A. Bryant and M. Vacha Absorption Linear Dichroism Measured Directly on a Single Light-Harvesting System: The Role of Disorder in Chlorosomes of Green Photosynthetic Bacteria. *J. Am. Chem. Soc.* **133** 6703–6710 (2011).

[114] D. Uchiyama, H. Oikawa, K. Otomo, M. Nango, T. Dewa, S. Fujiyoshi and M. Matsushita Reconstitution of bacterial photosynthetic unit in a lipid bilayer studied by single-molecule spectroscopy at 5 K. *Phys. Chem. Chem. Phys.* **13** 11615–11619 (2011).

[115] R. Kunz, K. Timpmann, J. Southall, R.J. Cogdell, A. Freiberg and J. Köhler Exciton Self Trapping in Photosynthetic Pigment-Protein Complexes Studied by Single-Molecule Spectroscopy. *J. Phys. Chem. B* **116** 11017–11023 (2012).

[116] S. Tubasum, S. Sakai, T. Dewa, V. Sundström, I.G. Scheblykin, M. Nango and T. Pullerits Anchored LH2 Complexes in 2D Polarization Imaging. *J. Phys. Chem. B* **117** 11391–11396 (2013).

[117] G.S. Schlau-Cohen, Q. Wang, J. Southall, R.J. Cogdell and W.E. Moerner Single-molecule spectroscopy reveals photosynthetic LH2 complexes switch between emissive states. *Proc. Natl. Acad. Sci. U. S. A.* **110** 10899–10903 (2013).

[118] M. Hussels and M. Brecht Effect of Glycerol and PVA on the Conformation of Photosystem I. *Biochemistry* **50** 3628–3637 (2011).

[119] A. Freiberg, M. Rätsep and K. Timpmann A comparative spectroscopic and kinetic study of photoexcitations in detergent-isolated and membrane-embedded LH2 light-harvesting complexes. *Biochim. Biophys. Acta, Bioenerg.* **1817** 1471–1482 (2012).

[120] H.M. Wu, M. Rätsep, R. Jankowiak, R.J. Cogdell and G.J. Small Hole-Burning and Absorption Studies of the LH1 Antenna Complex of Purple Bacteria: Effects of Pressure and Temperature. *J. Phys. Chem. B* **102** 4023–4034 (1998).

[121] A. Freiberg, M. Rätsep, K. Timpmann and G. Trinkunas Excitonic polarons in quasi-one-dimensional LH1 and LH2 bacteriochlorophyll *a* antenna aggregates from photosynthetic bacteria: A wavelength-dependent selective spectroscopy study. *Chem. Phys.* **357** 102–112 (2009).

[122] S.P. Rajapaksha, Y. He and H.P. Lu Combined topographic, spectroscopic, and model analyses of inhomogeneous energetic coupling of linear light harvesting complex II aggregates in native photosynthetic membranes. *Phys. Chem. Chem. Phys.* **15** 5636–5647 (2013).

[123] A. Schubert, A. Stenstam, W.J.D. Beenken, J.L. Herek, R. Cogdell, T. Pullerits and V. Sundström In Vitro Self-Assembly of the Light Harvesting Pigment-Protein LH2 Revealed by Ultrafast Spectroscopy and Electron Microscopy. *Biophys. J.* **86** 2363–2373 (2004).

[124] F. Yang, L.J. Yu, P. Wang, X.C. Ai, Z.Y. Wang and J.P. Zhang Effects of Aggregation on the Excitation Dynamics of LH2 from *Thermochromatium tepidum* in Aqueous Phase and in Chromatophores. *J. Phys. Chem. B* **115** 7906–7913 (2011).

[125] J.N. Sturgis, A. Gall, A. Ellervee, A. Freiberg and B. Robert The Effect of Pressure on the Bacteriochlorophyll *a* Binding Sites of the Core Antenna Complex from *Rhodospirillum rubrum*. *Biochemistry* **37** 14875–14880 (1998).

[126] A. Freiberg, A. Ellervee, P. Kukk, A. Laisaar, M. Tars and K. Timpmann Pressure effects on spectra of photosynthetic light-harvesting pigment-protein complexes. *Chem. Phys. Lett.* **214** 10–16 (1993).

[127] K. Timpmann, A. Ellervee, T. Pullerits, R. Ruus, V. Sundström and A. Freiberg Short-Range Exciton Couplings in LH2 Photosynthetic Antenna Proteins Studied by High Hydrostatic Pressure Absorption Spectroscopy. *J. Phys. Chem. B* **105** 8436–8444 (2001).

[128] M. Mukherjee, M. Bhattacharya, M.K. Sanyal, T. Geue, J. Grenzer and U. Pietsch Reversible negative thermal expansion of polymer films. *Phys. Rev. E* **66** 061801 (2002).

[129] A. Issac, C. von Borczyskowski and F. Cichos Correlation between photoluminescence intermittency of CdSe quantum dots and self-trapped states in dielectric media. *Phys. Rev. B* **71** 161302 (2005).

[130] C.J. Law and R.J. Cogdell The effect of chemical oxidation on the fluorescence of the LH1 (B880) complex from the purple bacterium *Rhodobium marinum*. *FEBS Lett.* **432** 27–30 (1998).

[131] S. Unterkofler, T. Pflock, J. Southall, R.J. Cogdell and J. Köhler Fluorescence Blinking of the RC-LH1 Complex from *Rhodopseudomonas palustris*. *Chem. Phys. Chem.* **12** 711–716 (2011).

[132] B.B. Owen, R.C. Miller, C.E. Milner and H.L. Cogan The Dielectric Constant of Water as a Function of Temperature and Pressure. *J. Phys. Chem.* **65** 2065–2070 (1961).

[133] R.B.M. Koehorst, R.B. Spruijt, F.J. Vergeldt and M.A. Hemminga Lipid Bilayer Topology of the Transmembrane α-Helix of M13 Major Coat Protein and Bilayer Polarity Profile by Site-Directed Fluorescence Spectroscopy. *Biophys. J.* **87** 1445-1455 (2004).

[134] A. Freiberg, M. Pajusalu and M. Rätsep Excitons in Intact Cells of Photosynthetic Bacteria. *J. Phys. Chem. B* **117** 11007–11014 (2013).

[135] R. Kunz, K. Timpmann, J. Southall, R.J. Cogdell, J. Köhler and A. Freiberg Fluorescence-Excitation and Emission Spectra from LH2 Antenna Complexes of *Rhodopseudomonas acidophila* as a Function of the Sample Preparation Conditions. *J. Phys. Chem. B* **117** 12020–12029 (2013).

[136] A.S. Davydov Theory of Molecular Excitons. *Plenum Press: New York* (1971).

[137] M.C. Chang, P.M. Callahan, P.S. Parkes-Loach, T.M. Cotton and P.A. Loach Spectroscopic Characterization of the Light-Harvesting Complex of *Rhodospirillum rubrum* and Its Structural Subunit. *Biochemistry* **29** 421–429 (1990).

[138] S.J. Jamieson, P. Wang, P. Qian, J.Y. Kirkland, M.J. Conroy, C.N. Hunter and P.A. Bullough Projection Structure of the Photosynthetic Reaction Centre-Antenna Complex of *Rhodospirillum rubrum* at 8.5 Å Resolution. *EMBO J.* **21** 3927–3935 (2002).

[139] S. Scheuring, R.P. Goncalves, V. Prima and J.N. Sturgis The Photosynthetic Apparatus of *Rhodopseudomonas palustris*: Structures and Organization. *J. Mol. Biol.* **358** 83–96 (2006).

[140] M. Şener, J. Hsin, L.G. Trabuco, E. Villa, P. Qian, C.N. Hunter and K. Schulten Structural model and excitonic properties of the dimeric RC-LH1-PufX complex from *Rhodobacter sphaeroides*. *Chem. Phys.* **357** 188–197 (2009).

[141] M.K. Şener, J.D. Olsen, C.N. Hunter and K. Schulten Atomic-level structural and functional model of a bacterial photosynthetic membrane vesicle. *Proc. Natl. Acad. Sci. U. S. A.* **104** 15723–15728 (2007).

[142] R.W. Visschers, M.C. Chang, F. van Mourik, P.S. Parkes-Loach, B.A. Heller, P.A. Loach and R. van Grondelle Fluorescence Polarization and Low-Temperature Absorption Spectroscopy of a Subunit Form of Light-Harvesting Complex I from Purple Photosynthetic Bacteria. *Biochemistry* **30** 5734–5742 (1991).

[143] D. Kleinfeld, M.Y. Okamura and G. Feher Electron-Transfer Kinetics in Photosynthetic Reaction Centers Cooled to Cryogenic Temperatures in the Charge-Separated State: Evidence for Light-Induced Structural Changes. *Biochemistry* **23** 5780–5786 (1984).

[144] Q. Xu and M.R. Gunner Trapping Conformational Intermediate States in the Reaction Center Protein from Photosynthetic Bacteria. *Biochemistry* **40** 3232–3241 (2001).

[145] H.M. Wu and G.J. Small Symmetry Based Analysis of the Effects of Random Energy Disorder on the Excitonic Level Structure of Cyclic Arrays: Application to Photosynthetic Antenna Complexes. *J. Phys. Chem. B* **102** 888–898 (1998).

[146] J. Baier, M.F. Richter, R.J. Cogdell, S. Oellerich and J. Köhler Do Proteins at Low Temperature Behave as Glasses? A Single-Molecule Study. *J. Phys. Chem. B* **111** 1135–1138 (2007).

[147] K. Timpmann, G. Trinkunas, P. Qian, C.N. Hunter and A. Freiberg Excitons in core LH1 antenna complexes of photosynthetic bacteria: Evidence for strong resonant coupling and off-diagonal disorder. *Chem. Phys. Lett.* **414** 359–363 (2005).

[148] R. Kunz, K. Timpmann, J. Southall, R.J. Cogdell, A. Freiberg and J. Köhler Single-Molecule Spectroscopy Unmasks the Lowest Exciton State of the B850 Assembly in LH2 from *Rps. acidophila*. *Biophys. J.* **106** 2008–2016 (2014).

[149] M. Bednarz, V.A. Malyshev and J. Knoester Temperature Dependent Fluorescence in Disordered Frenkel Chains: Interplay of Equilibration and Local Band-Edge Level Structure. *Phys. Rev. Lett.* **91** 217401 (2003).

[150] M. Bednarz, V.A. Malyshev and J. Knoester Low-temperature dynamics of weakly localized Frenkel excitons in disordered linear chains. *J. Chem. Phys.* **120** 3827–3840 (2004).

[151] V.I. Novoderezhkin, T.A. Cohen Stuart and R. van Grondelle Dynamics of Exciton Relaxation in LH2 Antenna Probed by Multipulse Nonlinear Spectroscopy. *J. Phys. Chem. A* **115** 3834–3844 (2011).

[152] C. Hofmann, H. Michel, M. van Heel and J. Köhler Multivariate Analysis of Single-Molecule Spectra: Surpassing Spectral Diffusion. *Phys. Rev. Lett.* **94** 195501 (2005).

[153] J. Baier, M. Gabrielsen, S. Oellerich, H. Michel, M. van Heel, R.J. Cogdell and J. Köhler Spectral Diffusion and Electron-Phonon Coupling of the B800 BChl *a* Molecules in LH2 Complexes from Three Different Species of Purple Bacteria. *Biophys. J.* **97** 2604–2612 (2009).

[154] R. Kunz, K. Timpmann, J. Southall, R.J. Cogdell, A. Freiberg and J. Köhler Fluctuations in the Electron-Phonon Coupling of a Single Chromoprotein. *Angew. Chem. Int. Ed.* **52** 8726–8730 (2013).

[155] R. Atta-Fynn, P. Biswas and D.A. Drabold Electron-phonon coupling is large for localized states. *Phys. Rev. B* **69** 245204 (2004).

[156] J. Hernando, E.M.H.P. van Dijk, J.P. Hoogenboom, J.J. Garcia-Lopez, D.N. Reinhoudt, M. Crego-Calama, M.F. Garcia-Parajo and N.F. van Hulst Effect of Disorder on Ultrafast Exciton Dynamics Probed by Single Molecule Spectroscopy. *Phys. Rev. Lett.* **97** 216403 (2006).

[157] M. Backer, W. Häfner and W. Kiefer Raman Studies of Pressure-induced Frequency Shifts in d_0- and d_8-Naphthalene. *J. Raman Spectrosc.* **13** 247–252 (1982).

[158] R.A. Crowell and E.L. Chronister A photon echo study of pentacene in naphthalene at high pressure. *Chem. Phys. Lett.* **216** 293–299 (1993).

[159] D. Rutkauskas, V. Novoderezhkin, A. Gall, J. Olsen, R.J. Cogdell, C.N. Hunter and R. van Grondelle Spectral Trends in the Fluorescence of Single Bacterial Light-Harvesting Complexes: Experiments and Modified Redfield Simulations. *Biophys. J.* **90** 2475–2485 (2006).

Deutsche Zusammenfassung

Das Thema dieser Arbeit war die Untersuchung der spezifischen Anordnung der Bakteriochlorophyll (BChl) *a* Moleküle im Lichtsammelkomplex 1 (LH1) von *Rhodopseudomonas (Rps.) acidophila*. Bei den Purpurbakterien bildet der LH1 Komplex zusammen mit einem Reaktionszentrum (RC) eine geschlossene Einheit, wobei der LH1 Komplex das RC direkt umschließt. Dieses Gesamtkonstrukt ist dann als RC-LH1 Kernkomplex bekannt. Im Rahmen eines zyklischen Elektronentransportes innerhalb der bakteriellen Photosynthese müssen reduzierte Ubiquinon Moleküle, Q_BH_2, das RC verlassen und, durch den LH1 Komplex hindurch, in die Membranumgebung diffundieren. Inzwischen ist allgemein bekannt, dass der LH1 Komplex bei manchen Purpurbakterienarten eine Lücke aufweist, mutmaßlich um den Transfer von Q_BH_2 zu ermöglichen, wohingegen für andere Arten, mit einem komplett geschlossenen LH1 Ring, Kanäle innerhalb des LH1 Komplexes den Durchtritt von Q_BH_2 ermöglichen könnten. Vor dieser Arbeit war nicht bekannt zu welcher dieser beiden Klassen von RC-LH1 Komplexen (unterbrochener *vs.* geschlossener LH1 Ring) der RC-LH1 Komplex von *Rps. acidophila* gehört, ganz zu schweigen von einer genauen Vorstellung über die Anordnung der BChl *a* Moleküle innerhalb des LH1 Aggregates. Es folgt eine kurze Zusammenfassung der Ergebnisse, die im Rahmen dieser Arbeit erzielt wurden.

In einer ersten Reihe von Experimenten wurde der RC-LH1 Komplex von *Rps. acidophila* wieder aufgegriffen, um daran einzelmolekülspektroskopische Untersuchungen durchzuführen. Dabei wurden die Pigment-Proteinkomplexe durch das relativ milde, nicht-denaturierende Detergens, dodecyl-β-D-maltoside (DDM), stabilisiert, anstatt durch das stärker deaktivierende Detergens, lauryldimethylamine N-oxide (LDAO), welches in einer vorangegangenen Studie verwendet wurde. Insgesamt wurden Tieftemperatur (1.2 K)-Fluoreszenzanregungsspektren von 61 einzelnen, in DDM stabilisierten RC-LH1 Komplexen aufgezeichnet, im Vergleich zu lediglich 24 Komplexen, die in der Vorgängerstudie vermessen wurden. Entsprechend ihrer spektralen Merkmale wurden die Komplexe entweder als intakt oder als defekt eingestuft. Durch die Verwendung von DDM anstatt LDAO als Detergens, konnte der Anteil an defekten (dissoziierten) RC-LH1 Komplexen bedeutend gesenkt werden, nämlich von 37.5% in der Vorgängerstudie auf 11.5% in der vorliegenden Arbeit. Aufgrund der verbesserten Qualität der Stammlösung war es möglich, polarisationsaufgelöste Fluoreszenzanregungsspektroskopie zu betreiben und dabei die Verteilungen der spektralen Merkmale der intakten RC-LH1 Komplexe mit einer verbesserten Statistik aufzunehmen. Sowohl diese Verteilungen als auch charakteristische spektrale Merkmale, wie z.B. eine schmale Linie, die für die meisten Komplexe

am roten Ende des detektierten Spektralbereiches auftritt, weisen eine verblüffende Ähnlichkeit mit den Daten von RC-LH1 Komplexen von *Rps. palustris* auf, die im Rahmen einer früheren Studie aufgezeichnet wurden. Für den *Rps. palustris* RC-LH1 Komplex ist eine gering aufgelöste Kristallstruktur verfügbar. Aufgrund der vorgenannten Ähnlichkeit der spektralen Merkmale, kommt man damit zu dem Schluss, dass die LH1 Komplexe von *Rps. acidophila* und *Rps. palustris* durch dasselbe Strukturmodell beschrieben werden können, nämlich durch eine elliptische Anordnung von BChl *a* Molekülen, die eine Lücke aufweist. Somit konnte durch die erfolgreiche Anwendung der Tieftemperatureinzelmolekülspektroskopie als einem Werkzeug für strukturelle Untersuchungen zum ersten Mal gezeigt werden, dass der RC-LH1 Komplex von *Rps. acidophila* eher zu den RC-LH1 Komplexen mit einem unterbrochenen LH1 Aggregat gehört, als zu jenen mit einer komplett geschlossenen LH1 Struktur.

In einer zweiten Reihe von Experimenten wurde der Einfluss der Umgebung auf die Spektren der RC-LH1 Komplexe von *Rps. acidophila* untersucht. Dabei wurden die Komplexe in Detergens (DDM)-Pufferlösung stabilisiert und in eine Phospholipiddoppelschicht rekonstituiert, und die Ergebnisse wurden mit jenen der ersten experimentellen Reihe verglichen (s.o.), die an DDM-stabilisierten RC-LH1 Komplexen durchgeführt wurde, die zusätzlich in einer Polyvinylalkohol (PVA) Matrix immobilisiert waren (DDM/PVA). Das Ziel dieser Experimente war es zu überprüfen, ob die Immobilisierung der RC-LH1 Komplexe in PVA möglicherweise zu einer Deformation der LH1 Struktur führt und somit die Aussagekraft der mithilfe der optischen Spektroskopie gewonnenen Ergebnisse deutlich einschränkt.
In Ensemble Absorptions- und Fluoreszenzanregungsspektren wurden spektrale Verschiebungen sowohl als Funktion der Matrix, als auch als Funktion der Temperatur beobachtet. Bezüglich zweiterem, wurden bei Abkühlung der Probe unterschiedliche spektrale Verschiebungen in den drei Umgebungen festgestellt. Dies konnte stimmig mit einer Erhöhung des lokalen Druckes auf die Komplexe in der Lipiddoppelschicht und in der DDM-Pufferlösung erklärt werden. Demgegenüber ist für die DDM/PVA Umgebung eine Verminderung des lokalen Druckes vorstellbar, da, aufgrund eines negativen thermischen Expansionskoeffizienten für dünne Polymerfilme unterhalb ihrer Glasübergangstemperatur, unter einer Absenkung der Temperatur, eher eine Expansion als eine Kontraktion des PVA-Filmes zu erwarten ist. Bei Tieftemperatureinzelmolekülmessungen wurde festgestellt, dass die in DDM-Pufferlösung befindlichen Komplexe, ohne zusätzliche Stabilisierung in einer PVA Matrix, schnellen spektralen Dynamiken ausgesetzt sind und somit die Erzielung von aussagekräftigen Ergebnissen mittels der Einzelmolekülspektroskopie verhindert wird. Ferner wurde für die in eine Lipiddoppelschicht rekonstituierten Komplexe aufgedeckt, dass der Rekonstitutionsprozess, im Vergleich zur Aufbereitung der Komplexe in einem PVA-Film, zu einem wesentlich höheren Anteil an defekten Komplexen führt. Jedoch wurde auch festgestellt, dass für die intak-

ten Komplexe die Statistiken der wesentlichen spektralen Merkmale, wie z.B. der spektrale Abstand der Banden und die gegenseitige Orientierung ihrer Übergangsdipolmomente, weitgehend identisch sind, falls entweder eine Lipiddoppelschicht oder PVA als Matrix verwendet werden. Trotz des zusätzlichen Aufwandes, der mit dem Rekonstitutionsprozess verbunden ist, findet man also, im Vergleich zur Einbettung der Komplexe in einer PVA Matrix, einen geringeren Anteil an intakten RC-LH1 Komplexen vor, sowie gleiche Ergebnisse für die maßgeblichen spektralen Eigenschaften. Damit kommt man zu dem Schluss, dass die Immobilisierung dieser Pigment-Protein Komplexe in einer PVA Matrix eine gute Wahl ist, um Tieftemperaturexperimente an einzelnen Lichtsammelkomplexen durchzuführen.

In einem nächsten Schritt wurden die Häufigkeitsverteilungen der spektralen Merkmale der intakten RC-LH1 Komplexe mit den entsprechenden Daten aus numerischen Simulationen unterschiedlicher LH1 Modellstrukturen verglichen. Damit sollten neue Erkenntnisse über die spezifische Anordnung der BChl *a* Moleküle innerhalb des LH1 Komplexes von *Rps. acidophila* gewonnen werden. Alle eingeführten LH1 Modellstrukturen lagen innerhalb der Auflösung der *Rps. palustris* RC-LH1 Kristallstruktur und folglich hatten alle LH1 Modelle eine Lücke in der Anordnung ihrer BChl *a* Moleküle. Im Vergleich zu einer früheren Simulationsstudie am RC-LH1 Komplex von *Rps. palustris*, wurden in der vorliegenden Arbeit realistischere Simulationsparameter verwendet, sowohl was den strukturellen Aufbau der RC-LH1 Komplexe angeht, als auch bezüglich der Stärke der elektronischen Kopplung zwischen den Pigmenten.
Zunächst wurden drei unterschiedliche LH1 Modellstrukturen ausgetestet. Bei zwei dieser Modelle wurden starre BChl *a* Dimereinheiten in gleichbleibenden Abständen auf einer Ellipse oder einem Rechteck mit abgerundeten Ecken platziert, wohingegen im dritten Modell die Positionierung der BChl *a* Moleküle der unregelmäßigen Anordnung der Pigmente aus der *Rps. palustris* Kristallstruktur entsprach. Als eine erste Folge der deutlich erhöhten Wechselwirkungsstärke in den Simulationen dieser Arbeit, nimmt die Übergangsenergie der einzelnen Pigmente in allen vorgestellten LH1 Modellen plausible Werte an. Jedoch wurde auch festgestellt, dass keines dieser drei vorläufigen LH1 Modelle in der Lage ist die experimentellen Häufigkeitsverteilungen der spektralen Merkmale der RC-LH1 Komplexe von *Rps. acidophila* zu reproduzieren. Eine sorgfältige Überprüfung der Lokalisierungsmuster der exzitonischen Zustände offenbarte jedoch, dass die beiden niedrigsten Exzitonzustände eines LH1 Komplexes, $k = 1$ und $k = 2$, jeweils in charakteristischen Bereichen des LH1 Aggregates lokalisieren, nämlich dort wo die Werte der Nächsten-Nachbar-Wechselwirkung zwischen den Pigmenten deutlich erhöht sind. Mit diesem Wissen war es möglich, durch eine minimale Veränderung der Positionen von lediglich vier Dimereinheiten in einem der 'regelmäßigen' LH1 Modelle (Rechteck mit abgerundeten Ecken), ein neues LH1 Modell zu generieren, dessen spektrale Eigenschaften sich in zufriedenstellender Übereinstimmung mit den expe-

rimentellen Einzelmolekülspektren befinden. Bei den durchgeführten strukturellen Veränderungen orientierte man sich an der RC-LH1 *palustris* Kristallstruktur und es könnte argumentiert werden, dass sie auf spezifische Wechselwirkungen zwischen RC und LH1 Komplex zurückzuführen sind. Das finale LH1 Modell 'übertrifft' das in einer früheren Studie eingeführte, verfeinerte *Rps. palustris* LH1 Modell deutlich, da für das gegenwärtige Modell sowohl realistischere Simulationsparameter verwendet wurden und es zudem eine wesentlich bessere strukturelle Überlappung mit der *Rps. palustris* RC-LH1 Kristallstruktur aufweist.
Es sollte allerdings beachtet werden, dass in der einzigen hochaufgelösten Kristallstruktur, die bislang von einem RC-LH1 Komplex zur Verfügung steht, kein Nachweis für die spezifischen Veränderungen an der 'regelmäßigen' LH1 Struktur gefunden werden kann. Zudem ist offensichtlich, dass ähnliche strukturelle Veränderungen, wie jene die oben beschrieben wurde, zu weiteren LH1 Strukturen innerhalb der *palustris* Röntgenstruktur führen können, die in der Lage sind die experimentellen Spektren wiederzugeben. Deshalb wird an dieser Stelle nicht behauptet, dass mit dem finalen LH1 Modell die 'einzig wahre' strukturelle Lösung für den LH1 Komplex von *Rps. acidophila* gefunden wurde. Es wurde jedoch gezeigt wie, im Rahmen eines relativ einfachen Simulationsansatzes (Heitler-London Näherung und Dipol-Dipol Wechselwirkung zwischen den Pigmenten), ein LH1 Modell mit einer regelmäßigen Anordnung der Pigmente verändert werden kann, um eine zufriedenstellende Wiedergabe der experimentellen Verteilungen der spektralen Merkmale zu erreichen. Dementsprechend ist das deutlich wichtigere und allgemeingültige Ergebnis aus diesem Teil der Arbeit, dass in exzitonischen Systemen, in denen die Modulation der Nächsten-Nachbar-Wechselwirkung die bestimmende Größe ist, anstatt der diagonalen Unordnung, die beiden niedrigsten Exzitonzustände in charakteristischen Bereichen des LH1 Aggregates lokalisieren, nämlich gerade dort, wo sich die Maxima der Nächsten-Nachbar-Wechselwirkung befinden. Diese Erkenntnis könnte allgemein, für stark gekoppelte Anordnungen von Pigmenten von Bedeutung sein.

Schließlich deckte, initiiert durch eine kürzlich erschienene Arbeit an LH2 Komplexen von *Rps. acidophila*, eine sorgfältige Nachuntersuchung der Spektren von individuellen RC-LH1 Komplexen, die als intakt klassifiziert wurden, auf, dass, anstatt der schmalen Linie am niederenergetischen Ende der Spektren, eine breite Bande von geringer Intensität, die rotverschoben im Vergleich zur schmalen Linie auftritt, möglicherweise den tiefsten Exzitonzustand, $k = 1$, der LH1 Komplexe darstellt. In zukünftigen Messungen könnte diese neue Interpretation überprüft werden, indem man gleichzeitig Fluoreszenzanregungs- und Emissionsspektren derselben individuellen RC-LH1 Komplexe aufzeichnet. Entsprechend der Arbeit an den LH2 Komplexen sollte in diesen Spektren das Kriterium für die Identifikation des niedrigsten Exzitonzustandes sein, dass das Emissionsspektrum direkt aus dem spektralen Bereich hervorgeht, in dem sich der niedrigste Exzitonzustand im Anregungsspektrum befindet. Unter Zuhilfenahme der numerischen Simulationen

aus dem vorherigen Abschnitt könnte argumentiert werden, dass möglicherweise nicht die lange Lebensdauer des $k = 1$ Zustandes im Vergleich zu den höheren Exzitonzuständen für die charakteristische schmale Linie in den RC-LH1 Fluoreszenzanregungsspektren verantwortlich ist, sondern die Lokalisierung der $k = 1$ und $k = 2$ Exzitonzustände auf entgegengesetzten Seiten des LH1 Aggregates. Dies würde die Relaxation des $k = 2$ Zustandes, dem nun die schmale Linie zugeordnet wird, in den $k = 1$ Zustand beeinflussen, da die Rate für diesen Prozess unter anderem von der räumlichen Überlappung der entsprechenden Exzitonwellenfunktionen abhängt. Folglich könnte es sein, dass, aufgrund der vernachlässigbaren Überlappung der $k = 2$ und $k = 1$ Exzitonwellenfunktionen, die schmale Linie, die vergleichsweise langsame Relaxation des $k = 2$ Zustandes in den $k = 1$ Zustand widerspiegelt. Im Gegensatz dazu wurden für die höheren Exzitonzustände ($k \geq 3$) deutlich größere Überlappungen mit der $k = 1$ Exzitonwellenfunktion beobachtet. Dies würde eine schnelle Relaxation dieser Zustände in den $k = 1$ Zustand plausibel machen und entsprechend auch die breiten Banden erklären, die für diese Zustände in den Anregungsspektren beobachtet werden.
Sollte sich diese neue Interpretation der spektralen Eigenschaften als richtig herausstellen, würde dies zum einen die Notwendigkeit unter Beweis stellen, dass gleichzeitig Fluoreszenzanregungs- und Emissionsspektren von individuellen LH Komplexen aufgezeichnet werden müssen, um die Vollständigkeit der Anregungsspektren dieser Komplexe nachzuweisen. Des Weiteren würde dies eine Reinterpretation der Daten nicht nur aus den vorangegangenen Teilen dieser Arbeit notwendig machen, sondern auch von früheren Einzelmolekülstudien an RC-LH1 Komplexen.

Danksagung

Zum Ende dieser Arbeit möchte ich die Gelegenheit nutzen, um mich bei einigen Personen zu bedanken, die wesentlich zum Gelingen ebendieser beigetragen haben.
Zuallererst möchte ich mich bei meinem Doktorvater Prof. Dr. Jürgen Köhler für die interessante Themenstellung bedanken. Diese hat es mir ermöglicht in das spannende Gebiet der RC-LH1 Komplexe einzutauchen, wobei ich (dank SMS) die Ehre hatte jeden Komplex einzeln kennenzulernen. Weiterhin möchte ich Jürgen für seine Fokussierung beim Erstellen der gemeinsamen, wissenschaftlichen Publikationen danken.
Gute Messungen sind nur möglich, wenn man Proben von hervorragender Qualität zur Verfügung gestellt bekommt. Deshalb gilt an dieser Stelle mein besonderer Dank June Southall und Prof. Dr. Richard Cogdell von der University of Glasgow, von denen ich erstklassiges RC-LH1 Material erhielt.
Dem gesamten EP IV Team danke ich für eine angenehme und kollegiale Atmosphäre. Ich werde die morgendlichen Kuchenverköstigungen und den nachmittäglichen Kaffeeplausch mit euch vermissen. Aus dem Sekretariatsteam möchte ich mich besonders bei Evelyn Hülsmann bedanken, die mir bei verwaltungstechnischen Angelegenheiten stets mit Rat und Tat zur Seite stand. Danke auch Werner Reichstein und Stefan Schlicht von der Technischen Abteilung des Lehrstuhls EP IV. Falls man das Glück hatte, dass sich ein vielbeschäftigter Werni einem annahm, war er stets mit vollstem Engagement um eine Problemlösung bemüht. Bei Stefan möchte ich mich insbesondere für das Abdichten meiner Denkzellentür bedanken. So war es mir möglich den Laborlärm auszuschließen, um in Ruhe über RC-LH1 nachzudenken.
Ganz besonderer Dank gebührt meinem langjährigen Laborpartner Ralf Kunz. Von ihm hat diese Arbeit in vielerlei Hinsicht profitiert, sei es durch seine wertvollen Tipps in Bezug auf allerlei Computerprogramme (*Origin, Adobe Illustrator, Pymol*) oder durch seine perfekte Justage des SMS-Aufbaus, ohne die auch die LH1 Messungen wohl nie so gut geworden wären, wie sie es letztlich geworden sind. Auch möchte ich mich bei Ralf dafür bedanken, dass er sich sogar noch nach seiner EP IV Laufbahn die Zeit nahm, diese Arbeit komplett Korrektur zu lesen.
Bei Tobias Pflock möchte ich mich für seine Einführung in die Kunst der Rekonstitution bedanken. Obwohl diese schon während meiner Diplomarbeit stattfand, waren die dort erlangten Kenntnisse für den Erfolg gewisser Teile dieser Arbeit wesentlich.
Richard Hildner gebührt Dank für das ausdauernde Korrekturlesen dieser Arbeit. Seine Tipps haben Struktur in diese Arbeit gebracht und sie leserlicher gemacht. Vielen Dank auch dafür, dass ich dich in den Kaffeepausen stets mit physikalischen Fragen belästigen durfte.

Bei Rebi möchte ich mich für das Korrekturlesen der deutschen Zusammenfassung bedanken, sowie für die Streichung der darin befindlichen, überzähligen Kommas. Schließlich ergeht entscheidender Dank an meine Eltern, ohne eure vielfältige Unterstützung (auch finanzieller Art) wäre diese Arbeit niemals möglich gewesen.

Bayreuth, im März 2015

Erklärung

Hiermit versichere ich an Eides statt, dass ich die vorliegende Arbeit selbstständig verfasst und keine anderen als die von mir angegebenen Quellen und Hilfsmittel benutzt habe.

Ich erkläre, dass ich keine früheren Promotionsversuche unternommen habe. Die vorgelegte Abhandlung wurde weder in gleicher noch in ähnlicher Form einer anderen Prüfungsbehörde zur Erlangung eines akademischen Grades vorgelegt.

Des Weiteren erkläre ich, dass ich Hilfe von gewerblichen Promotionsberatern bzw. -vermittlern oder ähnlichen Dienstleistern weder bisher in Anspruch genommen habe, noch künftig in Anspruch nehmen werde.

Bayreuth, den 15.10.2014

Paul Böhm